NUMERICAL INVESTIGATION OF LIGHT SCATTERING BY ATMOSPHERIC PARTICLES

A Dissertation

by

CHAO LIU

Submitted to the Office of Graduate Studies of
Texas A&M University
in partial fulfillment of the requirements for the degree of

DOCTOR OF PHILOSOPHY

Chair of Committee,	Richard Lee Panetta
Co-chair of Comittee,	Ping Yang
Committee Members,	Sarah D. Brooks
	Jean-Luc Guermond
Head of Department,	Ping Yang

August 2013

Major Subject: Atmospheric Sciences

ABSTRACT

Atmospheric particles, i.e. ice crystals, dust particles, and black carbon, show significant complexities like irregular geometries, inhomogeneity, small-scale surface structures, and play a significant role in the atmosphere by scattering and absorbing the incident solar radiation and terrestrial thermal emission. Knowledge of aerosol scattering properties is a fundamental but challenging aspect of radiative transfer studies and remote sensing applications. This dissertation tries to improve our understanding on the scattering properties of atmospheric particles by investigating both the scattering algorithms and the representation of the realistic particles.

One part of this dissertation discusses in details the pseudo-spectral time domain algorithm (PSTD) for calculating scattering properties, its advantages and the elimination of the Gibbs phenomenon. The applicability of the parallelized PSTD implementation is investigated for both spherical and nonspherical particles over a wide range of sizes and refractive indices, and the PSTD is applied for spherical particles with size parameters up to 200, and randomly oriented non-spherical ones with size parameters up to 100. The relative strengths of the PSTD are also shown by a systematic comparison with the discrete dipole approximation (DDA). The PSTD outperforms the DDA for particles with refractive indices larger than 1.4, and ones with smaller refractive indices by large sizes (e.g. size parameters larger than 60 for a refractive index of 1.2). The results suggest significant potential of the PSTD for the numerical investigation of the light scattering and corresponding atmospheric applications.

The other part of this dissertation investigates the effects of particle complexities on the light scattering properties of the atmospheric particles, and three aspects

corresponding to the irregular geometry, inhomogeneity and surface roughness are studied. To cover the entire particle size range from the Rayleigh to the geometric-optics regimes, the PSTD (for relatively small particles) is combined with the improved geometric-optics method (IGOM) that is only applicable for large particles. The Koch-fractal geometry is introduced to model the light scattering properties of aerosol, and performs an excellent job of reproducing the experimental measurements of various mineral dust particles. For the inhomogeneous particles, the applicability of the effective medium approximations (EMA) is tested, and the EMA can be used to approximate the scattering properties of inhomogeneous particles only when the particles are uniformly internal mixtures. Furthermore, an irregular rough model is developed to study the effects of the small-scale surface roughness on the light scattering properties. In conclusion, the dissertation finds that the complexities of atmospheric particles have to be fully considered to obtain their scattering properties accurately.

ACKNOWLEDGEMENTS

I would like to take this opportunity to sincerely thank all people who have helped and inspired me during my Ph. D. program. I would especially express my gratitude to my academic advisors, Dr. R. Lee Panetta and Dr. Ping Yang, not only for their insightful guidance, but also for their inspiration and encouragement in my study. I would never forget the days Dr. Panetta worked until 4 AM helping me to revise the manuscripts, and always immediate responses and suggestions from Dr. Yang at any time and any day. Dr. Ping Yang's research is supported by National Science Foundation (ATM-0803779), and NASA grants (NNX11AK37G), and the endowment funds related to the David Bullock Harris Chair in Geosciences at the College of Geosciences, Texas A&M University. Additional thanks are extended to the other committee members, Dr. Sarah Brooks, Dr. Guido Kanschat and Dr. Jean-Luc Guermond, for their detailed and constructive comments. Their suggestions on improving my research and the dissertation are very helpful.

I would also acknowledge Drs. George Kattawar and Lei Bi who gave me important guidance throughout this work. Their valuable ideals and advice have had a remarkable influence on my research. I appreciate discussions with my group members, Drs. Yu Xie, Yu You, Hua Li, and Shouguo Ding, and other colleagues in our group and the Department of Atmospheric Sciences. It is such an enjoyable experience to work with them.

Last, but not the least, special thanks go to my parents, uncle's family and friends for their unconditional love and support throughout my life.

NOMENCLATURE

PSTD	Pseudo-spectral time domain method
FDTD	Finite-difference time domain method
DDA	Discretise dipole approximation
IGOM	Improved geometric-optics method
P	Phase matrix
Q_{ext}	Extinction efficiency
SSA	Single-scattering albedo
g	Asymmetry factor
RE	Relative error
$RMSRE$	Root-mean-square of relative errors
$RMSAE$	Root-mean-square of absolute errors

TABLE OF CONTENTS

LIST OF FIGURES

FIGURE Page

LIST OF TABLES

TABLE Page

1. INTRODUCTION

The transfer of solar and thermal infrared radiation in the atmosphere involves absorption, scattering and emission, and has a significant impact on the weather system and climate of the Earth. To understand and account the radiative characteristics of the atmosphere, we must begin with the optical properties of the single particles that are abundant in the atmosphere, e.g. droplets in water clouds, ice crystal in cirrus, and airborne aerosol particles. Knowledge of the atmospheric particle scattering properties is a fundamental but challenging aspect of radiative transfer studies and remote sensing applications. However, even with narrow focus on single-scattering properties of atmospheric particles, significant obstacles are still remaining for a comprehensive understanding and further applications. This dissertation presents some numerical investigations on the single-scattering properties of the atmospheric particles, and encompasses models on both light scattering algorithm and representation of the realistic particles.

This chapter presents an introduction on light scattering and the motivation of this study. Section 1.1 briefly discusses the current light scattering models, most of which will be used in this dissertation, and Section 1.2 demonstrates the complexities of the atmospheric particles. The basic concepts and quantities interested will be introduced in Section 1.3, and Section 1.4 describes the organization of this dissertation.

1.1 Light scattering models

Numerical investigation on the light scattering by particles has a history of over a century [1, 2, 3, 4, 5, 6], and substantial effort has been devoted to improve our understanding on the single-particle scattering properties, especially those of non-

spherical particles. The early studies of particulate single-scattering properties were focused on spheres [7, 8, 9], and results of their work has become known as the Lorenz-Mie theory, the exact solution or "gold standard" in single scattering by homogeneous spheres. Based on the Lorenz-Mie theory, various improvement has been developed to consider more complicated particles with basic spherical geometries, e.g. the core-mantle Mie theory for stratified spheres [10, 11], and generalized multi-particle Mie for aggregates of spheres [12, 13]. Optical properties of nonspherical particles are more difficult to obtain than those of spheres, and will be the focus of this dissertation. This subsection briefly introduces some well-developed and accepted models that will be used as references in this study, and show the current modeling capabilities.

In scattering calculations, what is crucially important is the relation between the size of the particle and the wavelength of the incident light. For a spherical particle of radius a and incident wavelength λ, the size parameter x is defined by

$$x = \frac{2\pi\, a}{\lambda}.$$

In the regime of very large particles, $x >> 1$, i.e. known as the geometry-optics regime, ray theories and geometric optics are useful and computationally inexpensive, whereas, in the Rayleigh regime, $x << 1$, computations are also inexpensive. In the intermediate case, i.e. the resonant regimes, recourse must be made to numerical solution of some form of Maxwell's equations. In this case, CPU demands typically grow rapidly as x increases, especially for refractive indices m that become significantly larger than 1.

Considering the widely spread sizes of the atmospheric particles (from aerosol particles of submicron to ice aggregates with thousands of microns), there is still no

single model that can be applied to cover the complete particle size range from the Rayleigh to the geometric optics regimes. Given the current computational resources available to most researchers, the effective bound for all but truly heroic efforts begins to be felt for particles with $x \sim 100$. One of the interests of this dissertation is in pushing this technology-imposed boundary and we will present results indicating that the pseudo-spectral time domain method (PSTD) shows promise of helping us to do so.

In distinguishing various computational methods, the potentially confusing terminology "numerically exact" is sometimes used in electromagnetic scattering studies. We will use this terminology, and for clarity explain here what we understand by it. Underlying any computational method is a physical model and a numerical model. The physical model has mathematical expression in differential or integro-differential equations that have "exact" solutions; the numerical models are also expressed as equations, usually in algebraic form, and have "numerical" solutions. The numerical model is designed so that its numerical solution is an approximation of the exact solution of the corresponding physical model, and the closeness of this approximation is controlled by one or more key numerical parameters. In principle (that is, ignoring computational cost and machine-specific issues of round-off error) the numerical parameters can be adjusted to achieve any desired level of accuracy. In the terminology of numerical analysis this property of a numerical scheme is called "convergence." The term "numerically exact" has come to be reserved in electromagnetic scattering studies for a computational method in which the numerical scheme is convergent and the exact model is some form of Maxwell's equations.

A powerful and popular approach for atmospheric nonspherical particles is the T-matrix method based on the extended-boundary-condition technique (EBCM) [14, 15, 16, 17]. The central idea in the approach is to represent the incident and

scattered fields as expansions in vector spherical harmonic series, with the T-matrix being a transform matrix mapping the sequences of expansion coefficients for incident waves to those of scattered waves. Once the T-matrix is given, all the far-field scattering properties are derived from analytical formulas. The T-matrix itself involves calculation of various integral properties that depend on the particle doing the scattering. Using extended precision arithmetic, Mischenko and Travis [17] showed T-matrix results for spheroids or circular cylinders with size parameters over 100. The calculation of the T-matrix, in principle, is possible for particles of any size or shape, but can run into numerical difficulties in dealing with particles that have large aspect ratios or nonsymmetric geometries. Aside from such situations, the approach is widely regarded as a good source of "reference solutions," and we will make use of it as appropriate. Recently, the T-matrix method based on the invariant imbedding method (IIM) [18, 19] shows to be capable of solving light-scattering problems for large nonspherical particles where the standard EBCM fails to converge, and reaches size parameter of 300 for spheroids and circular cylinders.

The discrete dipole approximation (DDA) [20, 21, 22, 23, 24] and the finite-difference time domain method (FDTD) [25, 26, 27], are two methods which can be used for scatterers with arbitrary shapes, and have been widely applied to simulate single-scattering properties of atmospheric particles, e.g. hexagonal columns [26], droxtals [28], tri-axial ellipsoids [29], and other shapes. Both DDA and FDTD discretizes the three-dimensional spatial domain, with dipoles or grid cells, and solve Maxwell's equations. However, even with parallelized implementations [30, 31] on multi-processors, they are applicable for only particles with smaller-to-moderate size parameters, say x a few multiples of 10, and become computationally expensive and impractical for large ones.

To the best of our knowledge, the maximum size parameter of spheres with re-

fractive index significantly larger than 1.0 that has been simulated using DDA is 130 (using a refractive index of 1.2) [30]. Furthermore, because of the high requirement for the spatial resolution (10 to 20 grid cells per wavelength in the particle) and numerical dispersion, the FDTD technique is difficult to apply for particles with size parameter over 100. If results involving averaging over random orientations are required for non-spherical particles, both methods become prohibitively time-consuming (given current hardware) for averaging over tens to hundreds particle orientations.

The T-Matrix, DDA, and FDTD methods, all solve Maxwell's equations in this "numerically exact" sense, with the parameter controlling some form of expansion terms or spatial resolution. The methods can, aside from considerations of the computational cost that grows with particle size, be applied throughout the entire range of sizes of atmospheric aerosols. The limit on this use is essentially determined by the state of computational hardware. The various geometric-optics methods (GOM), on the other hand, are not numerically exact because they involve approximations whose physical justification limit use to "large" particles (size parameters up to few hundreds). The conventional GOM (CGOM) [32, 33, 34] and the improved GOM (IGOM) [35, 36, 37] have been developed to simulate light scattering by moderate-to-large sized particles. Although significant improvements have been included in IGOM, the near fields are approximated with the ray-tracing method in these approaches, making this an inappropriate method for small- to moderate-size particles. The recently developed physical-geometric optical hybrid method (PGOH) [38] is suitable for calculating the optical properties of particles with complex refractive indices and a fixed orientation. By employing a beam-splitting technique instead of the ray-tracing algorithm, virtually no limitation exists on the maximum particle size parameter for the PGOH method. However, it becomes greatly compromised

for particles with size parameters smaller than 50.

1.2 Atmospheric particles

Compared with the limitations on the scattering algorithms, our knowledge on the microphysical properties of the atmospheric particles poses a greater challenge on accurate modeling of their single-scattering properties, because the atmospheric particles are highly complex with irregularly geometries, heterogeneous components, and small-scale surface roughness [39, 40, 41, 42, 43, 44]. All those complexities have been considered to some degree in calculating the single-scattering properties of the ice crystals or aerosol particles, whereas a lot of over-simplified models and approximations that were not well validated are still widely used. Although in-situ and laboratory measurements provided some reliable information on both the microphysical and optical properties of various atmospheric particles, it is extremely difficult to represent them numerically, and numerical studies on their scattering properties are still necessary and important for radiative transfer and remote sensing applications. To validate the previous approximations and develop advanced models for more accurate representation of the atmospheric particles more accurately come as important research problems, and this dissertation will focus on the following three forms of particle complexities.

First, most atmospheric particles show complex irregular geometries. The most basic and common shape of the ice crystals is hexagonal column or plate, whereas, due to the complex atmospheric environment during their growth, air bubbles, hollow structures, aggregation, and surface roughness are present, which make the modeling quite challenging. The world of aerosol particles is even more complex because of the irregular geometries and significant variations, and substantial efforts have been reported to use simple geometry to simulate optical properties of the mineral dust

or black carbon particles. For dust aerosols, those geometries include the spheroids, tri-axial ellipsoids, and nor-symmetrical hexahedra [29, 45, 46], but most of them are based on over simplified convex particles and a combination of multiple geometries of different particles. However, those models may still underestimate the irregularity of the realistic particles, and different combinations have to be used to match the laboratory measurements of different kinds of aerosol, or even the same aerosol particles at two different wavelengths.

Furthermore, a large amount of natural aerosols occur as mixtures of various components whose optical properties are quite different, and the detailed particle shapes, sizes, fractions of the components, and mixing states vary significantly under different atmospheric environments. For simplification, the inhomogeneous particles are normally treated as homogeneous ones, the light scattering properties of which can be obtained much more easily, and the effective medium approximation (EMA) is used to calculate the effective refractive index for a mixture. For both theoretical and measurement-based studies, the EMAs usually consider only the fraction of each component, and calculate an effective refractive index, with which the homogeneous particle is expected to give similar optical properties to its inhomogeneous counterpart. Considering the complex mixing states of the atmospheric aerosols, the applicability of the EMAs for the aerosol particles of different kinds becomes highly doubtable but was seldom systemically tested. As a results, it becomes important to know the accuracy of those EMAs under different circumstances of mixing states, and, thus, to obtain useful guides for the application of the EMAs.

Last, but not the least, the small-scale surface roughness has been widely observed on atmospheric particles, and considered in modeling their optical properties as well as remote sensing applications [47, 48]. However, specifying the observed small-scale structures in quantitative detail is extremely difficult, and considering those surface

roughness in the light scattering models is even more challenging. Previous studies were applicable on either small-to-moderate sized particles based on the numerical exact methods or large ones in geometric optics ranges. For the large particles, the approximated method based on the GOMs were commonly used without sufficient validation. Thus, the effect of the surface roughness on the light scattering properties as well as the more realistic roughness representation is still a wide open question.

All those complexities of realistic particles are widely observed and considered to some degree in light scattering simulations, whereas, as mentioned above, our knowledge on these microphysical properties and corresponding optical effects is still significantly limited. In Chapter 3, we will not only develop new particle models that are used to reproduce the optical properties of the atmospheric particles, but also validate and test some widely used approximations related to the light scattering simulations.

1.3 Scattering properties of interest

The single-scattering properties encompass the entire absorption and scattering characteristics, the angular distribution and polarization state of the scattered radiation. In this dissertation, the central scattering quantities that will be heavily discussed are phase matrix (P), extinction efficiency (Q_{ext}), single-scattering albedo (SSA) and asymmetry factor (g).

Light scattering is the interaction between the electromagnetic field and particles, and the electric field associated with a monochromatic plane wave can be written as:

$$\vec{E}(\vec{r}) = \vec{\mathcal{E}} \exp^{i(\vec{k}\cdot\vec{r}-\omega t)}, \tag{1.1}$$

and the direction of propagation is given by the unit vector $\hat{k}$, where $\vec{k} = k\,\hat{k}$. The amplitude k is variously called the wavenumber or propagation constant, and

is related to the wavelength λ by $k = 2\pi/\lambda$. The constant vector $\vec{\mathcal{E}}$ has non-zero components only in directions orthogonal to the direction of propagation $\hat{k}$, and is normally decomposed into two components parallel and perpendicular to a reference plane:

$$\vec{\mathcal{E}} = \mathcal{E}_{\parallel}\hat{e}_{\parallel} + \mathcal{E}_{\perp}\hat{e}_{\perp} \tag{1.2}$$

The vector $\vec{\mathcal{E}}$ is thus specified by two components in $\hat{e}_{\parallel}$ and $\hat{e}_{\perp}$ directions with complex magnitudes $\mathcal{E}_{\parallel}$ and $\mathcal{E}_{\perp}$. (Or we can express $\mathcal{E}$ in the form of Ae^{ϕ}, and the real numbers A and ϕ indicate the amplitude and phase, repectively. Note that the phase angles $\phi_{\parallel}$ and $\phi_{\perp}$ neither are individually measurable nor have intrinsic physical significance. It is only the difference $\phi_{\parallel} - \phi_{\perp}$ that has intrinsic physical significance, so there are in fact only three significant quantities: $A_{\parallel}$, $A_{\perp}$, and $\phi_{\parallel} - \phi_{\perp}$.)

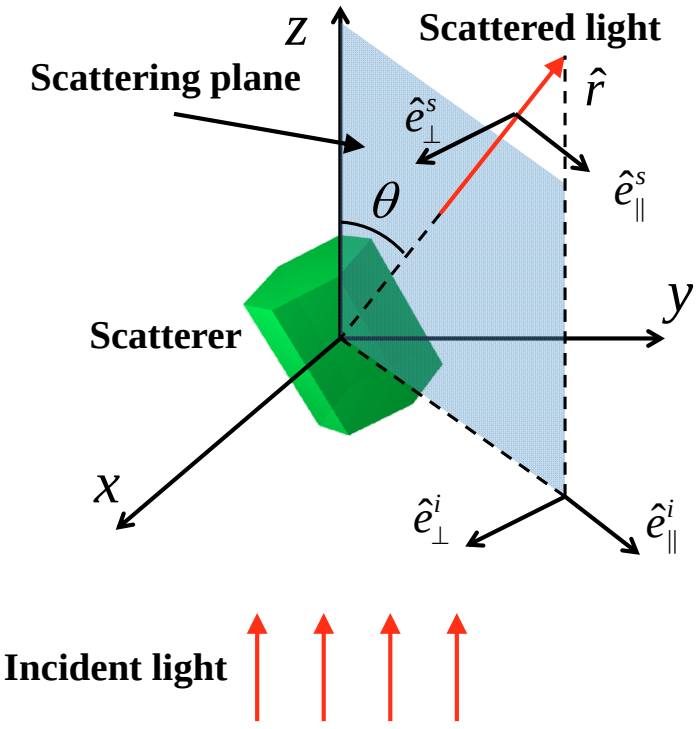

Figure 1.1: The geometry configuration associated with the scattering.

Figure 1.1 illustrates the basic geometry configuration associated with a scattering problem, and the scatterer is the green hexagonal column located in the origin. As shown in Figure 1.1, the incident wave is assumed to propagate along z direction. The incident wave interacts with the particle and the outgoing scattering wave will be excited and propagate over the entire 4π steradian angles. The angle between the incident and scattered directions is called the scattering angle (indicated as θ in the figure). A reference plane, which includes both the incident and scattering directions, is chosen to decompose the electric field, and the plane is refereed as the principal-scattering plane, shown in the figure with blue. For the incident wave, the horizontal component $\mathcal{E}_{\parallel}^{i}\hat{e}_{\parallel}^{i}$ is in the scattering plane, and the vertical component $\mathcal{E}_{\perp}^{i}\hat{e}_{\perp}^{i}$ is perpendicular to the plane. Similarly to the incident field, the scattered wave can be expressed by the two components of $\mathcal{E}_{\parallel}^{s}\hat{e}_{\parallel}^{s}$ and $\mathcal{E}_{\perp}^{s}\hat{e}_{\perp}^{s}$. Notice that $\hat{e}_{\parallel}^{i}$ and $\hat{e}_{\parallel}^{s}$ are the same, whereas $\hat{e}_{\perp}^{i} \cdot \hat{e}_{\perp}^{s} = cos\theta$.

In the immediate vicinity of the scatterer, the electromagnetic field can have quite complex structure, but, for an observer at a large distance r from the scatterer (i.e. $r >> \lambda$), the field is well approximated by a simple outgoing wave. With the interaction being linear, the scattered field can be related to the incident field by a matrix multiplication. With respect to each scattering plane, the relation between the incident and the scattered fields can be given by:

$$\begin{bmatrix} \mathcal{E}_{\parallel}^{s} \\ \mathcal{E}_{\perp}^{s} \end{bmatrix} = \frac{exp\,(ikr)}{-ikr} \begin{bmatrix} \mathcal{A}_2 & \mathcal{A}_3 \\ \mathcal{A}_4 & \mathcal{A}_1 \end{bmatrix} \begin{bmatrix} \mathcal{E}_{\parallel}^{i} \\ \mathcal{E}_{\perp}^{i} \end{bmatrix} \tag{1.3}$$

where the 2×2 matrix $\mathcal{A}$ is called the complex amplitude scattering matrix. It has four complex components that transform the incident electric field components to the scattered ones, and contains all the single-scattering property information of a

scatterer. (Considering that only the relative phase is meaningful, there are only seven independent real variables in the matrix.)

Meanwhile, the wave can also be described in terms of a related set of four real numbers, called the Stokes parameters, that are measurable:

$$I = \frac{1}{2}\sqrt{\frac{\epsilon}{\mu}}\left(\mathcal{E}_{\parallel}\cdot\mathcal{E}_{\parallel}^{*}+\mathcal{E}_{\perp}\cdot\mathcal{E}_{\perp}^{*}\right), \tag{1.4}$$

$$Q = \frac{1}{2}\sqrt{\frac{\epsilon}{\mu}}\left(\mathcal{E}_{\parallel}\cdot\mathcal{E}_{\parallel}^{*}-\mathcal{E}_{\perp}\cdot\mathcal{E}_{\perp}^{*}\right), \tag{1.5}$$

$$U = \frac{1}{2}\sqrt{\frac{\epsilon}{\mu}}\left(\mathcal{E}_{\parallel}\cdot\mathcal{E}_{\perp}^{*}+\mathcal{E}_{\perp}\cdot\mathcal{E}_{\parallel}^{*}\right), \tag{1.6}$$

$$V = i\cdot\frac{1}{2}\sqrt{\frac{\epsilon}{\mu}}\left(\mathcal{E}_{\parallel}\cdot\mathcal{E}_{\perp}^{*}-\mathcal{E}_{\perp}\cdot\mathcal{E}_{\parallel}^{*}\right). \tag{1.7}$$

It should be noticed that each of the components has the units of irradiance, whereas the constant factor $\frac{1}{2}\sqrt{\frac{\epsilon}{\mu}}$ is normally omitted because the Stokes parameters are often discussed in relative sense. These numbers are the four components of the Stokes vector $\vec{S}$. The component I gives the intensity of the wave; the pair (Q, U) are related to the linear polarization, and V is determined by the circular polarization [49].

Instead of the amplitude scattering matrix with complex numbers given in Equation 1.3, the relation between the incident and scattered waves can also be expressed in the form of the Stokes parameters that are all real. Using a spherical coordinate system centered on the particle and considering an observation point at scattering direction given by zenith and azimuth angles (θ, ϕ), the linear relation can be written

$$\vec{S}_s(\theta,\phi) = \frac{1}{k^2r^2}\,\mathbf{F}(\theta,\phi)\,\vec{S}_i \qquad\qquad (k\,r >> 1). \tag{1.8}$$

This form results in a matrix $\mathbf{F}$ whose component F_{11} has the property [50] that

integration over all scattering angles produces

$$\sigma_{sca} = \frac{1}{k^2} \int_0^{2\pi} \int_0^{\pi} F_{11}(\theta, \phi) sin\theta \, d\theta \, d\phi,$$

where σ_{sca} is the scattering cross section of the scatterer: the area that if oriented perpendicular to the incident wave would intercept an amount of energy equal to that scattered in all directions by the scatterer.

We will use the scattering cross section as part of a normalization of the matrix **F** in Equation 1.8, rewriting that equation in terms of the normalized phase matrix P:

$$\vec{S}_s = \frac{\sigma_{sca}}{4\pi r^2} \, P \, \vec{S}_i, \qquad\qquad (k\,r >> 1). \tag{1.9}$$

The terminology "phase matrix", i.e. the matrix defined by the relation in Equation 1.9, has nothing to do with the phase of a plane wave. The relation between the amplitude scattering matrix $\mathcal{A}$ and phase matrix P can be easily obtained from Equation 1.3 and the definition of the Stokes parameters [1, 50, 51], and will not be listed here. The P_{11} element of the phase matrix is normally called the phase function.

For a general scatterer with no geometric symmetries, there are sixteen non-zero elements $P_{i\,j}$ in the matrix P (same as the amplitude scattering matrix, only 7 of the 16 elements are independent), but for a spherical scatterer the phase matrix is independent of the azimuthal angle ϕ and has a particularly simple block diagonal

form with only four independent non-zero entries:

$$P_{sphere} = \begin{bmatrix} P_{11} & P_{12} & 0 & 0 \\ P_{12} & P_{11} & 0 & 0 \\ 0 & 0 & P_{33} & P_{34} \\ 0 & 0 & -P_{34} & P_{33} \end{bmatrix} \qquad \text{(all quantities functions of } \theta\text{)}.$$

Explicit expressions for these elements can be easily given by the Lorenz-Mie theory in the case of a homogeneous sphere. In the general case of a scatterer with no special symmetries, another variable enters the problem: the orientation of the scatterer with respect to the incident wave field. In many applications in remote sensing, where scattering is done by an ensemble of aerosols at random orientations, and, with the aerosols spatially separated by distances considerably greater than a wavelength so that multiple scattering effects may be neglected, it becomes useful to consider the phase matrix that results from averaging over "random" orientations (i.e., assuming a uniform probability distribution over orientation angles and equal number of particles and their mirror particles). In this case it can be shown by taking advantage of symmetry arguments that what results is a phase matrix P_{avg} having a similar block diagonal form but now six independent non-zero entries:

$$P_{avg} = \begin{bmatrix} P_{11} & P_{12} & 0 & 0 \\ P_{12} & P_{22} & 0 & 0 \\ 0 & 0 & P_{33} & P_{34} \\ 0 & 0 & -P_{34} & P_{44} \end{bmatrix} \qquad \text{(all quantities functions of } \theta\text{)}.$$

As mentioned above, the scattering cross section σ_{sca} is the area oriented perpendicular to the incident wave that would intercept an amount of energy equal to

that scattered in all directions by the scatterer. The scattering efficiency Q_{sca} is the non-dimensional number that expresses the ratio of this area to the projected area of the scatterer on a plane normal to the incident wave:

$$Q_{sca} = \frac{\sigma_{sca}}{\text{projected area}}\,.$$

Similar definitions give the absorption efficiency Q_{abs} and extinction efficiency Q_{ext} using their respective cross sections. According to the optical theorem, the total extinction cross section of light is given by:

$$\sigma_{ext} = \frac{2\pi}{k^2}\left[\mathcal{A}_1(0^o) + \mathcal{A}_2(0^o)\right],$$

Energy conservation requires that $Q_{ext} = Q_{sca} + Q_{abs}$, so any two of these efficiencies determine the third. A related variable is the fraction of extinction due to scattering, called the single-scattering albedo (SSA):

$$SSA = \frac{Q_{sca}}{Q_{sca} + Q_{abs}}.$$

As the particle gets less and less absorptive its SSA approaches 1.

Another integral parameter related to the asymmetry in scattering amplitudes between the forward and backward directions is quantified by the asymmetry factor g, defined by

$$g = \frac{1}{2}\int_0^\pi P_{11}(\theta) cos\theta sin\theta\, d\theta.$$

The extinction efficiency, single-scattering albedo, asymmetry factor are important parameters in many climate models, and, together with the phase matrix (especially the phase function P_{11}), will be the main quantities discussed in this disser-

tation.

1.4 Organization of the dissertation

The remainder of this dissertation is organized as follows. Chapter 2 discusses the PSTD method for light scattering simulations, and the spectral method will also be presented. The accuracy, efficiency and applicability of the parallelized PSTD implementation will be verified by comparison with the results from the Lorenz-Mie, T-matrix, core-mantle Mie, DDA and IGOM methods (Section 2.4). The relative strength of the PSTD is discussed by comparing with the DDA (Section 2.5). With the wide range of applicability shown by the PSTD, Chapter 3 presents its applications on considering complexity of atmospheric particles. The effects of particle irregular geometry (Section 3.1), inhomogeneity (Section 3.2), and surface roughness (Section 3.3) on the light scattering properties will be discussed, and particular attentions are paid to validation of old approximations for light scattering simulations and development of new particle models representing realistic atmospheric particles. In Chapter 4, we conclude the present research.

2. PSEUDO-SPECTRAL TIME DOMAIN METHOD *

Stemming from the traditional FDTD method, the PSTD solves Maxwell's curl equations in the time domain, and the central difference between the PSTD and FDTD methods is in the treatment of spatial differentiation, i.e. the spectral and finite difference methods, respectively. In place of a finite difference approximation to spatial derivatives (commonly second order), the PSTD method uses pairs of Fourier transforms at each time step and results in a much more accurate approximation, what is known as "spectral accurate." Furthermore, the spectral sweeps away the complexity of cell wall edge representation (Yee cell [25]) for purpose of the finite difference method, and evaluates variables at the grid points that are the centers of cells in the FDTD formulation. Furthermore, the spectral method has the nature of extremely low numerical dispersion, and can be carried out efficiently with the Fast Fourier Transform (FFT) and inverse FFT (IFFT). All those characters leads to the significant applicability of the PSTD in light scattering simulations that will be shown in this chapter.

Before we discuss on previous work with the PSTD in light scattering problems, it is useful to mention that the spectral methods have a long history starting in fluid dynamical studies the early 1970's [52, 53]. They now have achieved considerable sophistication and have extensive use in numerical studies of many partial differential

* Part of this section is reprinted with permission from "Application of the pseudo-spectral time domain method to compute particle single-scattering properties for size parameters up to 200" by C. Liu, R. L. Panetta, and P. Yang, J. Quant. Spectrosc. Radiat. Transfer, 113, 1728-1740, "Comparison between the pseudo-spectral time domain method and the discrete dipole approximation for light scattering simulations" by C. Liu, L. Bi, R. L. Panetta, P. Yang, and M. A. Yurkin, 2012, Optics Express, 20, 16763-16776, and a chapter in book "A pseudo-spectral time domain method for light scattering computations", by R. L. Panetta, C. Liu and P. Yang, 2013: Chapter 4 in Light Scattering Reviews Vol. 8: Radiative Transfer and Light Scattering, edited by A. A. Kokhanovsky, Springer-Praxis.

equations. Their principle advantage is their ability to approximate derivatives much more accurately and efficiently than is possible with the finite difference methods. The terminology "pseudo-spectral" was introduced by Orszag [53] to distinguish the method from true, or fully spectral, methods in which all calculations are carried out in wavenumber space. Fully spectral methods are made prohibitively expensive by the presence of quadratic nonlinearities in the equations of fluid motion. It was the breakthrough observation of Orszag [53] that a combination of approaches, computation of derivatives by Fourier transform methods and computation of nonlinear terms by grid point multiplication, could yield a significant improvement in numerical performance over the finite difference methods, provided that such an efficient Fourier transform algorithm as the Fast Fourier Transform (FFT) is available. The term pseudo-spectral has since come to mean any of a class of methods that generalize the Fourier interpolation method that we outline in Section 2.2.

The use of the PSTD in electromagnetic scattering problems was pioneered by Liu [54, 55, 56, 57], Yang et al. [58] and Yang and Hesthaven [59, 60], and has been applied in a number of forms to model the transient electromagnetic field by solving Maxwell's equations. The spectral method based on trigonometric polynomials [56] and Chebyshev polynomials [58] has been used to give a better approximation for the spatial derivatives, and the multi-domain PSTD method in general curvilinear coordinates has been developed to solve problems with complex structures in a manner avoiding the Gibbs phenomenon [59, 60, 61]. Chen et al. [62] have successfully used the PSTD to calculate the single-scattering properties of atmospheric particles, treating spheres with a maximum size parameter of 80 (refractive index of 1.31), and have also shown the PSTD to be a robust method for light scattering problems of non-spherical particles such as hollow hexagonal columns and hexagonal aggregates. Based on the work of Chen et al. [62] and Chen [63], this study improved and par-

allelized the PSTD implementation, using spectral filters in wavenumber space to eliminate the Gibbs phenomenon and stabilize the simulation in a manner that we explain below. At the stage of this dissertation, the applicability of PSTD has been demonstrated for spheres with size parameters up to 200, as well randomly oriented non-spherical particles with size parameters up to 100.

This chapter is organized into six parts. Section 2.2 describes the framework of the PSTD algorithm, and a detailed discussion on the PS is presented in the subsection 2.2.3. The parallelization of the PSTD implementation is given in Section 2.3. Section 2.4 presents the results for validation and shows the applicability of the current PSTD implementation. The relative strength of the PSTD is discussed by comparing with the DDA in Section 2.5, and Section 2.6 summaries this part.

2.1 Methodology

The PSTD, solving Maxwell's curl equations in time domain, is a numerically exact method for light scattering simulations. The PSTD in this study uses the spectral method to approximate the derivatives in the spatial domain, and the second-order finite difference method in the temporal domain. The scatterer is specified by the spatial distribution of the permittivity. The absorbtion boundary condition (ABC) is used to attenuate the outgoing waves, and a uniaxial perfectly matched layer (UPML) ABC [64] is used in this study. Figure 2.1 illustrates a two-dimensional cross-section of the computational domain for the PSTD. The scatterer, the light gray circle in the figure, is at the center of the computational domain surrounded by the UPML boundary layer (dark gray boarder). The white region between the scatterer and the UPML is meant to represent a free space region (i.e. vacuum). It should be noticed that the relative sizes of areas in the sketch do not correspond to the relative sizes in our simulations. The incident wave can be sent to the particle

from any direction, and, because of the presence of the particle, i.e. inhomogeneity of the optical constant in the space, it will interact with the scatterer and excite the scattered waves. The PSTD simulation tracks the electromagnetic field components in the discretized domain, and obtains the field components in frequency domain by the discrete Fourier transform. Then, the scattering properties, i.e. the far field information, are calculated by integrating the near field. This sub-section will discuss each part of the algorithm in detail.

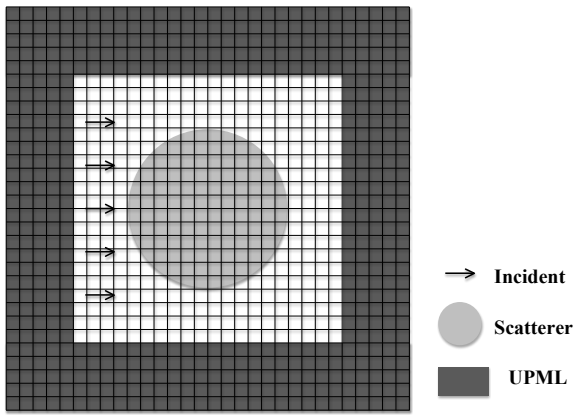

Figure 2.1: The computational domain for the PSTD simulation, which has three regions: scatterer, free space, and absorbtion boundary condition layers (i.e. UPML in this study).

2.1.1 Scattered field formulation

Maxwell's curl equations written in Gaussian units are

$$\frac{\epsilon(\vec{r})}{c}\frac{\partial \vec{E}(\vec{r},t)}{\partial t} = \nabla \times \vec{H}(\vec{r},t), \tag{2.1}$$

$$\frac{\mu(\vec{r})}{c}\frac{\partial \vec{H}(\vec{r},t)}{\partial t} = -\nabla \times \vec{E}(\vec{r},t). \tag{2.2}$$

We will not consider the presence of current densities or free charges in any of the calculations we present in this dissertation. Here ϵ is the permittivity of the dielectric medium, and μ is the permeability (from here on assumed to have the vacuum value of 1 everywhere). c is the speed of light in vacuum, and $\vec{E}$ and $\vec{H}$ are the electric and magnetic fields. The permittivity ϵ in absorptive (sometimes called"lossy") media is a complex parameter that is related to the complex refractive index m by

$$\epsilon = \epsilon_R + i\,\epsilon_I = m^2. \tag{2.3}$$

In a "frequency domain" approach, the time-evolution equations are Fourier transformed in time to get expressions in terms of temporal frequency ω. That is, for each ω, complex-valued solutions are sought of the form

$$\vec{E}(\vec{r},t) = \vec{\mathcal{E}}(\vec{r})e^{-i\,\omega\,t}, \qquad \vec{H}(\vec{r},t) = \vec{\mathcal{H}}(\vec{r})e^{-i\,\omega\,t},$$

where $\vec{\mathcal{E}}$ and $\vec{\mathcal{H}}$ are complex-valued functions of space. (As usual, physical solutions are found by taking real parts.) Then Maxwell's equations transform to

$$-i\,\omega\,\frac{\epsilon}{c}\vec{\mathcal{E}} = \nabla \times \vec{\mathcal{H}}, \tag{2.4}$$

$$-i\,\omega\,\frac{1}{c}\vec{\mathcal{H}} = -\nabla \times \vec{\mathcal{E}}, \tag{2.5}$$

This system can be easily seen to lead to an elliptic system of partial differential equations (Helmholtz equations for plane waves), and can be solved using any of a number of elliptic solvers.

The scattering problem we consider does not directly involve current densities,

but it does involve dielectric particles with complex refractive indices. This fact introduces complex numbers into calculations, and effectively doubles the demands on computer memory, since all field variables must then have both real and imaginary parts. As discussed in Yang and Liou [26], it is possible to get around this difficulty in the case of monochromatic incident waves by making an approximation to Maxwell's equations that is exact at precisely the frequency of the incident wave. With the complex permittivity decomposed into real and imaginary parts as in Equation 2.3 above, the frequency-domain Equation 2.4 becomes

$$-i\,\omega\,\frac{\epsilon_R}{c}\vec{\mathcal{E}} = \nabla \times \vec{\mathcal{H}} - \frac{\omega\,\epsilon_I}{c}\vec{\mathcal{E}}. \tag{2.6}$$

Thus the presence of a non-zero imaginary part of the permittivity at a point formally behaves (at one frequency) as would an "effective current density" there. Equation 2.6 is the Fourier transform of the evolution equation

$$\frac{\epsilon_R}{c}\frac{\partial \vec{E}}{\partial t} = \nabla \times \vec{H} - \frac{\omega\epsilon_I}{c}\vec{E}, \tag{2.7}$$

an evolution equation that has only real coefficients. This approximate equation, equivalent to the one derived in Yang and Liou [26] is used in place of Equation 2.1 in the PSTD calculations discussed. The natural choice $\omega = k\,c$ is made, where k is the wavenumber of the incident wave.

The new equation has purely real coefficients, so there will be no need to introduce complex numbers into the numerical simulations and we effectively halve the memory requirement of computations.

In the time-domain simulations, the total fields that appear in Equations 2.7 and

2.2 with $\mu = 1$ are decomposed in terms of incident and scattered fields,

$$\vec{E} = \vec{E}_{inc} + \vec{E}_{sca}, \qquad \vec{H} = \vec{H}_{inc} + \vec{H}_{sca},$$

where the incident fields satisfy

$$\frac{1}{c}\frac{\partial \vec{E}_{inc}}{\partial t} = \nabla \times \vec{H}_{inc}, \tag{2.8}$$

$$\frac{1}{c}\frac{\partial \vec{H}_{inc}}{\partial t} = -\nabla \times \vec{E}_{inc}. \tag{2.9}$$

The equations satisfied by the scattered field are then

$$\frac{\partial \vec{E}_{sca}}{\partial t} = \frac{c}{\epsilon_R}\nabla \times \vec{H}_{sca} - \omega\,\frac{\epsilon_I}{\epsilon_R}\vec{E}_{sca} + \left[\left(\frac{1-\epsilon_R}{\epsilon_R}\right)\frac{\partial}{\partial t} - \omega\,\frac{\epsilon_I}{\epsilon_R}\right]\vec{E}_{inc}, \tag{2.10}$$

$$\frac{\partial \vec{H}_{sca}}{\partial t} = -c\,\nabla \times \vec{E}_{sca}, \tag{2.11}$$

At each time step, the exact values for the expressions involving $\vec{E}_{inc}$ are used, and the particular form of the incident wave we use will be described in the next subsection. So the right-hand sides of the equations involve only spatial derivatives. The distinguishing feature of the PSTD method is how it evaluates these spatial derivatives, and will be discussed in the following section. The choice of time-stepping methods is a separate consideration, and the standard second-order finite difference method is used.

Using the PSTD, Equations 2.10 and 2.11 are solved in the region of the computational domain interior to the UPML region (see Figure 2.1), and in the UPML region the equations are augmented by the UPML expressions that match impedances across the layer boundary in such a way as to prevent any reflection as the outgoing waves enter the layer, and furthermore damp the entering waves sufficiently rapidly that

they never re-emerge upon reflection at the outer boundary of the computational domain.

2.1.2 Discrete formulation

The time domain methods solve the scattering problem by tracking the field components in the discretized domain, and, for convenience, any field component as a function of space and time will be defined in the form of:

$$F^n(I, J, K) = F(I\Delta x, J\Delta y, K\Delta z, n\Delta t),$$

in which Δx, Δy, and Δz are the grid sizes in the x, y, z axes in space, and Δt is the time step. The size of the grid cells relative to the wavelength is an important parameter for the simulation, and we define $\lambda/\Delta x$ as the spatial resolution. This study will use uniform cubes as the grid cells, thus, having $\Delta x = \Delta y = \Delta z$. In the discrete domain, the scattered field equations (Equations 2.10 and 2.11) for each grid point at each time step becomes:

$$\begin{aligned}
\frac{\partial \vec{E}^n_{sca}(I,J,K)}{\partial t} = & - \omega \frac{\epsilon_I}{\epsilon_R} \vec{E}^n_{sca}(I,J,K) \\
& + \frac{c}{\epsilon_R} \nabla \times \vec{H}^n_{sca}(I,J,K) \\
& + \left[\left(\frac{1-\epsilon_R}{\epsilon_R} \right) \frac{\partial}{\partial t} - \omega_0 \frac{\epsilon_I}{\epsilon_R} \right] \vec{E}^n_{inc}(I,J,K), \qquad (2.12) \\
\frac{\partial \vec{H}^{n+\frac{1}{2}}_{sca}(I,J,K)}{\partial t} = & - c \nabla \times \vec{E}^{n+\frac{1}{2}}_{sca}(I,J,K), \qquad (2.13)
\end{aligned}$$

Notice that the derivatives of the electric and magnetic field components are calculated at time steps with difference of $\frac{1}{2}\Delta t$ in Equations 2.12 and 2.13, and this is designed for the second-order finite difference method, i.e. leap-frog method, in the discrete time domain. To approximate the two terms in Equation 2.12 including

$\vec{E}^n_{sca}(I,J,K)$, we start from the Taylor expansions of $\vec{E}^{n+\frac{1}{2}}_{sca}(I,J,K)$ and $\vec{E}^{n-\frac{1}{2}}_{sca}(I,J,K)$ in time domain:

$$\vec{E}^{n+\frac{1}{2}}_{sca}(I,J,K) = \vec{E}^n_{sca}(I,J,K) + \frac{d\vec{E}^n_{sca}(I,J,K)}{dt}\frac{\Delta t}{2} + \frac{1}{2}\frac{d^2\vec{E}^n_{sca}(I,J,K)}{d^2t}(\frac{\Delta t}{2})^2 + O(\Delta t^3),$$
$$\vec{E}^{n-\frac{1}{2}}_{sca}(I,J,K) = \vec{E}^n_{sca}(I,J,K) - \frac{d\vec{E}^n_{sca}(I,J,K)}{dt}\frac{\Delta t}{2} + \frac{1}{2}\frac{d^2\vec{E}^n_{sca}(I,J,K)}{d^2t}(\frac{\Delta t}{2})^2 + O(\Delta t^3),$$

and they will give

$$\frac{\partial\vec{E}^n_{sca}(I,J,K)}{\partial t} = \frac{\vec{E}^{n+\frac{1}{2}}_{sca}(I,J,K) - \vec{E}^{n-\frac{1}{2}}_{sca}(I,J,K)}{\Delta t} + O(\Delta t^2), \tag{2.14}$$

and

$$\vec{E}^n_{sca}(I,J,K) = \frac{\vec{E}^{n+\frac{1}{2}}_{sca}(I,J,K) + \vec{E}^{n-\frac{1}{2}}_{sca}(I,J,K)}{2} + O(\Delta t^2). \tag{2.15}$$

Similarly, we can get the equations for the magnetic field, and, substituting Equations 2.14 and 2.15 into Equation 2.12, the field updating equations can be expressed in the form of:

$$\begin{aligned}
\vec{H}^{n+1}_{sca}(I,J,K) = \quad & \vec{H}^n_{sca}(I,J,K) \\
- \quad & c\Delta t\,\nabla\times\vec{E}^{n+\frac{1}{2}}_{sca}(I,J,K), \qquad (2.16)\\
\vec{E}^{n+\frac{1}{2}}_{sca}(I,J,K) = \quad & a(I,J,K)\vec{E}^{n-\frac{1}{2}}_{sca}(I,J,K) \\
+ \quad & b(I,J,K)\nabla\times\vec{H}^n_{sca}(I,J,K) \\
+ \quad & c(I,J,K)\frac{\partial\vec{E}^n_{inc}(I,J,K)}{\partial t} \\
+ \quad & d(I,J,K)\vec{E}^n_{inc}(I,J,K), \qquad (2.17)
\end{aligned}$$

The coefficients in Equation 2.17 are given by:

$$\begin{aligned} a(I,J,K) &= \frac{2\epsilon_R(I,J,K) - kc\Delta t\epsilon_I(I,J,K)}{2\epsilon_R(I,J,K) + kc\Delta t\epsilon_I(I,J,K)} \\ b(I,J,K) &= \frac{2c\Delta t}{2\epsilon_R(I,J,K) + kc\Delta t\epsilon_I(I,J,K)} \\ c(I,J,K) &= \frac{2(1-\epsilon_R(I,J,K))\Delta t}{2\epsilon_R(I,J,K) + kc\Delta t\epsilon_I(I,J,K)} \\ d(I,J,K) &= -\frac{2kc\Delta t\epsilon_R(I,J,K)}{2\epsilon_R(I,J,K) + kc\Delta t\epsilon_I(I,J,K)}. \end{aligned}$$

Here, $\epsilon_R(I,J,K)$ and $\epsilon_I(I,J,K)$ are spatial distribution of the permittivity, which can be defined arbitrarily at each grid point. This indicates one of the most powerful advantage of the time domain method that, theoretically, there is no limitation on the geometries and components of the scatterers. For each grid cell, it is straightforward to define the values of $\epsilon_R(I,J,K)$ and $\epsilon_I(I,J,K)$ based on the location of its center $(I\Delta x, J\Delta y, K\Delta z)$ and geometry of the scatterer.

Notice that Equations 2.17 and 2.16 are both for vectors, and can be expressed independently for each components in the x, y and z directions. Equation 2.17 indicates that four terms are used to update the electric field values: (1). the first term is the corresponding field value of the previous time step; (2). the second one involves the curl of the magnetic field, i.e. two spatial derivative terms that will be given by the spectral method; and, (3). the last two are related to the incident field and given analytically. Equation 2.16 for the magnetic field includes only the first two terms.

Also, there is no limitation on the format of the incident wave, and a plane wave

with a basic Gaussian shape is used:

$$\begin{aligned}\vec{E}_{inc}(\vec{r},t) &= \vec{E}_{inc}(\vec{k}\cdot\vec{r}-\omega t) \\ &= \vec{E}_o cos\left(\vec{k}\cdot\vec{r}-\omega t\right) exp\left[-\left(\frac{\vec{k}\cdot\vec{r}-\omega t-\phi_o}{4\pi}\right)^2\right], \end{aligned} \tag{2.18}$$

The ϕ_o is chosen so that the pulse reaches the particle with exponentially small amplitude at the start. Then, the incident fields as well as their temporal derivatives in the discrete domain can be easily obtained form this analytical express.

Now, the only undetermined values are the spatial derivatives, and it will be discussed in details in the next subsection. To keep the simulation stable, the temporal interval Δt must satisfy the stability condition that has been given by Liu [54]. This stability condition for the Fourier-based PSTD method in 3D Cartesian coordinate is given by:

$$c\Delta t \leq \frac{2}{\pi\sqrt{\frac{1}{\Delta x^2}+\frac{1}{\Delta y^2}+\frac{1}{\Delta z^2}}} \tag{2.19}$$

2.1.3 Spectral method

The essential difference between the FDTD and PSTD methods, which are otherwise closely related, is in the treatment of spatial differentiation, i.e. the curl terms in Equations 2.16 and 2.17. This sub-section not only introduces the spectral method, but also discusses the spectral filters to eliminate the Gibbs phenomenon.

For the purpose of the finite difference method, the FDTD, which is formulated in terms of grid cells, locates different components of the electric and magnetic fields at centers of either the edges (along the edge direction) or the walls (normal to the wall) of the cubic cells, and the complex field representation is widely known as the "Yee cell" [25], which is illustrated in Figure 2.2. The FDTD usually uses the

second-order finite difference methods in the form of:

$$\frac{\partial F(I,J,K)}{\partial x} = \frac{F(I+\frac{1}{2},J,K) - F(I-\frac{1}{2},J,K)}{\Delta x} + O(\Delta x^2), \tag{2.20}$$

where $F(I+\frac{1}{2},J,K)$ and $F(I-\frac{1}{2},J,K)$ are the values of the field at position $\big((I+\frac{1}{2})\Delta x, J\Delta y, K\Delta z\big)$ and $\big((I-\frac{1}{2})\Delta x, J\Delta y, K\Delta z\big)$, both of which are offset half of a grid from the cell center. For each components, the choice of the exact location follows Figure 2.2. However, the spectral method not only sweeps away the complexity but also provides much highter accuracy.

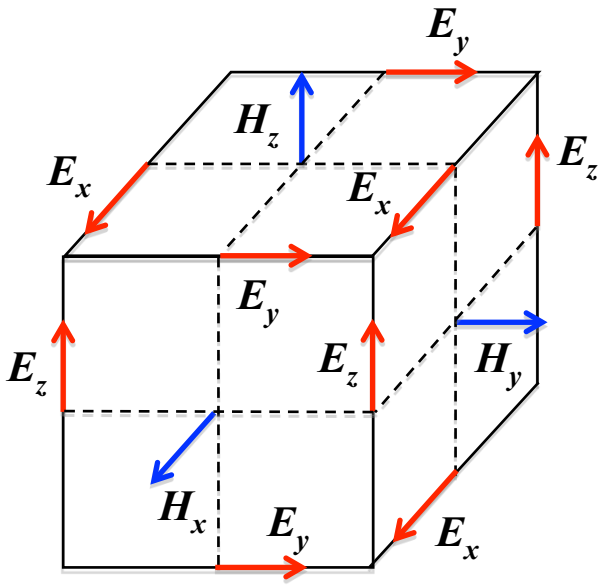

Figure 2.2: The field representation of the FDTD grid cell, i.e. Yee cell.

In the spectral method that we discuss here, a set of highly non-local (concentrated at no single grid point) complex exponentials is used as interpolation basis, and we write the interpolant of a function $f(x)$ (unknown function given by its values

at the grid points) in the form of:

$$F(x) = \sum_{k=-N/2}^{N/2-1} \tilde{F}_k e^{i\,\hat{k}\,x}, \tag{2.21}$$

where $\hat{k} = \frac{2\pi}{L}\,k$ is the wavenumber. The N coefficients $\tilde{F}_k$ are determined by the requirement that $F(x)$ be an interpolant of the values of $f(x)$ at grid points , i.e. $F(x_j) = f(x_j)$:

$$f(x_j) = \sum_{k=-N/2}^{N/2-1} \tilde{F}_k e^{i\,\hat{k}\,x_j}, \qquad\qquad j = 1,\, 2, \ldots N. \tag{2.22}$$

Given the $f(x_j)$, this is a system of N equations with N unknowns $\tilde{F}_k$. It can be shown using simple algebra and properties of the complex exponential that the solution is

$$\tilde{F}_k = \frac{1}{N} \sum_{j=1}^{N} f(x_j) e^{-i\,\hat{k}\,x_j}\,, \qquad\qquad -\frac{N}{2} \le k \le \frac{N}{2} - 1\,. \tag{2.23}$$

The association between the sequence of grid point values $\{f(x_j)\}$ and the sequence of Fourier amplitudes $\{\tilde{F}_k\}$ is the one established by the Discrete Fourier Transform and its inverse, and transforming between the two sequences can be done efficiently using a Fast Fourier Transform (FFT) algorithm. Notice that this approach associates a natural maximum wavenumber $K = \frac{N}{2}$ with a number of grid points, natural on the assumption of equal spacing of grid points. In terms of wavelengths, the smallest wavelength included in the interpolant is the "$2\,\Delta x$" wave. Conversely, the equally spaced N-point grid is called the "equivalent spatial grid" for the $N/2$-wave spectral representation.

According to the interpolant given by Equation 2.21, the spectral method can

calculate the derivatives easily:

$$\begin{aligned}
\frac{dF(x)}{dx} &= \sum_{k=-N/2}^{N/2-1} i\,\hat{k}\,\tilde{F}_k e^{i\,\hat{k}\,x} \\
&= \frac{1}{N}\sum_{k=-N/2}^{N/2-1} i\,\hat{k}\,e^{i\,\hat{k}\,x}\sum_{j=1}^{N} f(x_j)e^{-i\,\hat{k}\,x_j} \\
&= IFFT\left[i\,\hat{k}\,FFT\left(f(x_j)\right)\right]. \qquad (2.24)
\end{aligned}$$

We see that the derivative is easily expressed in terms of the same basis functions that are used in the interpolant itself. What's more important is that the basis is hightly non-local. Approximations to derivatives at grid points may be calculated by (1) finding the $\tilde{F}_k$ using an FFT, (2) constructing a new sequence $\tilde{D}_k = i\,\hat{k}\tilde{F}_k$, and (3) using an Inverse Fast Fourier Transform (IFFT) to construct the sum indicated in Equation 2.24 to get the derivative values at gridpoints.

The advantages of the spectral method compared with the finite difference method have been discussed in details by Panetta et. al. [65]. Three important features of the spectral method becomes important to calculate the spatial derivatives in the PSTD. First, the spectral method has much higher accuracy on approximating the derivatives of smooth functions, which is normally known as the "spectral accuracy." Second, the direct and inverse Fast Fourier transform (FFT) can be easily applied to improve the efficiency of the spectral simulations. Last but not the least, the spectral method shows much weaker numerical dispersion in propagation problem, when compared with the finite difference method. All of the three features becomes more and more important as the computational domain increases, because the computational burden requires small spatial resolution without significant loss of efficiency and the more propagation times are needed.

There is of course one difficulty with spectral methods that is well known: they work well with smoothly varying functions, but works poorly on discontinuous functions, known as the "Gibbs phenomenon." Spectral methods require inclusion of high wavenumbers (small scale oscillations) to represent rapidly varying features of functions, i.e. discontinuity, and if a function has variations, even at only one location, on very small scales, high-wavenumber terms are required in the Fourier representation and their omission through truncation will have deleterious effects everywhere.

An extreme example is what happens at a simple jump discontinuity, and the Gibbs phenomenon is shown in Figure 2.3, for the case of a simple "sawtooth" function $f(x)$ in the from of:

$$f(x) = \begin{cases} x & 0 < x < 1 \\ x - 2 & 1 < x < 2 \end{cases} \tag{2.25}$$

The approximation for $f(x)$ is given in the left panel, and the right panel is for the derivative of $f(x)$. The figure has $f(x)$ along with approximations using equally spaced grid points $N = 8$, 32, and 128. The evident agreement of the partial sums with each other right at the jump reflects the fact that the Fourier series of a function with an isolated jump discontinuity converges at the location of the discontinuity to the average value of the left- and right- hand limits. Notice that while the error for any choice of N is worst near the jump, and, even at the largest N we used (128), there are errors evident far from the jump in the form of a small-wavelength signal. In a time-dependent calculation, the possibility exists for the largest errors, originally located near the jump, to propagate away from it. In the right panel, we can see that the performance of the spectral method for the derivative is even worse. The largest errors show near the discontinuity and increase as N increase. Furthermore, the errors spread over the entire domain, and converge to the exact value as getting

away from the discontinuity.

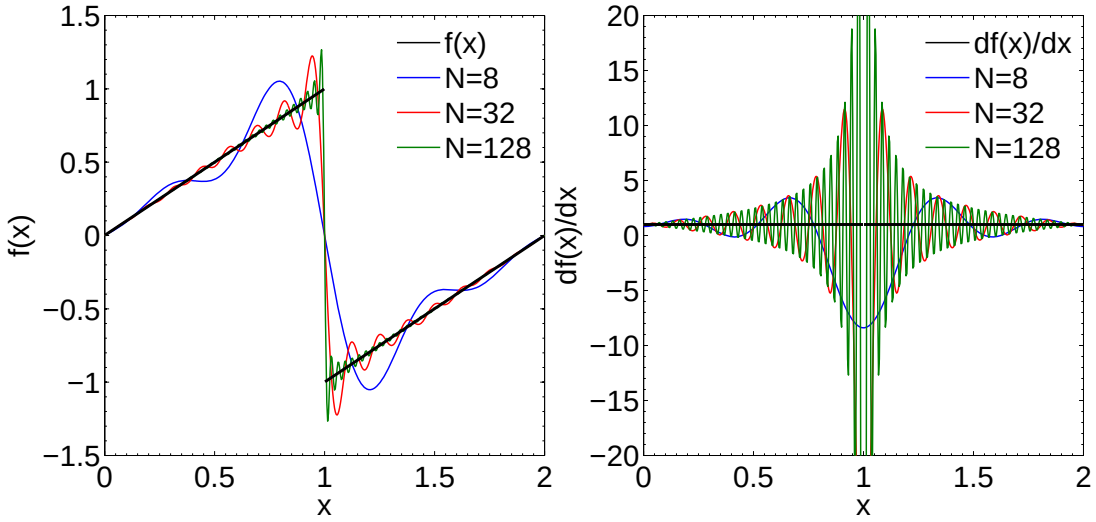

Figure 2.3: The Gibbs phenomenon at a simple jump discontinuity to approximate the original function $f(x)$ (left panel) and its derivative $df(x)/dx$ (right panel).

What leads to these errors is the presence of significant amplitudes in the high wavenumber Fourier components. With "infinite" resolution, these high wavenumber components destructively interfere, but, with any sum involving only finitely many of them, the destructive interference is incomplete and the result is the oscillatory error behavior away from the jump in Figure 2.3. Since scattering calculations involve changes that are effectively jump discontinuities in refractive indices at particle boundaries, and, thus, in the electromagnetic field. The oscillations caused by the Gibbs phenomenon will accumulate and enlarge with temporal iterations, and eventually, the PSTD simulation becomes divergent. This significantly limits the applications of the PSTD for large particles or particles with large refractive indices, becasue longer integration time are needed or more significant discontinuity is exist-

ing. It is a priori important to have a way of minimizing errors introduced by the Gibbs phenomenon.

The "spectral filter" is one of the most popular and simplest methods that can eliminate the Gibbs phenomenon. A number of "filtering" treatments have been applied to the high wavenumber modal amplitudes, essentially replacing $\tilde{F}_k$ with $\sigma(k)\,\tilde{F}_k$, where the filter function $\sigma(k)$ has the properties

$$\sigma(k) \begin{cases} \approx 1 & \text{for small } |k| \\ \to 0 & \text{"rapidly" for } |k| \text{ approaching } K. \end{cases} \tag{2.26}$$

A choice of $\sigma(k)$ that has a number of desirable properties is the "exponential filter" [66, 65] of order p in the form of

$$\sigma_p(k) = exp\left\{-\gamma\left(\frac{|k|}{K}\right)^p\right\},$$

where $\gamma = -ln(\varepsilon)$, and ε, a small number, is again the machine epsilon. It is clear that $\sigma_p(k)$ equals to 1 at $k = 0$, and decreases to ε as $|k|$ increase to K. Also, successively higher powers p give filters that stay near 1 for successively greater wavenumbers before dropping quickly to ε.

Another simple choice to eliminate the Gibbs phenomenon is to truncate the high spectral terms directly, and this is referred as the "truncation." The truncation method in the sense of the "truncation filter" is expressed as:

$$\sigma(k) = \begin{cases} 1 & \frac{|k|}{K} \leq \eta_c \\ 0 & \frac{|k|}{K} > \eta_c \end{cases} \tag{2.27}$$

where η_c indicates the truncation threshold, the coefficients of wavenumber with $\frac{|k|}{K}$ above which is set to be zeros. Figure 2.4 illustrates both the exponential and

truncation filters with different parameters, and the x-axis is normalized to 1. The order p of 2, 8 and 32 are used for the exponential filters, and η_c values are 0.2, 0.6 and 0.9. With the decrease of p or η_c, the filters become "stronger", and more spectral terms are removed. As shown by Figure 2.4, an exponential filter makes a smooth attenuation of the high wavenumber terms, whereas, as expected, the change based on the truncation filter is sharp.

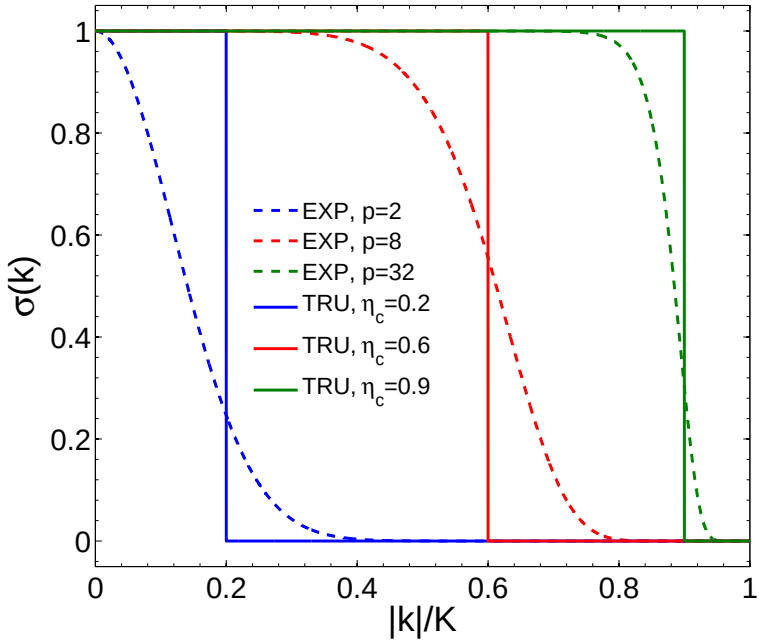

Figure 2.4: The exponential filters of different order and truncation functions with different thresholds.

With the spectral filter considered, the interpolant of $f(x)$ can be rewrite as:

$$F_\sigma(x) = \sum_{k=-N/2}^{N/2-1} \sigma(\,k\,)\,\tilde{F}_k e^{i\,\hat{k}\,x}. \tag{2.28}$$

Thus, Equation 2.24 for the derivative in the PSTD simulations is rewritten as:

$$\begin{aligned}
\frac{dF(x)}{dx} &= \sum_{k=-N/2}^{N/2-1} i\,\hat{k}\,\sigma(\,k\,)\,\tilde{F}_k e^{i\,\hat{k}\,x} \\
&= \frac{1}{N}\sum_{k=-N/2}^{N/2-1} i\,\hat{k}\,\sigma(\,k\,)\,e^{i\,\hat{k}\,x}\sum_{j=1}^{N} f(x_j)e^{-i\,\hat{k}\,x_j} \\
&= IFFT\left(i\,\hat{k}\,\sigma(\,k\,)\,FFT\,(f(x_j))\right). \qquad (2.29)
\end{aligned}$$

The performance of the exponential filter has been discussed by Panetta et al. [65], which will not be listed. Figure 2.5 shows the same approximations of $f(x)$ and $df(x)/dx$ as Figure 2.3 but with the truncation filters. In Figure 2.5, the truncation filter has η_c values 0.2, 0.6 and 0.9 from the top to the lower panels. A small value of η_c gives a filtered version which has very few oscillations away from the discontinuity, especially as the N increases. However, with such a small value of η_c, the jump is spread over a comparatively wide band around the true jump. It should also be noticed that, for small N (e.g. $N = 8$), the truncation filter with $\eta_c = 0.2$ is too strong that almost all spectral coefficients becomes zero. The middle panel shows what happens when η_c is increased to 0.6. The bottom panel illustrate the results for the filter using $\eta_c = 0.9$. As expected, the oscillations become more significant, whereas clear improvements over the entire domain are obtained compared with the unfiltered results in Figure 2.3 even with such a weak filter. Also the effects of the filters on the approximations of the derivatives are shown in the right panels, and similar improvements and variations are obtained.

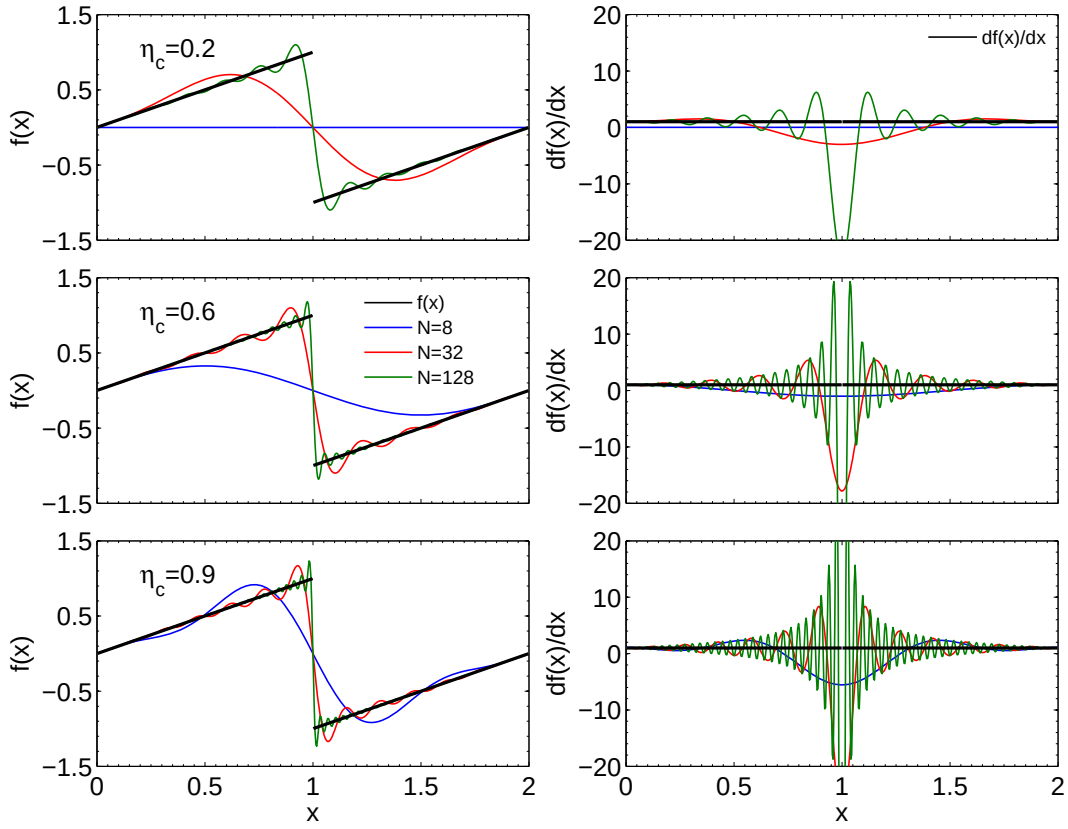

Figure 2.5: The effects of truncation filters with different thresholds.

The degree of discontinuity in the PSTD is significantly different from case to case considering different particle geometries and refractive indices, and there is no way to determine the best filter for each single simulation, even the appropriate one. Furthermore, our numerical results indicate that both the exponential and truncation filter can eliminate the Gibbs phenomenon and ensure the convergence of the simulation, and the scattering properties obtained are not sensitive to the filter type and parameter. Thus, this study uses the simple truncation filter in the simulations, and an empirical value of η_c ranging from approximately 0.8 to 1 are sufficient for most simulations.

2.1.4 Absorbtion boundary condition

An appropriate absorption boundary condition (ABC) should be included in the time domain simulation to truncate the outgoing fields and keep the simulation in finite spatial domain. Care must be taken at the boundary of the computational domain so that there is negligibly small reflection of what should be a purely outgoing scattered signal. For this purpose it is common now in numerical simulations to introduce at computational boundaries what is called a "perfectly matched" boundary layer [67, 68, 69]. Such a layer is used in both the FDTD and PSTD methods by proper adjustment of the optical characteristics of the layer, and waves incident on it from any direction are absorbed without reflection.

The earliest version of the method [67] was developed for use in FDTD simulations and is now known as the perfectly matched layer (PML) method. The PML can be achieved by specially defined distribution of the permittivity (ϵ), permeability (μ), conductivity (σ), and magnetic loss (σ^*), and considering that the PML is directly connected to the vacuum space containing the scatterer, $\epsilon_{PML} = \epsilon_o$, $\mu_{PML} = \mu_o$, and $\frac{\sigma_{PML}}{\epsilon_o} = \frac{\sigma^*_{PML}}{\mu_o}$ should be satisfied to vanish the reflection from any incident angles. The layer was constructed in a mathematical manner that made physical interpretation difficult, and applicability to more general unstructured grid simulations unclear. These deficiencies were removed in the reformulated "uniaxial" PML, or UPML by Gedney [64]. We use an implementation of the UPML in our PSTD simulations.

The UPML simplified the numerical algorithm of the ABC [68] by introducing the unisotropic permittivity and permieability, and is applied in the PSTD algorithm

by Liu [57]. Maxwell's curl equation in the UMPL boundary is in the from of:

$$\nabla \times \vec{\mathcal{E}} = i\omega\mu_o\mu^T\vec{\mathcal{H}} \tag{2.30}$$

$$\nabla \times \vec{\mathcal{H}} = -i\omega\epsilon_o\epsilon^T\vec{\mathcal{E}} \tag{2.31}$$

The permittivity and permeability in the UMPL are expressed as diagonal tensors in the forms of:

$$\epsilon^T = \mu^T = \begin{bmatrix} \frac{s_y s_z}{s_x} & 0 & 0 \\ 0 & \frac{s_x s_z}{s_y} & 0 \\ 0 & 0 & \frac{s_x s_y}{s_z} \end{bmatrix}, \tag{2.32}$$

where the relation $\frac{\sigma_{PML}}{\epsilon_o} = \frac{\sigma^*_{PML}}{\mu_o}$ is used for μ^T. We have:

$$s_x = 1 - \frac{\sigma_x}{i\omega\epsilon_o}, s_y = 1 - \frac{\sigma_y}{i\omega\epsilon_o}, and s_z = 1 - \frac{\sigma_z}{i\omega\epsilon_o}.$$

It should be noticed that s_x, s_y, and s_z are associated with the x, y and z-normal interface, respectively. In the UPML region, the field should attenuate smoothly, and, thus, the values of the electrical conductivities and magnetic losses are designed to increase gradually along the outward normal direction of the interface. Furthermore, s_x, s_y, and s_z are only spatially variant along the x, y and z directions, whereas invariant along their transverse directions. Take the interface on $x = 0$ plane as an example, and the PML is on the $x > 0$ region. For a boundary layer with a thickness h, the electric conductivity is given by:

$$\sigma_x(x) = -\left(\frac{x}{h}\right)^m \frac{(m+1)lnR_o}{2\sqrt{\frac{\mu_o}{\epsilon_o}}h}, \tag{2.33}$$

where R_o, a small number (e.g. 10^{-12}), represents the reflection errors of the layer,

and m, a real number, is usually chosen within $3 < m < 4$.

Considering the vectors:

$$\vec{D} = \begin{bmatrix} D_x \\ D_y \\ D_z \end{bmatrix} = \begin{bmatrix} \frac{s_z}{s_x} E_x \\ \frac{s_x}{s_y} E_y \\ \frac{s_y}{s_z} E_z \end{bmatrix}, \tag{2.34}$$

$$\vec{B} = \begin{bmatrix} B_x \\ B_y \\ B_z \end{bmatrix} = \begin{bmatrix} \frac{s_z}{s_x} H_x \\ \frac{s_x}{s_y} H_y \\ \frac{s_y}{s_z} H_z \end{bmatrix}, \tag{2.35}$$

we can get:

$$\nabla \times \vec{E} = - \mu_o \frac{\partial \vec{B}}{\partial t} - \begin{bmatrix} \sigma_y & 0 & 0 \\ 0 & \sigma_z & 0 \\ 0 & 0 & \sigma_x \end{bmatrix} \vec{B}, \tag{2.36}$$

$$\nabla \times \vec{H} = \epsilon_o \frac{\partial \vec{D}}{\partial t} + \begin{bmatrix} \sigma_y & 0 & 0 \\ 0 & \sigma_z & 0 \\ 0 & 0 & \sigma_x \end{bmatrix} \vec{D}. \tag{2.37}$$

Then the field updating equations for UPML in the distretized domain can be easily obtained, and take the components E_x and H_x as example:

$$\begin{aligned} E_x^{n+\frac{1}{2}}(I,J,K) = & \frac{2\epsilon_o - \sigma_y(I,J,K)\Delta t}{2\epsilon_o + \sigma_y(I,J,K)\Delta t} E_x^{n-\frac{1}{2}}(I,J,K) \\ & + \frac{2\Delta t}{2\epsilon_o + \sigma_y(I,J,K)\Delta t} \frac{s_x}{s_z} \left[\frac{\partial H_z^n(I,J,K)}{\partial y} - \frac{\partial H_y^n(I,J,K)}{\partial z} \right] \end{aligned}$$

$$H_x^{n+1}(I,J,K) = \frac{2\mu_o - \sigma_y(I,J,K)\Delta t}{2\mu_o + \sigma_y(I,J,K)\Delta t} H_x^n(I,J,K) - \frac{2\Delta t}{2\mu_o + \sigma_y(I,J,K)\Delta t} \frac{s_x}{s_z} \left[\frac{\partial E_z^{n+\frac{1}{2}}(I,J,K)}{\partial y} - \frac{\partial E_y^{n+\frac{1}{2}}(I,J,K)}{\partial z} \right]$$

The equations for other field components following similar format, and we will not list them here.

2.1.5 Field transformations

So far we have discussed the PSTD algorithm to calculate the electromagnetic field near the particle in time domain, and, in order to use the near-to-far-field transformation, the single frequency response in the near field time-domain calculations (PSTD or FDTD) must be extracted. As opposed to using some kind of FFT method, which would require storing all the temporal data over a long time integration before doing the FFT, we choose a method much more sparing of memory. The method can be appreciated by considering a simple example. Suppose $f(\vec{r},t)$ is a time-domain field component whose frequency transform $\mathcal{F}(\vec{r},\omega)$ at some frequency ω is desired. For any finite time interval of length T we can make the estimate

$$\mathcal{F}(\vec{r},\omega) \approx \frac{1}{T}\int_0^T f(\vec{r},t)e^{-i\omega\, t}\, dt, \tag{2.38}$$

with the estimate improving in accuracy with increasing integration length T. The time-discrete version of this is

$$\mathcal{F}^N(\vec{r},\omega) = \frac{1}{N}\sum_{n=1}^{N} f^n(\vec{r})e^{-i\omega n\Delta t}, \tag{2.39}$$

where $f^n(\vec{r}) = f(\vec{r}, n\Delta t)$ and $N\,\Delta t = T$. Notice that when $n\Delta t$ increases to $(n{+}1)\Delta t$,

$$\mathcal{F}^{n+1}(\vec{r},\omega) = \left(\frac{n}{n+1}\right)\mathcal{F}^n(\vec{r},\omega) + \frac{1}{n+1} f^{n+1}(x) e^{-i\omega(n+1)\Delta t}, \tag{2.40}$$

which allows us to update estimates of $\mathcal{F}(\vec{r},\omega)$ as we integrate in time. Thus, we need save only the data required by our time-stepping method, and run that method long enough for our transforms $\mathcal{F}^N$ to become constant. This should happen eventually can be understood by considering Equation 2.40, and remembering that the incident wave packet has a narrow width in time as it travels in free space. So as N increases, there comes point beyond which the incremental update becomes exponentially small. However, when exactly this decay sets in is not easy to estimate a priori, since the full interaction time of the packet with the particle is not easily approximated, and the best guide has been experimentation. It has found that the total time of integration needed for the Fourier transform to converge is between four and five times the amount of time that the packet would take to cross a distance in free space equal to one diameter of the particle.

With the near field in the frequency domain obtained, two integral methods can give the far field based on the surface integral or the volume integral. This study uses the surface integral method, which is more efficient and more accurate than the volume integral method [70], and the far field is given in the form of:

$$\vec{\mathcal{E}}(\vec{r}) = \frac{ik\,e^{i\,k\,|\vec{r}|}}{4\,\pi\,|\vec{r}|} \iint\limits_{\mathcal{S}} \hat{r} \times \{\hat{e}_{\mathcal{S}} \times \vec{\mathcal{E}}(\vec{r}') - \hat{r} \times [\hat{e}_{\mathcal{S}} \times \vec{\mathcal{H}}(\vec{r}')]\} e^{-i\,k\,\hat{r}\cdot\vec{r}'}\, d\,\vec{r}', \tag{2.41}$$

where $\mathcal{S}$ is the surface enclosing the scatterer, and $\hat{r} = \frac{\vec{r}}{|\vec{r}|}$ represent the scattering direction. $\hat{e}_{\mathcal{S}}$ is an outward-pointing unit vector normal to the surface. So the frequency response of both electric and magnetic field only on the surface $\mathcal{S}$ are

needed. Consider the scattering geometry shown in Figure 1.1, and rewrite Equation 2.41 in the components format:

$$\begin{bmatrix} \mathcal{E}_{\parallel}^{s}(\hat{r}) \\ \mathcal{E}_{\perp}^{s}(\hat{r}) \end{bmatrix} = \frac{ik\, e^{i\,k\,|\vec{r}|}}{4\,\pi\,|\vec{r}|} \iint\limits_{\mathcal{S}} \begin{bmatrix} \hat{e}_{\parallel}^{s} \cdot \vec{\mathcal{Z}} \\ \hat{e}_{\perp}^{s} \cdot \vec{\mathcal{Z}} \end{bmatrix} e^{-i\,k\,\hat{r}\cdot\vec{r}'}\, d\,\vec{r}', \tag{2.42}$$

where the vector $\vec{\mathcal{Z}}$ denotes $\hat{r}\times\{\hat{e}_{\mathcal{S}}\times\vec{\mathcal{E}}(\vec{r}')-\hat{r}\times[\hat{e}_{\mathcal{S}}\times\vec{\mathcal{H}}(\vec{r}')]\}$. Take the incident direction along the z-direction as illustrated in Figure 1.1 as an example, the horizontal and perpendicular components of the incident field are given by:

$$\begin{bmatrix} \mathcal{E}_{\parallel}^{i} \\ \mathcal{E}_{\perp}^{i} \end{bmatrix} = \begin{bmatrix} \hat{e}_{\perp}^{s} \cdot \hat{x} & \hat{e}_{\perp}^{s} \cdot \hat{y} \\ -\hat{e}_{\perp}^{s} \cdot \hat{y} & \hat{e}_{\perp}^{s} \cdot \hat{x} \end{bmatrix} \begin{bmatrix} \mathcal{E}_{x}^{i} \\ \mathcal{E}_{y}^{i} \end{bmatrix}, \tag{2.43}$$

$\mathcal{E}_{x}^{i}$ and $\mathcal{E}_{y}^{i}$ indicate the incident electric field components along the x and y directions in a Cartesian coordinate. The amplitude scattering equation shown in Equation 1.3 is then given by:

$$\begin{aligned} \mathcal{A} &= \begin{bmatrix} \mathcal{A}_2 & \mathcal{A}_3 \\ \mathcal{A}_4 & \mathcal{A}_1 \end{bmatrix} \\ &= \begin{bmatrix} \mathcal{F}_{\parallel,x} & \mathcal{F}_{\parallel,y} \\ \mathcal{F}_{\perp,x} & \mathcal{F}_{\perp,y} \end{bmatrix} \begin{bmatrix} \hat{e}_{\perp}^{s} \cdot \hat{x} & \hat{e}_{\perp}^{s} \cdot \hat{y} \\ -\hat{e}_{\perp}^{s} \cdot \hat{y} & \hat{e}_{\perp}^{s} \cdot \hat{x} \end{bmatrix} \end{aligned} \tag{2.44}$$

where

$$\begin{bmatrix} \mathcal{F}_{\parallel,x} \\ \mathcal{F}_{\perp,x} \end{bmatrix} = \frac{k^2}{4\pi} \iint\limits_{\mathcal{S}} \begin{bmatrix} \hat{e}_{\parallel}^{s} \cdot \vec{\mathcal{Z}} \\ \hat{e}_{\perp}^{s} \cdot \vec{\mathcal{Z}} \end{bmatrix} e^{-i\,k\,\hat{r}\cdot\vec{r}'}\, d\,\vec{r}'|_{\mathcal{E}_{x}^{i}=1,\mathcal{E}_{y}^{i}=0}, \tag{2.45}$$

and

$$\begin{bmatrix} \mathcal{F}_{\parallel,y} \\ \mathcal{F}_{\perp,y} \end{bmatrix} = \frac{k^2}{4\pi} \iint\limits_{\mathcal{S}} \begin{bmatrix} \hat{e}_{\parallel}^{s} \cdot \vec{\mathcal{Z}} \\ \hat{e}_{\perp}^{s} \cdot \vec{\mathcal{Z}} \end{bmatrix} e^{-i\,k\,\hat{r}\cdot\vec{r}'}\, d\,\vec{r}'|_{\mathcal{E}_x^i=0,\mathcal{E}_y^i=1}. \tag{2.46}$$

The subscripts $\mathcal{E}_x^i = 1, \mathcal{E}_y^i = 0$ and $\mathcal{E}_x^i = 0, \mathcal{E}_y^i = 1$ indicate the polarization of the incident electric field along the x and y directions, and, to calculate the full scattering and polarization properties for each particle orientation, the PSTD simulations are carried out twice independently with the two incident polarization states.

Therefor, the amplitude scattering matrix can be obtained following two transforms (i.e. the time-to-frequency domain transform for the near field and the near-to-far transform in the frequency domain), and the corresponding phase matrix could be calculated easily following [1, 50].

In this section, all the major schemes and technologies related to the PSTD simulations have been discussed. Because of the special features of the spectral method and the elimination of the Gibbs phenomenon, the PSTD does show significant applicability on light scattering simulations, and this will be shown in the rest of the chapter.

2.2 Parallelization of the implementation

The PSTD models light scattering by three-dimensional scatterers on discrete grid cells, and the number of operations would grow significantly with the increase of particle size. For large particles with size parameter over 50 or non-spherical particles with random orientations, it becomes extremely time-consuming and impractical to carry out the PSTD on single processor. However, by parallelizing the implementation and dividing the simulations on multiple processors, the computation wall-time will be greatly shortened, and the applicability of the PSTD will be significantly enhanced.

Brock et al. [31] and Yurkin et al. [71] used the MPI to parallelize the FDTD and DDA implementations. They separate the spatial domain into sub-domains, and each processor is assigned one. Both parallelized implementations show excellent performances on multiple processors. However, the MPI doesn't support shared memories, and the processors communicate with one another by sending and receiving messages. For each spectral simulation, the FFT requires all values of the field along the derivative direction, and the IFFT gives the spatial derivatives of all grid cells in the direction (see Equations 2.24). As a result, significant amount of computational time would be wasted for communication among the processors if the PSTD implementation is parallelized based on sub-domains with the MPI. However, for the atmospheric applications, light scattering by randomly oriented non-spherical particles is normally considered, which are averaged over results of tens to hundreds of different particle orientations, and the PSTD simulation for each particle orientation is independent. Thus, the MPI can be used to parallelize the PSTD implementation efficiently based on particle orientations: each processor is assigned simulations with respect to different particle orientations, and only the final scattering properties are necessary to be communicated among different processors.

Furthermore, the OpenMP supports shared memory multiprocessing programming, whereas can be carried out only on single node (that normally has 2 to 16 processors). It is simple and flexible to develop parallel applications using the OpenMP, and, with shared memory, the values of the field can be used directly by all processors without being sent and received. Thus, the PSTD implementation can be parallelized based on spatial sub-domains without significant loss of efficiency using the OpenMP. It should be noticed that only limited amount of memory and limited number of processors on single node can be used for the OpenMP implementation, whereas the MPI one has no such limitation. However, the OpenMP implementa-

tion still greatly enhances the applicability of the PSTD simulation, especially for the large particles that are impractical on single processor.

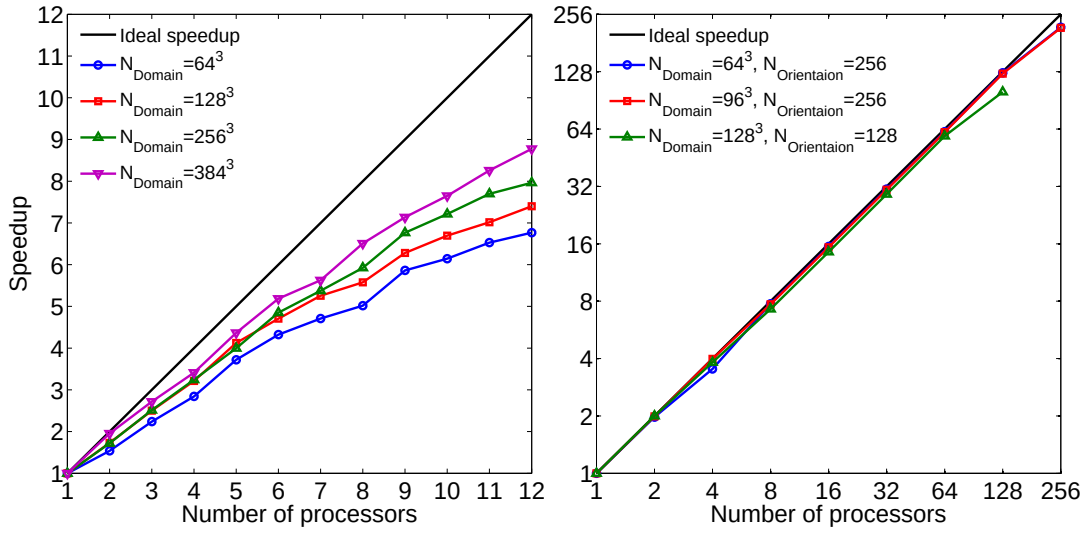

Figure 2.6: The speedup of the PSTD implementation parallelized using OpenMP (left panel) and MPI (right panel) as functions of the number of processors used in the simulation. N_{Domain} and $N_{Orientation}$ indicates the number of grid cells in the spatial domain, and the particle orientation simulated.

Figure 2.6 illustrates the speedup of the parallelized PSTD implementation at different computational domains. All tests were run on the Texas A&M University supercomputer facility EOS, each single node of which has 8 or 12 64-bit 2.8GHz processors and shares 24GB memory. The ideal speedup is indicated by the black line in the figure. The left panel is for the results of the OpenMP implementation, and a maximum of 12 processors can be used. The light scattering by spheres with single orientation is carried out, and four computational domain sizes (number of grid cells in the three-dimension space) of 64^3, 128^3, 256^3 and 384^3 are used. It is clearly show that, with the same amount of processors, the speedup given by the

OpenMP implementation increases as the computational domain increases. With 12 processors, the speedup of almost 7 is achieved for the domain size of 64^3, and it reaches to approximately 9 as the domain size increases to 384^3. This is because the fraction of operations that cannot be separated into different processors decreases as the computational domain increases. The right panel of Figure 2.6 is for the MPI implementation with up to 256 processors used. The light scattering by randomly oriented hexagonal columns (with an aspect ratio of 1) is simulated with domain size of 64^3, 96^3, and 128^3, and the number of particle orientations simulated are listed in the figure: 256, 256, and 128, respectively. The number of processors is chosen to ensure the same number of orientations assigned on each of them. The right panel indicates that the MPI implementation has very high efficiency with almost ideal speedup with $N_{orientations}/N_{processors}$ larger than 2.

With the implementation parallelized with both the OpenMP and MPI, the PSTD can be carried out for simulations involving both single and multiple orientations efficiently, and the applicability of it is greatly enhanced. In the following section, the accuracy, efficiency and applicability of the PSTD implementation will be discussed in details.

2.3 Validation and applicability

In this section we show generally two kinds of results. The first kind establishes the validity of the PSTD method by considering scattering problems for which either an exact solution or another highly reliable method is available. Both the homogeneous and inhomogeneous cases will be considered. In the case of homogeneous spherical particles the exact solution is the Lorenz-Mie solution, and in the case of spheroids and circular cylinders the reliable method is the T-matrix method. The core-mantel Mie theory is the exact solution for the stratified spheres, whereas the

DDA method will be used for the other mixing states. The second kind of results involve cases in which neither of these approaches to validation is available. In the section that follows this one we discuss the relative performance of the PSTD and DDA methods. All the calculations in this study were performed on at the Texas A&M Supercomputing Facility. A single node of an IBM iDataplex cluster with 8 2.8GHz processors will be used for the OpenMP implementation considering the scattering of oriented particles, and the number of processors used by the MPI implementation for randomly oriented non-spherical particles is normally a half of the number of particle orientations.

2.3.1 Comparison with the Lorenz-Mie theory

To validate the PSTD, we first calculate the light scattering by spheres and compare the results with the exact solutions given by the Lorenz-Mie theory [7, 8]. The size parameters range from 10 to 200, and three realistic refractive indices of ice at visible ($0.532\mu m$), near infrared ($3.78\mu m$), and infrared ($12.0\mu m$) wavelengths are used ($1.312 + 1.489 \times 10^{-9}i$, $1.384 + 7.055 \times 10^{-3}i$, and $1.276 + 4.133 \times 10^{-1}i$) [72]. Table 2.1 lists the computational wall-clock times and spatial resolutions used by the PSTD. For small spheres (size parameters smaller than 40), the spatial resolution is increased until accurate results are obtained, and the simulations take no more than 1.5×10^4 seconds. For larger size parameters, the computational times increase significantly as the computational domain increases, and high spatial resolution becomes unaffordable. Moreover, in this case, the particle surfaces, represented with the discrete grid points, become much smoother in terms of surface radii of curvature relative to particle size; thus, coarser spatial resolutions can be used. A spatial resolution of approximately 12 grid cells per wavelength is sufficient for spheres with size parameters ranging from 80 to 140; however, for size parameters larger than 140, sim-

ulations with spatial resolutions of approximately eight grid points per wavelength almost reaches our limitation of computational resources, especially the memory of $24GB$, corresponding to a domain size of 512^3 grid cells. From Table 2.1, we see that, overall, the computational time is a monotonically increasing function of the size parameter, whereas some exceptions are existing, e.g. a sphere with a size parameter of 60 uses less computational time than that of 40 at visible wavelength. This is because the spatial resolution used gives a larger computational domain for the sphere with a size parameter of 40. To have a quantitative sense on the efficiency of the PSTD implementation, let's see some examples. With 8 processors, the simulation for a sphere with a size parameter of 200 and a refractive index of $1.384 + 7.055 \times 10^{-3}i$ takes 3.4×10^5 seconds, i.e., less than 4 day, but the wall-clock time is no more than 1.0×10^5 seconds (about 27 hours) when the size parameter is equal to or less than 100.

To quantitatively evaluate the overall accuracy of the PSTD, we use the following parameters: relative error (RE) of Q_{ext}, RE of SSA (only for the two absorptive cases), RE of g, RE of $P_{11}(180^o)$, root-mean-square RE (RMSRE) of $P_{11}(\theta)$, and root mean-square absolute error (RMSAE) of $P_{12}(\theta)/P_{11}(\theta)$. In this study, the RE, RMSRE, and RMSAE are defined as:

$$RE = \left| \frac{A_{PSTD} - A_{exact-method}}{A_{exact-method}} \right|,$$

$$RMSRE = \left[\frac{1}{N} \sum_{i=1}^{N} \left(\frac{A_{\theta_i,PSTD} - A_{\theta_i,exact-method}}{A_{\theta_i,exact-method}} \right)^2 \right]^{1/2},$$

and

$$RMSAE = \left[\frac{1}{N} \sum_{i=1}^{N} \left(A_{\theta_i,PSTD} - A_{\theta_i,exact-method} \right)^2 \right]^{1/2},$$

where A_{PSTD} and $A_{exact-method}$ are the values of the scattering properties, e.g., Q_{ext}, given by the PSTD and the exact method, respectively, and A_{θ_i} indicates the associated quantity to be a function of scattering angle.

Table 2.1: Computational time and spatial resolution for numerical simulation of light scattering by spheres.

	Visible		Near-IR		IR	
	$(m = 1.31 + 1.93 \times 10^{-8}\, i)$		$(m = 1.36 + 1.34 \times 10^{-2}\, i)$		$(m = 1.16 + 3.54 \times 10^{-1}\, i)$	
x	time(s)	$\lambda/\Delta x$	time(s)	$\lambda/\Delta x$	time(s)	$\lambda/\Delta x$
10	2.9×10^2	26.7	1.8×10^2	22.9	1.5×10^2	22.9
20	2.5×10^3	24.6	2.2×10^3	26.5	6.5×10^2	21.5
30	5.5×10^3	18.5	2.6×10^3	18.5	1.5×10^3	16.4
40	2.0×10^4	23.3	1.1×10^4	20.8	4.6×10^3	17.0
60	1.5×10^4	14.5	1.3×10^4	14.5	6.8×10^3	12.2
80	2.0×10^4	10.4	4.2×10^4	14.1	2.1×10^4	11.7
100	1.1×10^5	14.3	5.8×10^4	11.3	4.3×10^4	10.6
120	1.5×10^5	12.0	1.5×10^5	12.0	6.5×10^4	9.45
140	1.8×10^5	11.9	1.9×10^5	10.3	1.2×10^5	8.46
160	2.2×10^5	8.97	1.8×10^5	8.03	1.5×10^5	8.03
180	2.9×10^5	8.53	3.0×10^5	8.53	2.6×10^5	8.53
200	3.4×10^5	7.68	3.5×10^5	7.68	3.0×10^5	7.68

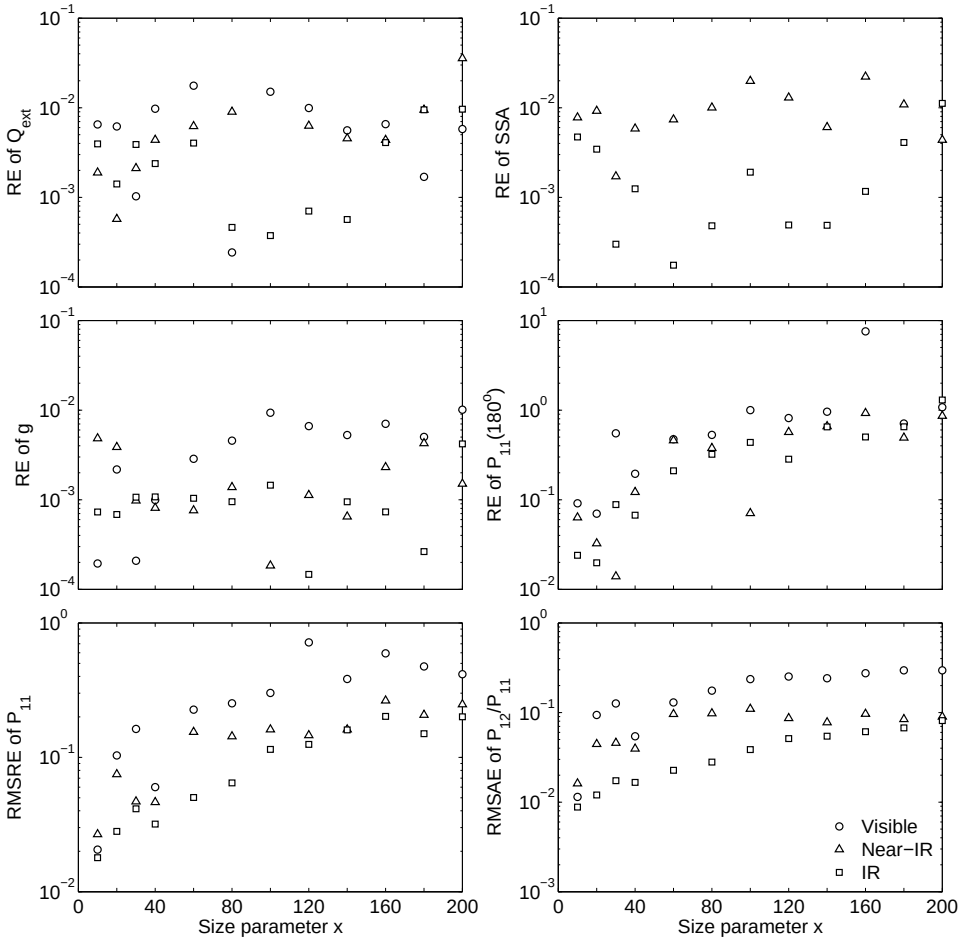

Figure 2.7: The REs, RMSREs, and RMSAEs to evaluate the accuracy of the PSTD for spheres with size parameters from 10 to 200 at visible (0.532 μm, $m = 1.312 + 1.489 \times 10^{-9}i$), near-IR (3.78 μm, $m = 1.384 + 7.055 \times 10^{-3}i$), and IR (12.0 μm, $m = 1.276 + 4.133 \times 10^{-1}i$) wavelengths.

Figure 2.7 illustrates the errors from the PSTD results for different size parameters and three refractive indices. In most cases, the REs of Q_{ext}, SSA, and g are, respectively, no more than 2%, 3%, and 1% and are not sensitive to the particle size or refractive index. Most of the REs for $P_{11}(180^o)$ are smaller than 50%. However, similar to other numerical methods, the PSTD cannot provide accurate $P_{11}(180^o)$ values in all cases over a wide range of particle sizes, and the REs are over 100% for

spheres with size parameters of 160 and 200 at visible, 120 at near-IR, and 200 at IR wavelengths. Overall, the RMSREs of P_{11} are smaller than 50% (except for spheres with size parameters of 120 and 160 at visible wavelengths), and the RMSAEs of P_{12}/P_{11} are all less than 0.3. Both the RMSREs of P_{11} and RMSAEs of P_{12}/P_{11} increase slightly with the increase in particle size as a result of the coarser spatial resolutions and more significant oscillations for the phase matrix elements. Furthermore, the errors for an absorptive case in the IR regime with $m = 1.276+4.133\times10^{-1}i$ are much smaller than those of non-absorptive or weak-absorptive cases. Considering the errors shown in Figure 2.7, the present PSTD implementation gives quite reliable solutions for light scattering by spheres with size parameters from 10 up to 200 and moderate refractive indices.

To illustrate the performance of the PSTD for large particles, Figure 2.8 gives the non-zero phase matrix elements of a sphere with a size parameter of 200 and a refractive index of $1.312 + 1.489 \times 10^{-9}i$. The REs of the normalized phase functions and the absolute errors for the ratios, P_{12}/P_{11}, P_{33}/P_{11}, and P_{34}/P_{11}, are given in right panels of the figure. Even with such a large size parameter and significant oscillations for the phase matrix elements, the PSTD results closely agree with the exact solutions given by the Lorenz-Mie theory in terms of their overall variation patterns. The REs in the forward direction phase function are generally less than 30%, but become quite significant in the backward direction with the REs at few scattering angles larger then 100%. Similar results are shown for the other three phase matrix elements.

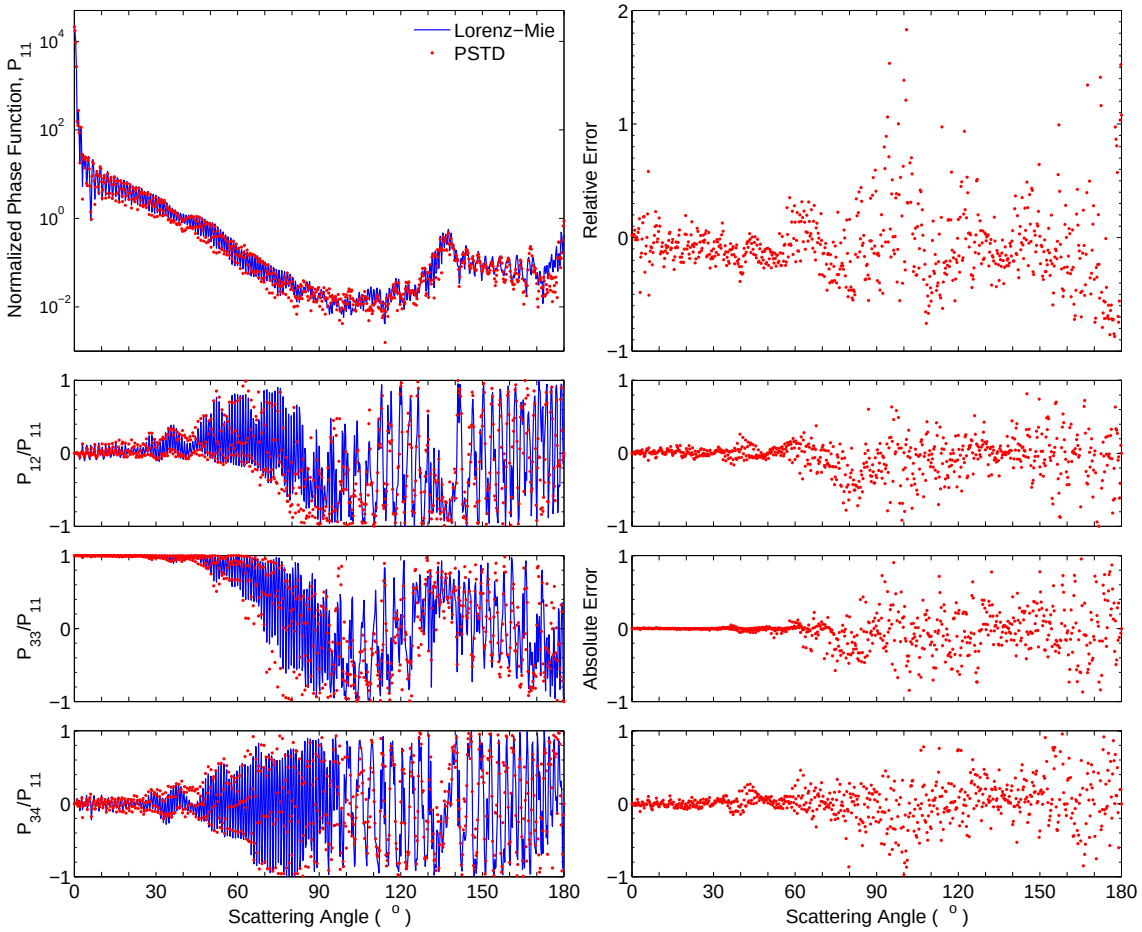

Figure 2.8: The non-zero phase matrix elements computed with the PSTD for a sphere with a size parameter of 200 and a refractive index of $m = 1.312+1.489\times10^{-9}i$. The relative errors of P_{11} and the absolute errors of P_{12}/P_{11}, P_{22}/P_{11} and P_{34}/P_{11} are shown in the right panels.

It seems that the results given by the PSTD have quite significant errors on the phase matrix of spheres, however, for practical applications, an ensemble of particles with different sizes, geometries and orientations are considered. Thus, the oscillations will be smoothed out by averaging, and all those errors will be canceled out and become much smaller, which will be shown in the next few sub-sections.

The real parts of the refractive indices of atmospheric particles are usually under 2 at various wavelengths, but those of either ice or water become very large at microwave wavelengths. Accurately calculating the optical properties of a particle with a large refractive index is quite challenging, considering the severe discontinuity in the permittivity across the particle surface. Yang et al. [73], Sun and Fu [74], and Zhai et al. [75] successfully employed the FDTD method to simulate the light scattering of particles with quite large refractive indices. We tested our parallelized PSTD implementation for water liquid spheres with size parameters up to 40 at the 3.2 cm wavelength and a refractive index of $7.150 + 2.914i$ [73].

Figure 2.9 illustrates the PSTD calculated Q_{ext}, SSA, and g and the exact solutions given by the Lorenz-Mie theory in the left panels, and the REs of the PSTD results in the right panels. Considering both the computational times and the accuracy, the spatial resolutions used decrease from approximately 300 to 30 for spheres with size parameters from 1 to 40. The REs of the three properties given by the PSTD are, respectively, no more than 3%, 1%, and 1.5%, and the absolute errors are smaller than 0.06, 0.006, and 0.01. However, the RE of g for the sphere with a size parameter of 1, which has a negative value close to zero (-0.0471), is approximately 15%. The PSTD was also found to always overestimate the Q_{ext} and underestimate the SSA for spheres with a large refractive index.

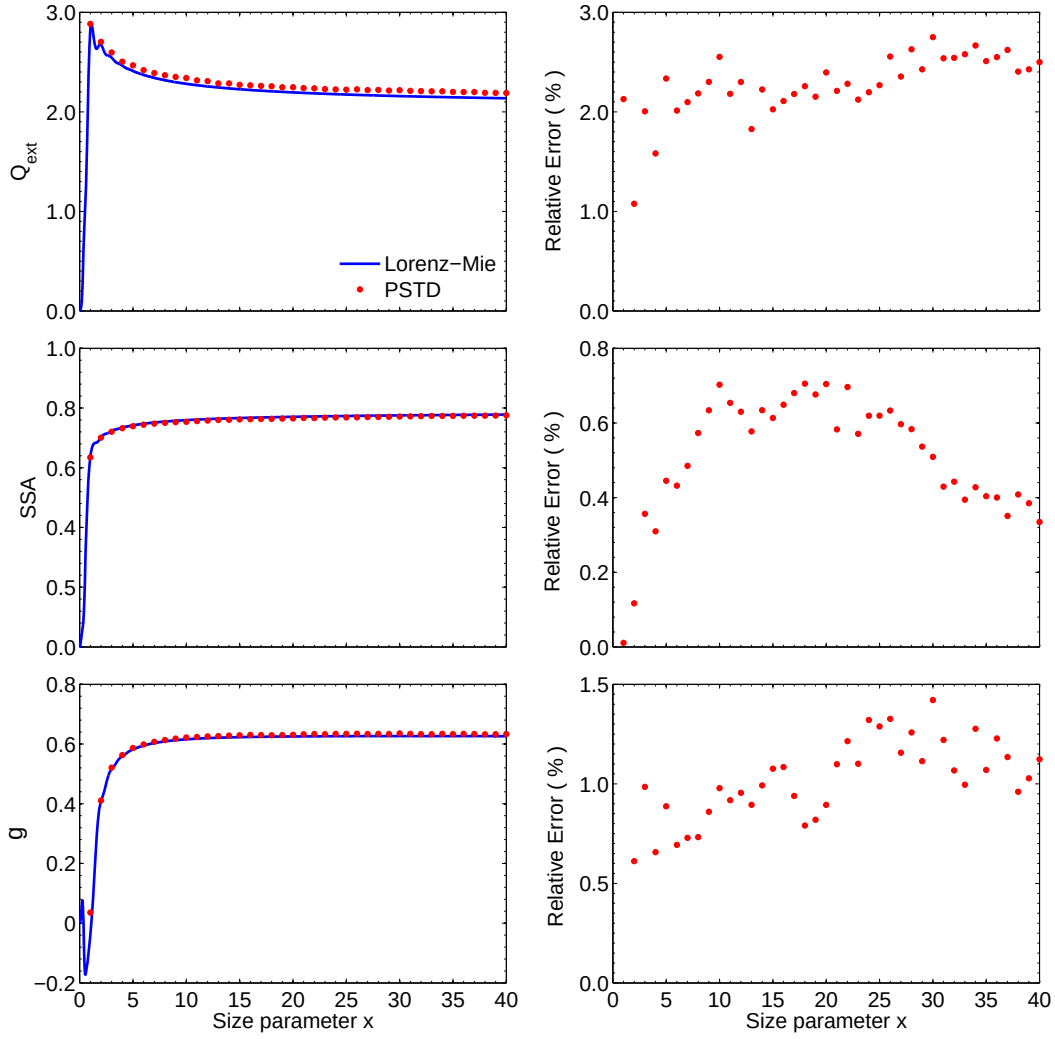

Figure 2.9: The Q_{ext}, SSA, and g of spheres as functions of the size parameter. The refractive index of the spheres is $7.150 + 2.914i$. The relative errors of the simulated quantities are shown in the right panels.

Figure 2.10 gives the non-zero phase matrix elements of a sphere with a size parameter of 40 and a refractive index of $7.150 + 2.914i$. The REs of the PSTD solutions for the phase function and the absolute errors of the ratios P_{12}/P_{11}, P_{33}/P_{11}, and P_{34}/P_{11} from the PSTD are shown in the right panels. The PSTD approximates the smooth backward scattering accurately with relative errors less than 5%. The

errors for the phase function are basically in the forward directions where the REs are no more than 20%. The errors for the ratios, P_{12}/P_{11}, P_{33}/P_{11}, and P_{34}/P_{11} are smaller than 0.4. The agreement between both the integral scattering properties and the phase matrix elements shown in Figures 2.9 and 2.10 illustrates the PSTD to be capable of calculating light scattering by particles with large refractive indices.

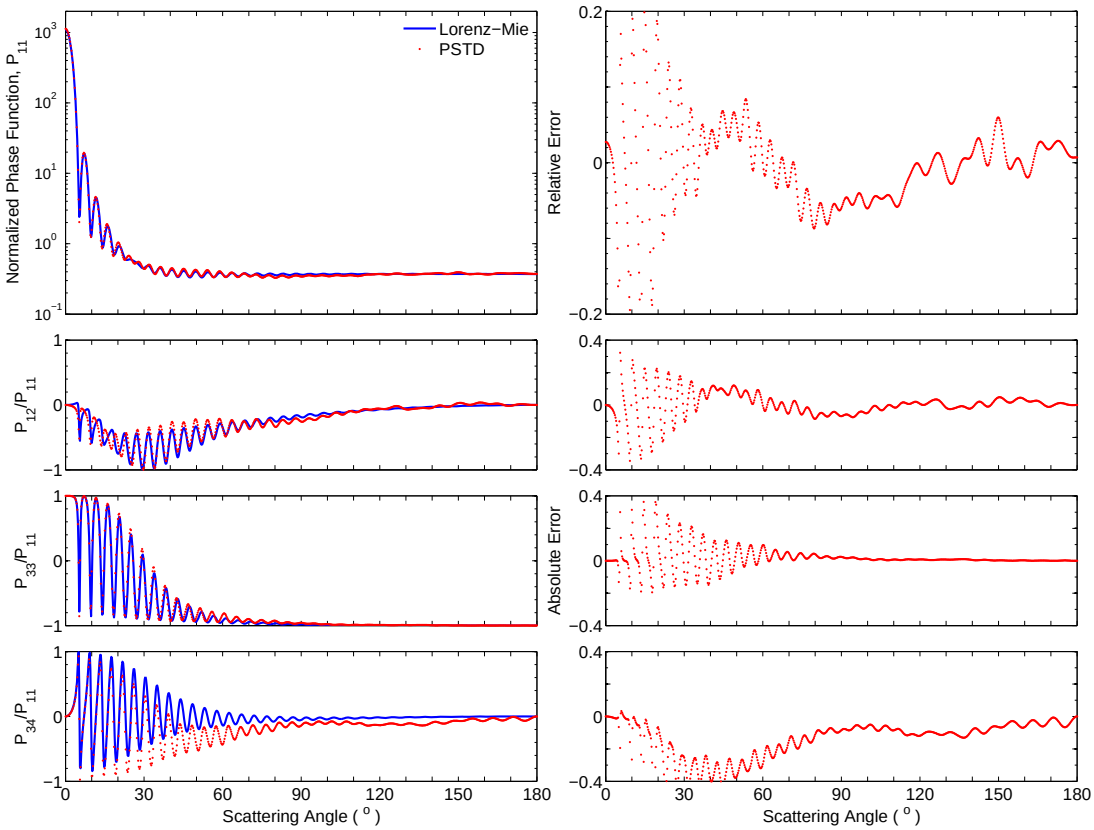

Figure 2.10: Same as Figure 2.8 but for a sphere with a size parameter of 40 and a refractive index of $7.150 + 2.914i$.

2.3.2 Comparison with the T-matrix method

The PSTD is also used to calculate the optical properties of randomly oriented non-spherical particles, e.g., spheroids and circular cylinders, which have highly reliable solutions given by the T-matrix method. The applicability of the T-matrix method is significantly dependent on the aspect ratio and refractive index of the particles, and the T-matrix implementation with extended precision is used for the comparison [17]. For this calculation, we use the refractive index of ice, $m = 1.312+1.489\times10^{-9}i$, at a wavelength of 0.532 μm. Furthermore, the single-scattering properties of spheroids or cylinders are averaged over 180 scattering planes for 32 particle orientations to account the effect of random orientations in the PSTD simulations.

Figure 2.11 shows the Q_{ext} and g of the spheroids as functions of the size parameter. The size parameter x is defined in the form of $2\pi b/\lambda$, where b is the semi-length of the symmetric axis. The aspect ratio a/b equals 0.5, and a is the equatorial radius. The solid lines in the figure are given by the T-matrix theory, and the dots are the PSTD results with size parameters up to 150. For the spheroids with an aspect ratio of 0.5 and a refractive index of $1.312 + 1.489 \times 10^{-9}i$, when the size parameters are larger than approximately $x = 112$, we did not obtain convergent T-matrix solutions. The relative errors of Q_{ext} and g are shown in the right panels of Figure 2.11. Spatial resolutions with more than 100 grid points per wavelength are used for the small particles, but a spatial resolution of 10 grid points per wavelength is used for spheroids with size parameters larger than 100. The REs of Q_{ext} are less than 0.8% and those of g less than 0.6%, but the errors generally increase with an increase in particle size. The absolute errors of Q_{ext} and g are smaller than 0.02 and 0.005, respectively.

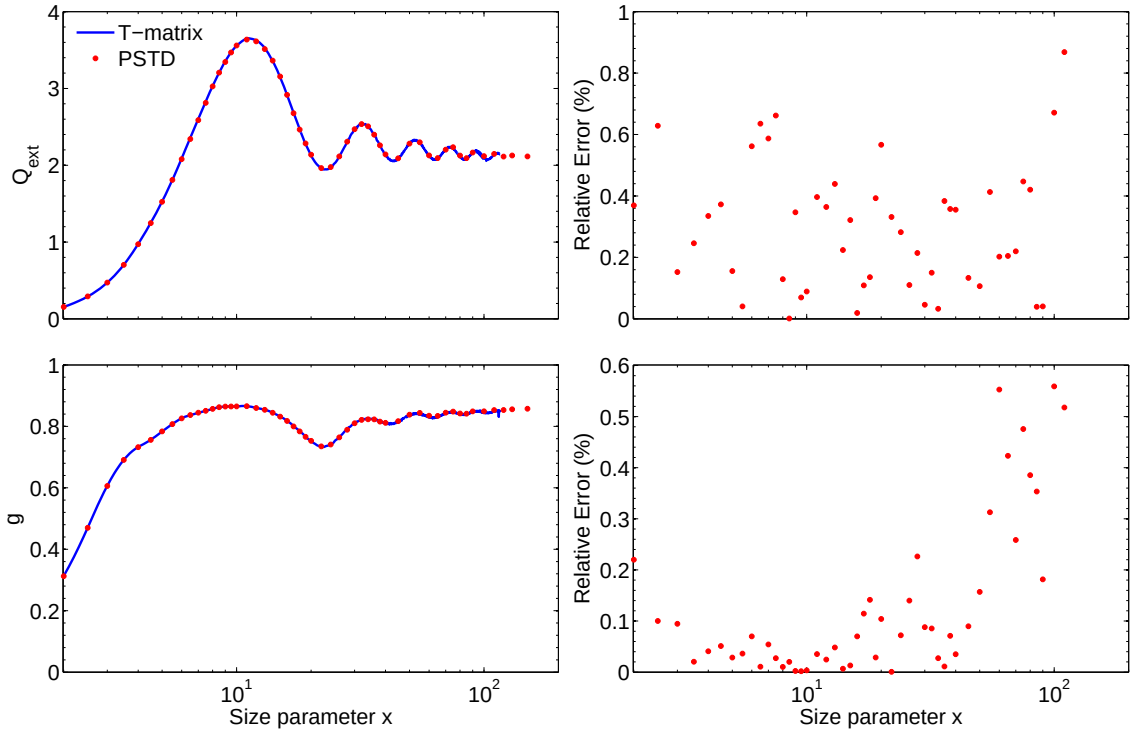

Figure 2.11: The Q_{ext} and g for randomly oriented spheroids as functions of the size parameter (left panels), and their relative errors (right panels). The refractive index used is $m = 1.312 + 1.489 \times 10^{-9}i$.

Figure 2.12 gives an example of the non-zero phase matrix elements of randomly oriented spheroids with a size parameter of 110. The PSTD generally agrees with the T-matrix theory for all elements, except for some disagreement (with REs about 30%) in P_{11} at scattering angles from 175^o to 180^o. The phase matrix results of the randomly oriented spheroid are much better than those of the spherical case, because the oscillations of the elements for a single orientation cancel each other, and relatively smooth values are obtained. For the ratios of other non-zero phase matrix elements to P_{11}, the absolute errors of the PSTD solutions are smaller than 0.1.

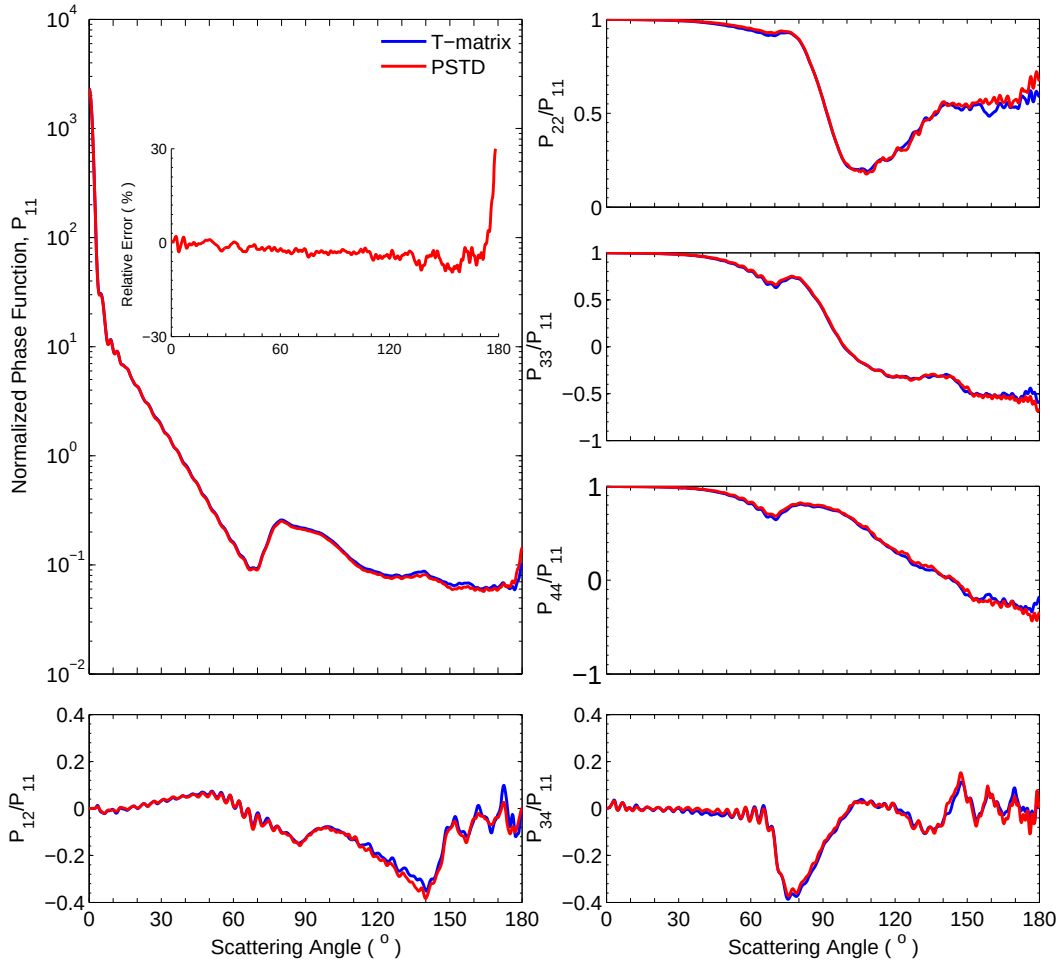

Figure 2.12: The non-zero phase matrix elements for randomly oriented spheroids with a size parameter of 110 and a refractive index of $m = 1.312 + 1.489 \times 10^{-9}i$ given by the T-matrix and PSTD methods.

The results from the randomly orientated circular cylinder calculations are given in Figures 2.13 and 2.14. The size parameter of the circular cylinder is defined in terms of $\pi L/\lambda$ where L is the length of the axis. The diameter-to-length ratio of the circular cylinders is chosen to be 1, and the maximum size parameter simulated is 75. The REs of Q_{ext} and g are neither more than 2%, and the absolute errors

are smaller than 0.05 and 0.015, respectively. The phase matrix elements for the circular cylinder with a size parameter of 75 are shown in Figure 2.14, with only slight differences in the phase function values at scattering angles from 100^o to 180^o, and the REs are less than 20%. The phase function scattering peak at 46^o is noticed in both the PSTD and T-matrix solutions. The ratios of other non-zero phase matrix elements to P_{11} computed by the PSTD have absolute errors smaller than 0.15.

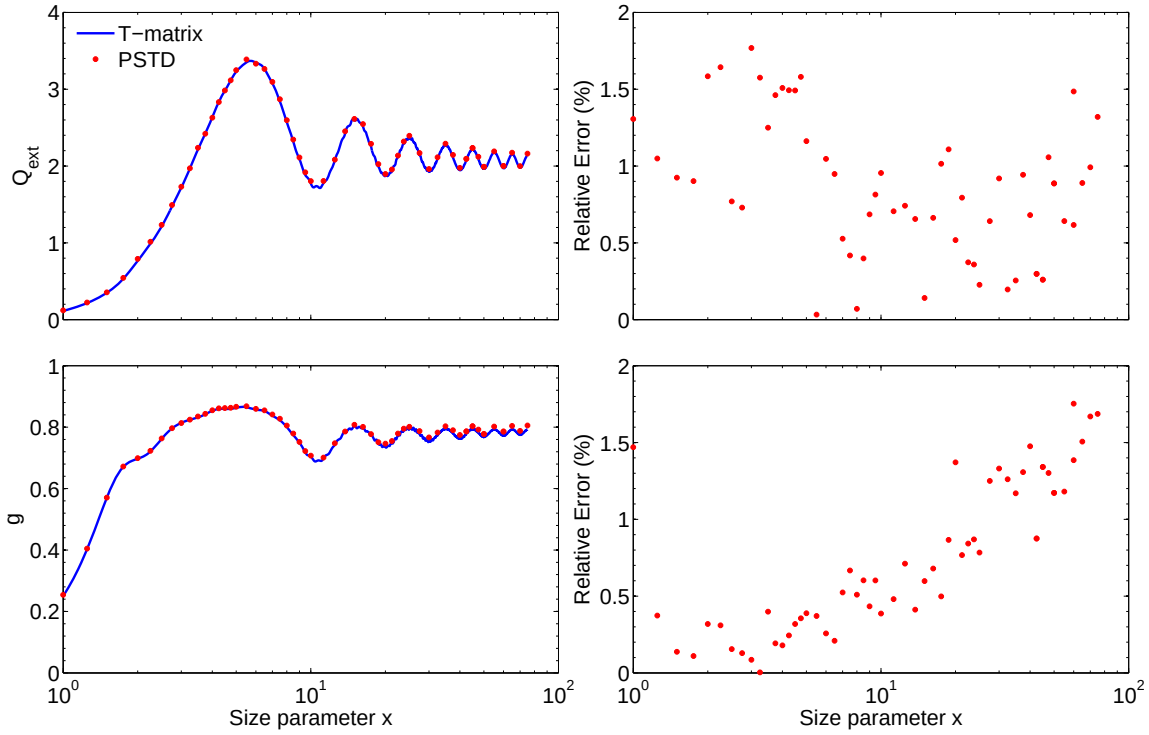

Figure 2.13: Same as Figure 2.11 but for circular cylinders with diameter-to-length ratio of 1.

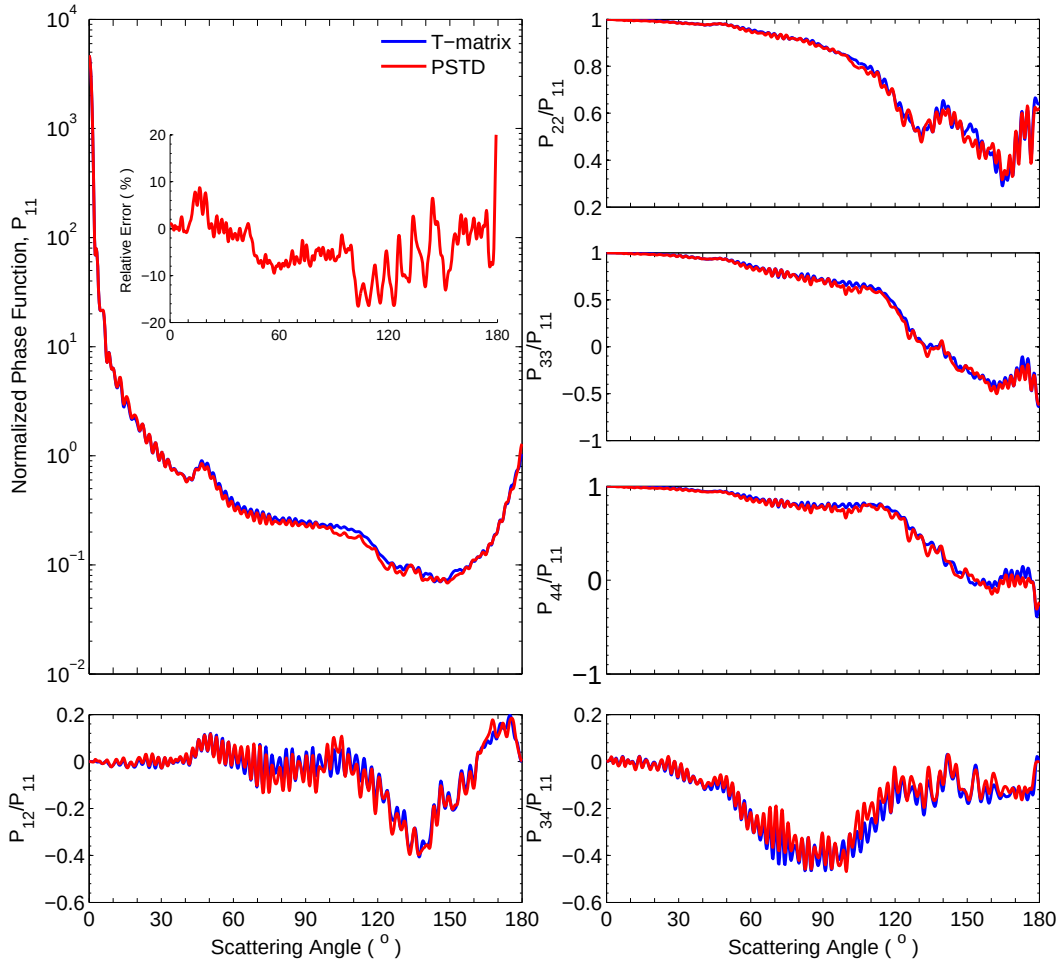

Figure 2.14: Same as Figure 2.12 but for circular cylinders with size parameter of 75 and a diameter-to-length ratio of 1.

2.3.3 Comparison with the IGOM

Considering the validations for spherical and non-spherical particles with wide ranges of size parameters and refractive indices, the PSTD appears to be a robust method for calculating light scattering problems with large size parameters of up to 200. However, the foregoing simulations focus only on the shapes having exact solutions given by some other methods, i.e., the Lorenz-Mie or T-matrix theories, in

order for accurate evaluations for the PSTD results to be obtained. In the present study, the PSTD is also employed to simulate the single-scattering properties of hexagonal columns, for which there is no exact solution. The size parameter of the hexagonal column is defined in terms of $\pi L/\lambda$, where L is the length of the column. The width-to-length ratio $2a/L$ is chosen to be 1.0, where a is the semi-width of the hexagonal cross section. The refractive index of $1.312 + 1.489 \times 10^{-9}i$ is used. The PSTD simulations are averged over 48 different particle orientations. Moreover, similar to the cases of randomly oriented spheroids or cylinders, the single-scattering properties of the hexagonal particles are also averaged over 180 scattering planes for each particle orientation. With this moderate size parameter, the PSTD results can only be compared with those given by the geometric optics methods. Here, the solutions based on the IGOM [35, 37] are used for the comparison.

Figure 2.15 shows the non-zero phase matrix elements of randomly oriented hexagonal columns with a size parameter of 50. The phase function given by the IGOM shows slight differences from that of the PSTD, particularly, at scattering angles from 135^o to 165^o. The ratios of P_{33}/P_{11} and P_{44}/P_{11} for the two methods show similar overall patterns, whereas quite obvious differences are noticed for P_{22}/P_{11}, P_{34}/P_{11}, and P_{12}/P_{11}. For a size parameter of 50, both the phase functions from the two methods show weak scattering peaks at scattering angles 22^o and 46^o, as evident from the P_{11} curves shown in Figure 2.15. The differences between the IGOM and OSTD results indicates that the accuracy of the geometric-optics method is sitll significantly challenged as the size parameter researches up to 50, whereas, for applications, they have been used for even smaller sizes, because of lack of an efficient numerically exact method at this size range. Even with the current PSTD implementation, it took about 600 CPU hours (that is about one day with 24 processors) for the the results in Figure 2.15, whereas the IGOM takes seconds for the

simulation.

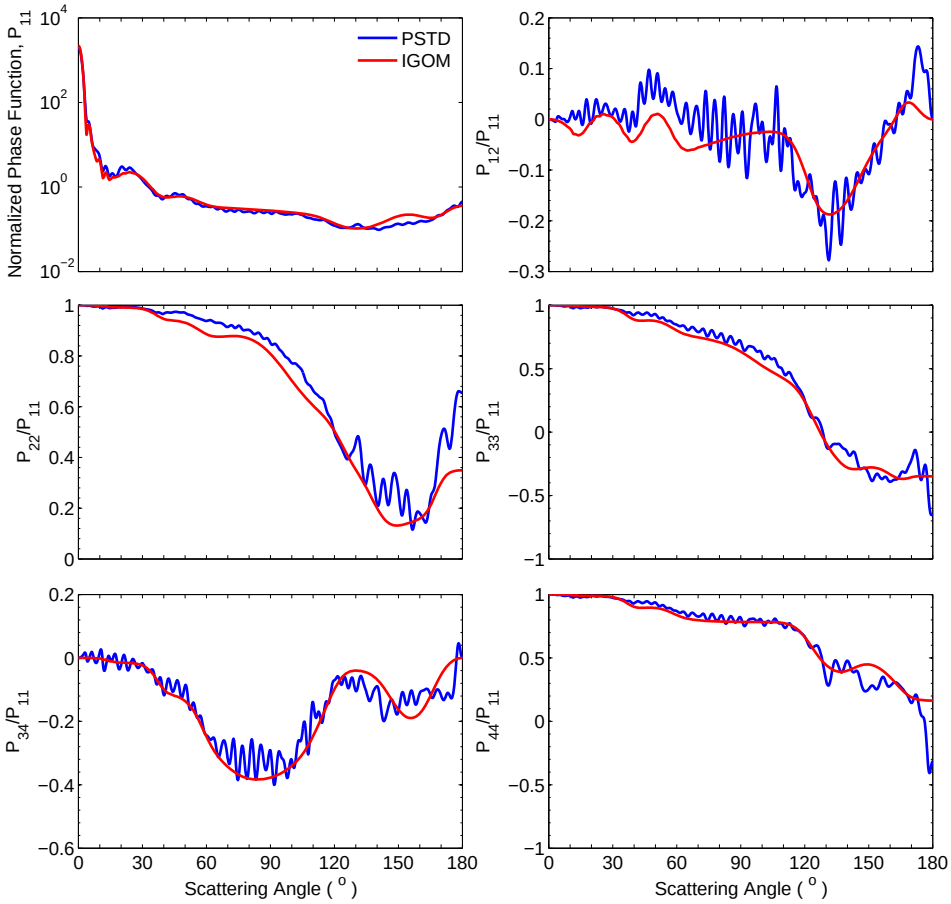

Figure 2.15: The non-zero phase matrix elements of randomly oriented hexagonal columns with a size parameter of 50 simulated by the PSTD and IGOM. The hexagonal column has a diameter-to-length ratio of 1 and a refractive index of $1.312 + 1.489 \times 10^{-9}i$.

We go one step further and apply the PSTD method to randomly oriented hexagonal columns with a size parameter of 100. In this case, the comparison between the PSTD and IGOM solutions are shown in Figure 2.16. A total of approximately 7000 CPU hours are used for the PSTD. Obviously, the IGOM results closely agree with

their PSTD counterparts. The two methods give almost the same overall variation patterns, particularly, for P_{11}; however, the PSTD solutions for P_{12}/P_{11}, P_{22}/P_{11}, P_{33}/P_{11}, P_{34}/P_{11} and P_{44}/P_{11} show pronounced variations versus scattering angle, and the IGOM results are relatively smooth. This occurs because, in the simulation, the PSTD rigorously takes into account the phase inference of the electromagnetic waves. Moreover, it is evident from Figure 2.16 that strong scattering peaks at 22^o and 46^o are clearly shown in the phase functions from both the PSTD and IGOM methods for a size parameter of 100.

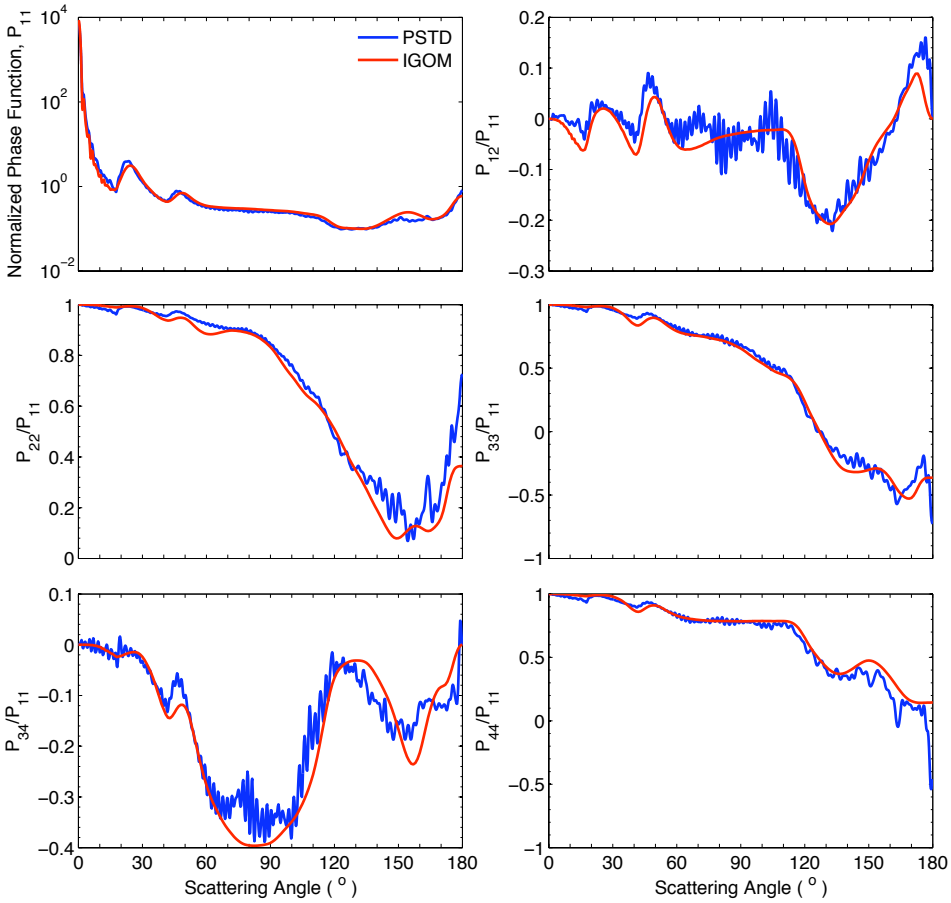

Figure 2.16: Same as Figure 2.15 but for randomly oriented hexagonal columns with a size parameter of 100.

Furthermore, it should be pointed out that, as mentioned in section 2.2.2, the PSTD is a straightforward method to simulate light scattering and absorption properties of other non-spherical particles with complex geometries and components, the application of which will be shown in the next sub-section and Chapter 3.

2.3.4 Inhomogeneous particles

Previous results show the applicability and performance of the PSTD for homogeneous particles, and this section focuses on the validation of some inhomogeneous cases, which will also show application in the next chapter. Three different inhomogeneous particles are considered, and all have the overall geometry of sphere. The first case is a stratified sphere, or concentric spheres, the exact solution of which can be given by the core-mantle Mie theory [10, 11]. The other two cases are referred as the attached and uniformly mixed particles, which will be introduced in details in Section 3.2.2, and the well-verified numerical method DDA will be used for the validation. The Amsterdam DDA implementation (ADDA) is used [24].

The PSTD, DDA and core-mantle Mie results of the stratified spheres with size parameters of 50 are shown in Figure 2.17, and the volume fractions of the spherical core, i.e. f_c, are 0.01, 0.1, 0.5, and 0.9 (from upper to lower panels, respectively). The refractive index of the core is 1.2 and of the mantle is 1.1. The left panels show the normalized phase function P_{11}, and the ratios of P_{12} to P_{11} are given in the right panels. The other non-zero phase matrix elements show similar agreement, and will not be illustrated. For the four volume fractions of the core ranging from 0.01 to 0.9, both the PSTD and DDA results show great agreement with those given by the core-mantle Mie theory, but slight differences are noticed for the PSTD results with f_c being 0.9 at some scattering angles (the lower left panel). Similar results are found for the ratios P_{12}/P_{11}. Figure 2.17 indicates both the PSTD and DDA to be robust

and accurate methods for calculating the scattering properties of inhomogeneous particles with stratified structures and can be applied over the entire range of the volume fractions.

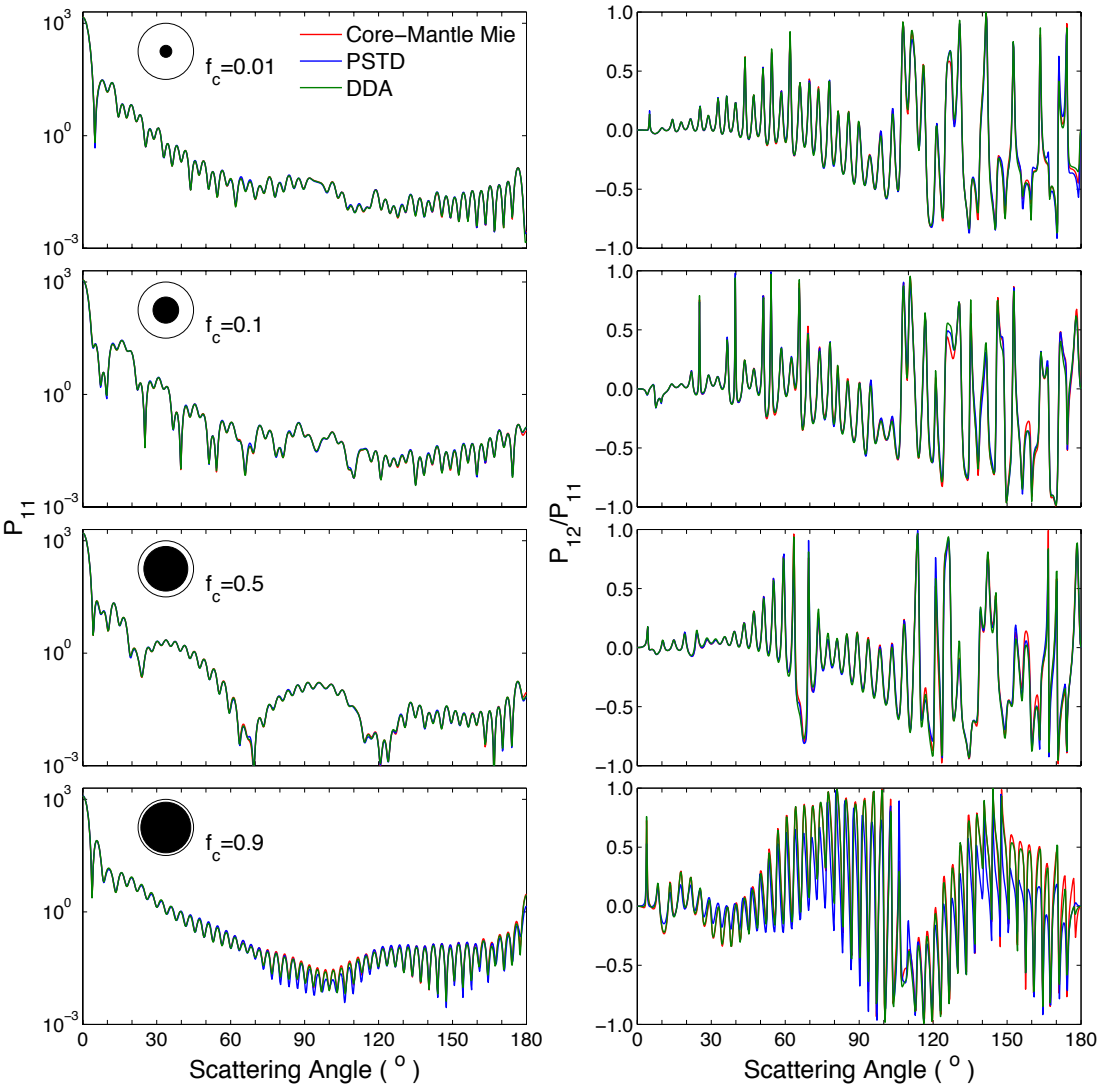

Figure 2.17: P_{11} (left panels) and P_{12}/P_{11} (right panels) for stratified spheres with size parameters of 50 given by the core-mantle Mie, PSTD and DDA methods, and, from upper to lower, the volume fractions of the core part, i.e. f_c, are 0.01, 0.1, 0.5, and 0.9. The refractive indices of the core and mantle are 1.2 and 1.1, respectively.

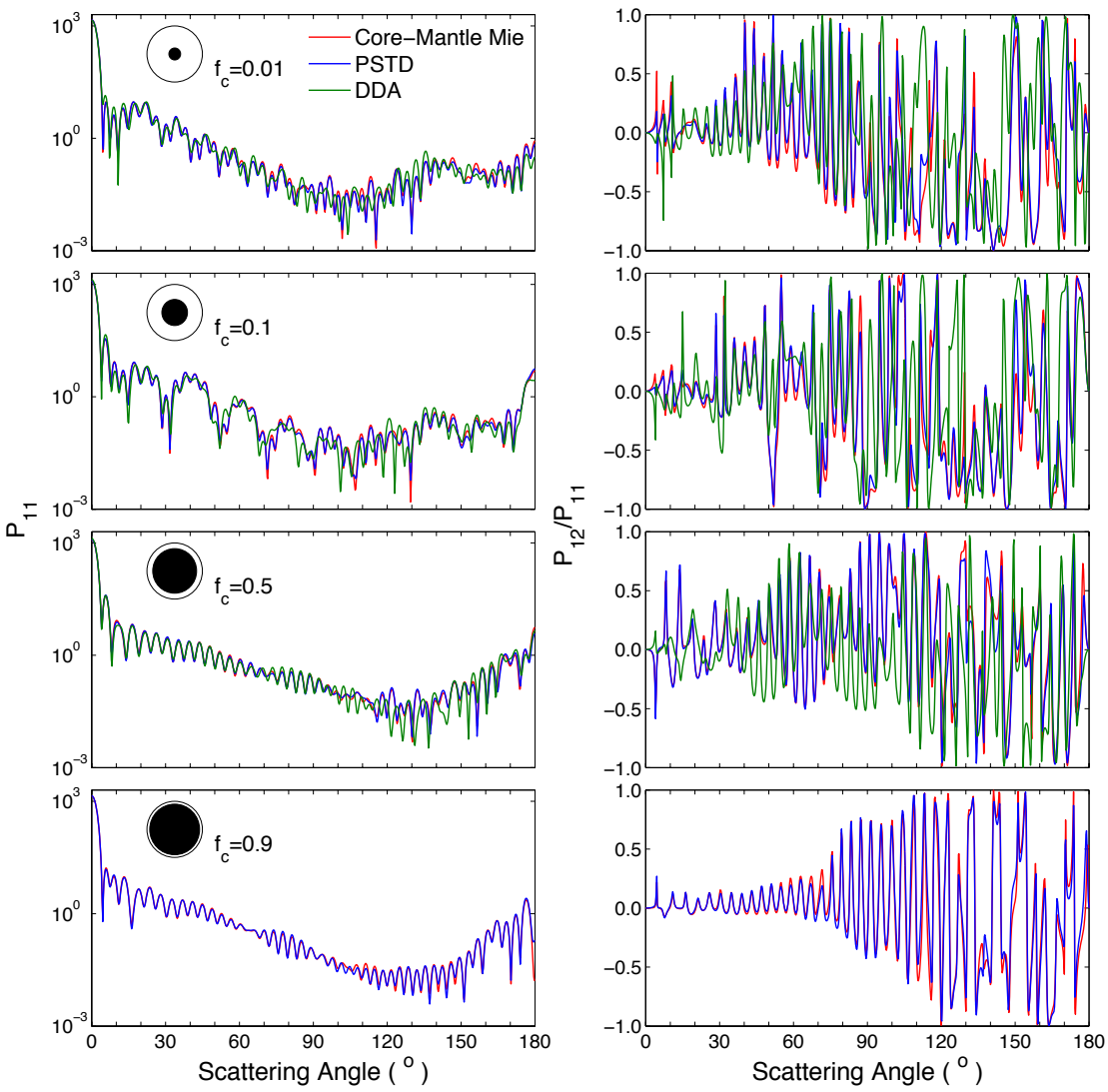

Figure 2.18: Same as Figure 2.17 but with the refractive indices of the core and mantle being $1.5 + 0.0001i$ and 1.3.

The conclusions are a little different if larger refractive indices are used, and Figure 2.18 is the same as Figure 2.17 but with more realistic refractive indices of atmospheric components. The refractive index of the core is $1.5 + 0.0001i$ (a typical value for mineral dust at visible wavelength [41]) and of the mantle is $1.3 + 0i$ (water

or ice at visible wavelength [72]). In Figure 2.18, it is obviously shown that the PSTD results still agree very well with the analytic solutions, whereas the DDA does not work as well. Furthermore, when f_c reaches 0.9, i.e. the components with refractive index of $1.5 + 0.0001i$ becoming the main part, the DDA converges very slow, and no DDA result is obtained. This indicates that the PSTD simulations and their accuracy are not sensitive to the refractive indices of the particles, whereas the DDA runs into trouble as the refractive index increases. This difference on the performance of the PSTD and DDA will be systematically compared in Section 2.5.

Figures 2.17 and 2.18 show the angular-dependent phase matrix elements of the inhomogeneous particles, and their integral scattering properties, i.e. Q_{ext} and g, as well as the relative errors are listed in Table 2.2. To show the relative efficiency of the PSTD and DDA at the two refractive indices groups, Table 2.2 also includes the ratios of the computational times used by the PSTD to DDA with the same resources. The performances of both methods are excellent for the coated spheres with relatively small refractive indices with all relative errors less than 1%, whereas the relative errors of the DDA results become as large as 6.8% for the large refractive indices case with $f_c = 0.1$. From the ratios of the computational times used by the two methods, we can see that the PSTD is more efficient for spheres with large refractive indices, whereas the DDA outperforms the PSTD for the small refractive indices.

Table 2.2: The integral scattering properties as well as their relative errors of the stratified spheres given by the PSTD and DDA compared with the core-mantle Mie solutions, and the ratios of the CPU times used for the PSTD to DDA calculations.

	f_c		0.01	0.1	0.5	0.9
$m_c = 1.2 + 0.0i$	Q_{ext}	core-mantle Mie	2.306	1.778	2.527	1.952
$m_m = 1.1 + 0.0i$		PSTD	2.289	1.765	2.551	1.981
		(RE [%])	(-0.73)	(-0.84)	(0.95)	(1.4)
		DDA	2.306	1.779	2.527	1.946
		(RE [%])	(0.0)	(0.056)	(0.0)	(0.36)
	g	core-mantle Mie	0.9480	0.9202	0.9068	0.8916
		PSTD	0.9480	0.9177	0.9068	0.8930
		(RE [%])	(-0.28)	(-0.27)	(-0.18)	(0.16)
		DDA	0.9493	0.9212	0.9102	0.8986
		(RE [%])	(0.14)	(0.10)	(0.20)	(0.79)
		T_{PSTD}/T_{DDA}	10.6	12.7	13.3	2.30
$m_c = 1.5 + 0.0001i$	Q_{ext}	core-mantle Mie	2.344	1.957	1.976	2.205
$m_m = 1.3 + 0.0i$		PSTD	2.342	1.958	1.978	2.226
		(RE [%])	(-0.085)	(0.051)	(0.10)	(0.95)
		DDA	2.262	2.091	1.978	
		(RE [%])	(-3.5)	(6.8)	(0.10)	
	g	core-mantle Mie	0.8582	0.7831	0.7803	0.8380
		PSTD	0.8642	0.7894	0.7796	0.8357
		(RE [%])	(0.70)	(0.80)	(-0.13)	(-0.27)
		DDA	0.8544	0.7984	0.7805	
		(RE [%])	(-0.44)	(2.0)	(0.026)	
		T_{PSTD}/T_{DDA}	0.4	0.3	0.2	

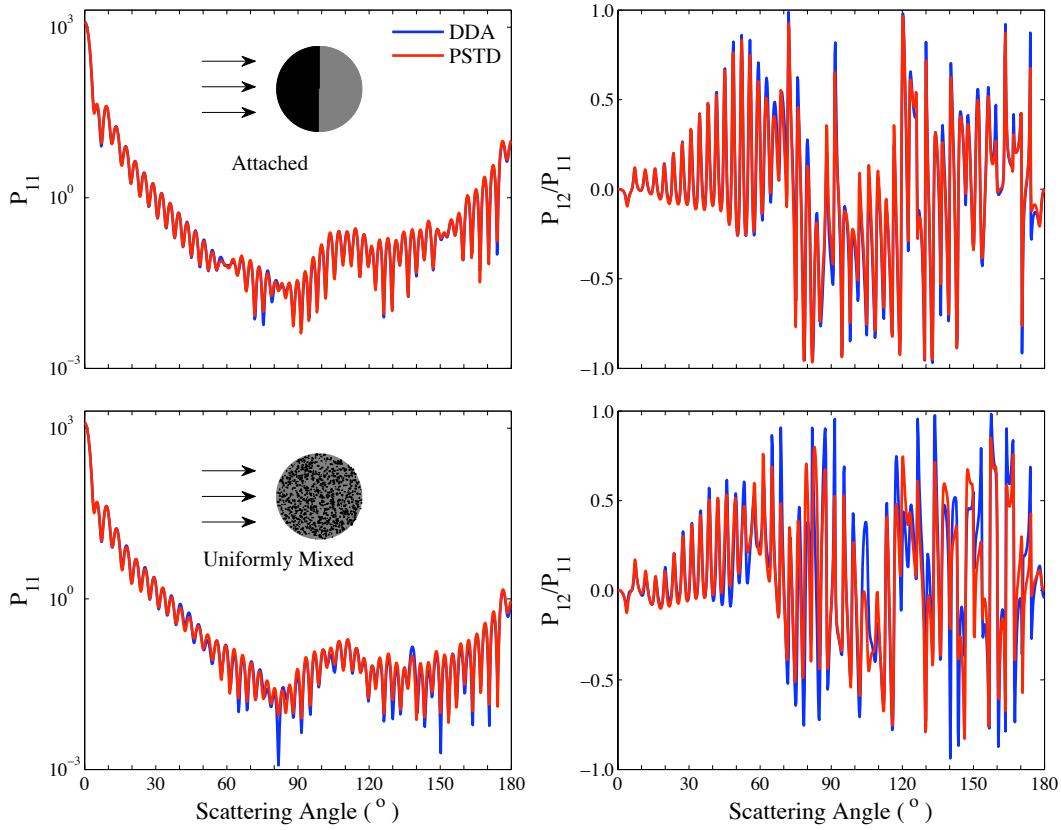

Figure 2.19: P_{11} (left panels) and P_{12}/P_{11} (right panels) of the attached and uniformly mixed spheres with size parameters of 50 given by the DDA and PSTD. The volume fractions of the two components with refractive indices of 1.1(light region) and 1.2 (dark region) are both 0.5.

Figure 2.19 shows P_{11} and P_{12}/P_{11} of the attached (upper panels) and uniformly mixed (lower panels) spheres given by the PSTD and DDA. The mixing structures and the incident direction is briefly illustrated in the figure, and will be detailed in section 3.2. For these two cases, there is no exact solution existing. The size parameters of the spheres are 50, and the volume fractions of the two components are both 0.5. The incident light of the attached particle is in the direction normal to the interface of the two components, and is illustrated in the figure. The refractive

index of the dark part is 1.2 and the light part 1.1. The curves calculated by the PSTD and DDA are almost undistinguishable for P_{11} in both cases, but the P_{12}/P_{11} ratio of the uniformly mixed sphere differs slightly at a few scattering angles. Again, the excellent agreement indicates the applicability of the PSTD for the attached and uniformly mixed particles. The integral scattering properties for the two cases are listed in Table 2.3, and the relative differences of the two methods are less than 1%.

Table 2.3: The integral scattering properties of attached and uniformly mixed spheres given by the PSTD and DDA.

	Maxing state	Attached	Uniformly mixed
Q_{ext}	PSTD	1.967	1.976
	DDA	1.978	1.977
g	PSTD	0.7884	0.8983
	DDA	0.7932	0.9034

When the volume fractions of the two uniformly mixed components are fixed, the small elements of each component are arranged randomly to form the overall inhomogeneous particle geometries uniformly. The realizations of these randomly generated particles can be very different, but the relationship to the scattering properties is unknown. We used the Monte-Carle method to generate five uniformly mixed spheres with a certain volume fraction and size parameters of 50, and Figure 2.20 shows the P_{11} and P_{12}/P_{11} of the spheres with different mixing realizations. The volume fractions of the component having a refractive index of $1.5 + 0.0001i$ are 0.1 (upper panels) and 0.5 (lower panels) and the other component has the refractive index of 1.3. The figure clearly shows the five spheres with the same size and volume

fractions, but different mixing realizations, to have almost the same P_{11} and the differences between the ratios P_{12}/P_{11} to be negligible. The indication is that the optical properties of the uniformly mixed particles are independent of the mixing realizations. The computational effort for uniformly mixed particles will be greatly reduced if the optical properties calculated for one realization of them with a given volume fraction can be used to represent the entire ensemble with the same volume fraction.

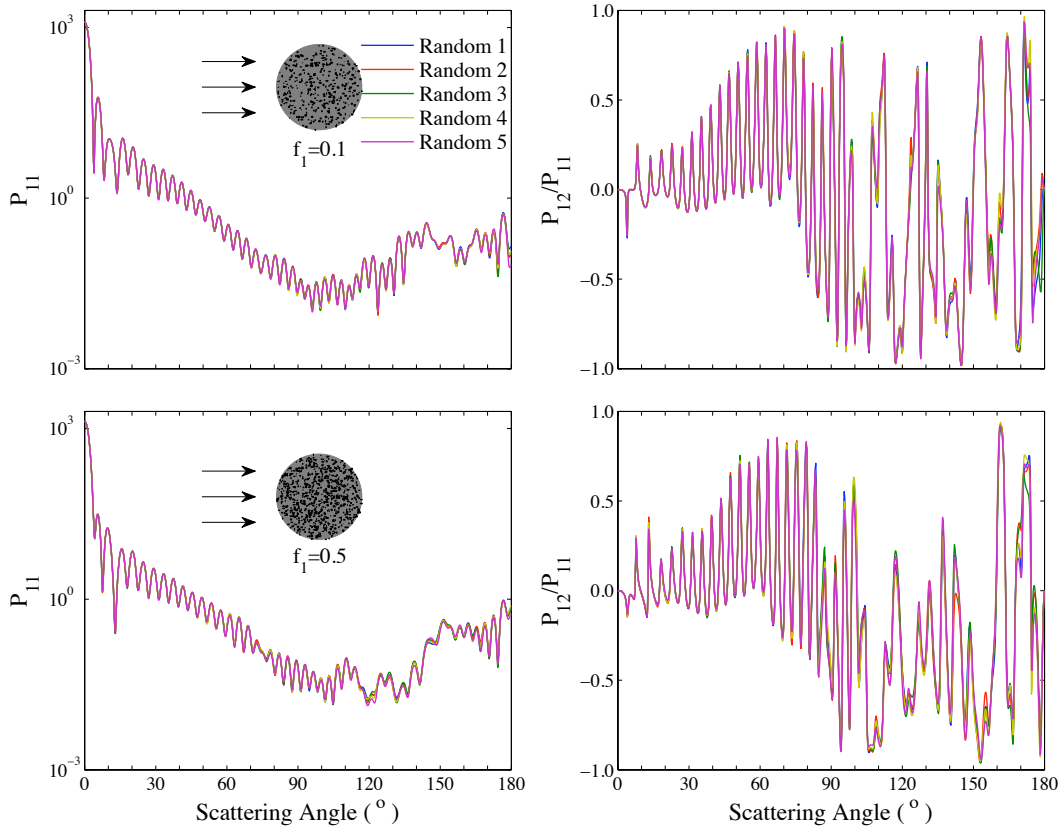

Figure 2.20: P_{11} (left panels) and P_{12}/P_{11} (right panels) of the uniformly mixed spheres with different mixing realizations given by the PSTD. The size parameters of the spheres are 50. The volume fractions of components having a refractive index of $1.5 + 0.0001i$ are 0.1 (upper panels) and 0.5 (lower panels), and the remaining component has a refractive index of 1.3.

These results indicate that the PSTD is a robust and accurate method to calculate the light scattering properties of inhomogeneous particles. The three basic mixing structures modeled in this section will be described in detail in Section 3.2, and used to study the effects of inhomogeneity on the scattering properties of atmospheric particles.

2.4 Comparison with the DDA

The DDA, FDTD and PSTD methods share similar domains of applicability and are numerically rigorous methods based on solving Maxwell's equations for electromagnetic scattering by arbitrarily shaped particles. The DDA and FDTD have been extensively studied [20, 21, 23, 25, 26, 27, 76] and systematically compared for simulating light scattering by spheres for the size parameters x up to 80 and the real part of refractive index m up to 2 [71]. The numerical performances of the two methods are found to strongly depend on the refractive index of the scattering particles; the DDA is faster for smaller m, and the FDTD is more computationally efficient for larger values of m. The "cross-over" refractive index between the two methods is at approximately 1.4 [71]. In comparison with the finite difference method, the spectral method has shown much higher orders of accuracy and smaller numerical dispersion errors while using relatively coarse spatial resolution in terms of number of grids per wavelength [54, 55]. However, the relative strengths of the PSTD in comparison with other numerical methods are still not clearly known.

The PSTD and DDA methods for the numerical simulation of light scattering by dielectric particles is compared. Specifically, we focus on spheres and spheroids because the accuracy of the results can be well quantified by comparison with their counterparts simulated from the Lorenz-Mie theory and the T-matrix method. The comparison is performed with the same prescribed accuracy criteria for both meth-

ods and covers a broad range of size parameters (up to 100 for spheres and 50 for spheroids) and non-absorbing refractive indices.

Code ADDA, developed by Yurkin and Hoekstra [24], is a widely used DDA implementation for light scattering simulations. Using a cluster of processors, ADDA can simulate light scattering by particles much larger than the incident wavelength, with reported maximum size parameters for spheres with refractive indices of 1.05 and 1.2 were 320 [24] and 130 [30], respectively. We used ADDA v.0.79 with the default settings for dipole polarizability (lattice dispersion relation) and iterative method (quasi minimal residual method). The convergence criterion of the iterative solver was set to be 10^{-3}; larger than the default value (10^{-5}) but sufficient to reach the accuracy required by this study. These code settings are identical to those used in [71] and correspond to the mainstream DDA. In particular, it is similar to the default settings of the DDSCAT [77], another widely used implementation of the DDA. Thus we focus on practical performance of ADDA (with default settings), instead of the best theoretically possible one. We also believe that the conclusions will be valid for the DDA method in general. However, we briefly discuss possible consequences of using the latest (1.1) version of ADDA in the end of this section. Both spheres and spheroids have symmetry, which is used by ADDA to halve the computational time compared to nonsymmetric shapes.

We simulated the single-scattering properties of spheres and spheroids with different sets of x and m by using the PSTD and DDA, comparing with the exact solutions to quantify the accuracies of the two numerical methods. Considering the axially rotational symmetry of the scattering particles, only one simulation of linearly polarized incident wave was sufficient to yield the 4 by 4 phase matrix P. The phase matrix in one scattering plane was calculated with the scattering angle varying from 0^o to 180^o in steps of 0.25^o. The extinction efficiency Q_{ext} and the normalized phase

function $P_{11}(\theta)$ are the two major quantities in the estimation of the accuracy of the two methods, but the asymmetry factor g and phase matrix element $P_{12}(\theta)$ will also be compared with the analytic solutions. With specified accuracy criteria for the Q_{ext} and $P_{11}(\theta)$ the computational time required to achieve the criteria became the most meaningful parameter to describe the overall performance of the methods.

The PSTD and DDA discretize the scattering particles with grid cells (PSTD) and dipoles (DDA), but their computational times are dependent not only on the number of grid points or dipoles in the computational domain, but also on the number of time steps for the PSTD or iterations of the iterative solver of a large linear system for the DDA. For a particle with a fixed size, the computational domain scales cubically with the spatial resolution, i.e. number of grid intervals or dipoles per wavelength. The accuracy of each method increases with an increase in the spatial resolution. We increase the spatial resolution until the required accuracy criteria are achieved, namely that the RE of Q_{ext} is less than 1%, and the RMSRE of $P_{11}(\theta)$ is less than 25% (same as in [71]). This procedure should not be considered as one-fits-all solution, since it is not suitable for certain applications. In particular, it may result in over 50% relative errors in backscattering intensity. However, both methods can produce smaller errors at the expense of extra computational resources, and used procedure does describe the general trends.

The DDA is the preferred method for optically soft particles (particles with refractive indices near 1) [71, 23], which has also been shown in the previous section for inhomogeneous particles. It may even outperform specialized methods, like discrete sources method, for axisymmetric particles [78]. Therefore, our comparison focused on refractive indices larger than 1.2. For spheres, we used real m ranging from 1.2 to 2.0 in steps of 0.2. The minimum size parameter for the comparison was 10. To keep the computational time manageable and achieve the accuracy criteria, especially for

the DDA simulations, the upper limit of x we considered decreased from 100 to 40 as m increased from 1.2 to 2.0. The exact sets of x and m involved in the computation are shown in Tables 2.4 and 2.5. Moreover, the comparison was extended to spheroids with realistic refractive indices of ice ($m = 1.312 + 1.489 \times 10^{-9}i$ at $0.532\mu m$ [72]) and mineral dust (approximate $m = 1.55 + 0.001i$ at the visible wavelength [79]). The size parameter of a spheroid was specified in terms of its equivalent-volume sphere. Aspect ratio values of 0.5 (corresponding to oblate spheroids) and 2 (prolate spheroids) were used. The size parameters of the spheroids ranging from 10 to 50 in steps of 10 were chosen for the simulation. The propagation direction of the incident field coincided with the symmetry axis. Again, all simulations were carried out using a single node containing 8 64-bit 2.8 GHz processors. It should be noted that for such shared-memory configuration parallelization scheme of ADDA (MPI) is less efficient than OpenMP used in PSTD, because MPI is originally designed for distributed-memory (multi-node) hardware. However, we estimate that the effect due to difference in parallelization scheme should not exceed 20% in computational times and, hence, does not influence the final conclusions.

Table 2.4 lists both the computational parameters and the simulation results and illustrates the numerical performance of the PSTD and DDA. In addition to m and x, Table 2.4 includes the spatial resolution, computational time, RE of Q_{ext}, and RMSRE of P_{11}. Indicated within parentheses are the results of cases in which the PSTD or DDA failed to reach the prescribed accuracy even with a very fine spatial resolution. Computations too time-consuming (taking more than 4 days) to reach the prescribed accuracy for the DDA are marked as "NR" (i.e. "no results") in the table. The PSTD simulations covered all sets of x and m chosen for study and achieved the prescribed accuracy in 24 of the 28 total pairs. To achieve the prescribed accuracy criteria, the spatial resolutions used by the PSTD varied from

10 to 30 without systematic dependence on x or m. The accuracy values for the DDA do show significant sensitivity to m. The DDA used spatial resolutions smaller than 10 for a refractive index of 1.2 and increased monotonically to 40 for $m = 2.0$. As an extra verification of the DDA results, we note that they agree well with those of [71], where an earlier version of the ADDA code (version 0.76) was used. In particular, we obtained almost identical values of spatial resolution and simulation error for the two ADDA versions when using the same x and m ($x \leq 60$, 40, and 10 for $m = 1.2$, 1.4, and 2.0 respectively).

With the same accuracy criteria achieved by the PSTD and DDA simulations, the behavior of both with respect to the computational time show substantial variations for different x and m. With size parameters up to 100, the PSTD simulations were finished within 9.0×10^4 seconds (i.e. 25 hours), and the most time-consuming simulation was for a sphere with $x = 100$ and $m = 1.4$. Furthermore, neither the efficiency nor the accuracy of the PSTD was significantly influenced by an increase of m. However, the computational time used by the DDA simulations increases dramatically with both particle size and refractive index due to the simultaneous increases of the spatial resolution, computational domain, and iteration number. For example, for $m = 1.2$, only a few seconds were required for spheres with $x = 10$ and 20; whereas, a sphere with $x = 80$ took 7.3×10^4 seconds (over 20 hours). When m is larger than 1.4, the DDA encounters difficulties with respect to both efficiency and accuracy. A sphere with a size parameter of 30 and $m = 2.0$ took 5.1×10^5 seconds (almost 6 days, the only case that takes over 4 days) and obtained Q_{ext} with RE of 2.0% and P_{11} with RMSRE of 55%. The DDA achieved the prescribed accuracy criteria for spheres at a size parameter of 30 for $m = 1.6$ and only 10 for larger m. The DDA did not achieve convergence for most large (spheres with $x > 60$ and $m = 1.4$ or 1.6 and $x > 40$ and $m = 1.8$ or 2.0) cases (7 spheres out of 28).

Table 2.4: Parameters and performance results for the comparison of PSTD and DDA for spheres with different x and m.

		time (*s*)		$\lambda/\Delta x$		$RE(Q_{ext})$ (%)		$RMSRE(P_{11})$ (%)	
m	x	PSTD	DDA	PSTD	DDA	PSTD	DDA	PSTD	DDA
1.2	10	2.1×10^1	1.0×10^0	13	10	0.34	0.071	5.6	0.74
	20	4.4×10^1	2.0×10^0	7.7	7.5	0.0083	0.54	8.5	13
	30	3.0×10^3	1.2×10^1	20	6.7	0.83	0.25	4.2	16
	40	3.9×10^4	1.2×10^2	30	7.5	1.0	0.43	25	19
	60	2.5×10^4	2.3×10^3	18	8.4	0.91	0.20	15	13
	80	1.0×10^4	7.3×10^4	9.2	9.4	0.26	0.62	19	19
	100*	2.3×10^4	2.7×10^4	9.3	10	0.050	0.25	18	13
1.4	10	2.3×10^2	2.0×10^0	22	15	0.30	0.69	6.1	12
	20	3.3×10^3	1.1×10^3	22	25	0.78	0.98	10	22
	30	3.8×10^2	9.8×10^3	11	17	0.87	0.74	19	25
	40	6.7×10^3	1.8×10^4	18	18	0.99	0.68	18	15
	60	2.9×10^3	NR^{**}	18	NR	1.0	NR	21	NR
	80	(1.2×10^4)	NR	(9.2)	NR	(0.32)	NR	(38)	NR
	100	8.9×10^4	NR	13	NR	0.47	NR	23	NR
1.6	10	4.9×10^1	5.4×10^1	12	25	0.85	0.76	14	7.1
	20	(1.1×10^3)	(3.2×10^4)	(20)	(40)	(5.4)	(5.7)	(44)	(45)
	30	8.3×10^2	4.4×10^4	13	30	0.78	0.75	25	15
	40	2.7×10^3	(2.4×10^5)	14	(20)	0.23	(1.5)	24	(33)
	60	(3.2×10^4)	NR	(18)	NR	(0.035)	NR	(29)	NR
1.8	10	2.7×10^2	6.4×10^2	26	35	0.92	0.88	10	8.8
	20	1.5×10^3	(3.0×10^3)	23	(40)	0.85	(2.7)	10	(19)
	30	3.0×10^3	(9.5×10^4)	19	(25)	0.70	(5.4)	15	(52)
	40	1.5×10^4	NR	21	NR	0.63	NR	19	NR
	60	1.7×10^4	NR	15	NR	0.28	NR	22	NR
2.0	10	5.1×10^1	2.0×10^3	13	40	0.90	0.45	16	16
	20	5.6×10^2	(5.0×10^4)	16	(35)	0.58	(8.9)	13	(35)
	30	1.3×10^3	(5.1×10^5)	14	(25)	0.21	(2.0)	21	(55)
	40	(3.4×10^3)	NR	(14)	NR	(2.3)	NR	(26)	NR

Note:
* the DDA for a sphere with $x = 100$ and $m = 1.2$ did not converge with the default iteration method (quasi minimal residual), and the bi-conjugate stabilized method was used instead.
** "NR" means no result (see text).

On contrary, the DDA was very efficient for spheres with small m and x and was one-two orders of magnitude faster than the PSTD. However, a critical size parameter existed above which the PSTD outperformed the DDA for small refractive indices (1.2 or 1.4) and as the value of x decreased from 80 to 30 as the refractive index increased from 1.2 to 1.4. For m larger than 1.4, the PSTD became more efficient for all size parameters in the range from 10 to 60 and was almost two orders of magnitude faster than the DDA for spheres with x larger than 30.

In the (x, m) domain, Figure 2.21 clearly illustrates the strengths of the two methods, and summarizes the data in Table 2.4 with a "regime diagram." It is a representation of the (x, m) plane, and the value entered at a location in the diagram is the time ratio ρ of PSTD to DDA CPU time required for the scattering calculation. Cases in which the PSTD produced results meeting the accuracy criteria but the DDA did not are indicated by open rather than solid circles. The green symbols at the lower left of the plane indicate parameter choices (x, m) for which the DDA seems to be the preferable method, based on CPU time needed to meet accuracy criteria, and red symbols at the top right indicate choices for which the PSTD was preferable (ratio ρ larger than 1). This is the same as the one based on the inhomogeneous particles, which is shown in the validation section. Furthermore, comparing Figure 2.21 with results of [71], we can conclude that the PSTD is similar to the FDTD when compared with the DDA, except for an increase in the relative relative performance of the PSTD with an increase in size parameter, even for $m = 1.2$.

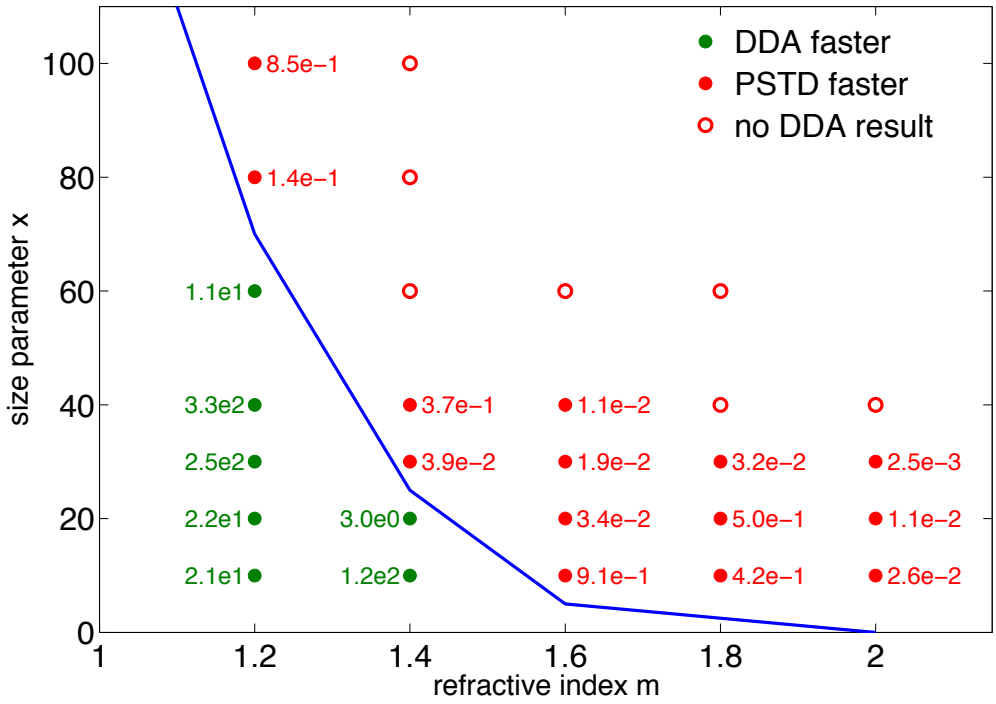

Figure 2.21: The relative performance of the PSTD and DDA for spherical particles with different x and m. Numbers in the figure are the ratios ρ of PSTD to DDA CPU time required for the scattering calculation at indicated (x, m). Open circles indicate that a PSTD result was calculated, but the DDA calculation failed to converge.

Table 2.5 lists some other optical property errors with which to compare the performances of the two methods, but no separate accuracy criterion was prescribed for these quantities. The table includes RE of g, maximum RE of P_{11}, RE of P_{11} at 180^o (i.e., backscatter), and RMSAE of P_{12}/P_{11}. Both the PSTD and DDA show similar accuracy on those scattering properties, when the prescribed accuracy criteria for Q_{ext} and P_{11} are achieved. Overall, the differences between the four errors given by the PSTD and DDA are relatively small and dependent on x or m in the following manner:

(1). When the prescribed accuracy was achieved, both methods gave the asym-

metry factors with REs smaller than 2%. The DDA was more accurate for spheres with a refractive index of 1.2, whereas the PSTD was more reliable for the refractive indices of 1.8 and 2.0.

(2). The maximum REs of P_{11} of the PSTD and DDA results were of the same order and either could reach over 100%, especially for cases with large size or refractive index. This is caused by the significant oscillations in the phase functions, and these maximum errors generally occurred at the scattering angles with a sharp trough or peak for P_{11}. Large values of the maximum REs indicate that neither method could track P_{11} accurately for all sizes and refractive indices over all scattering angles. However, those errors will be canceled out when the scattering properties are averaged over particles orientations or an ensemble of particles of different sizes.

(3). The PSTD gave relatively more accurate backscatter for spheres with large m (> 1.6) and for those with small x and small m. However, similar to other numerical models, both methods worked poorly in some cases, i.e. the RE of $P_{11}(180^o)$ was 80% for a sphere with $m = 1.4$ and $x = 100$ by the PSTD and 240% for $m = 1.6$ and $x = 40$ by the DDA.

(4). The PSTD and DDA both approximated P_{12}/P_{11} accurately with the RMSAEs smaller than 0.25, when the prescribed accuracy criteria are achieved, and the values of RMSAE (P_{12}/P_{11}) are significantly correlated to those of the RMSREs of P_{11} in Table 2.4.

Table 2.5: Same as Table 2.4 but for some accuracy results (all values have the unit of %)

		RE of g		Maximum RE of P_{11}		RE of $P_{11}(180^o)$		RMSAE of P_{12}/P_{11}	
m	x	PSTD	DDA	PSTD	DDA	PSTD	DDA	PSTD	DDA
1.2	10	0.11	0.063	21	33	9.4	33	5.2	5.9
	20	0.18	0.036	28	84	15	18	6.9	11
	30	0.079	0.028	19	66	17	24	3.2	14
	40	1.7	0.11	3.5×10^2	87	12	34	25	15
	60	0.060	0.084	79	70	79	8.4	15	12
	80	0.88	0.71	1.3×10^2	1.2×10^2	44	54	16	17
	100	0.42	0.083	1.0×10^2	79	53	42	14	14
1.4	10	1.5	0.83	29	65	28	60	1.9	5.9
	20	0.25	1.3	36	1.8×10^2	5.1	18	8.4	9.5
	30	0.14	0.38	84	1.4×10^2	48	30	17	23
	40	0.091	0.030	1.1×10^2	1.4×10^2	20	1.3×10^2	13	13
	60	1.3	NR	1.6×10^2	NR	28	NR	16	NR
	80	(1.9)	NR	(2.9×10^2)	NR	(10)	NR	(36)	NR
	100	0.050	NR	1.3×10^2	NR	80	NR	18	NR
1.6	10	1.3	0.55	51	23	16	8.5	7.4	6.9
	20	(6.0)	(6.5)	(1.5×10^2)	(1.8×10^2)	(78)	(77)	(44)	(41)
	30	1.3	0.69	2.2×10^2	68	32	61	16	9.8
	40	1.2	(1.6)	1.2×10^2	(2.4×10^2)	22	(2.4×10^2)	17	(24)
	60	0.060	NR	(1.5×10^2)	NR	(30)	NR	(22)	NR
1.8	10	0.78	1.2	32	21	1.6	21	12	5.5
	20	0.41	(1.5)	30	(1.1×10^2)	8.8	(26)	6.7	(15)
	30	0.17	(5.2)	49	(2.1×10^2)	6.2	(17)	13	(36)
	40	1.1	NR	83	NR	3.3	NR	14	NR
	60	0.15	NR	(1.2×10^2)	NR	2.6	NR	19	NR
2.0	10	2.3	0.44	46	40	1.1	24	17	11
	20	0.56	(3.2)	51	(1.3×10^2)	4.4	(47)	7.7	(35)
	30	0.042	(1.6)	85	(2.4×10^2)	20	(43)	13	(49)
	40	(2.3)	NR	(1.2×10^2)	NR	(37)	NR	(18)	NR

A further comparison of the numerical accuracy of the two methods, the P_{11} of spheres with the same size parameter of 30 and different refractive indices, is

illustrated in the left panels of Figure 2.22. The time ratio is also included in the figure. From the upper to the lower panel, the refractive index is increased from 1.2 to 2.0 in steps of 0.2. Shown in the figure are the exact solutions given by Lorenz-Mie theory (blue lines) and the results of the PSTD (red lines) and DDA (green lines) simulations. The relative errors of P_{11} are shown in the right panels of Figure 2.22. The RMSREs of P_{11} for the spheres, as given by the PSTD and DDA, range from 4.2% ($m = 1.2$ for the PSTD) to 55% ($m = 2.0$ for the DDA). For spheres with $x = 30$, the DDA simulation achieves the prescribed accuracy only for refractive indices from 1.2 to 1.6. However, the PSTD results achieved the 25% criterion for all five refractive indices. With small values of m (from 1.2 to 1.6), the relative errors of the PSTD and DDA (right panels) are smaller than 30% at most scattering angles, but became significant, even as large as 100%, near the angles where sharp troughs or peaks occurred in the phase function. In comparison, the REs of the phase functions given by the PSTD and DDA were of the same order for spheres with refractive indices of 1.2 and 1.4. At a refractive index of 1.6, the REs, simulated by the DDA, of the backward scattering at scattering angles larger than 140^o became 50% or larger. As m increase to 1.8 and 2.0, the REs are then comparable to those with small m and indicate the weak influence of m on the PSTD simulation accuracy, whereas the performance of the DDA becomes very poor with the RMSRE reach over 50% even with large dpl and large amount of computational times. When particle size distributions or different orientations of non-spherical particles are taken into consideration in practical applications, the strong oscillations in the phase function are smoothed. Thus, both methods will provide much more accurate and reliable phase matrix elements. The comparison shown in Figure 2.22 indicate the results for forward scattering are apparently more accurate than those of backward scattering.

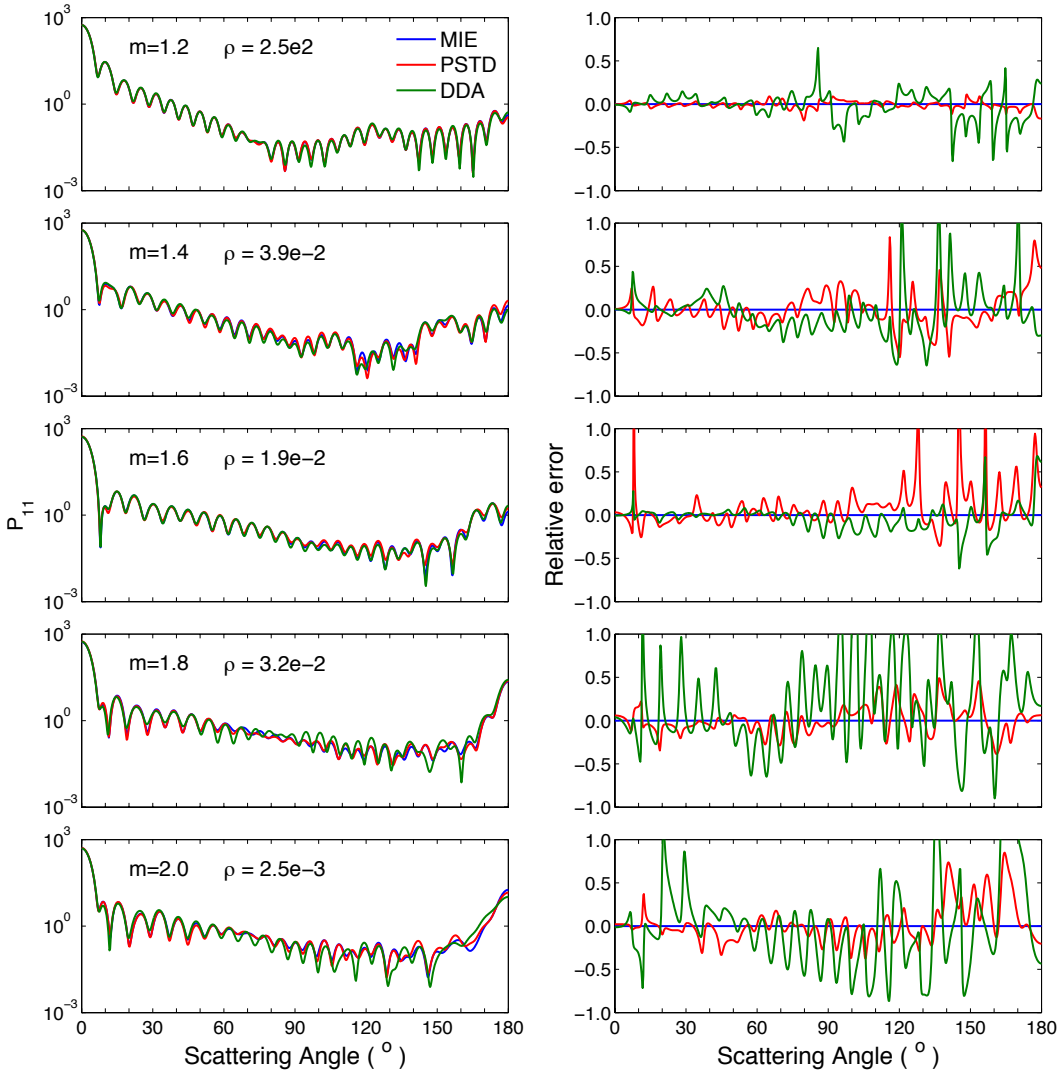

Figure 2.22: Comparison of P_{11} given by the PSTD and DDA with the exact solutions for spheres with $x = 30$ and refractive indices ranging from 1.2 to 2.0 from the upper to the lower panels. The parameter ρ indicates the ratio of PSTD to DDA CPU times. The relative errors of the two numerical methods are in the right panels.

For the same spheres with size parameters of 30 and refractive indices ranging from 1.2 to 2.0, the left panels of Figure 2.23 show the ratios of P_{12}/P_{11} as functions of scattering angles and the right panels the absolute errors. The RMSAEs of the ratios given by both the PSTD and DDA are approximately between 0.03 and 0.5

(from Table 2.5), and the absolute errors at most scattering angles are less than 0.2. Again, the results given by the PSTD and DDA for m=1.2, 1.4 and 1.6 are comparable. For refractive indices up to 1.8 and 2.0, the PSTD simulations give results with similar accuracy to those with small m, whereas the results given by the DDA becomes quite significant, reaching even over 1.0 at some scattering angles.

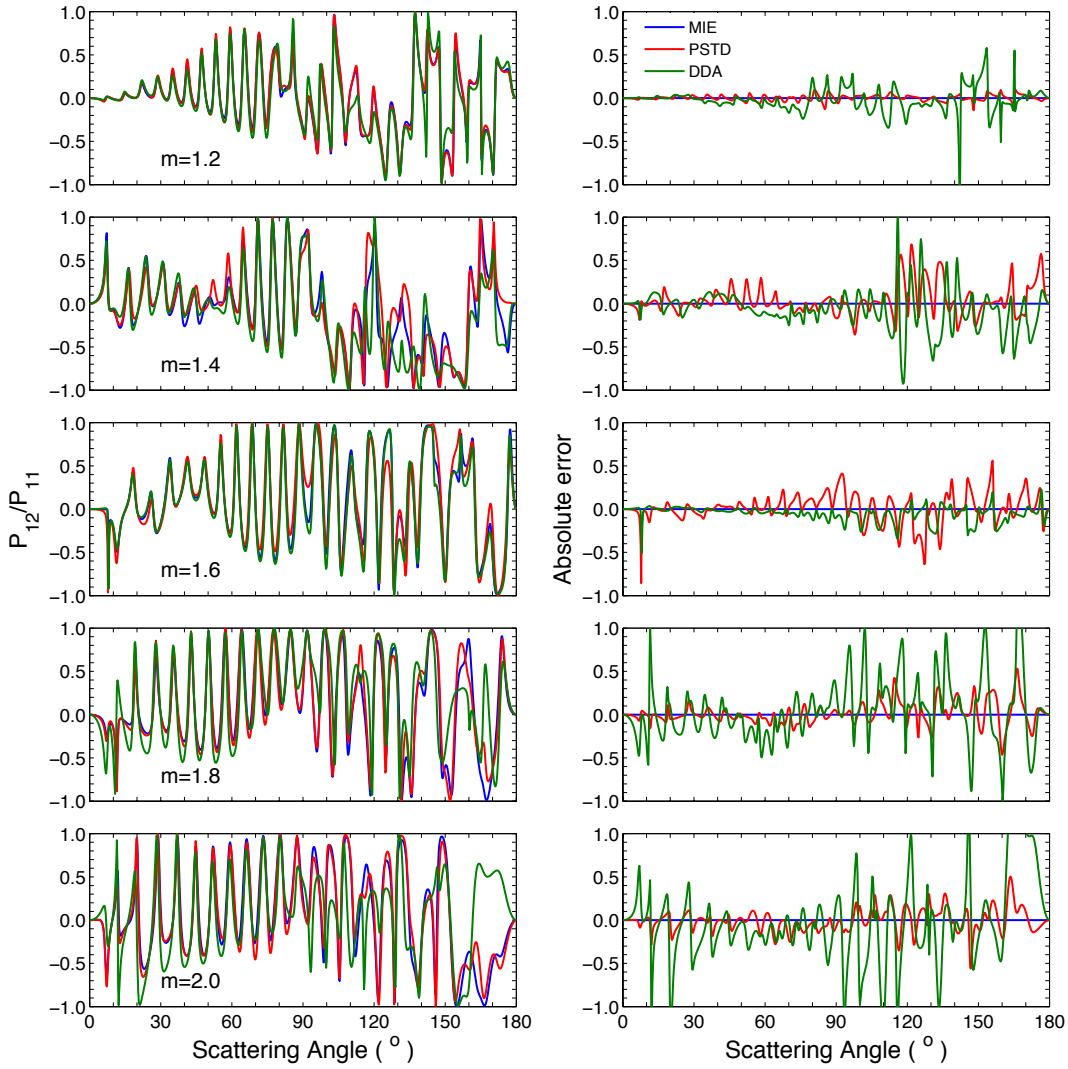

Figure 2.23: Same as Figure 2.22, but for P_{12}/P_{11} (left panels) and their absolute errors (right panels)

Similar to Table 2.4, Table 2.6 shows the comparison between the PSTD and DDA for spheroids, and the results compared with the solutions given by the T-matrix method. With the refractive index of ice, both the PSTD and DDA fail only at a spheroid with $x = 50$ and $a/b = 2$. When the spheroids had the refractive index of mineral dust, the PSTD achieved the accuracy criteria for all sizes and aspect ratios except the one with $x = 50$ and $a/b = 0.5$. However, the DDA simulations could only be carried out for x smaller than 30 and achieved the criteria for sizes less than or equal to 20. As expected, the PSTD outperforms the DDA for large spheroids with $x = 50$ when $m = 1.3117 + 1.489 \times 10^{-9}i$, and was the preferable method for all spheroids with $m = 1.55 + 0.001i$, except the one with $a/b = 2$ and $x = 10$. The relative performance of the two methods shows no dependence on the spheroid aspect ratio. Generally, the refractive indices of ice at different wavelengths have a real part of approximately 1.3, and those of aerosol particles, i.e. dust and back carbon, are 1.5 or larger. Thus, our comparison suggests the DDA to be suitable for numerical simulations of ice crystals with size parameters smaller than 50, whereas the PSTD is more efficient and more accurate for ice crystals with size parameters larger than 50 and aerosol particles of all sizes. The PSTD and DDA results with respect to the REs of g, maximum REs of P_{11}, REs of $P_{11}(180^o)$ and RMSAEs of P_{12}/P_{11} for spheroids are similar to those of spheres and will not be included here.

Table 2.6: Same as Table 2.4 but for spheroids with size parameters from 10 to 50, aspect ratios of 0.5 and 2.0, and refractive indices of $m_1 = 1.31 + 1.489 \times 10^{-9}i$ and $m_2 = 1.55 + 0.001i$.

			time (*s*)		$\lambda/\Delta x$		$RE(Q_{ext})$ (%)		$RMSRE(P_{11})$ (%)	
m	a/b	x	PSTD	DDA	PSTD	DDA	PSTD	DDA	PSTD	DDA
m_1	0.5	10	6.0×10^1	4.0×10^0	15	18	0.51	0.58	6.9	4.4
		20	9.9×10^2	9.9×10^1	21	16	1.0	0.62	3.4	7.3
		30	2.8×10^3	9.1×10^2	19	15	0.95	0.16	8.1	16
		40	1.3×10^4	5.2×10^3	21	15	0.64	0.40	8.3	20
		50	8.4×10^3	1.3×10^4	15	15	0.54	0.89	23	20
	2.0	10	7.2×10^1	1.0×10^0	18	9.5	0.29	0.65	8.1	20
		20	8.3×10^1	1.0×10^1	10	7.2	0.86	0.43	9.9	25
		30	1.4×10^3	2.1×10^2	16	8.1	0.83	0.67	8.7	22
		40	2.9×10^3	2.9×10^3	12	12	0.57	0.052	22	21
		50	(1.3×10^4)	(3.5×10^4)	(19)	(15)	(1.3)	(1.7)	(27)	(88)
m_2	0.5	10	6.7×10^1	3.3×10^0	15	51	0.28	0.89	5.3	2.4
		20	2.6×10^3	(4.1×10^0)	27	(60)	0.95	(5.2)	11	(3.5)
		30	4.6×10^3	(1.8×10^5)	21	(35)	0.87	(2.5)	7.6	(10)
		40	3.1×10^3	NA	14	NA	0.57	NA	19	NA
		50	(3.5×10^4)	NA	(18)	NA	(1.3)	NA	(10)	1NA
	2.0	10	1.3×10^2	6.6×10^1	20	30	0.73	0.42	0.39	8.7
		20	6.8×10^2	9.5×10^2	15	20	0.27	0.75	13	19
		30	8.1×10^3	(1.1×10^5)	18	(35)	0.89	(1.6)	24	(31)
		40	8.9×10^3	NA	21	NA	0.19	NA	21	NA
		50	2.0×10^4	NA	17	NA	0.77	NA	12	NA

The left panels of Figure 2.24 show P_{11} of the spheroids with $x = 30$ and the right panels the relative errors of the PSTD and DDA results compared with the T-matrix solutions. The aspect ratios and refractive indices are labeled in the figure. In general, the PSTD and DDA results both had excellent agreement with the T-matrix results, although the relative errors became significant at a few scattering angles around the troughs or peaks in P_{11}. For the spheroid with $x = 1.55 + 0.001i$ and $a/b = 2.0$, the DDA gave the RMSREs of P_{11} to be 31%, which is larger than

the criterion, but Figure 2.24 shows the relative errors to be larger than 50% only at the scattering angles around 80^o and the ones larger than 130^o.

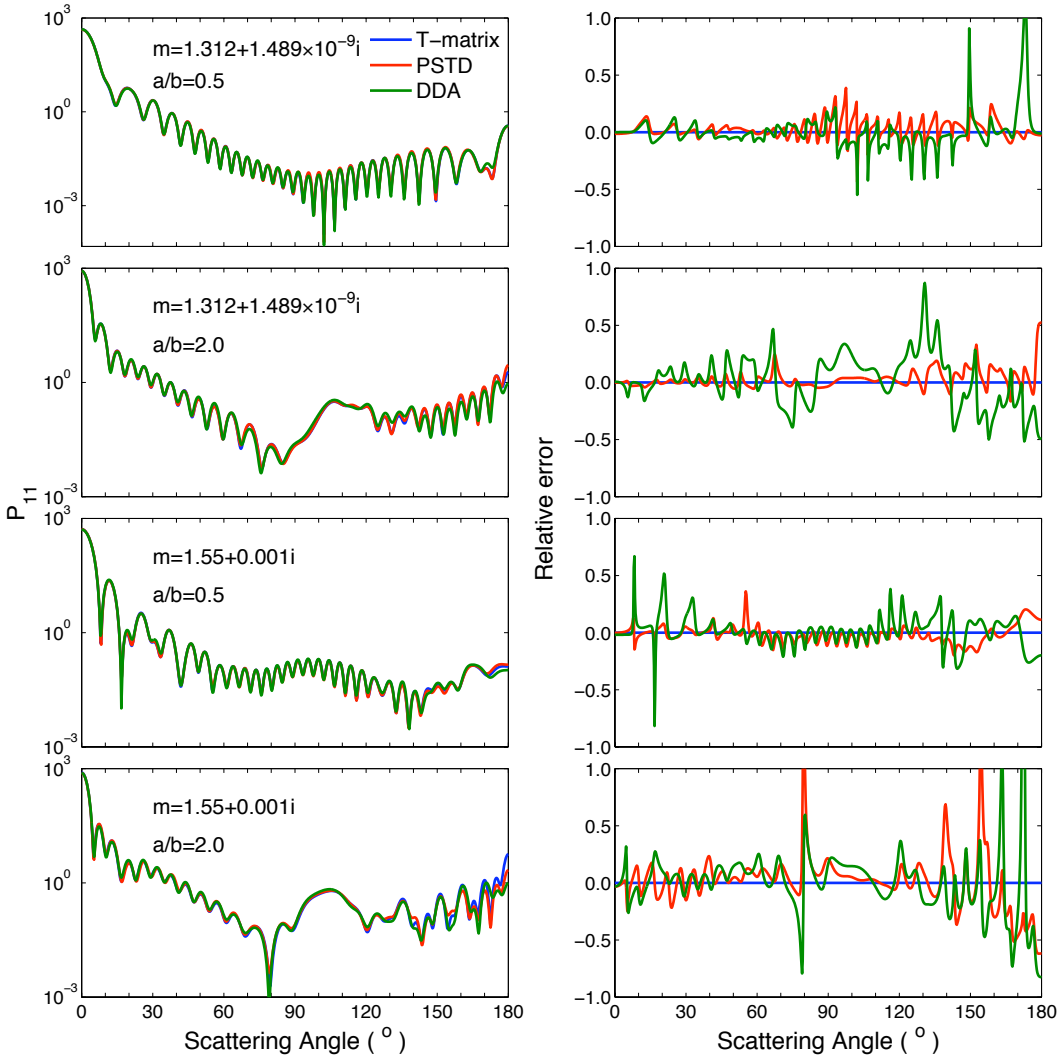

Figure 2.24: Same as Figure 2.22, but for spheroids with aspect ratios of 0.5 and 2.0, and refractive indices of $1.312 + 1.489 \times 10^{-9}i$ and $1.55 + 0.001i$.

The ratios of P_{12}/P_{11} for the spheroids with the same size parameters and the absolute errors are illustrated in Figure 2.25. The absolute errors of P_{12}/P_{11} are

no more than 0.2 at most scattering angles. For the spheroid with $a/b = 2.0$ and $m = 1.55 + 0.001i$ simulated by the DDA (lower panels), the errors became larger than 0.5 at the scattering angles that had relative errors of P_{11} larger than 50%. From Figures 2.24 and 2.25, we notice that, for spheroids, the PSTD results of P_{11} and P_{12}/P_{11} are slightly more accurate than those of the DDA.

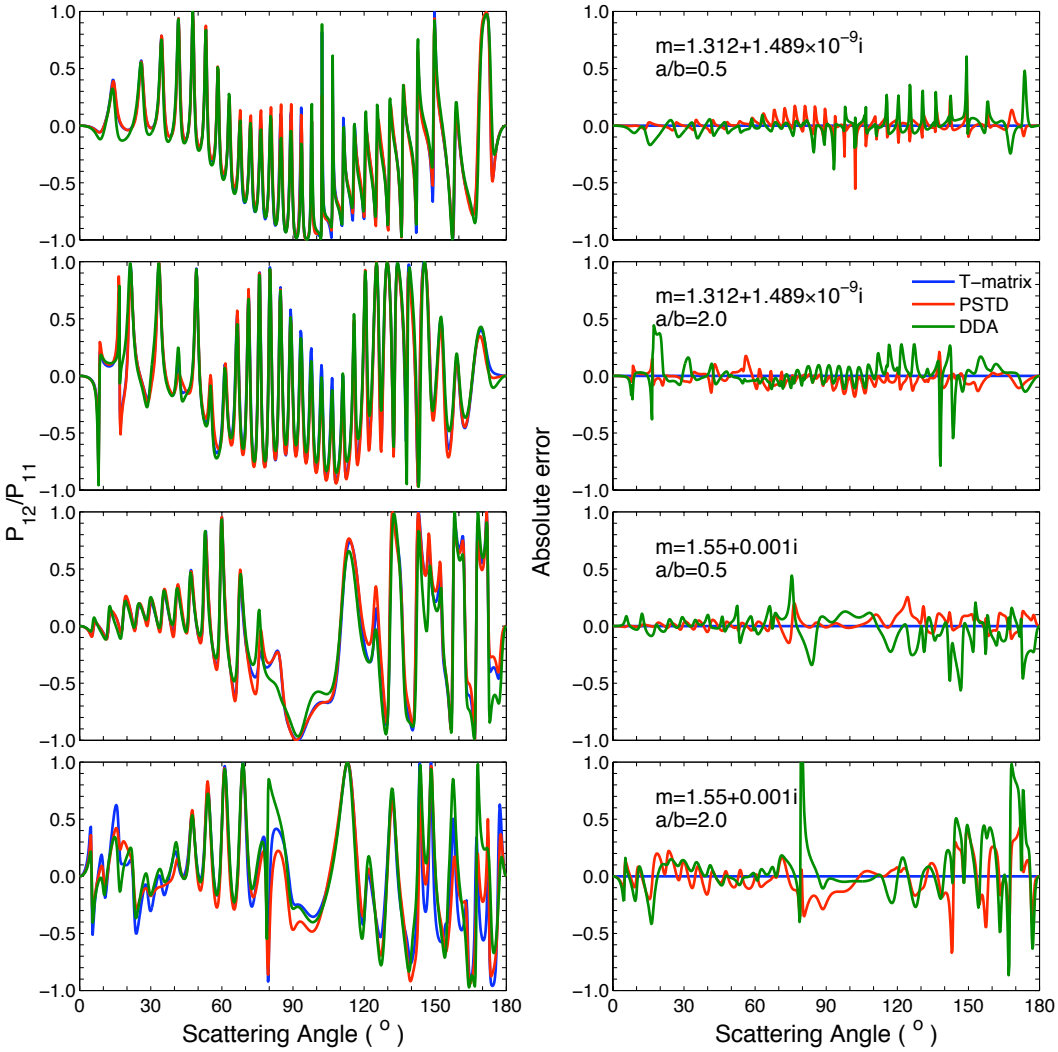

Figure 2.25: Same as Figure 2.24, but for P_{12}/P_{11} (left panels) and their absolute errors (right panels)

Before drawing our final conclusions, we reflect once more on the parameters of the DDA simulations. As noted before, the comparison is based on an older version of the ADDA and (almost) default settings, but we performed a limited set of simulations (for two spheres) with the current development version of ADDA (1.1b6 as of May 1, 2012), trying different DDA formulations and iterative solvers to maximize performance.

For the sphere with $x = 10$ and $m = 2.0$ the best result was obtained with the filtered coupled dipoles (FCD) formulation of the DDA [80, 81]. The version decreased the number of iterations by 25% and largely improved the accuracy such that a spatial resolution of 20 was sufficient for a prescribed accuracy threshold. The resulting computational time was 140 seconds: 14 times faster than the DDA with the default settings, but still 3 times slower than the PSTD. For the sphere with $x = 80$ and $m = 1.2$, the FCD formulation halves the number of iterations but has little effect on the accuracy. The best performance, however, was achieved by using a CSYM iterative solver [82], which resulted in an almost four times smaller number of iterations, and a computational time of 2.0×10^4 seconds, only two times larger than that of PSTD.

A systematic comparison between the PSTD and DDA for light scattering computations was made by using the parallelized implementations of the two methods on the same multi-processor hardware, although we have no reason to believe that the relative performance is significantly affected by the hardware used. For spheres, size parameters up to 100 and refractive indices up to 2.0 were used, and for spheroids, two aspect ratios and two realistic refractive indices of ice and dust were used with equivalent-volume size parameters up to 50. The same prescribed accuracy criteria were required for the extinction efficiency and the phase function, and the computational time was used as the key parameter to evaluate and compare the two methods.

The DDA was more economical for numerical simulations of spheres with small refractive indices and small size parameters; whereas, the PSTD was more economical for large x and m. The critical size parameter, above which the PSTD outperformed the DDA, decreased from 80 to 30 as the refractive index increased from 1.2 to 1.4. The PSTD was more CPU-efficient and applicable to a wider range of x when the refractive index was larger than 1.4. Similar conclusions were obtained for the spheroids. Furthermore, the overall accuracy of the asymmetry factor, backscatter, and linear polarization given by the PSTD and DDA were comparable.

The implementation of each of the two compared methods has been substantially enhanced through our recent effort. For instance, we showed that most recent formulations of the DDA can decrease the required computational time by an order of magnitude. However, this is expected only to shift the boundary between the methods in (x, m) plane but not to principally affect the conclusion of this comparison. Moreover, potential users are advised to test (and fine-tune) these and other light-scattering methods for their particular applications before performing large-scale simulations. Finally, we note that the comparison was performed only for real refractive indices or those with negligible imaginary part. Significant absorption is known to largely improve the convergence of the iterative solver in the DDA [83]. Therefore, comparison of the PSTD and DDA for absorbing, including metallic, refractive indices is an interesting topic for future research.

2.5 Summary

This section discussed the theoretical development and numerical performance of the PSTD algorithm to calculate the single-scattering properties of idealized particles in detail. The advantages of using the spectral method instead of the finite difference method for the spatial derivatives were shown in the discussion, and the

spectral filters to eliminate the Gibbs phenomenon in the spectral simulations were introduced. With the parallelized implementation, the applicability of the current PSTD has be significantly enhanced, and validations are carried out by comparing with results from various scattering models at scatterers of different sizes, shapes and refractive indices. The PSTD has shown capability to calculate the scattering properties of spheres with size parameters up to 200, and randomly oriented non-spherical particles with size parameters over 100. The performance of the PSTD on the scatterers with large refractive indices and inhomogeneous components is also tested. A systematical comparison between the PSTD and DDA has been carried out for spherical and spheroidal particles over wide ranges of size parameters and refractive indices, and the PSTD outperforms the DDA not only for particles with larger refractive indices (real part lager than 1.4), but also for ones with small refractive indices but large size parameters (e.g. size parameters larger than 80 for refractive index of 1.2).

Because of the lack of an efficient and accurate numerical model for light scattering properties of particles in the resonant range, our understanding on the single-scattering properties of the atmospheric particles is still limited, and various numerical approximations were involved for scattering simulations. The significant applicability provided by the current PSTD implementation shows great potentials on the atmospheric application. The following section of this dissertation will show some studies on accounting the effects of complexities of the realistic particles for the scattering properties, and, as we will see, the PSTD implementation provides to be a robust and powerful method for our approach.

3. COMPLEXITY OF THE ATMOSPHERIC PARTICLES *

Compared with the limitation on the scattering methods, our knowledge on the microphysical properties of the atmospheric particles poses even greater challenge on accurate modeling of their single-scattering properties, because the atmospheric particles are highly complex with irregularly nonspherical geometries, heterogeneous components, and small-scale surface roughness. All those complexities have been considered to some degree in calculating the single-scattering properties of the ice crystals or aerosol particles, whereas a lot of approximations were involved due to the lack of an accurate and efficient light scattering model and quantitative knowledge on the atmospheric particles.

In this section, the effects of three factors related to the realistic atmospheric particles on the single- and bulk-scattering properties will be investigated, and each of the following sub-sections discusses one of them, i.e. irregularity (Section 3.1), inhomogeneity (Section 3.2) and surface roughness (Section 3.3). A state-of-art combination of the PSTD and IGOM will be used to cover the entire particle size range from the Rayleigh to the geometric-optics regimes.

3.1 Irregularity

Mineral dust, one of the major components of atmospheric aerosols, is distributed over a large area of the globe, especially in desert and semi-arid regions, and considerable theoretical and experimental effort has been expended to quantify its radiative impact [84, 85, 86, 87, 88, 89]. Because of the significant differences in the single and

* Part of this chapter is reprinted with permission from "Modeling the scattering properties of mineral aerosols using concave and fractal polyhedral" by C. Liu, R. L. Panetta, P. Yang, A. Macke and A. J. Baran., Appl. Opt., 52, 640-652, and "The effects of surface roughness on the scattering properties of hexagonal columns with sizes from the Rayleigh to the geometric-optics regimes" by C. Liu, R. L. Panetta, and P. Yang, in press, J. Quant. Spectrosc. Radiat. Transfer.

bulk scattering properties between spherical and non-spherical particles, the irregular geometry of the mineral aerosols becomes an important issue in aerosol retrieval and climate modeling [84, 88, 89, 90]. (Here we adopt conventional terminology: a "bulk" property is one obtained by averaging over some specified ensemble, e.g. size distribution.) Scanning electron microscope (SEM) images show mineral aerosols to have very irregular and non-spherical morphologies [41], and the complexity of the morphologies greatly limits the theoretical understanding of aerosol scattering properties.

It is extremely difficult, and perhaps beyond our current mathematical understanding, to describe the exact geometries of naturally occurring dust particles. In view of these realities, a reasonable approach to the study of scattering in such a situation is to construct a simple model to represent the complex aerosols of interest, a model that embodies features that appear to be important differences from symmetrical particles, yet are simple enough that they can be handled with numerical scattering codes that are available. Comparison of numerical results with laboratory measurements may then be used to assess the degree to which the simple models can reproduce the scattering properties of aerosols actually observed. Among the various scattering properties, the full scattering phase matrix is widely accepted as a focus for studying dust scattering properties, and it will be the focus in this section. The laboratory results that will be used are taken from the Amsterdam Light Scattering Database (ALSD), which provides the phase matrices of mineral aerosols over broad ranges of sample sizes, kinds, and shapes [85, 41]. In that database, the measured scattering matrices show similar featureless patterns, even though the size distributions, shapes, and refractive indices of the aerosol samples are quite different. Comparing mineral aerosol samples of known components and size distribution, the particle shape emerges as one of the most important and uncertain factors in

determining the overall light scattering behavior of dust aerosols.

Laboratory measurements alone are not enough to establish a complete knowledge of the size, shape, and wavelength-dependent aerosol optical properties. However, the measurements serve as the best reference for numerical approximations and models. A number of simplified and quasi-realistic shapes have been used to model the optical properties of mineral aerosols, e.g., Gaussian random particles [91], spheroids [92, 93], triaxial ellipsoids [29], non-symmetric hexahedra [46], polyhedral prisms [93], agglomerate debris particles [94]. Each study attempted to represent the mineral aerosols and their optical properties more realistically and accurately, but used relatively regular convex geometries that was quite different from the actual particles. Interactions with incident radiation becomes substantially more intricate when concave surfaces are present, with rays being "trapped" near the particle surface and forced to undergo multiple reflections and refractions. Furthermore, most of those studies used a combination of multiple geometries and considered the scattering properties at single wavelength, or different geometry fractions are used to match the scattering properties from measurement at different wavelengths.

Considering the extremely irregular shapes and small-scale structure of the mineral aerosols, we attempt to define the particles as complicated and disordered concave polyhedra in order to obtain similar optical properties to those of the aerosols. Fractal geometries are widely applied to model the irregular and complicated structures in nature [95, 96]. As described below, it is based on a method using tetrahedron elements, with both the overall and small-scale structures of the particle being constructed iteratively by tetrahedra of different sizes and shapes.

In order to obtain some understanding on the light scattering characteristics of irregularly shaped particles, Macke and Tzschichholz [97] and Macke et al. [34] first simulated light scattering by two-dimensional and three-dimensional fractal particles.

Mishchenko et al. [4] and Kokhanovsky [98, 99] used fractal particles to model the scattering properties of irregular atmospheric particles. However, the previous work used the CGOM, focused only on large particles in the geometric-optics regime, and resulted in limited results and conclusions. Osborne et al. [88] used the method of ray tracing diffraction on facets (RTDF) [100, 101] to model the light scattering properties of fractal mineral dust aerosol, although the RTDF method does not include phase information or treatment of the inhomogeneity condition for highly absorbing mineral dust particles.

This section investigates the single-scattering properties of randomly oriented fractal particles with size ranges from the Rayleigh to geometric-optics regimes. Fractal particles will be used to reproduce the bulk-scattering properties of the mineral aerosols, and the results will be compared with laboratory measurements from the ALSD. The bulk-scattering properties of multiple mineral dust particles (feldspar, red clay, quartz and volcanic ash) at two wavelengths (0.6328 μm and 0.4416 μm) will be used for the comparison. A detailed discussion on the fractal particle model and two parameters to specify what we call "irregular fractal particles" is presented in the next sub-section. The single-scattering properties of the fractal particles will be discussed in Section 3.1.2, and their applicabilities to represent the scattering properties of mineral dust particles will be verified in Section 3.1.3.

3.1.1 Fractal particles

Fractal particles, also called Koch-fractal particles, were used to model atmospheric particles by Macke et al. [33], and their scattering properties were expected to give some insight into the typical scattering features of highly complicated particles. Two kinds of fractal particles were used: "deterministic" and "random." Each kind of fractal is constructed by an iterative method that is based on a single funda-

mental sequence $\{T_n\}$ of successively smaller regular tetrahedra that are constructed from an initial regular tetrahedron T_0. T_0 has four faces, each an equilateral triangle with sides of length s_o. In Figure 3.1 (a), T_0 is shown with vertices labeled $A_oB_oC_oD_o$ and altitude $O_oD_o = \sqrt{6}s_o/3$, as is easily verified by elementary trigonometry. The sequence of regular tetrahedra is constructed by successively halving the lengths of the sides of faces: if s_n is the length of a side of T_n, then $s_{n+1} = s_n/2$. The sequence $\{T_n\}$ is used in different ways, depending on whether the fractal particle being constructed is deterministic or random, to construct successive "generations" of fractal particles.

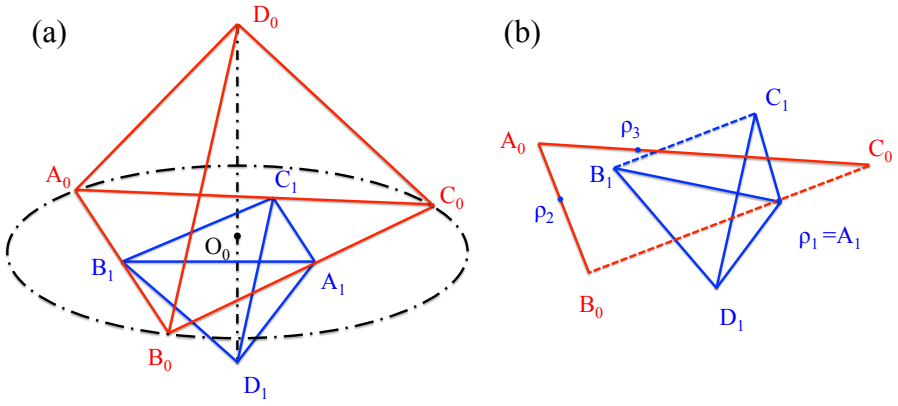

Figure 3.1: Constructions of (a) regular and (b) irregular fractal particles.

Figure 3.1(a) illustrates the geometry of the procedure used in constructing a first-generation regular (or deterministic) fractal particle. To each face of the starting (or "zeroth-generation") fractal $F_0 = T_0$, a copy of T_1 is attached, with the vertices of the T_1 copy placed at the midpoints of the sides of the given face of T_0: in Figure 3.1(a), the attachment shown is to the bottom face. The same procedure is used for each of the remaining three faces, and the result is a "first-generation deterministic

fractal" F_1. This first-generation fractal has faces that are all equilateral triangles, and to each of these faces a copy of T_2 can be attached in an analogous manner to produce a second-generation deterministic fractal F_2: this construction can be further iterated as often as desired. The nth generation fractal F_n has 4×6^n faces, each of which is an equilateral triangle with sides of length $s_n = s_0 \times 2^{-n}$. Figures 3.2 (a)-(d) show deterministic fractals of generations zero to three.

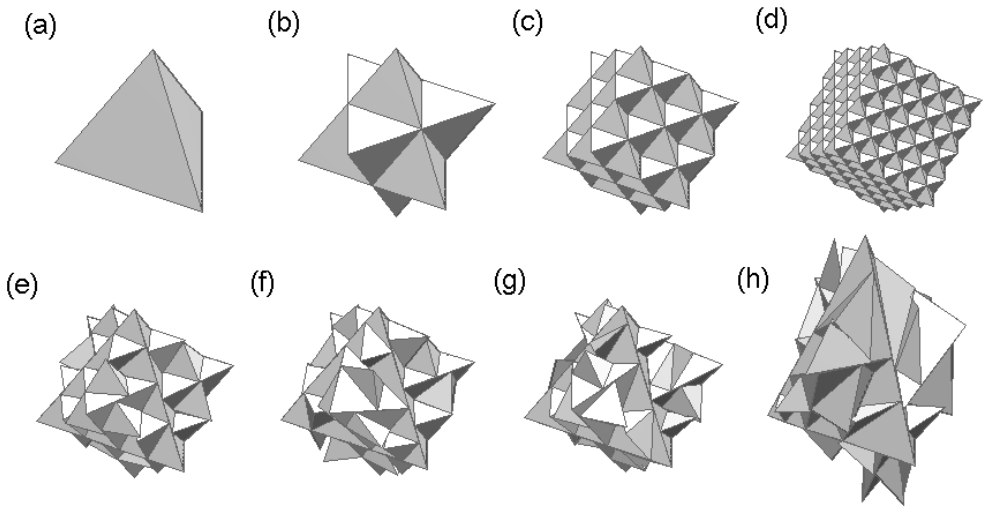

Figure 3.2: The regular fractal particles from the zero to the third generations ((a) - (d)), and the second generation irregular particles (the irregularity parameter of (e), (f), (g) and (h) are 0.1, 0.2, 0.3 and 0.3, and the aspect ratio of (h) is 1.7).

Two important features of this construction should be noted. First, while $F_0 = T_0$ is convex (any two points in T_0, including points on the surface, can be connected by

a straight line segment lying within T_0 or on its surface), all succeeding generations are concave: for n larger than 0 there exist points within F_n for which the connecting line segment lies all or in part outside F_n. The second point is that, in the particle construction, the height of the fractal particle never exceeds the sum of the altitudes of T_0 and T_1, i.e. D_0D_1 in the figure (i.e., $D_0D_1 = OD_0 + OD_1 = \frac{\sqrt{6}}{3}s_0 + \frac{\sqrt{6}}{6}s_0 = \frac{\sqrt{6}}{2}s_0$).

The aspect ratio of the fractal particle, intuitively the "Height" divided by the "Width," may be defined as follows. Consider the orientation of T_0 in Figure 3.1(a) as determining the vertical and horizontal directions. For successive generations, the height H will be the maximum length of a vertical line segment that lies entirely within the particle, and the width W will denote the diameter of a circle that circumscribes the area of the particle's projection on a horizontal plane. The aspect ratio is then defined to be

$$Aspect\,Ratio = \frac{H}{W} = \frac{Height}{Width}$$

Simple geometrical arguments establish the fact that the aspect ratio of a first or higher generation regular tetrahedron is

$$Aspect\,Ratio(F_1) = \frac{3\sqrt{2}}{4} \approx 1.06$$

The construction of regular fractal particles is deterministic, and results in concave particles whose surfaces may be complicated but have symmetries inherent in the use of regular tetrahedra. Naturally occurring mineral particles are much more complicated and irregular. Following Macke et al. [33], we eliminate the symmetries in fractal particle construction by at each successive generation using irregular tetrahedra constructed by making random displacements of attachment points on a face,

and random determinations of the position of the apex of the attached tetrahedron. The process involves an irregularity parameter β, a real number in the interval [0, 0.5), where to attach a successor generation tetrahedron, and how to determine the position of its apex. In this generation process, T_0 is used as a starting point, but the successor T_n are only used as guides, in a manner that is now described (illustrated in Figure 3.1 (b)).

As in the case of the regular fractal the starting point is the regular tetrahedron T_0. In the case of a regular fractal, the first generation particle is constructed by attaching a copy of the tetrahedron T_1 to each face: the attachment points were the midpoints of the edges of a face. Now, instead, attachment points (ρ_1, ρ_2, ρ_3) are chosen (independently) at random to be in intervals of length $2\beta s_0$ that are centered on each of these midpoints. The ρ_i define the base of the irregular tetrahedron to be attached to the face. What remains is determination of the apex ρ_4 of this tetrahedron. For the determination we make temporary use of an auxiliary copy T_1', with vertices (A_1, B_1, C_1, D_1) of the regular tetrahedron T_1. The face of T_1' with vertices (A_1, B_1, C_1) is brought in contact with the bottom face of T_0, as in the beginning of the regular construction, so that the bottom face of T_0 and the face (A_1 , B_1 , C_1) of T_1' are in the same plane. One of the ρ_i is chosen at random (say ρ_1 on edge B_0C_0) to be an attachment point for a vertex (say A_1) of T_1' (see Figure 3.1(b)). We then rotate T_1', keeping it in contact with the bottom face of T_0, as needed until the edge B_1C_1 of T_1' opposite this vertex becomes parallel to the edge B_1C_1 of T_0 on which the point ρ_1 lies (the two edges referred to are indicated with dashed lines in Figure 3.1(b)). During this rotation about the point ρ_1 the vertex D_1 changes its position. Given this position at the completion of the rotation, the apex ρ_4 being sought is a point chosen at random in a cube of side $\beta s_1/4$ centered at the position and oriented parallel to the faces of T_0 and T_1' that are in contact. The tetrahedron T_1'

is then discarded, and the next generation (irregular) tetrahedron that is being added to the fractal particle under construction is constructed to have vertices (ρ_1, ρ_2, ρ_3, ρ_4). This process is repeated on the other three faces to produce the first generation irregular fractal particle. It should be clear how the construction can proceed to higher generations, with copies of T_n used as auxiliary guides at generation n.

Previous studies using fractal particles have chosen aspect ratios near unity. We would like to consider particles with aspect ratios departing significantly from 1. However, as mentioned above the aspect ratio of the regular fractal particle is approximately 1.06. Moreover, the aspect ratio of the irregular fractal particles constructed in the manner just described does not depart significantly from this value, essentially due to the constraint on the aspect ratio of the irregular fractal particle construction imposed by the fact that T_0 is a regular tetrahedron. To weaken this constraint, we introduce another degree of freedom in the construction of irregular fractal particles by including a compression/stretching transformation governed by a parameter that we call the "aspect ratio for a fractal particle," or AR for short. In terms of this parameter, we stretch or compress the particle in the vertical direction by changing the vertical distance z of each point in the particle from the base plane of T_0 according to the linear mapping:

$$z' = \frac{AR}{1.06} z.$$

Depending on whether AR is larger or smaller than 1.06 this is a vertical stretching (giving a "prolate" particle), or compression (giving an "oblate" particle).

In Figure 3.2, panels (e) to (h) show examples of second generation irregular particles: in panels (e)-(g) the choices of β are 0.1, 0.2, 0.3 and $AR = 1.06$, while in panel (h) the result is shown of applying the stretching transformation to the fractal

in Figure 3.2 (g), with $AR = 1.7$.

3.1.2 Single-scattering properties of fractal particles

With the fractal geometry constructed, we will consider the scattering properties of the fractal using both the IGOM and PSTD. The single scattering properties shown in this section include the following three parts. First, the IGOM is used to simulate the scattering properties of the large particles, which may much larger than the mineral dust particles. The second part shows the PSTD results for particles with relatively small particles sizes, and the combination of the PSTD and IGOM results are given at the end of this section. The size of fractal particle is specified by the length of the initial tetrahedron side, or by the size parameter $x = 2\pi r/\lambda$, where r is the radius of a sphere with the same projected area as that of the fractal particle (averaged over random orientations). In what follows we will show some results with fractals of different generations, but our main focus will be on second-generation fractal particles, each of which has 144 triangular surfaces.

Figure 3.3 shows how the phase matrix elements, as calculated using the IGOM, change with particle generation for the first 5 generations in a regular (deterministic) construction. The length of the initial tetrahedron side is fixed at 100 μm. The incident wavelength and refractive index are 0.6328 μm and $a.5 + 0.001i$ (, which are used in this section). The figure shows that the phase matrix elements of the zero generation fractal particle, a regular tetrahedron, differ significantly from those of higher generations, especially for backward scattering. The phase functions of all the generations greater than zero have a peak around the scattering angle of 50^o from the initial tetrahedron surfaces. A second peak that is not present for the zeroth generation particle occurs around 160^o, caused by the surfaces of the first generation tetrahedra. With an increase in the fractal generation, the peak at around

50^o becomes weaker, whereas the phase functions with scattering angles larger than 60^o become higher, as do the 160^o peaks. The fractal particle backscatter increases significantly with the growth of the fractal generation. However, for the ratios of the non-zero elements to the phase function, the differences between the zero and first generations are significant, while the higher generations (second to fourth) show similar ratios to those of the first generation.

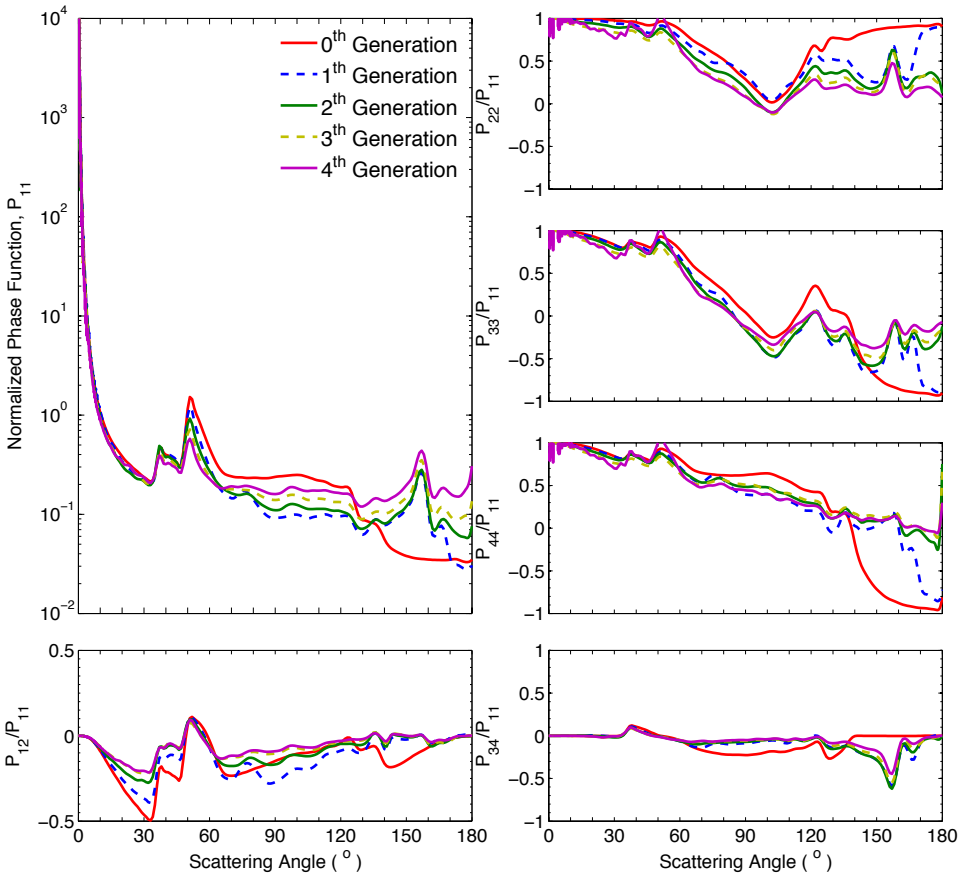

Figure 3.3: Comparison of the non-zero phase matrix elements of the zero to fourth generation regular fractal particles given by the IGOM. The length of the initial tetrahedron's side is 100 μm.

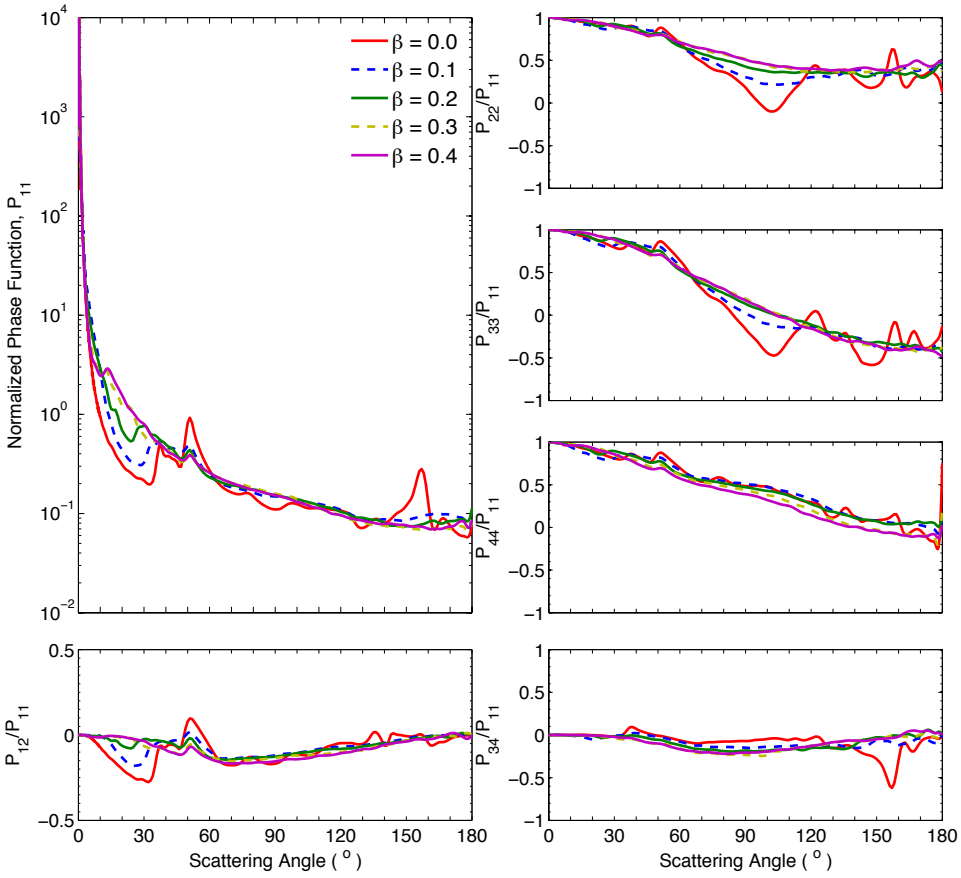

Figure 3.4: Comparison of the non-zero phase matrix elements of the second generation regular and irregular fractal particles having different values of the irregularity parameter β. Computations use the IGOM and the length of the initial tetrahedron's side is 100 μm.

Figure 3.4 compares the phase matrix elements of the second generation regular and irregular fractal particles, with the length of the initial tetrahedron side still taken to be 100 μm. (A fractal particle with $\beta = 0$ indicates a regular particle, and values with $\beta > 0$ are "irregular" particles.) The initial aspect ratio 1.06 is kept for all fractal particles. With an increase of β, random displacements for the vertices of the fractal particles can become greater and the angles between the triangular

surfaces show more variation. The effects of this are that the scattering peaks at 50^o and 160^o are smoothed, and the ratios of the non-zero elements to the phase functions become considerably more even. This is because the scattering peaks are due to special surface symmetries and relations between face intersection angles, and these symmetries and angle relations are increasingly disrupted as increases of β bring increasing displacement of vertices.

For each value of β used in Figure 3.4 a particular sequence of random-number calls as indicated in the previous paragraph was made, the result being a single "realization" of the fractal construction. It may be expected that different realizations may produce particles with different phase matrix elements. Figure 3.5 shows results from five different realizations of construction of second generation particles using $\beta = 0.3$: while differences among realizations all having the same shape parameters are noticeable, the differences are much less than the differences seen in Figure 3.4 when results with different values of β are compared. This indicates that, for fractal particles with specified shape parameters, the individual realizations result in differences in geometrical features that have relatively little influence on the scattering properties. The implication is that the scattering properties of a single particle realization is enough to represent that of fractals with the same shape parameters, a finding of considerable importance when computations of individual realizations become costly due to large particle size.

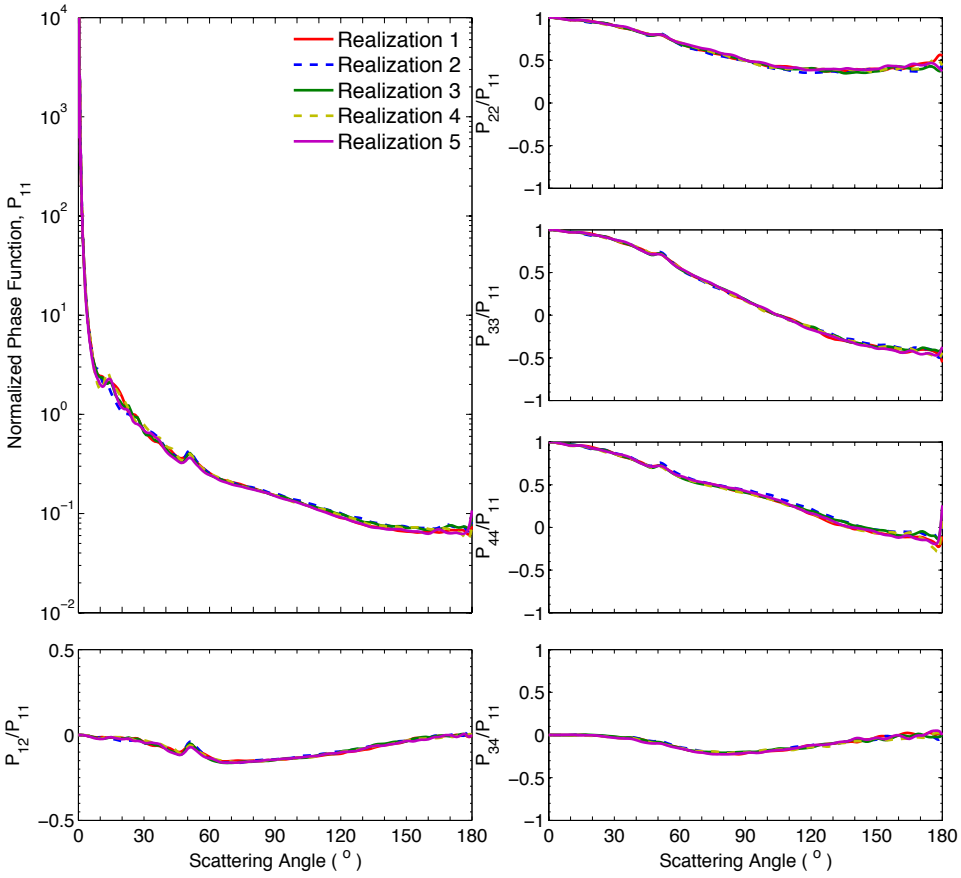

Figure 3.5: Comparison of results for the non-zero phase matrix elements of the second generation irregular fractal particles, with different realizations of fractal particles all having $\beta = 0.3$ and $AR = 1.06$. Computations use the IGOM and the length of the initial tetrahedron's side is 100 μm.

Figure 3.6 illustrates the phase matrix elements of second generation fractal particles with different aspect ratios but the same size as in the calculations shown in Figures 3.4 and 3.5. Two oblate fractals with aspect ratios of 1/3 and 1/2, and two prolate fractals with aspect ratios of 2 and 3, as well as the regular one ($AR = 1.06$), are used for the simulations. Regular fractals with $\beta = 0$ are used; without random displacements of the vertices, the fractal surfaces can retain some of the regularity

in facial intersection angles that can give the scattering peaks. The most significant differences for the regular fractals with different aspect ratios are the scattering angles at which the various peaks occur. This is presumably due to differences in the angles between the fractal faces. As the AR departs from 1.06, either increasing or decreasing, the peak at scattering angle near 50^o moves to the forward direction. There also appears to be an enhancement of backscattering at about 170^o as AR decreases from 3 to 1/3, but the enhancement is not entirely systematic.

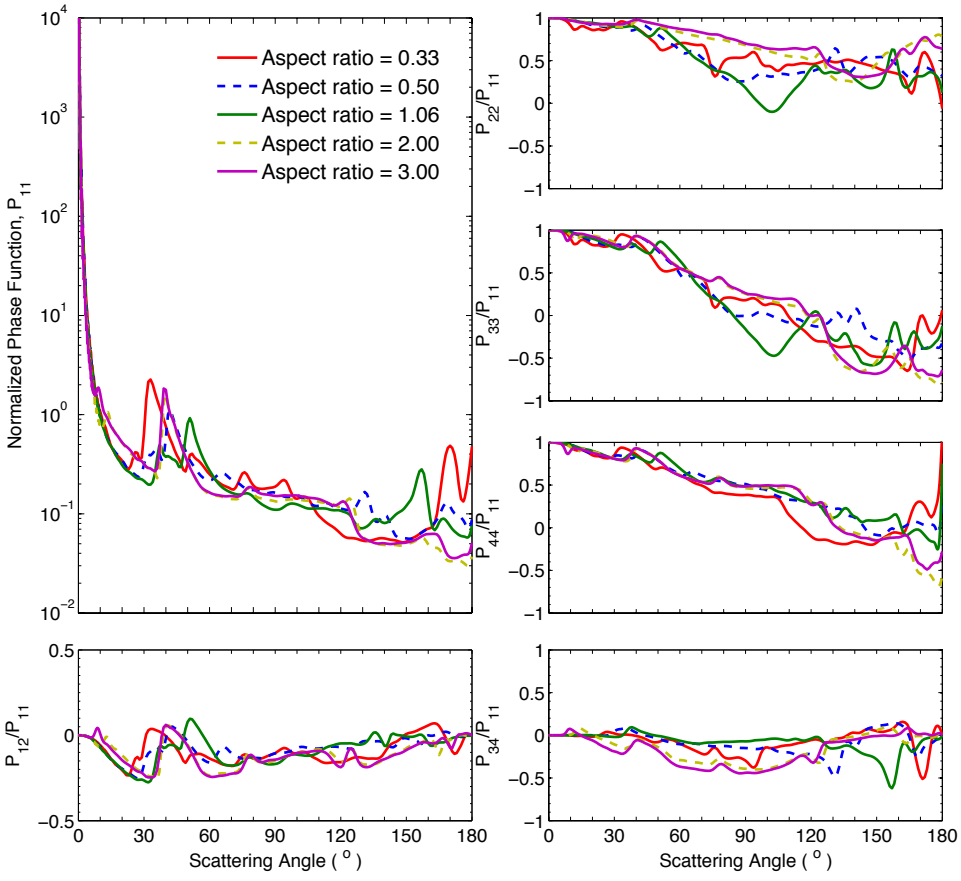

Figure 3.6: Comparison of the non-zero phase matrix elements of second generation regular particles with different aspect ratios. Computations use the IGOM and the length of the initial tetrahedron's side is 100 μm.

The previous results were calculated by the IGOM for particles much larger than the wavelength. Figures 3.7 and 3.8 show the phase matrix elements given by the PSTD for relatives small particles, and the equivalent-projected-area size parameter of the fractal particles is 30. Figure 3.7 illustrates the effects of the irregularity parameter with fixed aspect ratio of 1.0, and Figure 3.8 shows the influences of the aspect ratios on the irregular fractals with second generation and irregularity parameter 0.3. Different from the IGOM results, the irregularity parameter shows little influence on the phase matrices in Figure 3.7, especially the phase functions, because, for the small particles, the detailed fractal structures are comparable or even smaller than the incident wavelength. The small differences on the particle geometries are all smoothed out by average over particle orientations. However, the aspect ratios of the fractal particles are still important on determining scattering properties of irregular fractal particles as shown by Figure 3.8. The black cures in the figure indicates the results of a fractal particle with an aspect ratio of 1, and, as the aspect ratio departs 1, P_{11} at scattering angles lager then 50^o decrease. The other non-zero phase matrix elements also show some sensitivities on the aspect ratios, whereas similar trends are obtained for all aspect ratios. Furthermore, the prolate (AR larger than 1) or oblate (AR smaller than 1) particle has the same effects on the phase matrix elements, and this is clearly shown by the close scattering properties for the fractal particles with aspect ratios of 0.6 and 1.7.

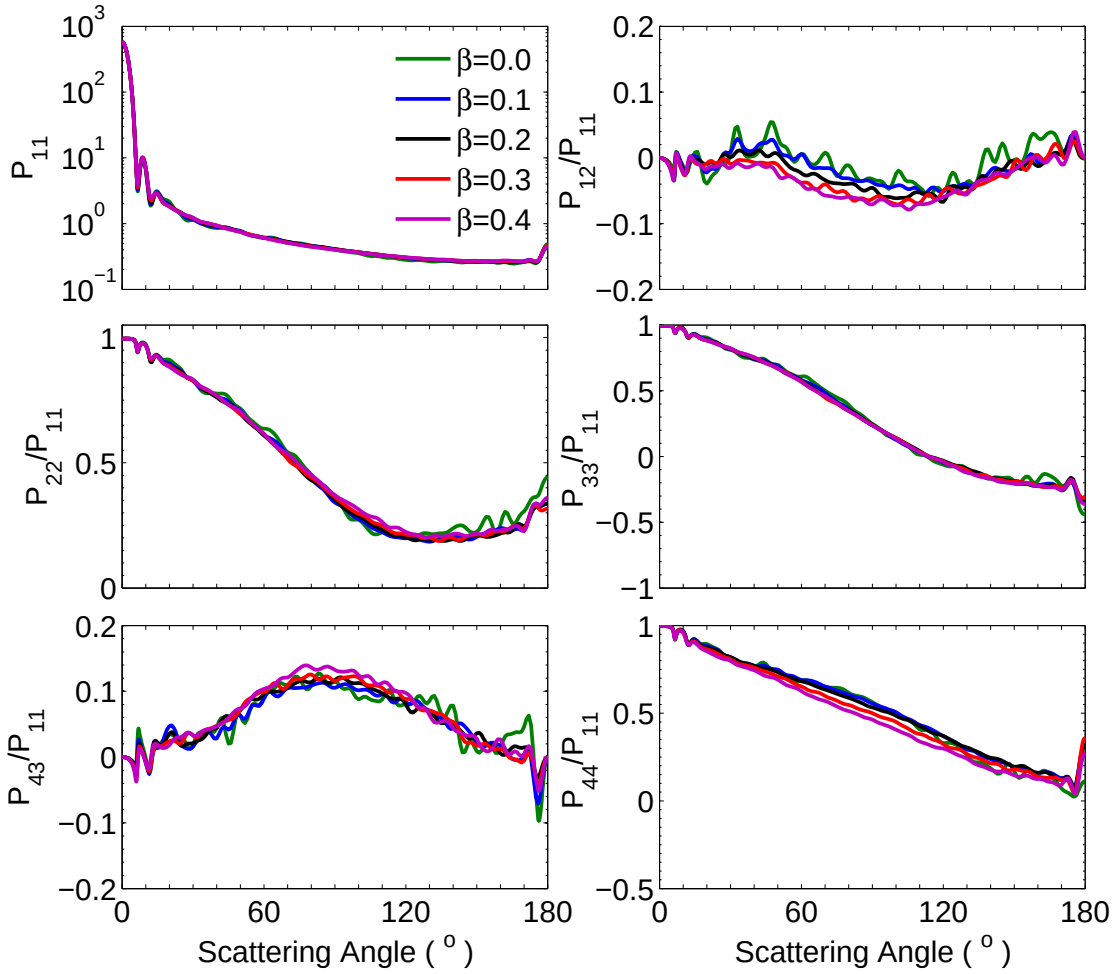

Figure 3.7: Comparison of the non-zero phase matrix elements of second generation fractal particles with different irregular ratios given by the PSTD. The aspect ratio of the particle is set to be 1, and the equivalent-projected-area size parameter is 30.

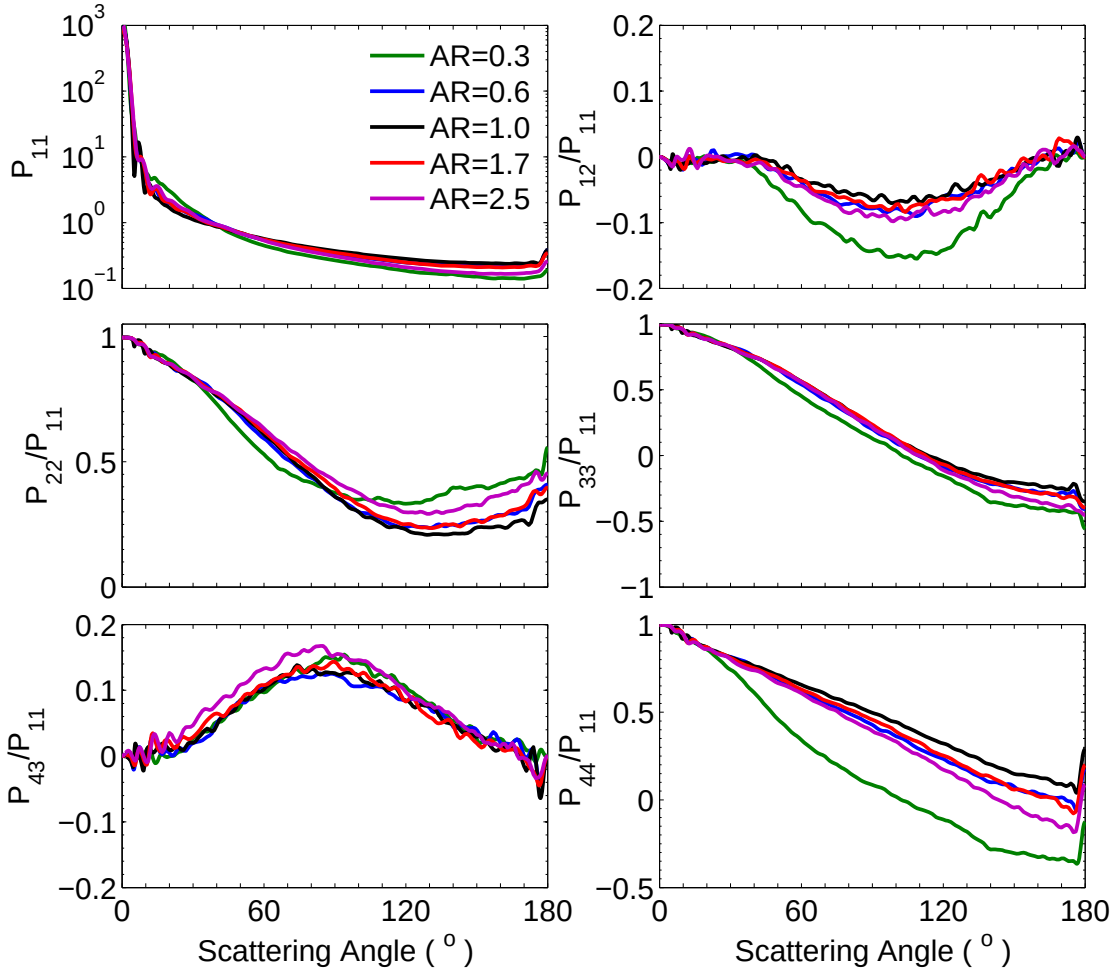

Figure 3.8: Same as Figure 3.7 but for fractal particles with different aspect ratios. The irregular ratio of the particles is set to be 0.3.

In Figure 3.9, a combination of the PSTD and IGOM was used to calculate the integral scattering properties of particles within the entire size range from the Rayleigh to geometric-optics regimes. Both IGOM results with and without the edge effects included are shown. Figure 3.9 illustrates the Q_{ext}, Q_{abs}, SSA, and g of second generation irregular fractal particles, with size parameters from approximately 0.4 to over 4000. The values of β and aspect ratio of the fractal particle are 0.3 and 1.7, respectively, and the size parameter is defined in terms of the equivalent-projected-

area sphere. To cover the whole size range, the PSTD is employed for particles with size parameters less than 25, and the scattering properties of the larger particles are calculated by the IGOM. An exact solution for the edge effect in the case of complicated geometries is not available, so a semi-empirical method is used to bridge the gap between the results given by the numerically exact methods and those of the IGOM [38]. For size parameter x, the edge effect contributions are:

$$Q_{ext,edge} = \frac{f_{ext}}{x^{2/3}},$$

$$Q_{abs,edge} = \frac{f_{abs}}{x^{2/3}}.$$

The factors f_{ext} and f_{abs} are the differences between the values of the extinction and absorption efficiencies, calculated by the twomethods, according to the phase matrices they determine. The total extinction and absorption efficiencies are then the sum of the IGOM results and the contributions from the edge effects, $Q_{ext,edge}$ and $Q_{abs,edge}$. Comparing the IGOM results with and without the edge effect, we see that small inconsistencies between the efficiencies given by the PSTD and IGOM results are removed by considering the edge effects. As expected, the extinction efficiency converges to 2 for the large particles. The absorption efficiency is close to zero for small particles, because of the relatively small imaginary part of the refractive index used, and increases to over 0.9 for large size parameters. The asymmetry factors of the fractal particles oscillate slightly for size parameters from 5 to 30, but the oscillations decrease with increasing size parameter x, and results merge smoothly with those of IGOM calculations at about $x = 25$. A combination of the PSTD and IGOM can evidently provide accurate single-scattering properties of fractal particles over the entire range of size parameters. Similar results were obtained for triaxial

ellipsoids and nonsymmetric hexahedra by Bi et al. [29, 46].

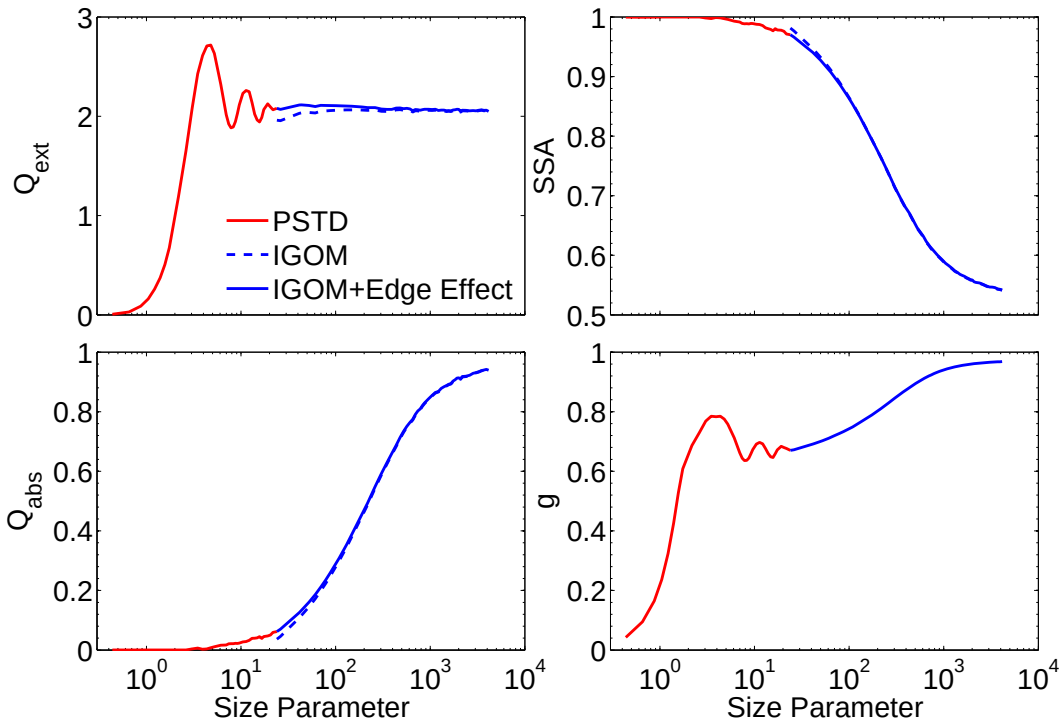

Figure 3.9: The integral scattering properties of fractal particles given by the PSTD and IGOM. The irregularity parameter and aspect ratio of the fractal particles are 0.3 and 1.7.

To validate the IGOM results, a calculation was done using both IGOM and PSTD. Figure 3.10 illustrates the phase matrix elements of the irregular second generation fractal particle calculated by each of the two methods. The same fractal realization as that used for Figure 3.9 was chosen, and the size parameter based on the equivalent-projected-area sphere is 25, which appears to be the critical size parameter for the two methods, and above which the PSTD and IGOM results agree quite well. Here, for $x = 25$, the phase functions given by the PSTD and IGOM show excellent agreement, except for the backward scattering around 180^o. Differences for

the other phase matrix elements are noticeable, but the same patterns are obtained. The agreement indicates the safety of applying the IGOM for fractal particles with size parameters larger than 25, even though the fractal particles have numerous small-scale structures.

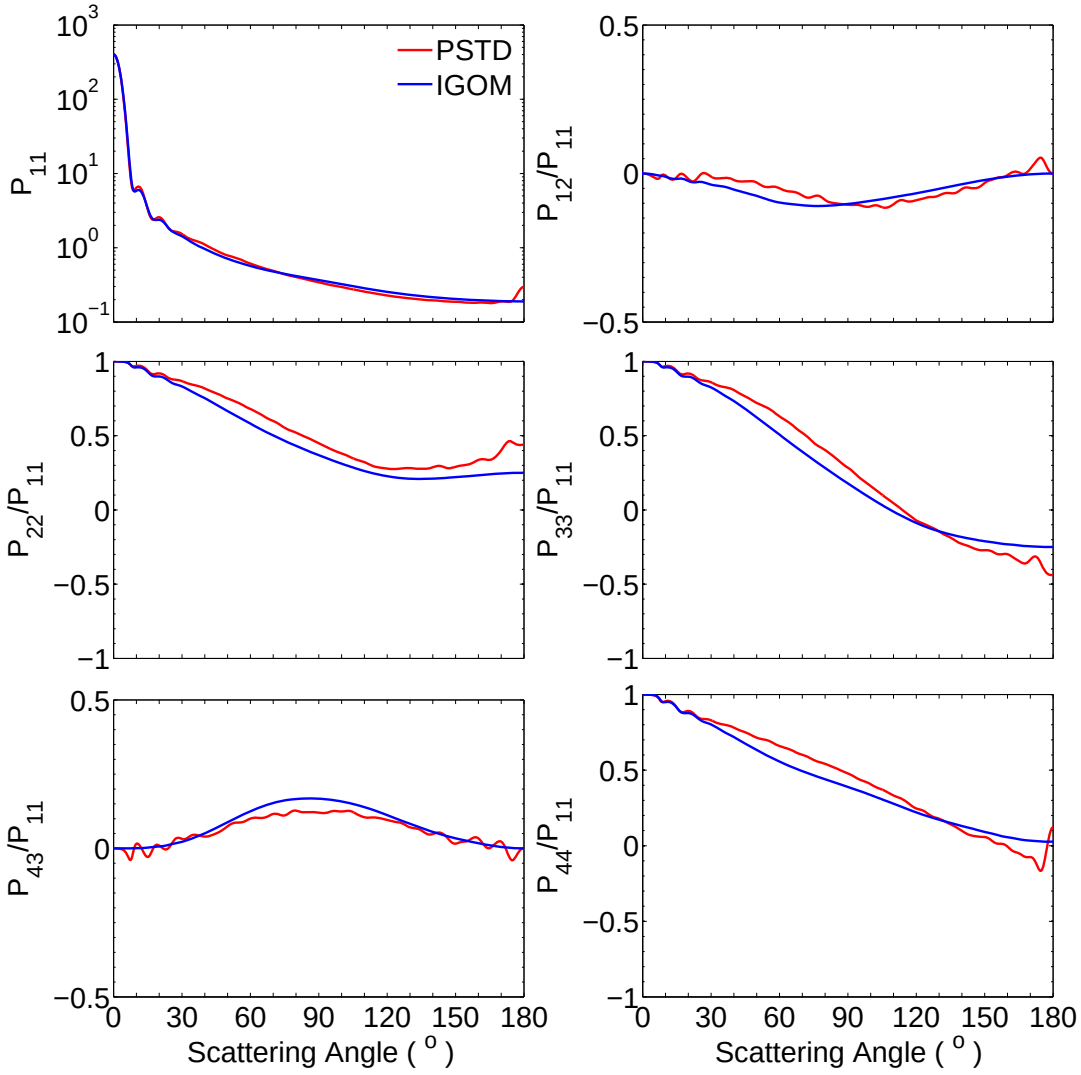

Figure 3.10: Comparison of the non-zero phase matrix elements of irregular second generation fractal particles given by the PSTD and IGOM. The same particle realization as that of Figure 3.9 is used, and the equivalent-projected-area size parameter of the particle is 25.

3.1.3 Comparison with the measurements

The ALSD [41, 85] provided measured bulk phase matrices of various mineral dust particles, and this section compares the calculated scattering properties with those measurements to show the applicability of the fractal particles. Based on the results shown in the previous section, we use the second-generation irregular fractal particles, and, to match the scattering properties of different mineral dust samples at two different wavelengths, fractal particles with different aspect ratios are used. The refractive index of $1.55 + 0.0001i$ and irregularity parameter $\beta = 0.3$ are used for the fractal particles. Figure 3.11 shows the integral scattering properties Q_{ext}, SSA and g as functions of particle size parameter, and the PSTD and IGOM are used for the simulations. The size parameter is defined based on the equivalent-projected-area sphere. Four fractal geometries with aspect ratios of 0.6, 1.0, 1.7 and 2.5 are used for the simulation, and the results are similar to those in Figure 3.9. It is show that Q_{ext} of the four fractal geometries all converge to 2 as the size increases, whereas shows different oscillations and peaks. The SSA and g of the fractal particles with aspect ratio of 1 show smaller values than those with aspect ratios larger or smaller than 1. It should be noticed that, similar to the phase matrix elements of single-size fractal particle in Figure 3.8, the integral scattering properties of fractal geometries with the aspect ratios of 0.6 and 1.7 are also coincident. Thus, this study uses the scattering properties of only three fractal geometries with aspect ratios of 1.0, 1.7 and 2.5 to match the laboratory measurements.

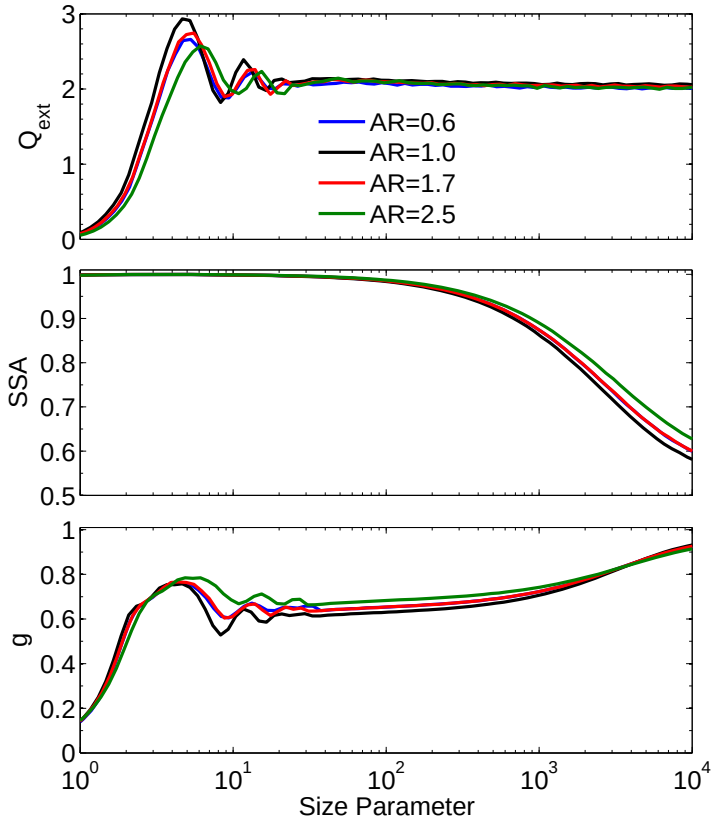

Figure 3.11: The integral scattering properties of randomly oriented second generation fractal particles with four different aspect ratios given by the PSTD and IGOM. The irregularity parameter of the fractal particles are 0.3.

The phase matrix elements from four kinds of mineral dusts at two wavelengths (0.4416 μm and 0.6328 μm) are modeled, and we change the habit fractions of the three fractal particles to get the best agreement of the phase functions at the two wavelengths. Table 3.1 lists the size parameters for the mineral dusts and habit fractions "F" of fractal particles. The feldspar, red clay, quartz and volcanic ash (Pinatubo) have effective radii from 1.0 to 3.0 μm, and variances up to 12.3, and the details of those measurement can be found from [41]. We use no more than two particle geometries for each sample. Similar comparisons have been obtained using

model shapes that are simpler than the fractal particle, e.g. spheroids [92, 93], triaxial ellipsoids [29], non-symmetric hexahedra [46], polyhedral prims [93], agglomerate debris [94]. It is important to note that in these studies a combination of multiple geometries was needed to match the experimental data (more than two), or different habit fractions were used for the phase matrix elements at two different wavelengths. Dubovik et al. [102] indicated that the most widely used spheroid model cannot reproduce the spectral-dependence of the feldspar particles. Zubko et. al. [94] used the agglomerate debris of same habits to achieve acceptable agreement with the measurement at two wavelengths, whereas only the feldspar particles that have a relatively small effective radius are used for the comparison. As we will show later, the scattering properties based on the fractal geometries cannot only match the phase matrix elements of all those four mineral dusts much better but also show good performance at both wavelengths with the same habit fraction.

Table 3.1: The size parameters of the mineral dusts and habit fractions of fractal particles with different aspect ratios to reproduce the phase matrix elements of the mineral dust.

Mineral Dust	r_{eff} (μm)	v_{eff}	F(AR=1.0)	F(AR=1.7)	F(AR=2.5)
Feldspar	1.0	1.0	0.0	0.3	0.7
Red clay	1.5	1.6	0.0	1.0	0.0
Quartz	2.3	2.3	0.3	0.7	0.0
Volcanic ash (Pinatubo)	3.0	12.3	0.6	0.4	0.0

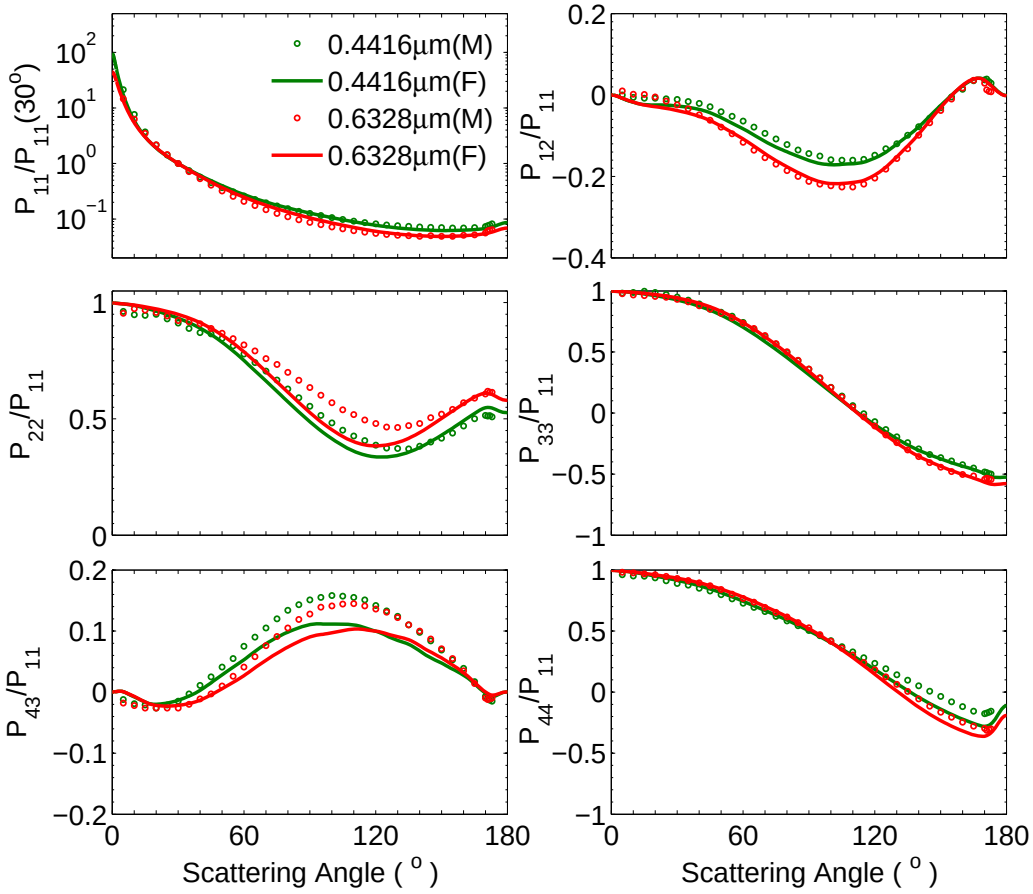

Figure 3.12: Comparison between results of the bulk phase matrix elements of numerically simulated fractal particles and the laboratory measurements for feldspar particles at the 0.4416 μm and 0.6328 μm wavelengths. The particles have an effective radius of $r_{eff} = 1.0$ μm and effective variance of $v_{eff} = 1.0$.

Figure 3.12 shows a comparison between the bulk phase matrix elements of numerical simulations based on the fractal particles and laboratory measurements for sampled feldspar. The results at wavelength 0.4416 μm are indicated by blue, and the red are for 0.6328 μm. The measurements are shown by the circles (as "M" in the figure), and the curves are those from the fractal models (as "F"). It should be noticed that not only the phase functions, but also P_{12}/P_{11} and P_{33}/P_{11} given by the fractal particle fit almost exactly with the measurements at both wavelengths,

and only slight differences at the scattering angles from 120^o to 150^o are shown for P_{44}/P_{11}. However, the agreements for P_{22}/P_{11} and P_{43}/P_{11} are not as well as the others, and the differences reach as larger as 0.2 and 0.05 at scattering angles from 50^o to 150^o, respectively.

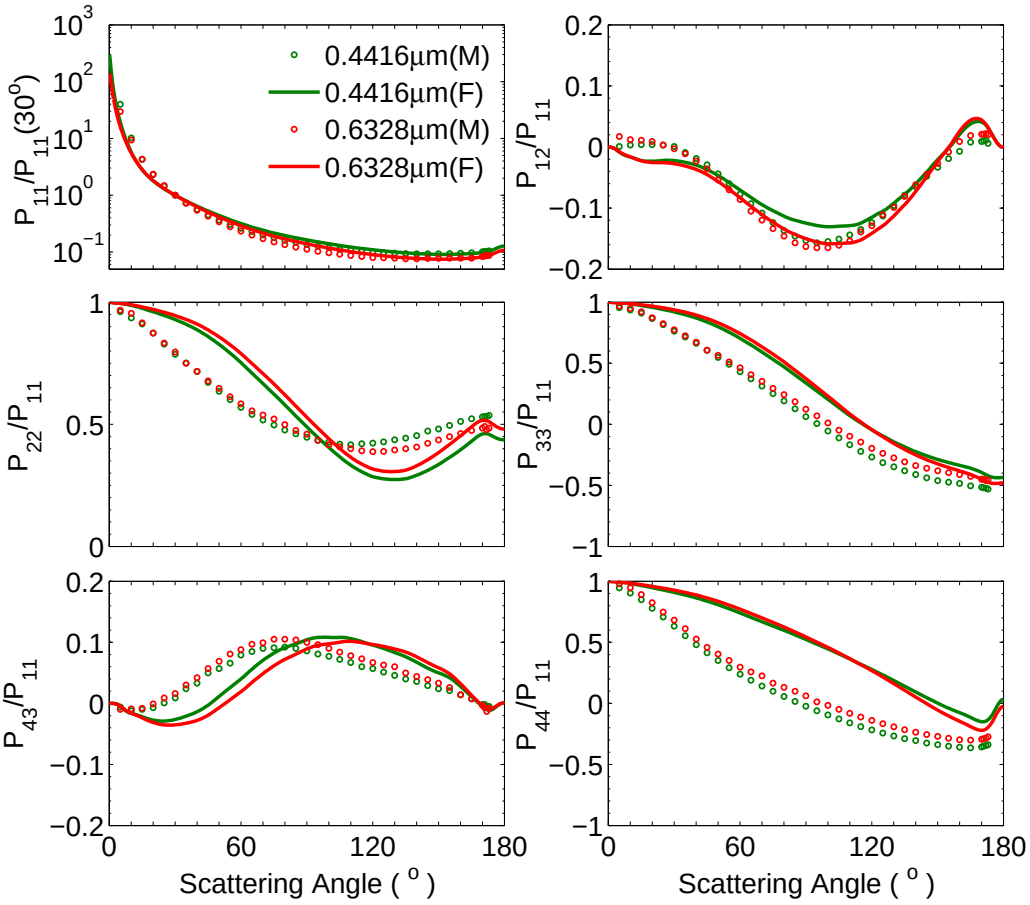

Figure 3.13: Same as Figure 3.12 but for red clay ($r_{eff} = 1.5\ \mu m$ and $v_{eff} = 1.6$).

Figures 3.13, 3.14 and 3.15 are the same as Figure 3.12, but for different dust particles: red clay, quartz, and volcanic ash (Pinatubo), respectively. The worst agreements are for the red clay with only P_{11} and P_{12}/P_{11} achieve good agreement,

and the deviations for other four elements are quite significant. Similar deviations for the red clay comparison were also obtained for spheroids models [92]. For quartz, only the fractal particle with an aspect ratio of 1.7 is used, and all elements show close agreement with the measurements (expect in the case of P_{43}/P_{11}). The computed results (a combination of fractal particles with aspect ratios of 1.0 and 1.7) for the volcanic ash are similar to those for the quartz with significant disagreement only for the P_{43}/P_{11} elements.

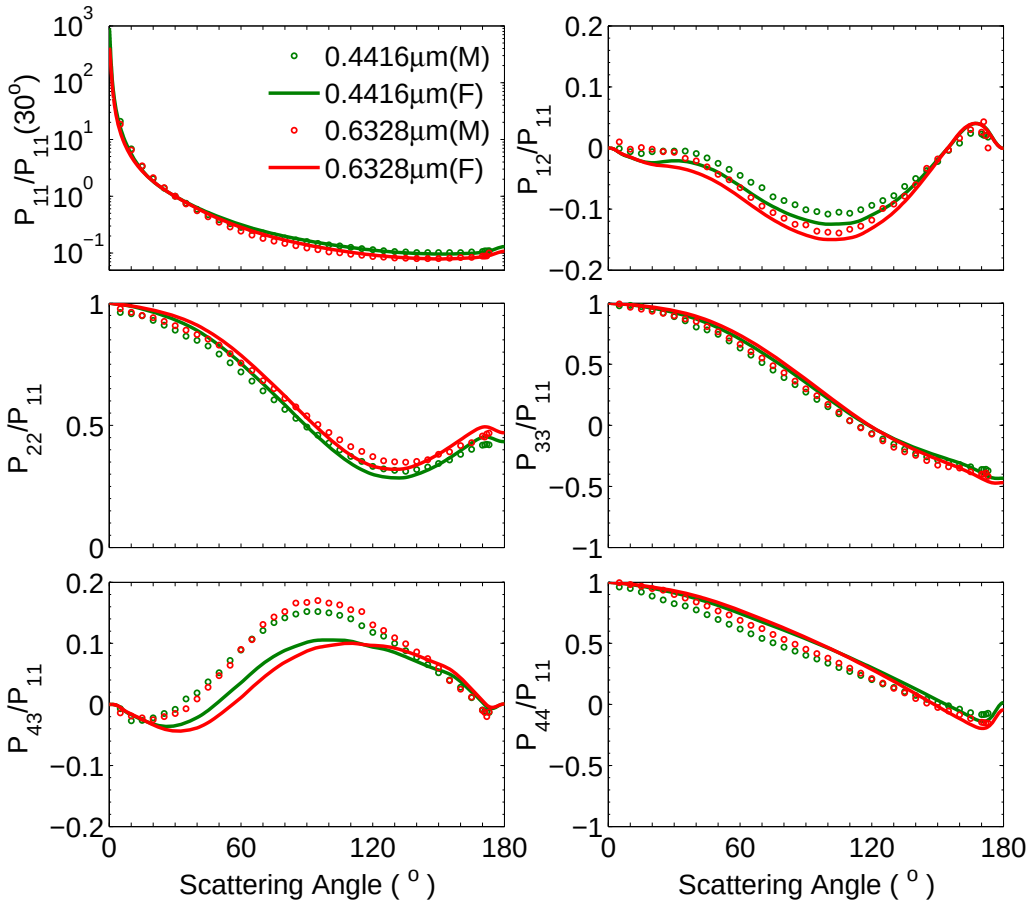

Figure 3.14: Same as Figure 3.12 but for quartz ($r_{eff} = 2.3\ \mu m$ and $v_{eff} = 2.3$).

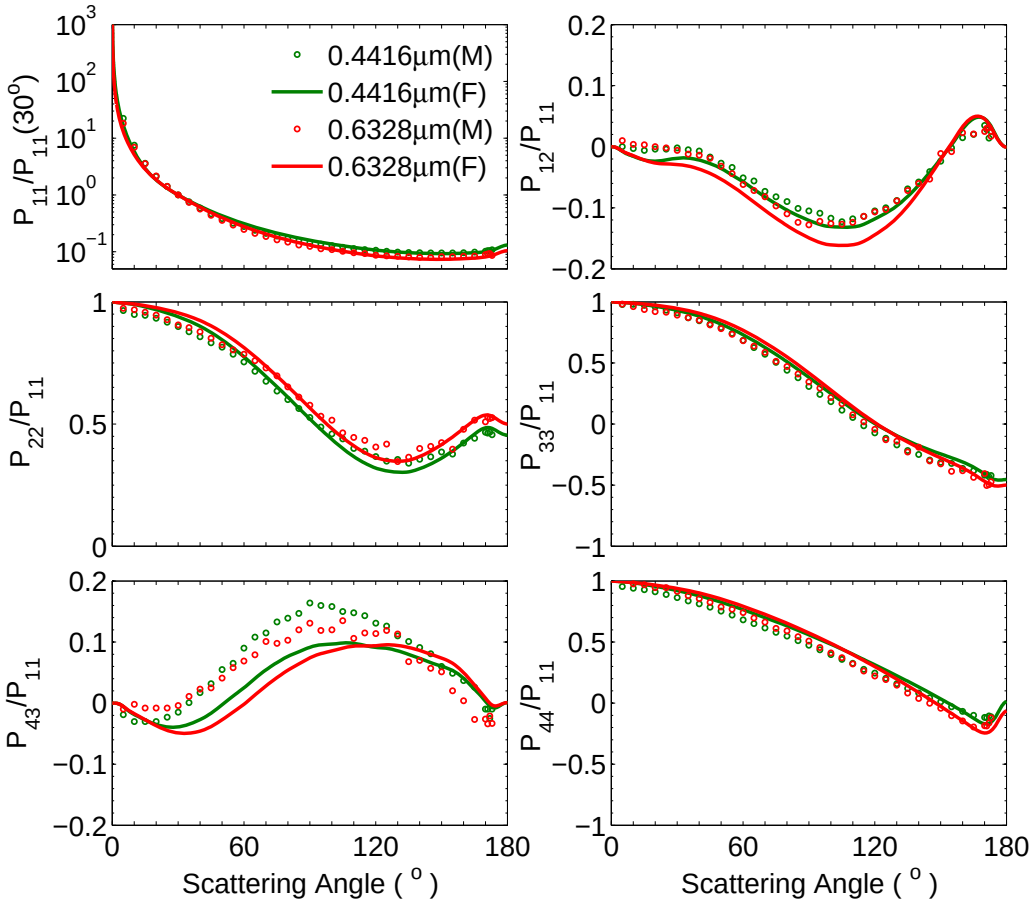

Figure 3.15: Same as Figure 3.12 but for volcanic ash (Pinatubo, $r_{eff} = 3.0\ \mu m$ and $v_{eff} = 12.3$).

Overall, with only three geometries, the fractal particles modeled the phase matrices of four mineral dusts at two wavelengths. All results show accurate agreements for the phase functions and linear polarization ratios ($-P_{12}/P_{11}$) that are two most widely used elements in current applications. Meanwhile, the fractal model gives relatively poor performances for P_{43}/P_{11} of all mineral dusts. The measured P_{22}/P_{11}, P_{33}/P_{11} and P_{44}/P_{11} of the red clay have slightly different trends from those of other samples, and, similar to the spheroid models, the calculated results from the fractal model give a poor representation of them. This may be caused by uncertainties in

the refractive indices or some special geometric characteristic of the samples.

3.1.4 Conclusion

This section investigates the single-scattering properties of complicated concave polyhedra, regular and irregular fractal particles, with sizes ranging from the Rayleigh to geometric-optics regimes. To compute the single-scattering properties of fractals across this range, a combination of the PSTD method and the IGOM has been applied. The PSTD method is used to calculate the scattering properties of particles with small-to-moderate size parameters, and the IGOM is employed for particles with moderate-to-large size parameters. The scattering properties of the fractal particles of different generations have been investigated, and the effect of the irregularity parameter β and aspect ratio used to define the irregular fractal particles has been illustrated. The phase functions, given by the PSTD method and the IGOM, show acceptable agreement for randomly oriented fractal particles with size parameters starting approximately 25 to 30. A smooth transition for the integral scattering properties as particle size increases given by the PSTD method to those given by the IGOM has been demonstrated.

The fractal geometry shows significant applicability in modeling the scattering properties of mineral dust. The numerically simulated bulk phase matrices are compared with the laboratory measurements for feldspar, red clay, quartz, volcanic ash at wavelengths of $0.4416\mu m$ and $0.6328\mu m$. Different from the pervious studies that use multiple geometries and different habit fractions at different wavelengths, a single or two irregular second-generation fractal particles can accurately represent the laboratory-measured bulk optical properties of mineral dust aerosols of different kinds at two wavelengths, even with most of the polarization states of the scattered light considered. However, the polarization properties of some dust particles are sig-

nificantly different, and the performance of the fractal particles is also challenged for some other mineral dusts with larger effective diameters.

In reality, of course, mineral aerosols are more complicated than even the irregular fractals considered here. Nevertheless, this study shows success in using to a simplified fractal model to capture the main optical properties of irregular particles in the atmosphere, without significant loss of accuracy. Compared with the previous approaches [91, 92, 29, 46, 93], more complicated concave particle morphologies are represented by the fractal particles. The comparison between the numerical simulations and laboratory measurements suggests the irregular fractal particles might be used to model the scattering properties of the mineral aerosols and have a promising future for aerosol retrieval applications and climate research.

3.2 Inhomogeneity

In general, the natural aerosols occur as mixtures with various components whose optical properties vary significantly, and the quantitative particle shapes, sizes, numbers of components, and mixing states are unknown [103, 104, 105]. However, in radiative transfer and remote sensing simulations, the atmospheric particles are usually treated as homogenous ones, the optical properties of which are easier to be estimated [90, 102]. The effective medium approximations (EMAs) are used to calculate an effective refractive index for a mixture, with which the homogeneous one is expected to have similar optical properties to its inhomogeneous counterparts, and a variety of EMAs have be developed and used for atmospheric aerosols [106, 107].

The first developed EMA, the Maxwell-Garnett (MG) theory [108, 109], was used on dust aerosols by Longtin et al. [110] in 1988. The Bruggeman (BR) theory [111, 112], another popular EMA, has also been widely used to study the radiative properties of the mineral aerosols [113, 114]. In addition to the MG and BR

theories, Sokolik and Toon [113] chose the simple volume average approximation to calculate the effective refractive indices of aerosols. The performances of nine EMAs, developed for a variety of different shapes, size distributions, physical properties, and inhomogeneous internal structures, have been reviewed by Kolokolova and Gustafsonm [107].

The EMAs and the homogenous approximations are widely used in atmospheric research [90, 102, 107, 113, 114], whereas the applicability and accuracy of them are still limited and not well tested. Chylek et al. [115] and Kolokolova and Gustafsonm [107] compared the EMA results with experiments for spheres with small inclusion amounts, and both found acceptable agreement between the calculated and measured values. From numerical computations, Perrin and Lamy [116] found the application of the EMAs to the study of the interaction of light with the inhomogeneous dust particles to be limited. However, Voshchinnikov et al. [117] indicated the EMAs could be used to simplify the computation of the optical properties of aggregates containing only Rayleigh inclusions. Both studies [116, 117] used the sphere as the particle shape. The EMAs have also been applied to some specific cases, e.g., water coated soot aggregates by Liu et al. [118], and the MG was found to provide more accurate approximations for the scattering properties of coated aggregates than the BR. However, each of the studies used the EMAs with significant limitations on particle size, shape, mixing structure, or volume fraction of the components, and drew substantially different conclusions.

This section provides a systematic insight on the applicability of the EMAs in solving problems of light scattering by the inhomogeneous atmospheric aerosols. Four EMAs, three mixing states, and two particle shapes will be considered. The details of the four EMAs, i.e. MG, BR, VA1, and VA2, are discussed in Section 3.2.1. We consider mixtures containing only two components with the volume fractions of each

varying from 0 to 1. For each inhomogeneous particle, an approximated and an exact method are used to calculate their scattering properties. The approximated method treads the inhomogeneous particles as homogeneous one with the EMA, and the Lorenz-Mie theory or the T-matrix theory is then used to calculate the scattering properties of the equivalent homogeneous particles. It should be noticed that the Lorenz-Mie and T-matrix results are understood as the approximations, because they are used for the equivalent homogeneous particles, not the original inhomogeneous one. Meanwhile, as references, the PSTD method and the core-mantle Mie [10, 11] theory are used to give the exact scattering properties of the inhomogeneous particles. Thus, the applicability and accuracy of the EMAs can be evaluated by comparing the results from the PSTD/core-mantle Mie methods with the results from a combination of the EMAs and Lorenz-Mie/T-matrix theories.

3.2.1 Effective medium approximation

Models using the EMAs try to replace an inhomogeneous particle, i.e. particles having internal variations of refractive indices, with a homogeneous particle, having a single "effective" refractive index, which yields approximately the same scattering properties. The MG [108, 109], whose history dates back to 1904, was one of the first attempts to approximate the optical properties of inhomogeneous materials. The MG considers a mixture of two components as the medium and the inclusion with small volume fractions; whereas the BR describes two components of an inhomogeneous particle symmetrically [111, 112]. The MG and BR are two of the most popular EMAs, and the effective permittivities ϵ_{eff} in the two approaches are defined to satisfy the following relations:

The MG:

$$\frac{\epsilon_{eff} - \epsilon_1}{\epsilon_{eff} + 2\epsilon_1} = f_1 \frac{\epsilon_1 - \epsilon_2}{\epsilon_1 + 2\epsilon_2}, \tag{3.1}$$

and the BR:

$$f_1 \frac{\epsilon_1 - \epsilon_{eff}}{\epsilon_{eff} + s(\epsilon_1 - \epsilon_{eff})} + f_2 \frac{\epsilon_2 - \epsilon_{eff}}{\epsilon_{eff} + s(\epsilon_2 - \epsilon_{eff})} = 1, \tag{3.2}$$

where ϵ_1 and ϵ_2 are the permittivities of the two components, and f_1 and f_2 are their volume fractions. In Equation 3.2, s is a geometric factor depending on the shape of the inclusion, and, for three-dimensional spherical inclusions, s is 1/3. In the frame of the MG, the volume fraction of the inclusion (ϵ_2 in Equation 3.1) is assumed to be "small" [119], but this limitation will not be considered in our study. However, the BR is designed to give a symmetric description for the effective permittivity of the two components without limitation on the volume fraction of the constituent materials. For atmospheric aerosols, the complex refractive index m is generally used to specify different materials, and is related to the complex permittivity ϵ by $m^2 = \epsilon$. The real and imaginary parts of the refractive index m are expressed as n and k, i.e., $m = n + ki$.

In this study, we also employ the most straightforward method to obtain the effective refractive indices based on the volume averages (VA). The VA can be performed with respect to linear average of either the permittivities or refractive indices, and ϵ_{eff} are given by the following equations:
the VA1:

$$\epsilon_{eff} = m_{eff}^2 = (f_1 m_1 + f_2 m_2)^2 = (f_1 \sqrt{\epsilon_1} + f_2 \sqrt{\epsilon_2})^2 \tag{3.3}$$

and the VA2:

$$\epsilon_{eff} = f_1 \epsilon_1 + f_2 \epsilon_2 \tag{3.4}$$

The VA based on a linear combination of refractive indices (Equation 3.3) will, thereafter, be referred to as VA1, and the average based on the permittivities (Equations 3.4) will be mentioned as VA2.

Besides the four EMAs mentioned above, there are a couple of more complex and specified approaches, and an extensive review of the existing mixing rules can be found in [107]. However, most of them give relatively close effective refractive indices, and this study will focus on only those four simple and popular EMAs, i.e. MG, BR, VA1, and VA2 represented by Equations 3.1 to 3.4.

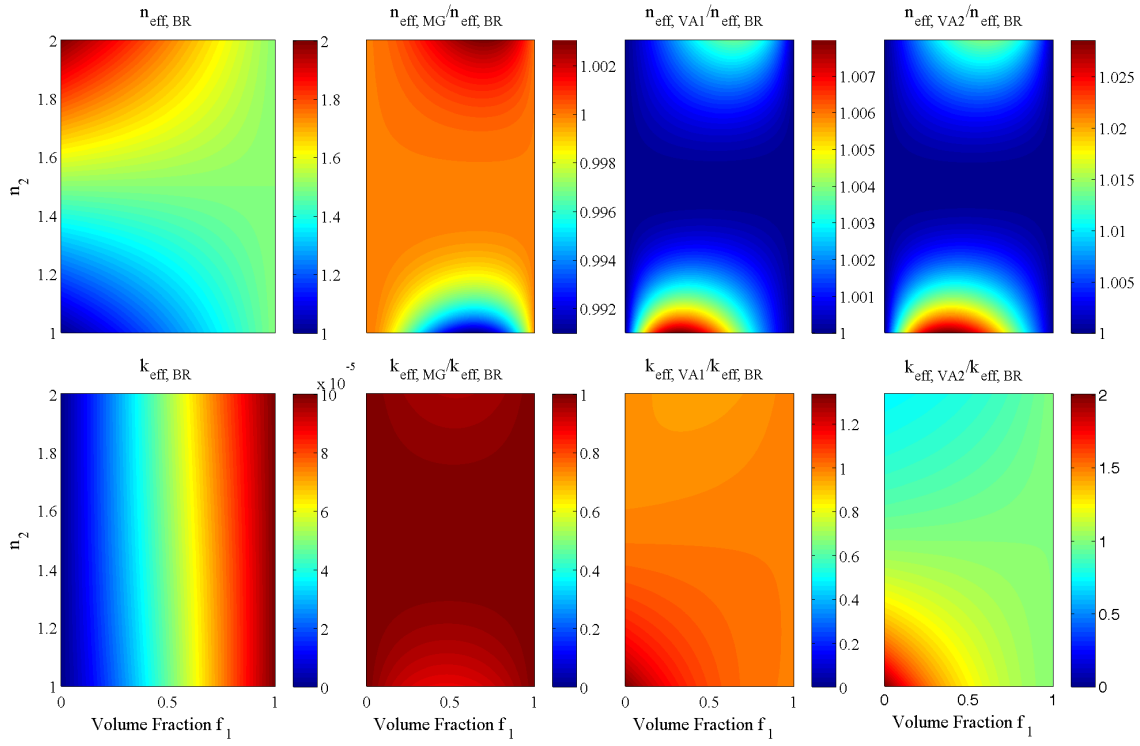

Figure 3.16: The real (upper panels) and imaginary (lower panels) parts of the effective refractive indices calculated by the four EMAs as functions of the volume fractions (f_1) and real part n_2 of refractive index m_2. m_1 is fixed to be $1.5 + 0.0001i$ and $k_2 = 0$.

Before comparing the optical properties of the inhomogeneous and equivalent homogeneous particles, we directly compare the effective refractive indices given by the four EMAs. Figure 3.16 illustrates and compares the real parts n_{eff} (top

panels) and imaginary parts k_{eff} (lower panels) of the effective refractive indices m_{eff} calculated by the four EMAs. In Figure 3.16, the refractive index of one component is fixed, $m_1 = 1.5 + 0.0001i$, but the volume fraction f_1 and the real part n_2 of the other refractive index are changing as the x- and y-axes, respectively. The imaginary part of m_2 is set to be 0. The left most panels of Figure 3.16 show $n_{eff,BR}$ and $k_{eff,BR}$, and the subscript BR indicates that values are calculated by the BR. With the volume fraction f_1 increasing from 0 to 1, $n_{eff,BR}$ gradually changes to 1.5, and, for different n_2, the changes of $n_{eff,BR}$ are significantly different. However, with k_1 and k_2 fixed at 0.0001 and 0, the $k_{eff,BR}$ shows little variance for a different n_2 at a given volume fraction f_1. In Figure 3.16, to illustrate the relative difference of the four methods, the n_{eff} and k_{eff} calculated by the MG, VA1, and VA2 are shown as ratios to the corresponding values from the BR. When n_2 is close to n_1 (1.5), i.e., with $|n_2 - n_1| < 0.1$, the three ratios are all approximately 1, and this indicates that the four EMAs are equivalent on calculating effective refractive index of two components with their differences between the real parts of the refractive indices less than 0.1. When $|n_2 - n_1| > 0.1$, the differences of n_{eff} given by the different EMAs become more noticeable and increase with an increase of $|n_2 - n_1|$. However, the magnitude of the relative differences between the MG or VA1 results and those given by the BR is no more than 0.8%. Both $n_{eff,VA1}$ and $n_{eff,VA2}$ are larger than those given by the BR, and $n_{eff,VA2}$ can be over 2% larger than those given by the BR. With both fixed and relatively small (0.0001 and 0) imaginary parts for the two components, the $k_{eff,BR}$ is almost independent on n_2. k_{eff} given by the BR, MG and VA1 are relatively close, and the differences increase as $|n_1 - n_2|$ increases. Both the VA1 and VA2 give larger k_{eff} than those from the BR when f_1 and n_2 are small, and the ratios of $k_{eff,VA2}$ to $k_{eff,BR}$ even reach 2. To limit the number of variables, we will not consider the absorption in this study, and only very small imaginary

parts are used. However, some of the atmospheric particles are highly absorptive, and the influences of the EMAs on the scattering properties of absorptive particles are interesting topics for further studies.

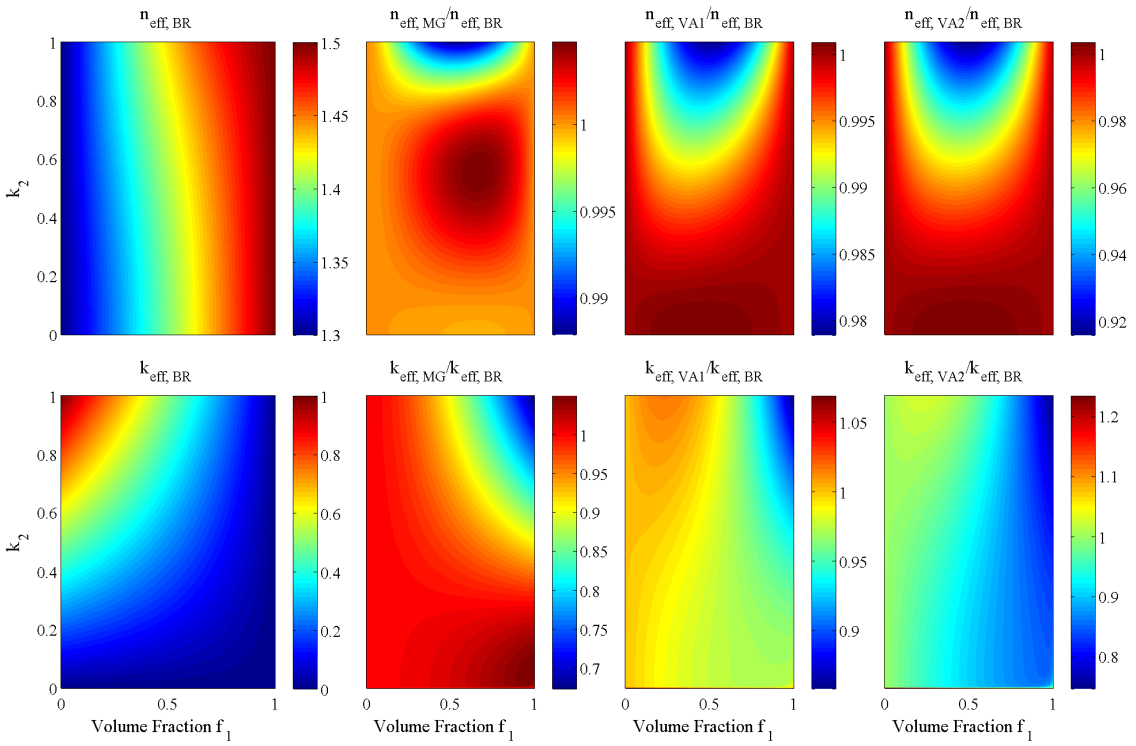

Figure 3.17: Same as Figure 3.16 but as functions of the imaginary part k_2 of refractive index m_2. m_1 is fixed to be $1.5 + 0.0001i$ and $n_2 = 1.3$.

Similar to Figure 3.16, Figure 3.17 illustrates the real and imaginary parts of the effective refractive indices as functions of volume fraction f_1, but the y-axis is for k_2. m_1 is $1.5 + 0.0001i$, and n_2 is fixed to be 1.3. The figure shows the influence of the imaginary part of the refractive indices on the EMA results, and is organized the same as Figure 3.16. Although n_1 and n_2 are fixed, the $n_{eff,BR}$ shows slight differences with an increase of k_2 at fixed volume fraction f_1, and the variance becomes larger

when k_2 becomes close to 1. With the small imaginary part for the component 1, $k_{eff,BR}$ decreases as an increase of the volume faction f_1, and show totally different rates with a different k_2. When k_2 is smaller than 0.2, all four EMAs give almost the same n_{eff}. The differences become obvious when k_2 is larger than 0.4. The MG may give either smaller or larger n_2 values than the BR, but the VAs' results are always smaller. However, the relative differences between the BR and the MG (or VA1) are no more than 1%, except for the n_{eff} given by VA1 with k_2 larger than 0.9. The $n_{eff,VA2}$ may be over 5% smaller than the BR results with k_2 larger than 0.7 and f_1 around 0.5. For k_{eff}, the values given by the four EMAs differ significantly, and the difference increases with increases of k_2 and f_1.

3.2.2 Inhomogeneous particles

As discussed in the previous section, the application of the four EMAs depends only on the volume fractions of the components, and is independent of the particle shape or mixing state. However, the scattering properties of inhomogeneous particles with different shapes or mixing states may be substantially different. In current remote sensing and global climate models [90, 102], the aerosol particles are widely treated as either homogeneous spheres or spheroids, and this study specifies the particle overall shapes as both spheres and non-spherical (i.e. spheroids with an aspect ratio of 0.5 as an example).

Another important factor that is widely investigated is the mixing state of the atmospheric aerosols. The attached and uniform mixtures are the most widely used structures to model inhomogeneous aerosols [104, 120], e.g. attached mineral dust and black carbon [121], the uniformly mixed sulfate and organic particles [122], and sea salt and silicate mineral component [123]. The stratified particles are also very common in the atmosphere, e.g., aerosol particles surrounded by condensed water

vapor [124] and black carbon coated by sulfate [125]. Based on the reality of the atmospheric aerosol particles, three mixing states are considered:

1) Stratified particles: one component coated by the other. The core and mantle parts are concentric, and the spheroids have the same aspect ratios;

2) Attached: a combination of two attached parts with different components to form the overall shape of a sphere or spheroid. The connecting surface is assumed to be planar and is perpendicular to the symmetric axis of the spheroids; and,

3) Uniformly mixed: the two components mixed uniformly throughout the entire particle. The spherical or spheroidal particle is formed by randomly arranged small cubical elements of the two components, and the single elements are small enough to be treated as Rayleigh scatterers ($x << 1$). The PSTD or DDA simulations, in which the particles are described in discrete domain (using either grid cells or dipoles), are straightforward to consider this case, and each single grid cell or dipole is randomly defined as one of the components with given overall volume fraction.

Figure 3.18 illustrates the inhomogeneous spheres (upper panels) and spheroids (lower panels) with the three mixing states. The dark and light regions represent components that have different refractive indices m_1 and m_2. For the stratified particles, one component can be either the core or the mantle, and the scattering properties of both cases will be studied.

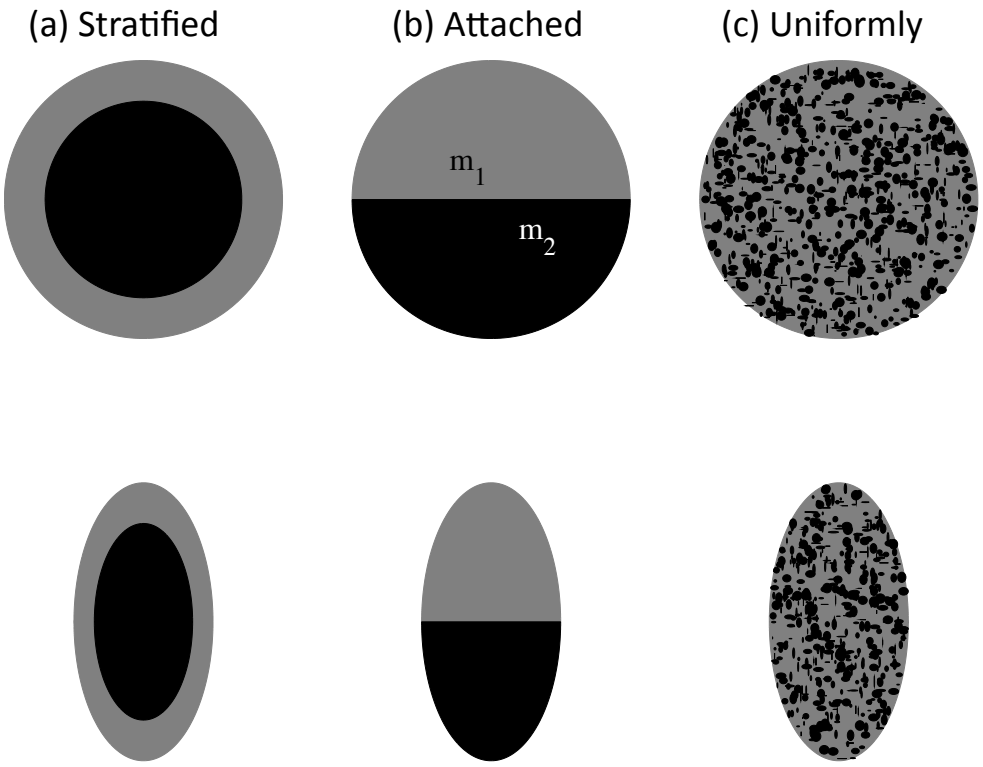

Figure 3.18: Three mixing states to model the inhomogeneous particles: (a) Stratified; (b) Attached; and, (c) Uniformly mixed, with overall geometries of sphere and spheroid.

The two components with the refractive indices of $m_1 = 1.5 + 0.0001i$ and $m_2 = 1.3$ are used in this study. In what follows, when we refer to the volume fraction, we mean the fraction of m_1, i.e., f_1 (and $f_2 = 1 - f_1$). The size parameter x of a spheroid is defined in the form of $x = 2\pi b/\lambda$, where b is the semi-length of the symmetry axis. The aspect ratio a/b equals 0.5, and a is the equatorial radius. For stratified particles, the "stratified 1" refers to the case with the component m_1 being the core, and "stratified 2" with m_1 being the mantle. As we have discussed in Section 2.4.4,

the applicability and accuracy of the PSTD on those inhomogeneous particles have been well verified by comparing with the exact or highly-reliable results, and their results will be used to validate the EMAs. Meanwhile, the core-mantle Mie will be used for the spheres with stratified structures. All scattering properties considered are for randomly oriented particles. To account for the effect of random orientations in the PSTD simulations, the single-scattering properties of spheroids with three mixing states and the attached spheres are averaged over 180 scattering planes for 16 particle orientations.

3.2.3 Applicability of the EMA

This sub-section compares scattering properties of inhomogeneous and corresponding equivalent homogeneous particles. Both single- and bulk-scattering properties will be considered, and the integral scattering properties as well as the phase matrix elements will be discussed. The comparison will draw conclusion on two areas: (1) the relative performance of the four EMAs, and (2) the performance the EMAs to approximate the scattering properties of the inhomogeneous particles.

Figure 3.19 shows Q_{ext} (upper panels) and g (lower panels) of inhomogeneous spheres (left panels) and spheroids (right panels) with size parameters of 30 as functions of the volume fraction. The markers in the figure indicate the core-mantle Mie and PSTD results of inhomogeneous particles with the three mixing states: the hollow circles for "stratified 1"; the solid circles for "stratified 2"; the solid triangles for attached particles; and the solid squares for uniformly mixed particles. The values of Q_{ext} and g vary dramatically with the change in volume fraction. Particles with various mixing states have significantly different integral scattering properties, especially the two stratified cases. The four curves in Figure 3.19 are the results given by the EMAs for equivalent homogenous particles (combined with the Lorenz-Mie

theory for spheres and the T-matrix theory for spheroids). Of the four EMAs, the MG, BR, and VA1 have almost the same Q_{ext} and g for all volume fractions from 0 to 1. However, when the volume fraction is between 0.1 and 0.9, the Q_{ext} and g based on the VA2 are significantly different from those given by the other three, especially for spheres. The discrepancy can be explained by the relatively large differences in the effective refractive indices between VA2 and the other three methods, which are illustrated in Figures 3.16 and 3.17. Comparing the results of the inhomogeneous and equivalent homogeneous particles, we notice that the results from the equivalent homogeneous cases (based on the BR, MG, and VA1) only agree accurately with those given by the uniformly mixed spheres and spheroids, and the values are consistent over the entire range of volume fractions. However, the Q_{ext} and g of the two stratified and attached particles are very different from those of the homogeneous particles, and may be over 30% larger or smaller at some volume fractions. Thus, the EMAs can give accurate approximations for only the uniformly mixed particles, but are very poor for the stratified and attached particles. Because the same results are obtained for both the spheres and spheroids over the entire volume fractions, we conclude that the applicability of the EMAs is independent of the overall particle shape and mixing fractions.

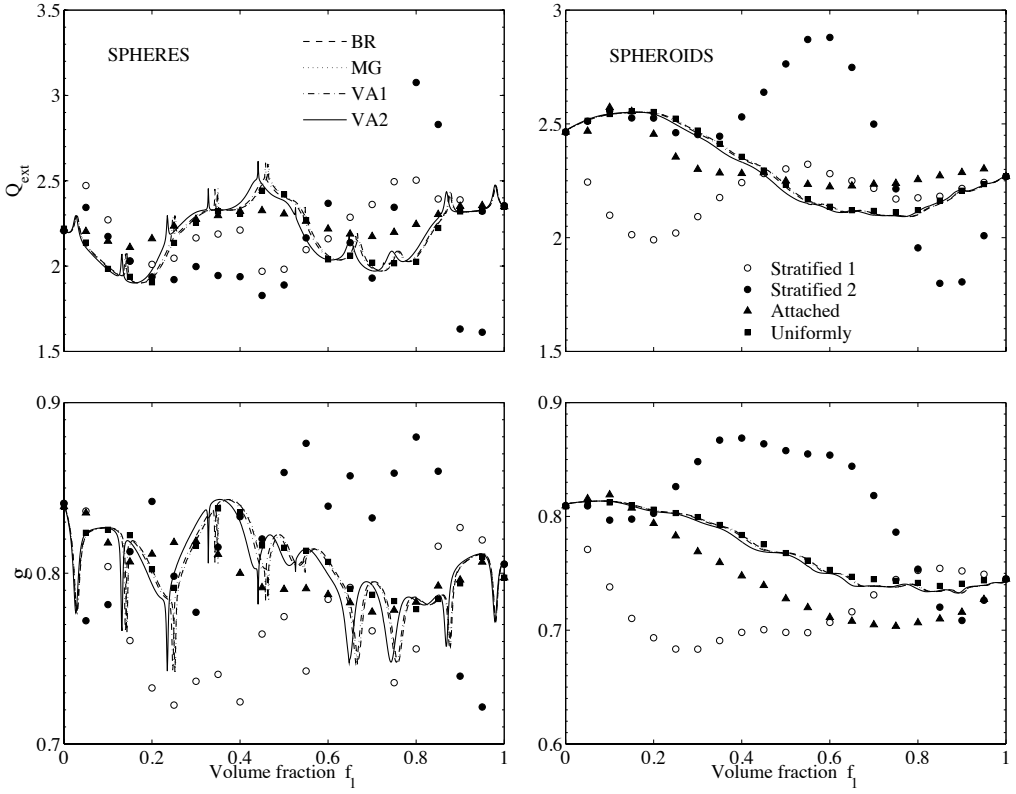

Figure 3.19: The integral scattering properties of inhomogeneous spheres (left panels) and spheroids (right panels) with size parameters of 30 as functions of volume fractions.

Figure 3.20 illustrates the angular-dependent P_{11} (left panels) and P_{12}/P_{11} (right panels) of inhomogeneous and equivalent homogeneous spheres with volume fractions of 0.5 and size parameters of 30. For a clearer comparison, the results are shown in three panels: 1) the upper panels are the approximations of equivalent homogenous spheres given by a combination of the four EMAs and the Lorenz-Mie method; 2) the middle panels are the results from the two stratified spheres and the homogenous sphere based on the effective refractive index given by the BR; and, 3) the lower panels are the same as the middle ones but for attached and uniformly mixed spheres.

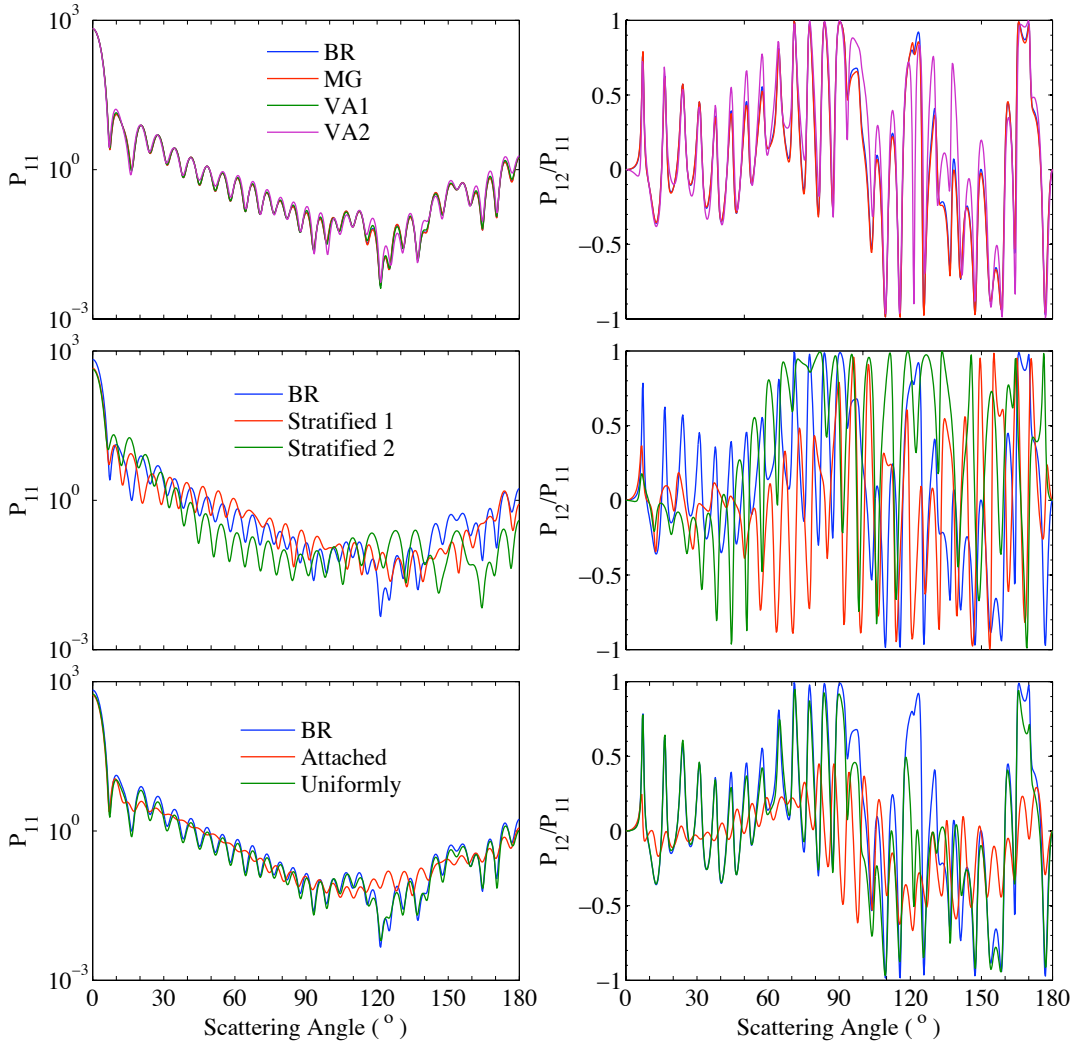

Figure 3.20: P_{11} (left panels) and P_{12}/P_{11} (right panels) of the inhomogeneous spheres with size parameters of 30. The results for the homogeneous spheres are given by a combination of the EMAs and Lorenz-Mie theory, and the results for the inhomogeneous spheres are from the core-mantle Mie theory and the PSTD.

The upper panels of Figure 3.19 indicate the BR, MG, and VA1 give quite similar approximations for both phase matrix elements, but the VA2 results are slightly different from the other three around some peaks. The middle and the lower panels compare the P_{11} and ratio P_{12}/P_{11} of the equivalent homogeneous and inhomoge-

neous particles. The inhomogeneous stratified spheres (middle panels) give totally different phase matrix elements from the equivalent homogeneous spheres for both the oscillations and the overall trends. Similar to the integral scattering properties, the results from a combination of the BR and Lorenz-Mie theory agree very well with those of the uniformly mixed sphere, except slight differences for P_{12}/P_{11} existing at some scattering angles. The phase function of the attached sphere follows the same overall trend as the homogeneous sphere, but shows much weaker oscillations, and the P_{12}/P_{11} ratio appears very different. The comparison for other non-zero phase matrix elements are similar to those of P_{12}/P_{11}, and will not be shown. From Figure 3.20, we see the EMAs provide an accurate approximation for the phase matrix elements P_{11} and P_{12}/P_{11} of the uniformly mixed spheres, but cannot be applied to the stratified or attached spheres.

Similar to Figure 3.20, the P_{11} and P_{12}/P_{11} of randomly oriented spheroids with a size parameter of 30 and volume fractions of 0.5 are given in Figure 3.21. Here, the effective refractive indices from the EMAs are used by the T-matrix method. The agreement between the four EMAs becomes much better for spheroids, and the P_{11} given by the VA2 shows a little differences from the other three at scattering angles about 175^o. Furthermore, Figure 3.21 indicates that EMA applicability for calculating the phase matrix of non-spherical particles is also limited to the uniformly mixed ones, and both P_{11} and P_{12}/P_{11} of the stratified and attached particles are significantly different from the ones given by the EMAs.

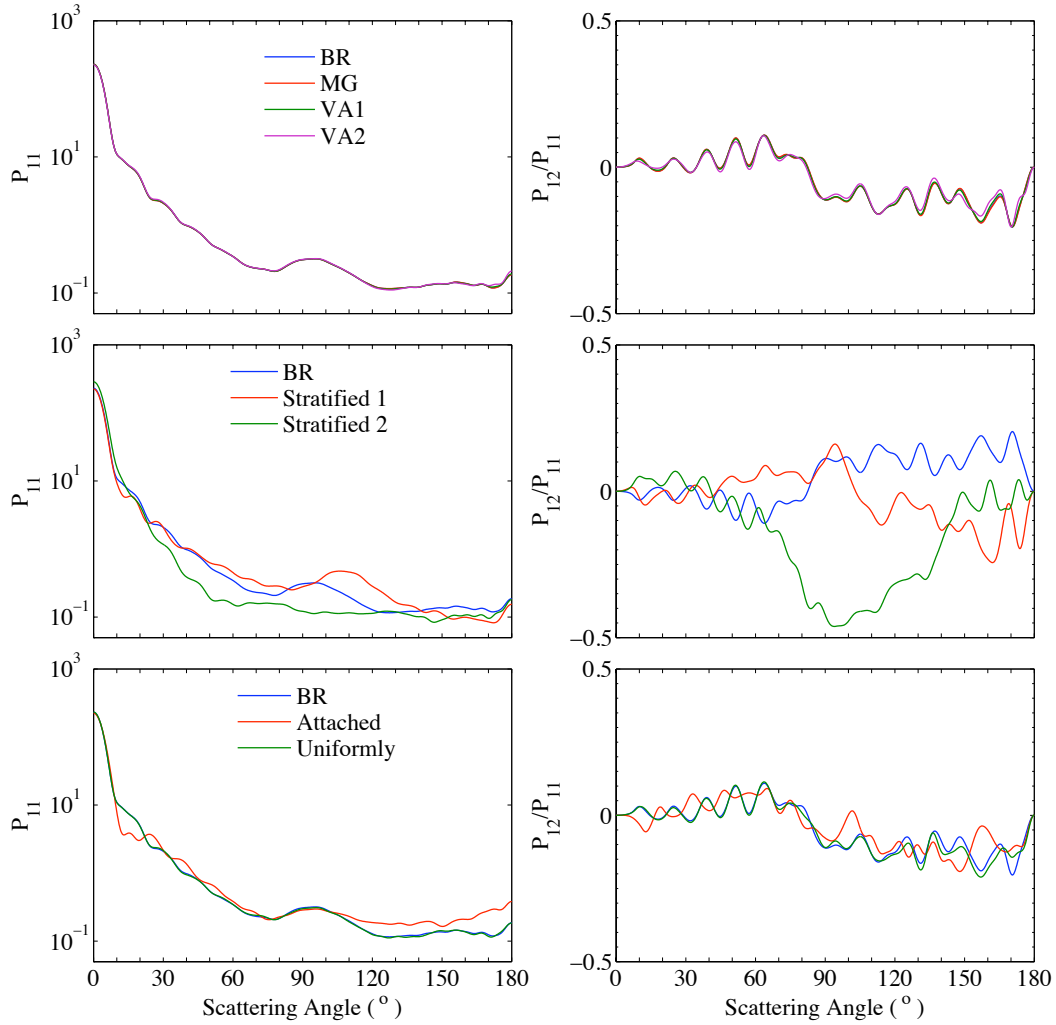

Figure 3.21: Same as Figure 3.20 but for the spheroids. The homogeneous results are given by a combination of the EMAs and the T-matrix theory.

The previous results are for particles with the same size parameter and varying volume fractions, and Figure 3.22 shows the Q_{ext} and g of the inhomogeneous spheres (left panels) and spheroids (right panels) as functions of the particle size parameter. The size parameter increases from 1 to 100, and the volume fraction is fixed at 0.5. Same as Figure 3.19, Figure 3.22 illustrates the EMA results by the curves, and the markers indicate those of the two stratified, attached, and uniformly mixed particles.

When the size parameter is small ($x < 5$), the Q_{ext} and g of inhomogeneous particles in the three mixing states are quite similar, and the homogeneous approximations based on the EMAs are close to those of the inhomogeneous ones. However, the differences become significant for particles with larger size parameters except for those of uniformly mixed particles. For particles with $x > 5$, the EMAs can give accurate approximations for only the uniformly mixed particles. However, for the stratified or attached cases, their scattering properties can agree with the homogeneous counterpart only at some size parameters. Again, the conclusion is independent of the particle overall shape, and the applicability of the EMAs is independent of the size parameter.

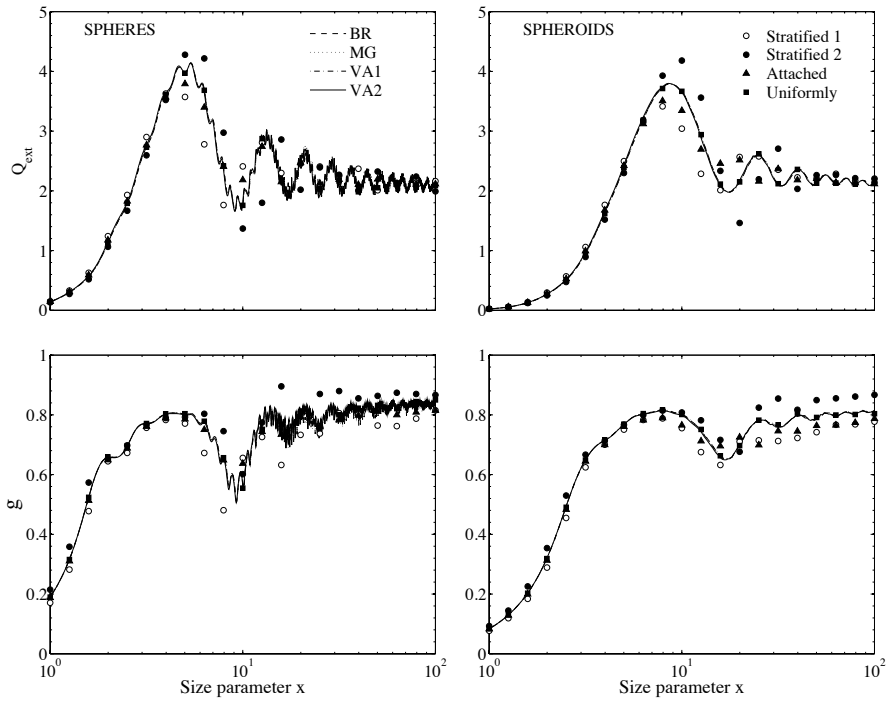

Figure 3.22: The integral scattering properties of the inhomogeneous spheres (left panels) and spheroids (right panels) as functions of the particle size parameters. The volume fractions are both 0.5.

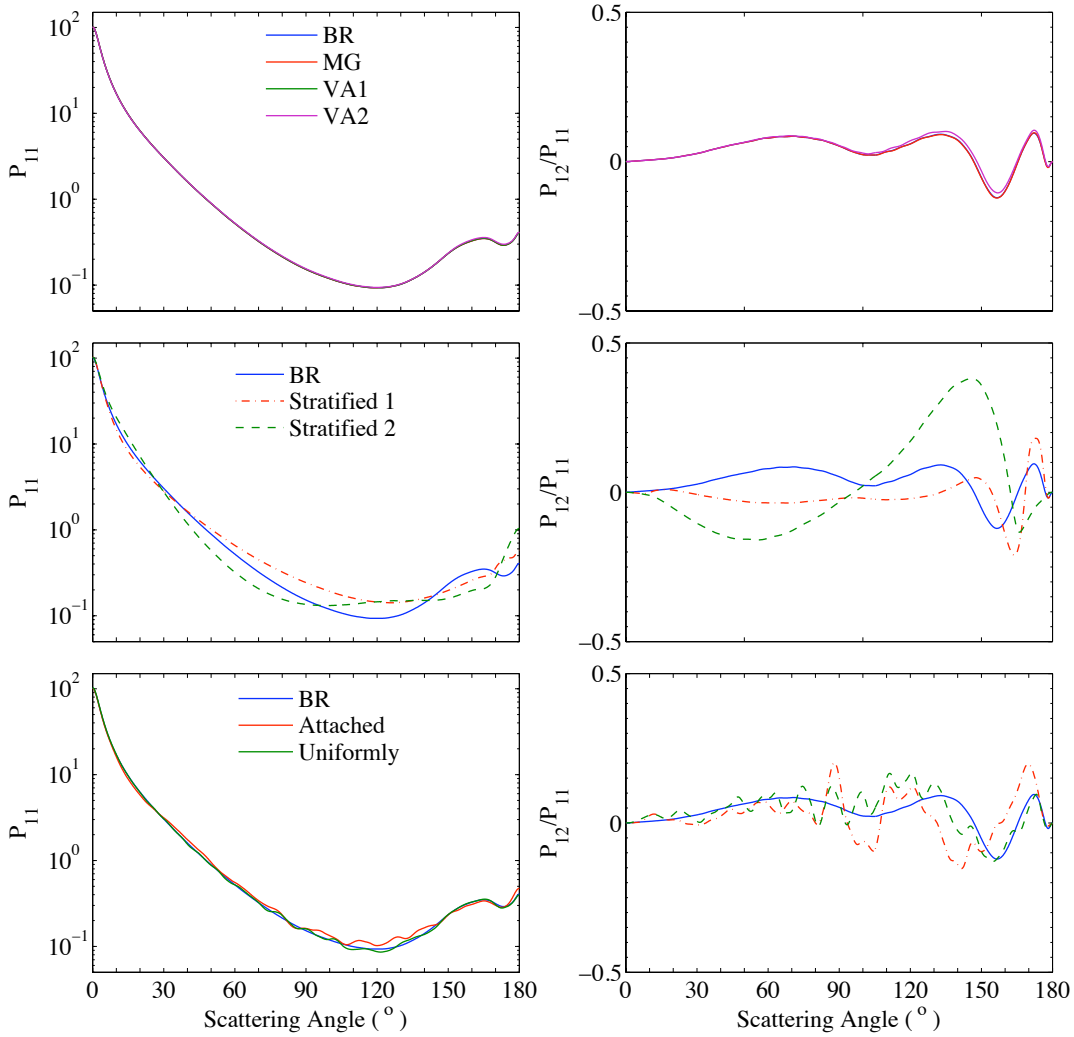

Figure 3.23: The bulk P_{11} and P_{12}/P_{11} of an ensemble of spheres with effective radius of 1 μm and variance of 1.

The results indicate the EMAs cannot be used to approximate the single-scattering properties of the stratified and attached particles, and Figure 3.23 shows the EMA performance for the bulk phase matrix elements of spheres. As an ensemble of particles with different sizes, their scattering properites are averaged based on the given size distribution, and becomes more smooth and relatively featureless. The incident

wavelength is 0.6328 μm and the volume fraction is 0.5. The size distribution of feldspar given by the ALSD [41] is used, and the ensemble particles have an effective radius of 1.0 μm and a variance of 1.0. Figure 3.23 is organized similar to Figures 3.20 and 3.21. For the bulk phase matrix elements P_{11} and P_{12}/P_{11}, the four EMAs are equivalent. However, the results of the homogeneous particles are dramatically different from the two stratified cases. For attached particles, the EMA results are quite close to the exact solutions given by the PSTD, but some differences are noticed at scattering angles from 90^o to 150^o. As expected, the P_{11} given by the EMAs and Lorenz-Mie theory agree very well with those for the uniformly mixed particles, but the agreement becomes relatively poor for the ratio P_{12}/P_{11}.

Figure 3.24 is the same as Figure 3.23, but the overall particle shape is a spheroid with an aspect ratio of 0.5. The same incident wavelength and particle size distribution are used to give the bulk phase matrix. The upper panels of Figure 3.24 show the consistency of the four EMAs to approximate the bulk scattering properties of the inhomogeneous spheroids. From the middle panels, neither stratified results for the P_{11} or P_{12}/P_{11} agrees with those given by the combination of the EMAs and T-matrix method, whereas similar overall trends are achieved and the results are much more close than those of spherical cases. In the lower left panel, the bulk P_{11} of attached spheroids and the homogeneous results show accurate agreements for the forward scattering, but significantly underestimate the backward scattering, and similar results was observed at the phase function of the single spheroid with size parameter of 30 (see Figure 3.21). Considering the exact solutions of the inhomogeneous particles with the three mixing states, only the uniformly mixed results, both P_{11} and P_{12}/P_{11}, coincide with the ones given by the homogeneous approximations, and the choice of the EMAs is not essential.

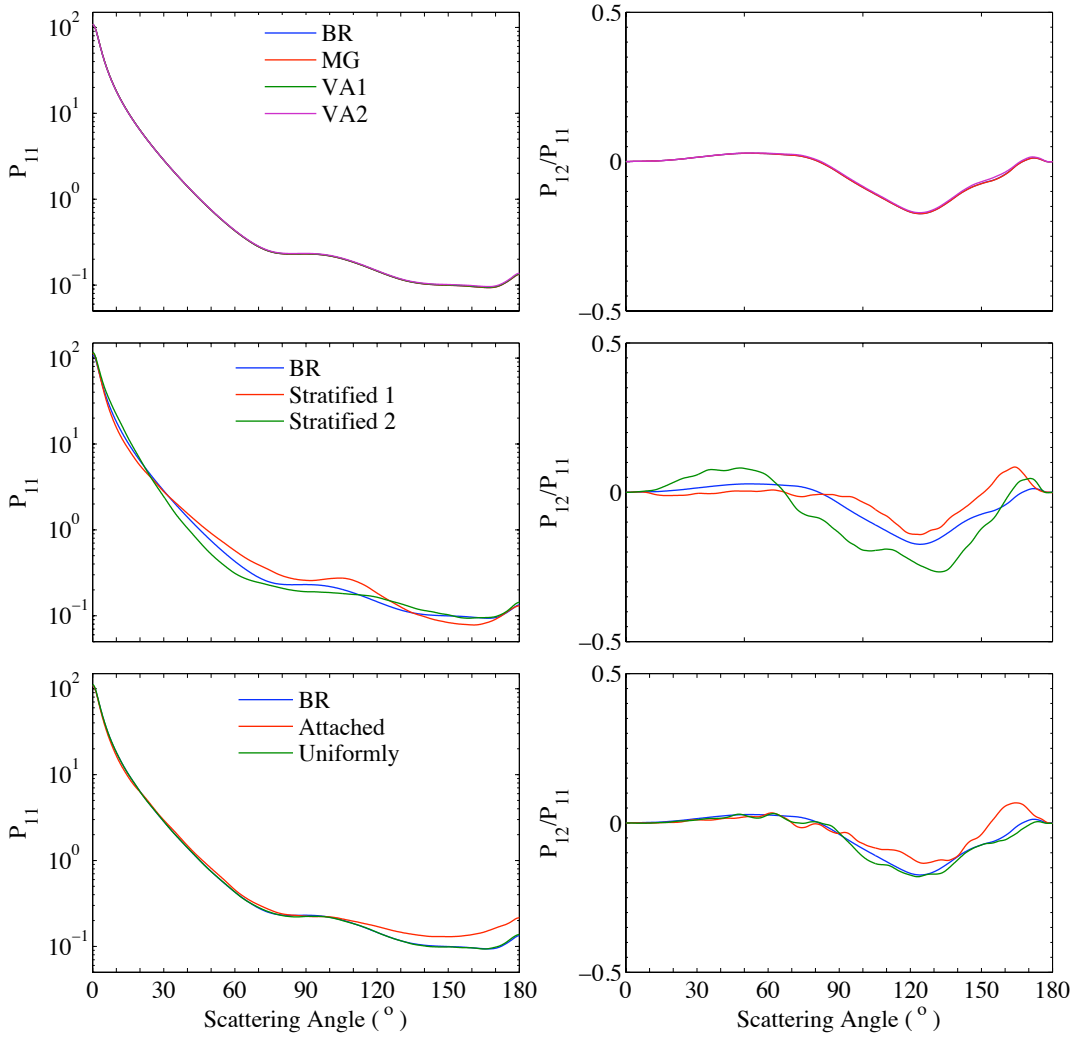

Figure 3.24: Same as Figure 3.23 but for the spheroids.

Figures 3.19 to 3.24 compare the scattering properties of the inhomogeneous and equivalent homogeneous particles. The scattering properties of particles with the three different mixing states show significant variations. The homogeneous approximations based on the EMAs are not accurate enough for the stratified and attached particles, and the detailed mixing states should be considered when studying light scattering by inhomogeneous atmospheric aerosols.

3.2.4 Conclusion

This section systematically investigates the applicability of EMAs for calculating the scattering properties of inhomogeneous atmospheric particles, and four EMAs, three mixing states, and two overall particle shapes are considered. The EMAs are combined with the Lorenz-Mie or T-matrix theories to approximate the scattering properties of the equivalent homogeneous particles, and the results are verified by comparing with the standards given by the core-mantle Mie theory or the PSTD, which consider the exact inhomogeneous mixing structures of the particles. Although the four EMAs give effective refractive indices with only slight differences, the Maxwell-Garnett theory, Bruggeman theory, and volume-average method based on refractive indices are almost equivalent to approximate the scattering properties of the inhomogeneous particles, but single scattering properties given by the volume-average method based on the permittivity differ slightly from those based on the other three EMAs. The applicability of the EMAs is independent of the volume fractions of the components and the overall shape and size of the particles, but is determined by the mixing state. The scattering properties of the equivalent homogeneous particles are significantly different from those of the stratified or attached inhomogeneous particles, but agree accurately with those of the uniformly mixed particles.

Considering the significant irregularity of the atmospheric particles, this section shows some extremely idealized models for both the mixing states and particle overall geometries. If the EMAs is used as an approximation for the bulk scattering properties, the particular choice of the EMAs will show little differences. To achieve more accurate scattering properties of atmospheric particles, the detailed mixing states and overall geometries have to be considered.

3.3 Surface roughness

Laboratory and aircraft-based observations [40, 41, 42, 126, 127] indicate that atmospheric particles are almost exclusively nonspherical and have some degree of surface roughness. Numerical studies indicate the surface roughness to be important in determining the single-scattering properties of the particles [127, 128, 129, 130], and to have significant impact in radiative transfer models and remote sensing. The effect of surface roughness on light scattering depends on the particle size, refractive index, and surface structure [45, 130, 131, 132]. Small-scale surface roughness has significant influence on the backward scattering and single-scattering albedo of small spheres, and the effects are sensitive to the surface structures [132]. For large nonspherical ice crystals, surface roughness smooths out the peaks in the phase functions as well as other elements of the phase matrix [128, 47]. In ice cloud retrievals, Yang et al. [48] found the surface roughness to decrease the retrieved optical thickness and to increase the retrieved effective particle size in comparison with the smooth counterparts. When the polarization properties are considered, a number of studies found simulations of the polarized reflectance using the scattering properties of smooth particles to produce a poor fit with the satellite measurements. Meanwhile, simulations based on particles with inhomogeneity, distortions or rough surfaces to give much better agreement [133, 134, 135], because relatively featureless and smooth phase matrix elements are obtained.

In spite of considerable research effort, our knowledge on microphysical properties and related optical effects of surface roughness remains limited. Previous studies have considered the effect of surface roughness by using either the numerically exact methods, e.g. the FDTD [129], DDA [130], or T-matrix methods [131] for relatively small particles, or the GOMs for particles much larger than the incident wavelength.

In the GOM studies no attempts were made to construct a rigorous particle geometry for the scattering calculations, but the approximated method named as the tilted-facet (TF) method is employed. In the TF approximation, each individual ray reaching a point on the particle surface has an interaction with a surface element with orientation that is chosen at random and hence is unique to that ray. While the GOM methods have had some successes for application, the fact that they involve no well-defined surface of the particle makes it challenging to relate results to any particular kind of surface roughness observed in naturally occurring atmospheric particles or ones used in the more sophisticated light scattering models.

This section focuses on the effects of surface roughness on the scattering properties, and we will employ a numerical model that considers roughness to be "essentially random deviations from smoothness at small spatial scales." The model enables us to characterize the roughness in terms of a key parameter, the variance of surface slopes, which is widely used for previous approximations based on the TF. The surfaces we construct are not intended to reflect the operation of some known physical process of crystal aging or crystal growth, but instead are intended to give a sense of "generic" optical effects of random small scale surface variations. Although we confine our attention in this study to roughened hexagonal columns, there is nothing in our methods of representing surface roughness or scattering simulation that requires restriction to roughening of that particular shape. We instead focus on the effects, given the particle geometry, of size parameter and roughening on the scattering properties over the entire size range from the Rayleigh to the geometric-optics regimes. The same combination of the PSTD and IGOM will be used to calculate their scattering properties over the entire size range. Considering the significant drawbacks for the TF approximation in the GOMs, the ray-tracing algorithm will improved to consider the roughness more rigorously in the simulation.

Section 3.3.1 reviews the roughness models used for the atmospheric particles and discusses a new irregular roughness model used in the PSTD and IGOM in this study, and the limitation of the TF approximation will be discussed in section 3.3.2. The light scattering properties of roughened particles with the entire size range will be presented in Section 3.3.3, and Section 3.3.4 concludes this part.

3.3.1 Roughness model

Surface roughness is commonly observed on atmospheric particles, for examples ice crystals in cirrus clouds [40] and mineral dust [41], but specifying the observed small-scale structures in quantitative detail is extremely difficult. This subsection will review some of the previous models used to represent rough surfaces of ice crystals or aerosol particles, and will introduce a model that we have developed that was motivated by a more complicated one used in studies of the optical properties of "random" sea surface wave fields.

In a 2-D study, Sun et al. [136] used the FDTD and discretized a circular surface into sub-elements. A roughened surface was created by a method that involved independent tilting of these sub-elements. In three dimensions, Gaussian-random spheres have been the most widely used geometric shapes for studying the effects of surface roughness, and their single-scattering properties have been calculated using the GOM [137, 138, 139], DDA [140], and T-matrix method [130, 131]. Models based on regular or stochastic surface perturbations show substantial applicability and flexibility in defining rough particles, and are widely used for particles in the resonant size-parameter region (i.e., the particle size is on the order of the incident wavelength). Li et al. [129] introduced random 2-D "Gaussian spikes" on spherical surfaces,

$$r(\theta, \phi) = R_0 \left[1 + \alpha e^{-\Delta\theta^2/(2\sigma^2)}\right] \tag{3.5}$$

and used the FDTD to calculate the scattering properties of roughened spheres with size parameters from 5 to 20. They found the effects of surface roughness to be significantly dependent on the parameter α, which they called the "size" of the roughness. Kahnert et al. [130] compared the effects of four different rough surfaces on the absorption and scattering properties of spheres with size parameters of 5 and 50 by using the DDA and T-matrix methods. The models they used applied a form of structured roughness to spherical particles that could have very small scales while retaining enough symmetry to make T-matrix methods feasible, at least up to size parameter 50. Our approach is aimed at removing all symmetries at small scales, and in doing so presenting an ostensibly more realistic-looking form of roughness, while expanding the particle size well into the geometric optics range.

To rigorously define surface perturbations in the framework of the GOMs is challenging. Yang and Liou [141] investigated the effect of surface roughness on the single scattering properties of particles in the geometric-optics regime (i.e., the scatterer size is much larger than the incident wavelength) using the TF approximation. In this method, the surface roughness is modeled by assuming that, at each reflection and refraction event, the local normal direction of a "facet" on a particle surface is randomly tilted from its smooth counterpart. To specify the degree of the surface roughness and the magnitude of individual facet slopes, Yang and Liou [141] introduced a first order Gram-Charlier density, i.e., a Gaussian density, motivated by sea surface observations [142]. In their approach, slopes s_x and s_y of individual facets in directions x, y, in local coordinate systems with facet-normal direction the local z axis, are randomly determined to follow

$$P\left(s_x, s_y\right) = \frac{1}{\pi\sigma^2} exp\left[-\frac{s_x^2 + s_y^2}{\sigma^2}\right], \tag{3.6}$$

where $P(s_x, s_y)$ is the joint probability density for the local slopes.

The more general Weibull distribution was introduced by Shcherbakov et. al. [143] to the TF approximation and applied for retrieval of ice crystal parameters from the measured phase function [143]. The Weibull distribution is given by:

$$P(s_x, s_y) = \frac{\eta}{\pi\sigma^2}\left(\frac{s_x^2 + s_y^2}{\sigma^2}\right)^{\eta-1} exp\left[-\left(\frac{s_x^2 + s_y^2}{\sigma^2}\right)^{\eta}\right], \tag{3.7}$$

The additional shape parameter η in the Weribull distribution provides flexibility in the construction of a distribution. Notice that when $\eta = 1$, Equation 3.7 reduces to the 2D Gaussian distribution given by Equation 3.6.

Various drawbacks and uncertainties inherent in the TF method will be discussed more in the next section, but for now we simply mention the fact that the method does not involve specification of a single definite particle. This fact raises the questions of how to compare results obtained using the method with results from a numerically exact approach that requires such a specification, and how to compare the numerical particles with the naturally occurring ones .

As mentioned above, for a comparison using the PSTD method we want to specify a particle geometry in a way that embodies the notion of random, small scale roughness. The geometry should be applicable in a natural way for comparisons with results from the TF method and the GOMs. We are not aware of any explicit expressions for naturally occurring rough surfaces of ice crystals or aerosol particles that could serve as a guide. What we instead use as a guide is a model for sea surface roughness constructed by Schwenger and Repasi [144]. They modeled surface roughness as a combination of representations of pure linear gravity waves, swells and choppy waves. The same model has been applied in a study of radiative transfer in an ocean with a dynamic surface [145]. We consider only a generalized linear grav-

ity wave, and the model represents the surface as a superposition of Fourier modes with random phases, and spectral amplitudes determined by a spectral theory that includes functional dependence on parameters special to the physics of surface gravity wave. We omit these special parameters which have no meaning in the context of atmospheric particles, and retain the essential shape-determining features of the approach, as well as the crucial feature of random phases in the Fourier modes.

One way to describe our approach of roughening is to imagine that an initially smooth particle is covered by "wrinkled wrapping paper" with identical optical properties to those of the particle. For each smooth face of the particle we cut a piece from this paper to replace that face. (We describe below the manner in which we join the pieces at edges of the particle.) The wrapping paper comes in sheets that are squares with sides of length L, where L is the greatest linear dimension of the faces of the particle. In the geometric case that we use as an example in this study, namely the hexagonal column, a sheet would be a square A having sides of length

$$L = max(D, H), \tag{3.8}$$

where the diameter D of the circumscribing circle for the hexagonal end-plate is twice an edge-length of the plate, and H is the height of the column. We take then a coordinate system (x, y, z) with $z = 0$ corresponding to points on A. Denoting by $\vec{r} = (x, y)$ the horizontal position vector of such points, we define the "elevation" z of the wrinkle at that point by

$$z\,(\vec{r}) = \sum_{\vec{k}\in\mathcal{K}} Z\left(\vec{k}\right) exp\left[i(\vec{k}\cdot\vec{r}\,\frac{2\,\pi}{L} + \phi(\vec{k}))\right], \tag{3.9}$$

where $Z(\vec{k})$ is a real number to be defined and $\phi(\vec{k})$ is a random phase. The index

set $\mathcal{K}$ of wave numbers retained in the sum is defined by

$$\mathcal{K} = \{\vec{k} \,|\, min(k_x, k_y) > 1\}. \tag{3.10}$$

(This is to explicitly exclude very "long-wave" components.) The phases are chosen independently from a uniform distribution on $[0, 2\pi)$ for each wavevector $\vec{k} \in \mathcal{K}$ with positive k_x, and are defined by $\phi(-\vec{k}) = -\phi(\vec{k})$ for the remaining wavenumbers. This constraint on phase choices ensures that $z(\vec{r})$ is in fact a real number.

To explain our definition of the spectral amplitude $Z(\vec{k})$, we first note that our numerical implementation of Equation 3.9, as well as the implementation of the IGOM, will involve discretization with N gridpoints in each horizontal direction, with isotropic gridpoint separation $\Delta x = \frac{L}{N}$. Then at the gridpoint $(x_m,\, y_n)$ we have for the term appearing in the exponential

$$\vec{k} \cdot (x_m,\, y_n)\frac{2\pi}{L} \;\; = \;\; \vec{k} \cdot (m\Delta x,\, n\Delta x)\frac{2\pi}{L} = \frac{2\pi}{N}\vec{k} \cdot (m,\, n) \tag{3.11}$$

This explains the appearance of the combination $\frac{2\pi}{N}\,\vec{k}$ in the following definition of $Z(\vec{k})$:

$$Z\left(\vec{k}\right) = aS(k) = a\frac{1}{k^b}e^{-\frac{c}{k}} \qquad with \qquad k = \left|\frac{2\pi}{N}\,\vec{k}\right|, \tag{3.12}$$

where a, b, and c are constants. The function $S(k)$ of positive real numbers k, a product of an exponential term and a negative power term, is known as the 1-D semi-empirical Pierson-Neumann density function. It goes to zero at both large and small k, having a maximum at wavenumber $k_{max} = c/b$.

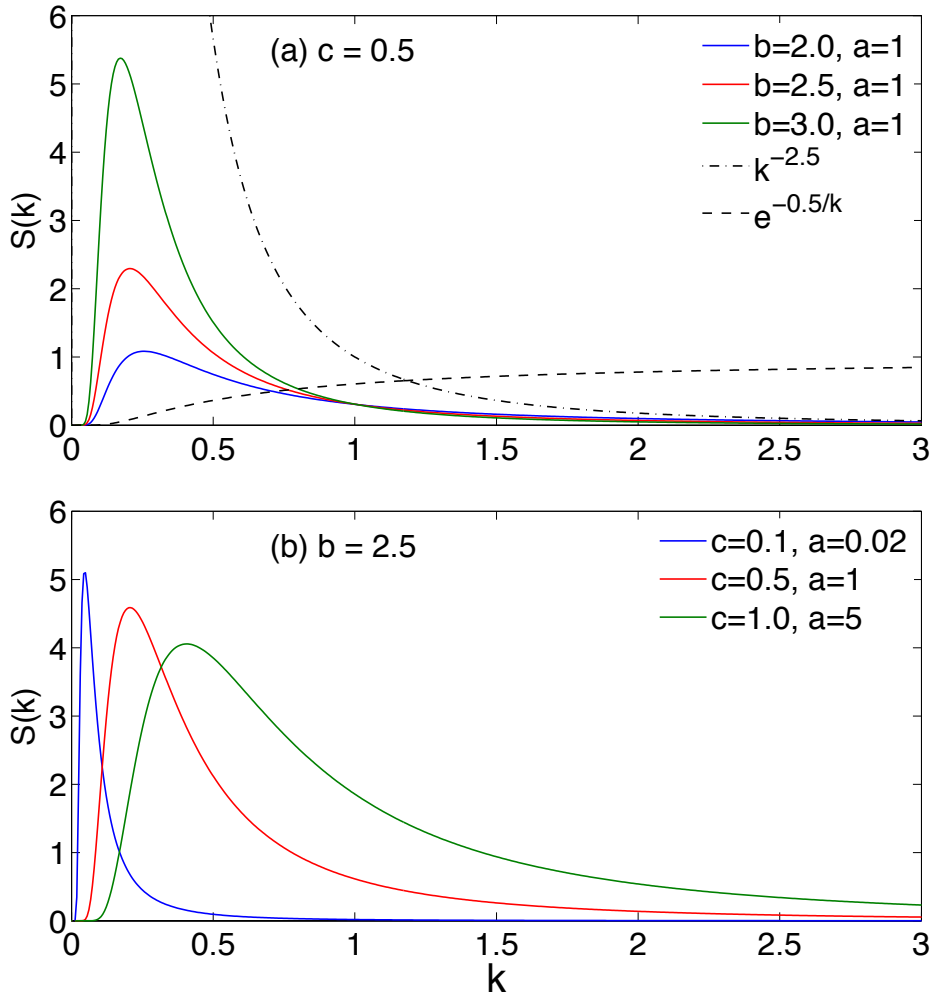

Figure 3.25: Solid curves show the effects of parameters b and c. The dashed curves in the upper panel show the two terms whose product gives the $b = 2.5$ solid curve in that panel.

Figure 3.25 graphically illustrates the effects of b and c variation on the shape of $S(k)$. The function $S(k)$ goes to zero at small k because the rate at which the exponential term goes to zero is so rapid that it dominates the rate at which any positive power of k^{-1} increases. For large k the exponential term, shown by the dashed curve in Figure 3.25, asymptotes to 1, so in the limit of large k the product

$S(k)$ goes to zero essentially like k^{-b} (shown by the dash-dot curve in Figure 3.25). (These features are what we above referred to as the essential shape-determining ones in the distribution used in Schwenger and Repasi [144].) The rate at which $S(k)$ goes to zero in turn controls the smoothness of the function $z(\vec{r})$, and $b \geq 2$ is more than sufficient for the existence of the first partial derivatives needed for our study. For fixed b, the parameter c has the effect of postponing the decay of $S(k)$ as can be seen in the lower panel of Figure 3.25. For the figure the constant a, which determines the overall amplitude of $z(\vec{r})$, has been chosen to make qualitative comparison easy, while in our numerical experiments the constant a is chosen in a manner explained next.

As mentioned above, the key parameter in the TF method is the variance σ^2 of slopes of the imagined tilted facets, and the amplitude parameter a in Equation 3.12 is chosen to adjust the variance in slopes in $z(\vec{k})$. The distributions of slopes s_x and s_y are found numerically to very nearly follow a Gaussian, with the same variance σ^2 in each direction. If we consider just the slope in one direction, we calculate from Equations 3.9 and 3.12 that

$$\begin{aligned} s_x &= \frac{\partial z}{\partial x} = \sum_{\vec{k}\in\mathcal{K}} \left(\frac{ik_x 2\pi}{L}\right) aS(\hat{k}) exp\left[i(\vec{k}\cdot\vec{r}\,\frac{2\,\pi}{L} + \phi(\vec{k}))\right], \\ &= \frac{a}{L}\sum_{\vec{k}\in\mathcal{K}} 2\pi i k_x S(\hat{k}) e^{i\phi(\vec{k})} e^{i(\vec{k}\cdot\vec{r}\,\frac{2\,\pi}{L})} \\ &\equiv \frac{a}{L}\sum_{\vec{k}\in\mathcal{K}} B(k) e^{i(\vec{k}\cdot\vec{r}\,\frac{2\,\pi}{L})} \end{aligned} \tag{3.13}$$

It is clear that s_x has zero mean, so the variance of s_x is just

$$
\begin{aligned}
var(s_x) &= \frac{1}{L^2}\int\int\left(\frac{a}{L}\sum_{\vec{k}\in\mathcal{K}} B(k)e^{i(\vec{k}\cdot\vec{r}\,\frac{2\pi}{L})}\right)^2 dxdy && (3.14)\\
&= \left(\frac{a}{L}\right)^2\sum_{\vec{k}\in\mathcal{K}}|B(k)|^2 && (3.15)\\
&\equiv \left(\frac{a}{L}\right)^2\mathcal{B}, && (3.16)
\end{aligned}
$$

where we have used Parseval's relation in Equality 3.15, and $\mathcal{B}$ does not involve L. An identical argument applies for the variance of s_y. So if we want to obtain a specified variance σ_0^2, we must take

$$a^2 = \frac{L^2\sigma_0^2}{2\mathcal{B}}. \tag{3.17}$$

(the factor of two in the denominator comes from the addition of two equal model variances). With this choice of a, we see an important feature of our definition of z, namely that

$$z\,(\vec{r}) = \frac{\sigma_0 L}{\sqrt{2\mathcal{B}}}\sum_{\vec{k}\in\mathcal{K}} S(\hat{k})exp\left[i(\vec{k}\cdot\vec{r}\,\frac{2\,\pi}{L}+\phi(\vec{k}))\right]. \tag{3.18}$$

As pointed out above, $\mathcal{B}$ does not depend on L, so as we change the size of the particle considered, the surface roughness amplitude scales exactly with L.

The TF method assumes that the slopes of the tilted facets follow a Gaussian distribution. We will demonstrate computationally the claim mentioned above that the slopes in our roughness model are approximately Gaussian. To sample the slopes, we first discretize the surface into triangular sub-elements. For a roughened surface given as in Equation 3.9, we use as vertices of the triangular elements the points $P_{i,j} = (x_i,\, y_j,\, z(x_i,\, y_i))$, where (i, j) runs over indices of nodes on a triangulated grid

on the smooth ($z = 0$) surface. The forms of this triangulation used for the sides and ends of the smooth hexagonal column are indicated in Figure 3.26. We then take advantage of the computational observation we mentioned above, namely that, for a wide range of parameters b and c, once a choice (a, b, c) has been made for $S(k)$, the sets of grid point values $D_x = \{(s_x)_{i,j}\}$ and $D_y = \{(s_y)_{i,j}\}$ with $(s_x)_{i,j} = \frac{\partial z}{\partial x}(x_i, y_j)$, $(s_y)_{i,j} = \frac{\partial z}{\partial x}(x_i, y_j)$, have very nearly Gaussian distributions with the same variance (examples are shown in Figure 3.28). With this observation, we can then use the parameter a to adjust the common variance to have any desired value.

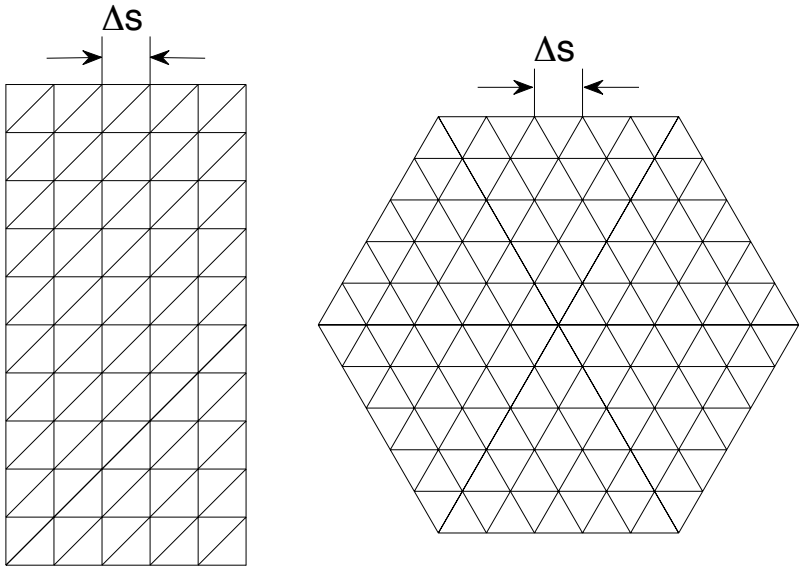

Figure 3.26: The triangulation of smooth sides (left) and ends (right) of the hexagonal column. Vertices of the triangles are the points referred to in the text as (x_i, y_j).

Figure 3.27 shows two images of a model surface (a) and (b) constructed with $\sigma^2 = 0.2$, together with three images (c) to (e) of ice crystal surfaces (after Figures 3, 1, 13 at pages 83, 84 and 90 of [40], respectively). As indicated in the figure, the image in Figure 3.27 (b) is a magnification of a region of (a), and provided for visual comparison with the photographic image in panel (e). The image in (e) is also a magnified image of part of a much larger particle (see [40]). The reason no specific length is indicated in panels (a) and (b) of the modeled surface because this length can differ according to the overall size of the model particle being constructed. A choice of a specific value L for this overall size then immediately determines, given the value of σ^2 chosen for the roughness, the actual size of the amplitude variations shown in panels (a) and hence (b).

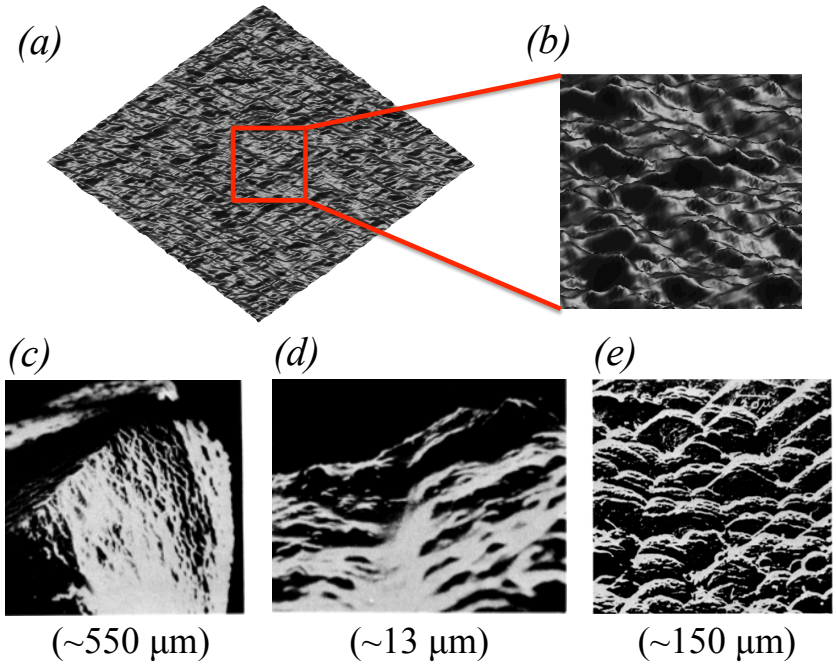

Figure 3.27: (a) A rough surface generated with $\sigma^2 = 0.2$; (b) a magnified view of a region in (a). (c)-(e) surface images of ice crystals (after Figures 3, 1, 13 at pages 83, 84 and 90 of [40], respectively). The lengths (approximately) in the horizontal direction of the images are given under the images.

We can see that the images of the ice crystals show a variety of complex structures of different scales, and it appears to be a truly daunting task to create a single model with a few simple scaling parameters that represent all ice crystals or aerosol particles. In fact, the focus in recent studies has been on the overall size and geometry of particles, with relatively little quantitative information being made available concerning roughness features like those shown in (c)-(e). Having said this, it is clear from the comparison of Figure 3.27 (b) and (e) that our numerical model has some plausibility as a representation of naturally occurring roughness.

The left panel of Figure 3.28 presents in a more quantitative way the roughness shown in Figure 3.27 (a). To understand the proper interpretation of the horizontal and vertical scales in the left panel of Figure 3.28, note that the total extents of the "X" and "Y" axes being expressed in non-dimensional form (size parameter of 100) mean that the model is being applied to a case in which the overall size of the particle is, in dimensional units, $100\lambda/\pi$. In terms of the definition that we give below, the particle has size parameter $x = 100$. In addition to the choice $\sigma^2 = 0.2$, the surface in the figure has $b = 2.5$ and $c = 0.5$, which will be the values we mainly use in our model of rough surfaces. (We will give the context for this choice in Section 3.3.3, where we demonstrate the dependence of scattering properties on values of b and c.) The scale on the colorbar in Figure 3.28 indicates that these choices of b, c, and σ^2 lead in our model to a maximum dimensional amplitude of roughness of about $1.5\lambda/\pi$: put differently, they lead to a maximum amplitude of the roughness that is about 1.5% of the overall size of the particle. Crude estimates based on visual inspection of the image in Figure 3.27 (e) and an image of the whole particle presented in [40] suggest that this value of roughness amplitude is not unreasonable. (An even closer match could be easily obtained by changing the value of σ^2 slightly, but such fine-tuning toward a particular case is not our intent here.) The right panels

of the figure show the distribution of the slopes along the x and y-directions as well as the Gaussian shape with $\sigma^2 = 0.2$, and we can see clearly that the slopes fit the Gaussian distribution very well.

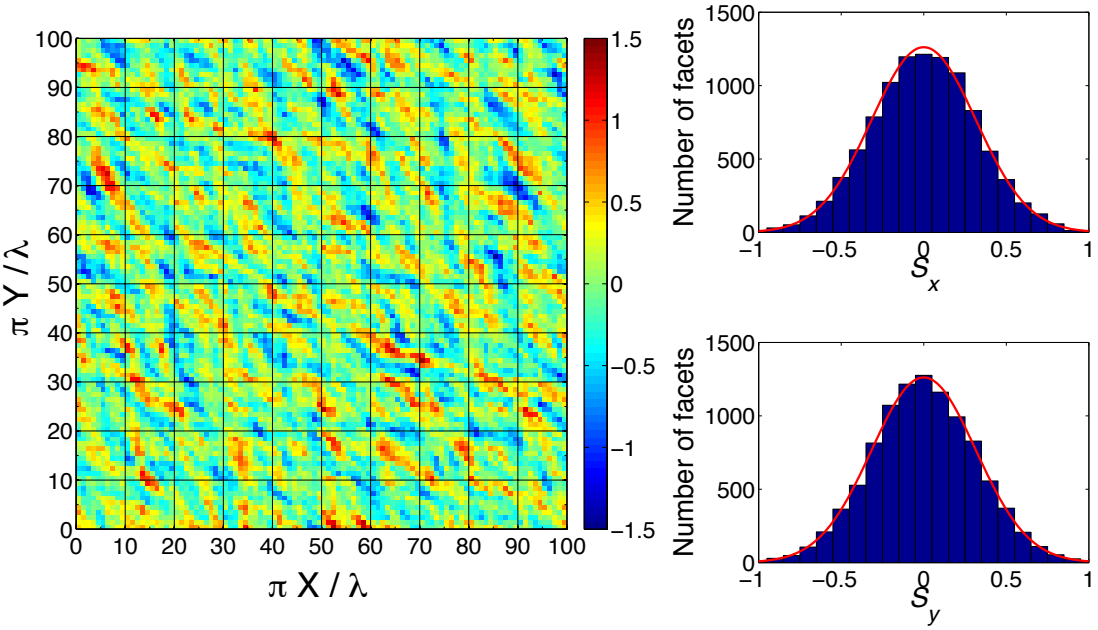

Figure 3.28: The non-dimensional perturbation $\pi z/\lambda$ of a roughened surface with non-dimensional size of 100×100 (left panel) and the distributions of the slopes in the x (upper right panel) and y (lower right panel) directions.

We turn now to the matter of handling the edges along sections whose planar structure is given by Equation 3.9 are joined. The roughening provided independently according to the equation on two adjacent faces will in general disconnect the faces along the edge that joined the previously smooth faces. To remove this problem, we consider not the surfaces themselves but the points $P_{i,j}$ of the mesh that is used in the corresponding discretization. Figure 3.29 shows an end-on view of the juncture

of two faces at some point along an edge different from a corner (i.e. from a three-way intersection of faces). The end mesh points A and A' from the discretized roughening of the side and top faces are each discarded and replaced by the point B on the midpoint of a line segment joining the positions of A and A' (AA'), i.e. the point whose position vector is the average of the position vector of A and A'. In the case of a corner, there are three edge points that are dropped and replaced by the point having the vector average of the position vectors of these dropped points. The result of such a construction, with all the mesh points joined by triangular faces, is shown in Figure 3.30. Illustrated in the figure are three hexagonal particles with aspect ratios of 0.2 (oblate plate), 1.0, and 5.0 (prolate column), all of them having surfaces with $\sigma^2 = 0.2$.

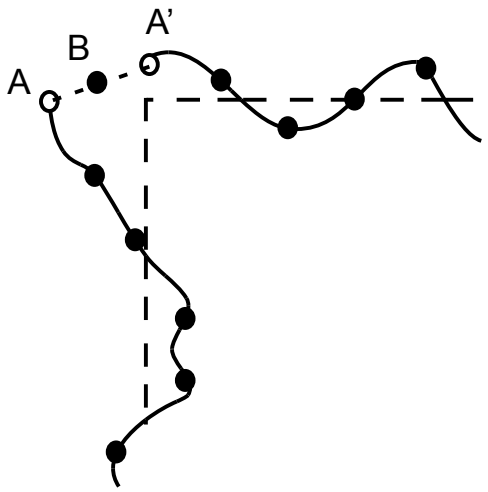

Figure 3.29: An edge-on view for the process of joining surface meshes at an edge. The straight long-dashed lines indicate positions of the un-roughened surfaces and the solid curves the position of the roughened surfaces which no longer meet. The filled circles indicate mesh points in the discretization of the roughened surfaces. The open circles represent mesh points A and A' that are discarded, each being replaced by the point B.

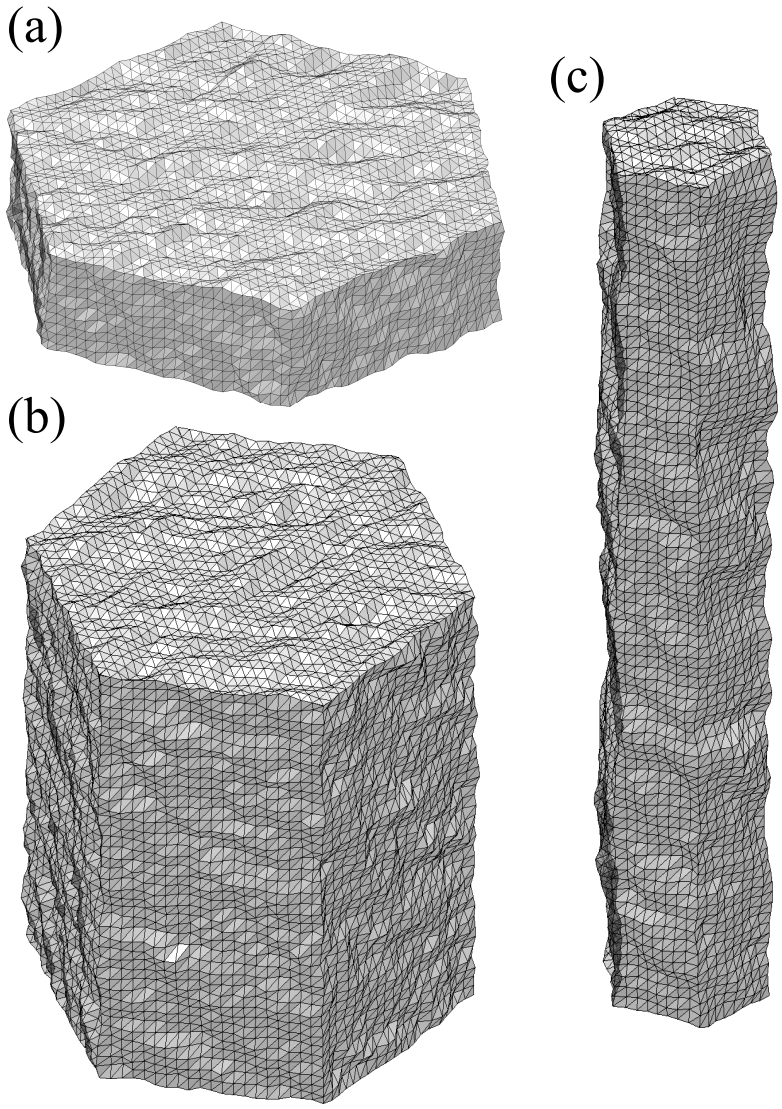

Figure 3.30: The roughened hexagonal columns with the aspect ratios of (a) 0.2, (b) 1.0, and (c) 5.0.

3.3.2 Roughness in the GOM

Even with the parallelized implementation and state-of-the-art supercomputing facilities, as particle sizes increase the PSTD eventually becomes too time-consuming to be practical and recourse must be made to another method based on geometric

optics. Taking the particle size parameter 100 as a threshold size for computational methods in our study, we use the PSTD for hexagonal columns with size parameters up to 100 and the IGOM for columns with larger size parameters.

The IGOM method, original developed by Yang and Liou [35], was systematically improved by Bi et al. [37], and has been tested and applied to various typical ice crystals [146]. The IGOM considers the light scattering by particles to have three independent components: 1) reflection and refraction; 2) diffraction; and, 3) edge effects. The contribution from the reflected and refracted rays is obtained by a ray-tracing technique based on geometric optics theories (i.e., Snell's law and Fresnel formulae). With the near field given by the ray-tracing technique, the scattered far field is calculated by mapping the near field to its radiation zone counterpart on the basis of the electromagnetic equivalence theorem [35]. Meanwhile, the Fraunhofer diffraction theory can be used to give the contribution from the diffraction by line integration over the closed polygon of the particle projections [141]. For each particle orientation, it is straightforward to evaluate the diffraction with the shadow boundary expressed as a polygon. In addition to the reflection, refraction, and diffraction, a nonzero edge effect [29, 46] caused by the penumbra region between the illuminated and non-illuminated areas of the particles also contributes to the extinction and absorption of light. A semi-empirical method is used to bridge the gap between the results given by the numerically exact PSTD method and the IGOM results [29, 46].

As mentioned above, the surface roughness is commonly treated using IGOM combined with an approximation to the ray-tracing at surfaces based on the TF treatment [141, 128]. We consider the implications of the approximation in more detail now. In a geometric optics calculation, the outcome of a reflection or refraction event at a point on a surface is determined by the orientation of the local surface element on which the point lies. For each such event, the TF method imagines that

the actual local surface element is replaced for that event alone with another ("tilted facet") that has an orientation randomly obtained from the Gaussian distribution given by Equation 3.6, and calculates the event outcome accordingly. No change is made to the actual particle surface, and the orientations chosen in two events occurring at the same point but at different times can (and in fact most probably will) be different. Thus, there is no single roughened particle that is constructed for the scattering calculations, but only an algorithm for computing surface interactions using geometric optics given the single parameter σ^2 that characterizes the Gaussian distribution. This presents an obvious difficulty if comparison is desired with scattering results obtained by a numerically exact method like the PSTD, which requires a geometrically specified particle.

The TF method has shown wide applications, but also drawbacks due to the nature of its ray-tracing procedure. Figure 3.31 illustrates an entirely plausible sequence of events that might occur when an incident beam encounters a roughened surface element that has no obvious counterpart in any calculation using the TF method. The figure shows a beam incident from the left, an actual roughened surface (indicated by solid curve), and the non-roughened surface (dashed line). In the TF method, the beam would not encounter the particle until it reaches O', and there it would interact with a tilted facet. But what is indicated in the figure instead is that the point O' is in the "shadow" of the surface-roughening prominence on which O sits. The interaction shown in the figure involves a reflection/refraction event at O, followed by a reflection/refraction event at point A, and another event of the same kind after re-entering the particle at point B. Nothing like this physically plausible sequence of events occurs in calculations based on the TF method.

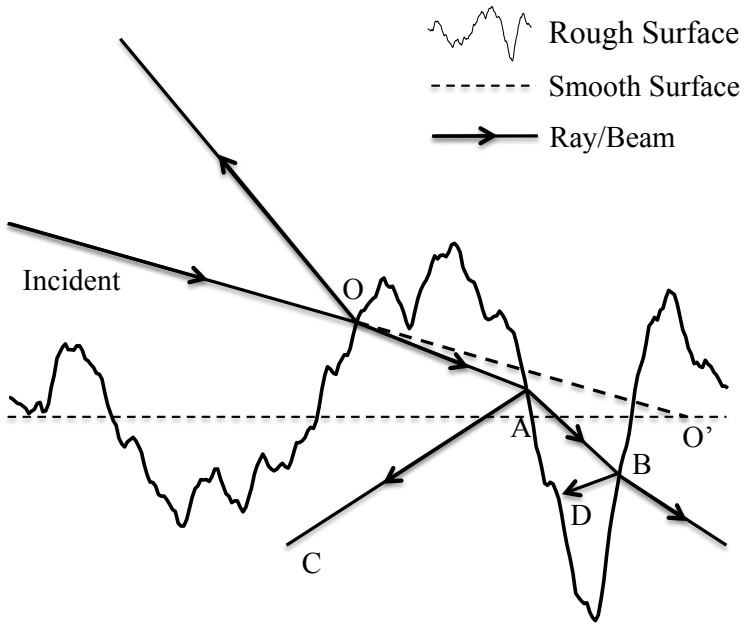

Figure 3.31: The geometry of the ray-tracing cases that cannot be considered by the TF approximation.

Yang et al. [47, 48] investigated the accuracy of the TF approximations in two dimensions by using ray-tracing with well-defined rough surfaces, and found that the simplified TF can only approximately account for the effects of surface roughness on particle single-scattering properties. However, both definition of the rough surface and ray-tracing algorithm in the three dimensions are much more challenging and complex. In the large size parameter part of our study, we will use IGOM but construct geometrically definite rough surfaces and carry out the "rigorous" ray-tracing algorithm on the rough surface. Thus, it will be able to extend the examination of the accuracy of the TF approach to the case of three dimensional simulations. In what follows, when we refer to the IGOM, we mean the version that involves rigorous ray-tracing with a geometrically defined roughened surface. We will refer to

the version of the IGOM that uses instead the tilted facet approximation simply as "TF."

In our version of the IGOM, a given specification of a particle's roughened surface is discretized into a number of triangular sub-elements (see Figure 3.30). Ray-tracing algorithms are applied to the geometry described with thousands of the sub-elements, and all the complex cases indicated in Figure 3.31 that cannot be calculated in the TF can be considered. The initial reflection and refraction for the incident beam occurs at the first encountered triangle. After the event, the internal and external beams continue to be traced among the triangular elements. Beams that remain internal are traced until their amplitude becomes weak enough that we regard it to be negligible ($< 10^{-6}$ of the incident amplitude). Outgoing beams that emerge from the particle with non-negligible amplitude are traced until (perhaps after encounter and reenter another part of the particle) they become truly free and contribute to the scattered field. Given the growth of the number of surface triangles as the particle size gets large, the ray-tracing calculation does become demanding in terms of CPU time, but the increases of CPU time required are from seconds to minutes, nothing like the much greater CPU-time (several hours to days) required by the PSTD method in the large particle regime.

3.3.3 Effects of the surface roughness

Figure 3.32 compares the phase functions of the smooth and roughened hexagonal columns with fixed (left three columns) or random orientations (right column) given by the PSTD. The hexagonal columns have size parameters of 10 (upper panels), 20 (middle panels), and 50 (lower panels), and the value of σ^2 for the rough surface is 0.1. The angles between the incident direction and the axis of the fixed oriented hexagonal column are 0^o, 45^o, and 90^o. We verified that the spatial resolution in

the PSTD simulations are sufficiently fine to define the small-scale structures of the rough surfaces by checking that the same results are obtained when finer spatial resolutions are used. At size parameter 10, the phase functions of the smooth and roughened particles show substantial differences at scattering angles from 80^o to 140^o when the incident direction is perpendicular to the hexagonal surfaces, and approximately the same results are obtained for the other two incident directions. As the particle size increases, the phase functions of smooth particles with fixed orientations show more oscillations, and become obviously different from those of roughened particles, especially $x = 50$. When the results are averaged over hexagonal column orientations, the phase functions of the smooth and rough particles coincide at size parameter 10, and show only slight difference at size parameter 20. This indicates that the differences of the phase functions obtained with fixed orientations cancel out. As the size parameter of the hexagonal column increases to 50, weak scattering peaks at scattering angles 22^o and 46^o appear in the phase function of the smooth hexagonal columns. However the particles with surface roughness have a smooth phase function, one obviously different from that of the smooth particles. Figure 3.32 indicates that, for the form of roughness and degree we have chosen, the influence of roughness on the phase functions of randomly oriented non-spherical particles becomes noticeable as the size approaches approximately 20.

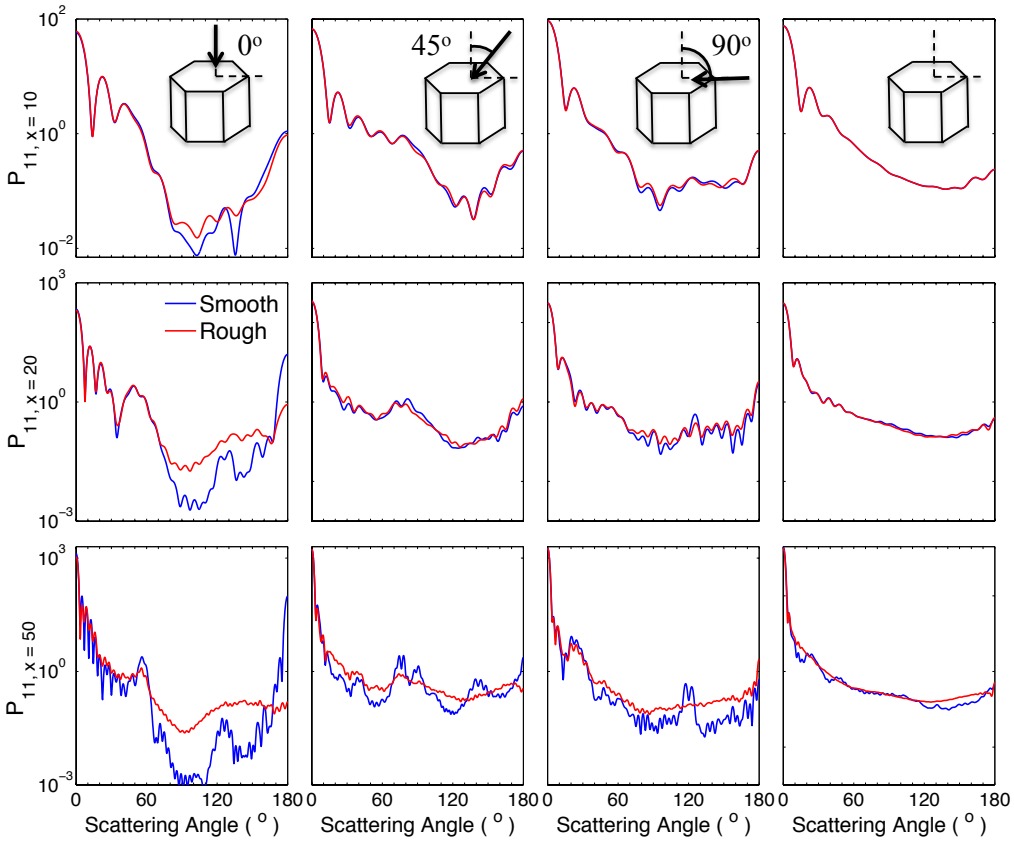

Figure 3.32: The phase functions of fixed and randomly oriented hexagonal columns with different sizes given by the PSTD. The hexagonal columns have size parameters of 10 (upper panels), 20 (middle panels), and 50 (lower panels).

Figure 3.33 illustrates the non-zero phase matrix elements of roughened hexagonal columns with a size parameter of 100. The asymmetry factors g are also listed in the figure. The calculations are performed using the IGOM, for two different surface roughness parameters $\sigma^2 = 0.05$ and $\sigma^2 = 0.2$. As mentioned above, in the IGOM-based calculation the roughened surfaces are discretized into a mesh formed by small triangular sub-elements, and the size of these triangular elements becomes the spatial resolution parameter of the simulation. We define the computational size parameter

of the mesh triangle as

$$S = 2\pi\Delta s/\lambda,$$

where Δs is the minimum length of the triangular sides (see Figure 3.26). Figure 3.33 shows results with choices $S = 5$ and $S = 2$: for the entire surface of the hexagonal column, the first choice corresponds to a total number of triangular subelements equal to $14,400$, and the second to a total of $90,000$ (different surface realizations are used to reach the same σ^2). The figure also shows comparisons between the IGOM results and those obtained with the TF approximations. As illustrated in the figure, for rough surfaces with the same value of σ^2, the IGOM gives approximately the same phase matrix elements for the two triangular sizes, which means that a grid size parameter of $S = 5$, i.e. $14,400$ total sub-elements, is sufficient for the IGOM simulation to track the effect of surface roughness. In addition, the roughened particles with different surface configurations but the same σ^2 apparently have the same scattering properties. In Figure 3.36, the three curves in the left two panels are overlapping each other. However, only the blue and red curves in the right two panels are coincide with each other, and both are separated from the green ones. When $\sigma^2 = 0.05$, which corresponds to what we consider a moderately rough surface, the TF method that gives almost the same results for phase function as the IGOM also shows only small differences for the other five polarization elements. However, when the σ^2 value becomes as large as 0.2, the differences between the IGOM and TF simulations become noticeable: the TF method overestimates the phase function at scattering angles around 50^o but underestimates the backward scattering. Differences for the other phase matrix elements are also noticeable.

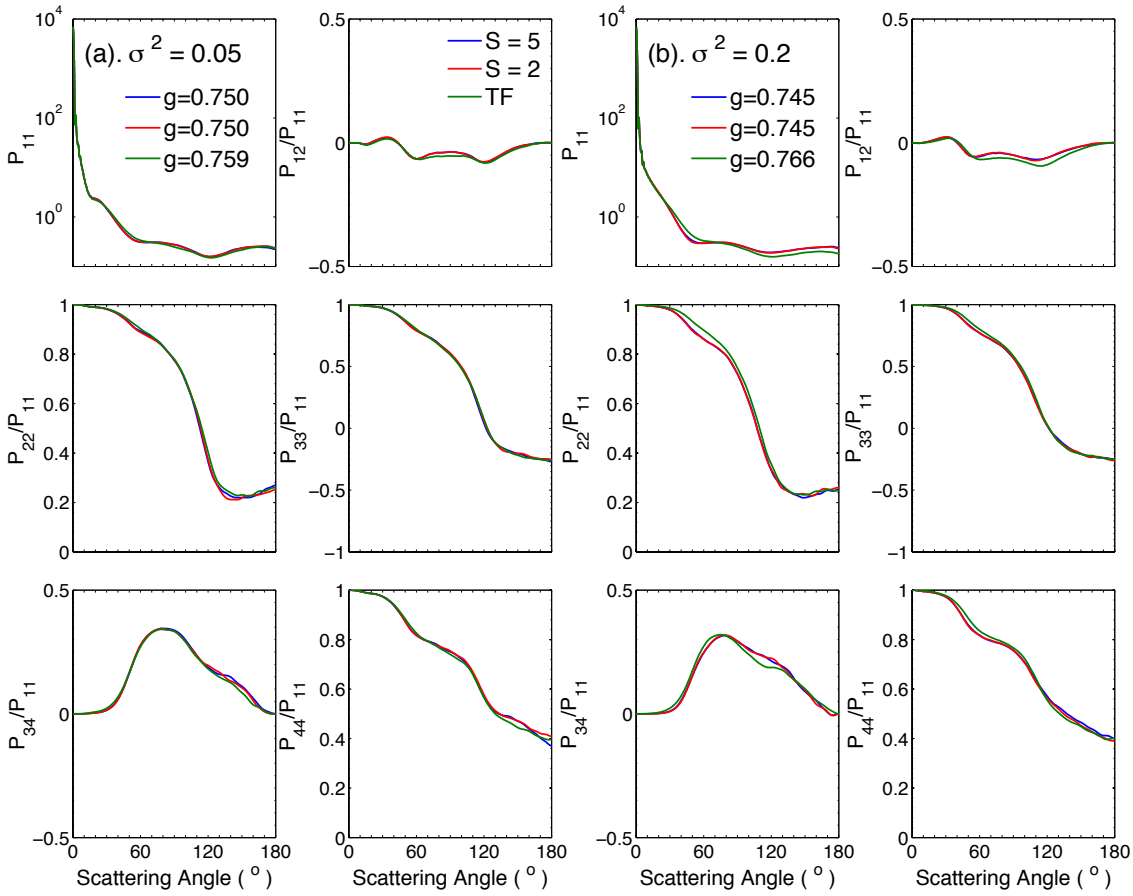

Figure 3.33: The non-zero phase matrix elements of roughened hexagonal columns given by the TF and IGOM methods with (a) $\sigma^2 = 0.05$ (two panels in the left) and (b) $\sigma^2 = 0.2$ (two panels in the right). Two sub-elements sizes for the triangles are used: $S = 5$ and $S = 2$. The hexagonal columns have a size parameter of 100.

As we have explained in Section 2, with the flexibility of adjusting the amplitude parameter a as needed, for a fixed value of σ^2 (all that the TF method uses) we may regard parameters b and c as being independent. But, as we will show shortly, different choices of b and c certainly appear to determine qualitatively different surface roughness. To illustrate the influence of the two parameters on the surface structure and the optical properties of the roughened particles, perturbations of the rough sur-

faces with the same σ^2 but different spectral densities are illustrated in Figure 3.34. Although the surfaces in the figure visually present substantially different patterns and structures, the slopes of all these surfaces follow the same Gaussian distribution very well, which will not be shown (their distributions appear much like those in the right panels of Figure 3.28).

The left panels of Figure 3.34 show effects of b variation: from the top to bottom the values of b are 2.0, 2.5 and 3.0, all with $c = 0.5$. The right panels are for different values of c (0.1, 0.5 and 1.0), again from the top to bottom and now with same $b = 2.5$. (For this and the following discussion it is useful to look back at Figure 3.25.) Figure 3.34 indicates that, for the different values of b we used, the roughness features have comparable overall magnitudes, all being approximately 1.5 in non-dimensional units of size (see the colorbar in the figure). However, as b increases, the rough surface becomes more dominated by the low wavenumber terms, i.e. perturbations with longer wavelengths. Much more significant differences are seen for surfaces with different values of c. At $c = 0.1$, the surface shows significant overall variation with perturbations between the high and the low areas becoming over 8 in non-dimensional units, whereas little in the way of differences in small-scale structure are observed. However, as c increases to 1.0, the surface becomes totally different, with the entire surface being made up of disordered small-scale variations with very small perturbation amplitude (the magnitudes are about 20% of the ones with $c = 0.1$). This effect, a change in the value of c bringing out the prominence of small scale features, can be easily understood by considering the lower panel of Figure 3.25.

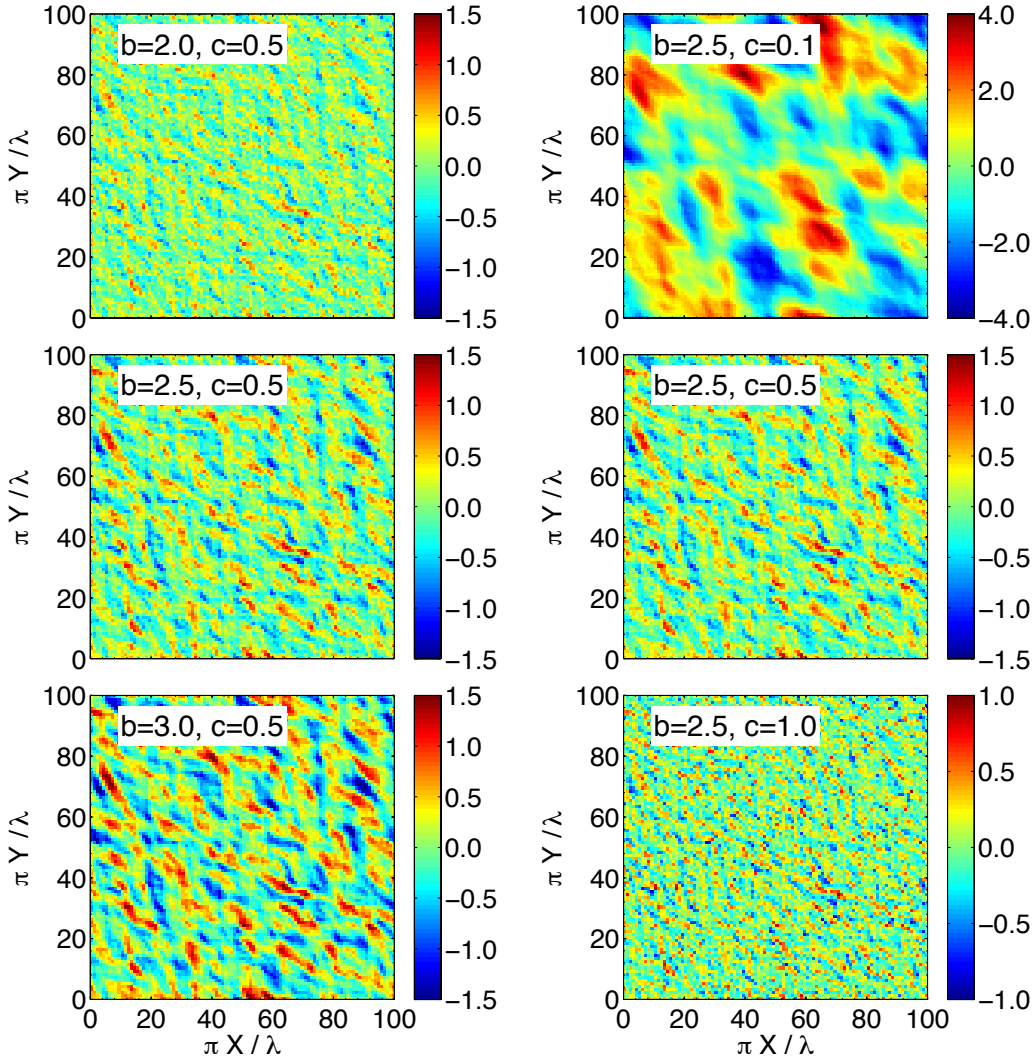

Figure 3.34: Same as the left panel of Figure 3.28 but for surfaces with different spectral density parameters.

The non-zero phase matrix elements of the hexagonal columns with roughened surfaces as shown in Figure 3.34 are given in Figure 3.35. All the roughened columns have σ^2 of 0.2, whereas the left panels are for surfaces with different b, and the right ones are for different c. For both cases, the phase functions given by the hexagonal columns with the same σ^2 but different types of rough surfaces are almost the same,

and there are only small differences for the other non-zero elements (P_{22}, P_{34}, and P_{44}) in the backward directions. This indicates that, at least according to IGOM, once the overall distribution of the slopes is determined (through σ^2), the detailed rough structure does not significantly affect the scattering properties of the particles.

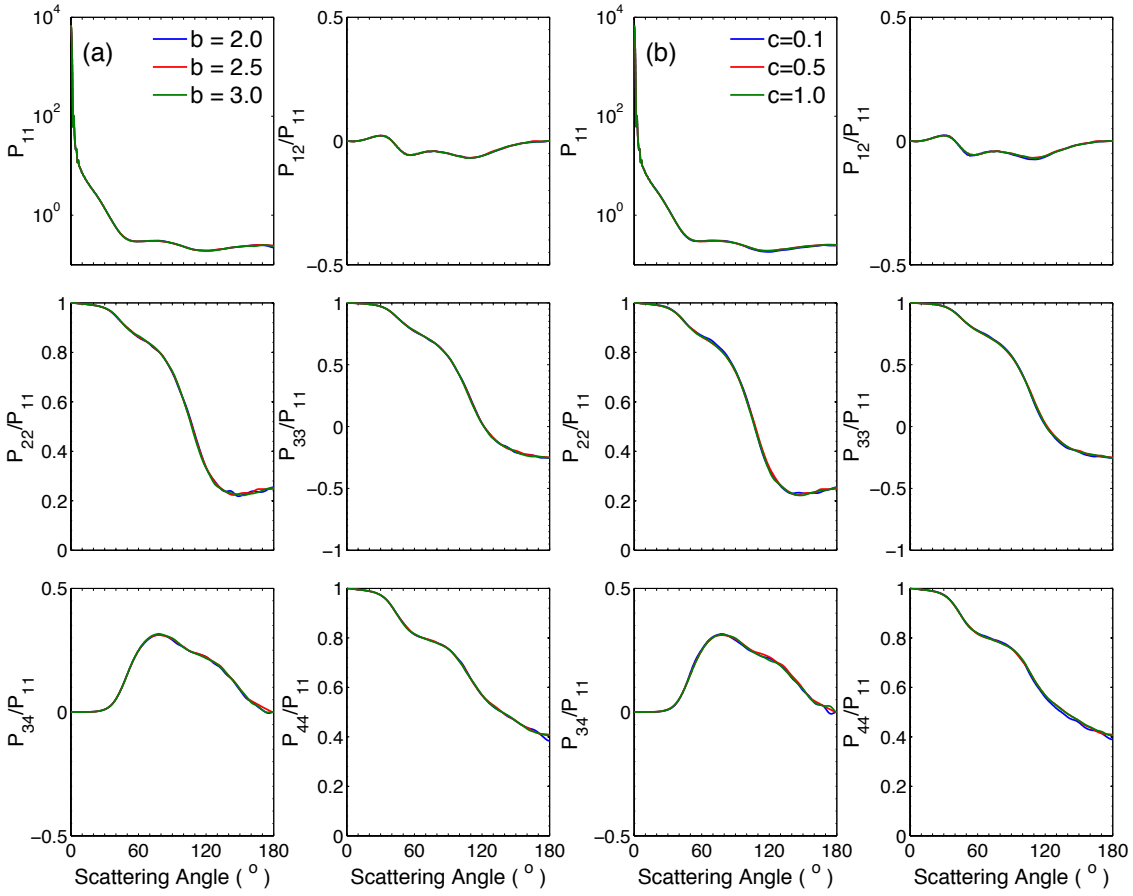

Figure 3.35: The non-zero phase matrix elements of roughened hexagonal columns with a size parameter of 100 given by the IGOM. The rough surfaces with different spectral density parameters but the same value of σ^2 are used. The left and right panels are for (a) different values of b and (b) different values of c in Equation 3.12, respectively.

Figure 3.36 illustrates the phase matrix elements of randomly oriented hexagonal particles with different aspect ratios given by the IGOM, and the asymmetry factors for all cases are also shown in the parentheses of the top panels. The geometries of the particles were given in Figure 3.30. The figure shows the results of particles with different surface structures with $\sigma^2 = 0.05$, and $\sigma^2 = 0.2$. The hexagonal particle with aspect ratio of 1.0 has a size parameter of 100, and the volume of the three hexagonal column is kept the same. The roughened particles all give very smooth phase functions, and the values of the P_{12}/P_{11} for the roughened particles become close to zero. The rough surfaces also smooth out the peaks and oscillations in the other phase matrix elements of the smooth particles, and only slight differences for the results given by the particles with weakly and moderately roughened surfaces are obtained. The hexagonal particles with aspect ratio 1 have the smallest asymmetry factors, and both the columns and plates has lager values. We also notice that the asymmetry factors becomes smaller as the surface becomes rougher, i.e. larger values of σ^2 for this study. These features for the variation of the asymmetry factors have also been reported by previous studies [47, 34].

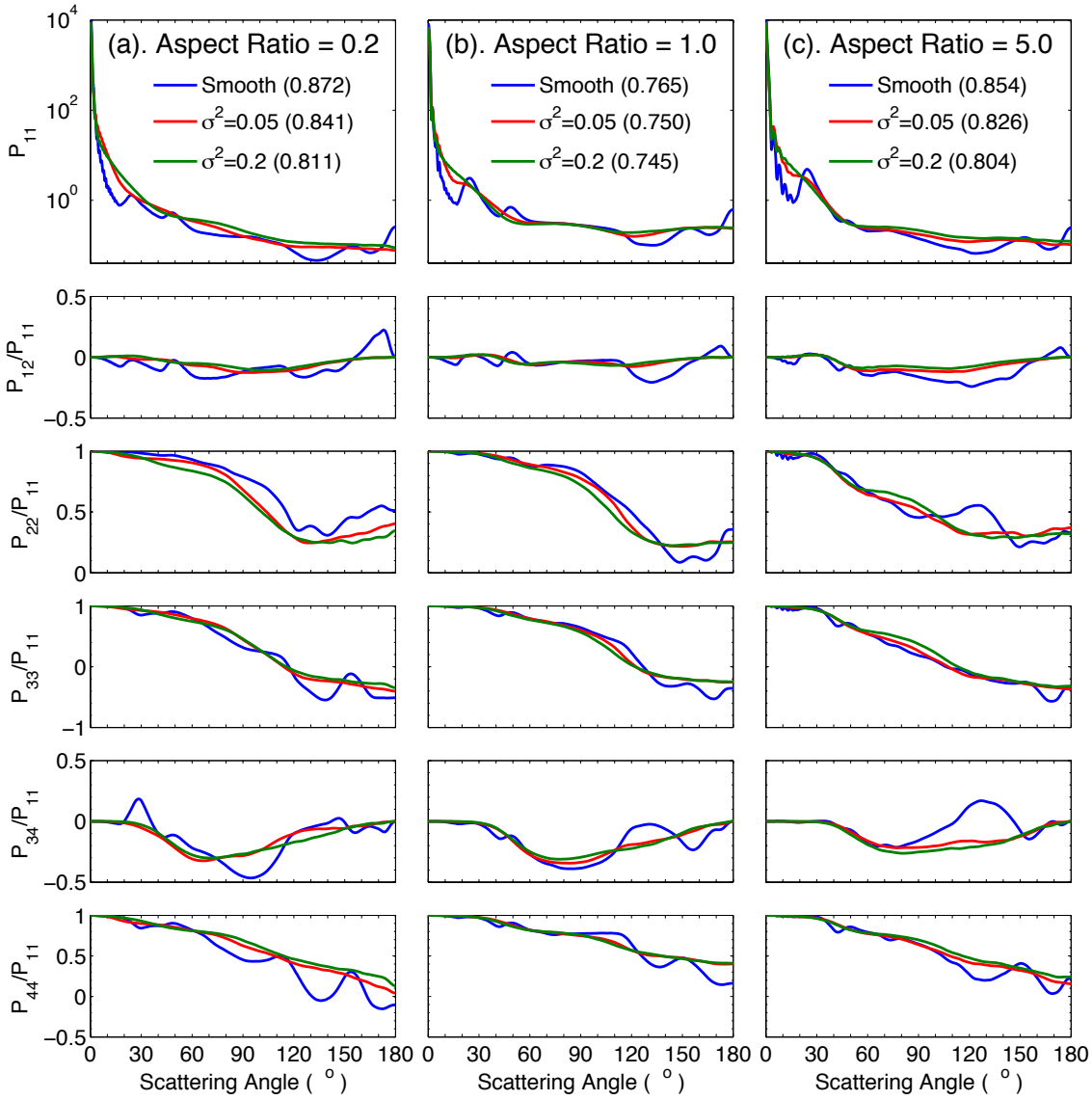

Figure 3.36: The non-zero phase matrix elements given by the IGOM for randomly oriented hexagonal particles with different aspect ratios and surface roughness. The aspect ratios of the three hexagonal particle are: (a) 0.2 (left column); (b) 1.0 (middle column); and (c) 5.0 (right column). The size parameter of the hexagonal particle with aspect ratio of 1 is 100, and the volume of the three particles are kept the same.

Figure 3.37 compares the non-zero phase matrix elements of the smooth (left column) and roughened hexagonal columns given by the PSTD and the two geometric

optics methods, TF and IGOM. The relative errors of phase functions given by the IGOM and TF compared with the PSTD results are also illustrated in the figure. The hexagonal columns have size parameters of 100, and the values of σ^2 for the roughened particles are 0.02 (middle column) and 0.1 (right column). The strong scattering peaks at 22^o and 46^o are clearly shown in the phase functions of the smooth particle in both the PSTD and IGOM results. The other non-zero phase matrix elements given by the PSTD show slight oscillations that occur because, in the PSTD method the phase interference of the electromagnetic waves is rigorously considered. The IGOM results are much smoother and have almost the same overall variation patterns as those given by the PSTD. With moderately roughened surfaces, $\sigma^2 = 0.02$, the backward scattering of the phase function as well as the region of what was a 46^o peak in the smooth case become featureless; whereas the peak at scattering angle 22^o is only weakened but still obtained by both the PSTD and IGOM. Moreover, the oscillations appearing in the polarization properties of the smooth particles given by the PSTD are no longer obtained, and excellent agreement between the PSTD and IGOM results are achieved. When the surface becomes severely rough ($\sigma^2 = 0.1$), the phase function peaks disappear and all three methods provide very smooth phase matrix elements. At the three different surfaces: smooth, moderately rough, and severely rough, results with both the TF and the IGOM agree very well with those from the PSTD.

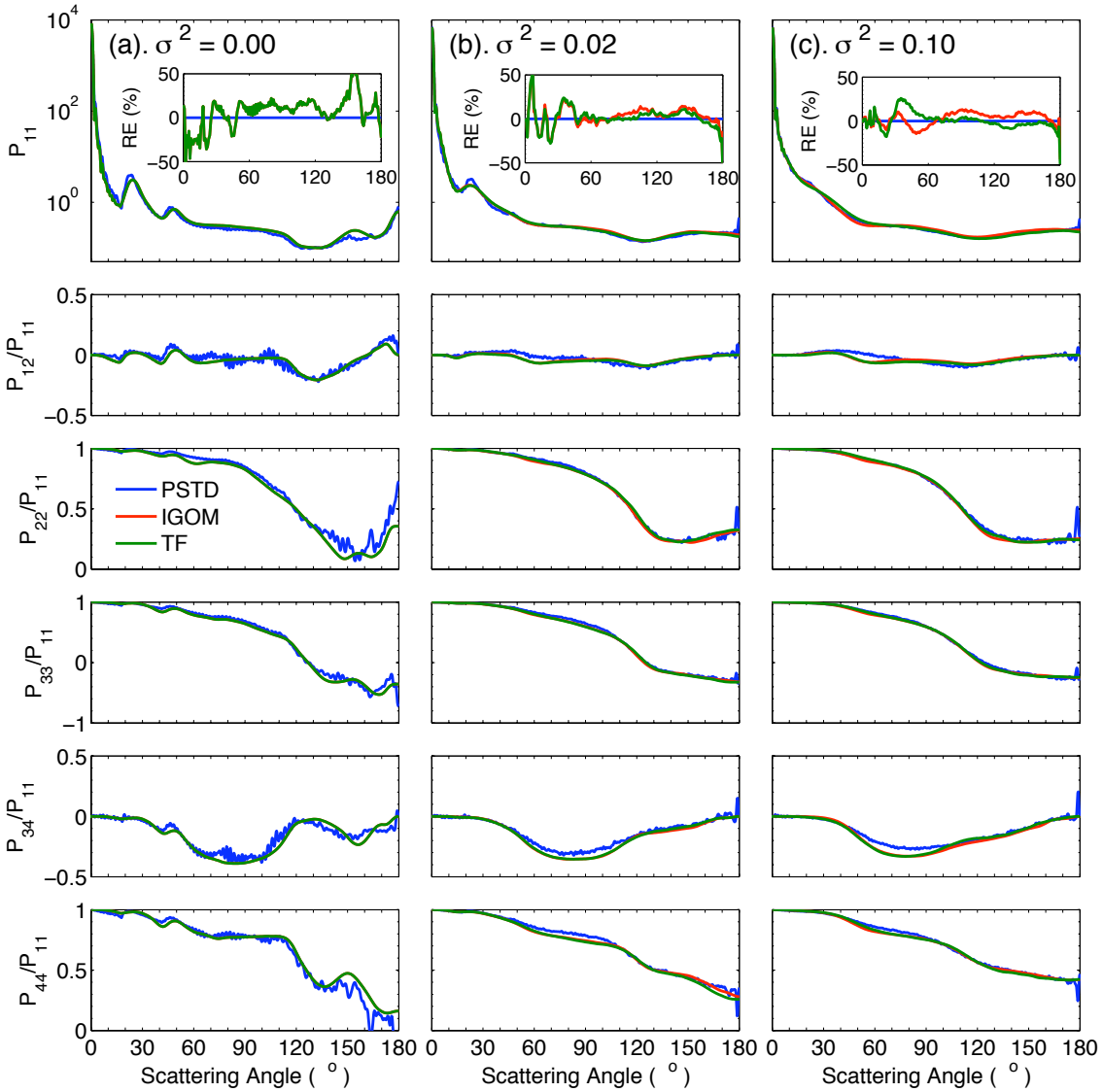

Figure 3.37: The non-zero phase matrix elements given by the TF, IGOM and PSTD for randomly oriented hexagonal columns with surfaces of different degrees. The hexagonal columns have a size parameter of 100, and σ^2 of the rough surfaces are: (a) 0 (left column); (b) 0.02 (middle column); and (c) 0.1 (right column) .

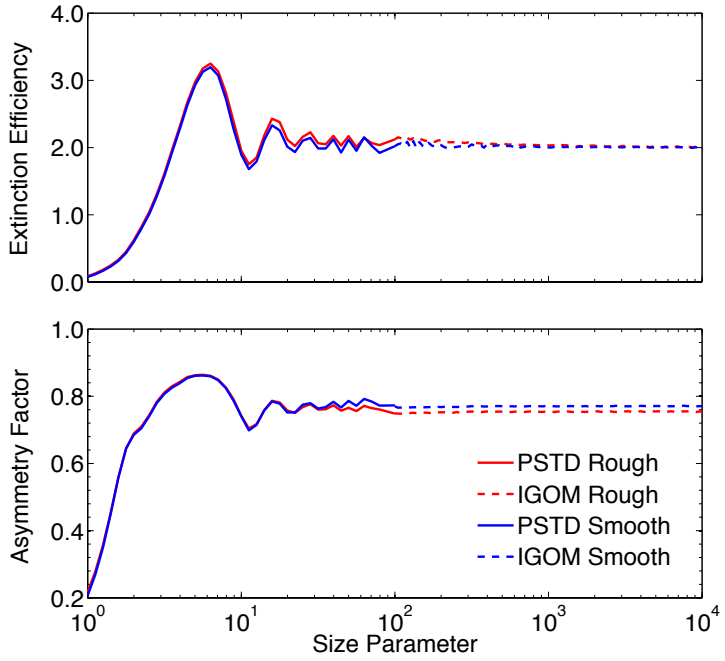

Figure 3.38: The Q_{ext} and g of randomly oriented hexagonal columns with size parameter ranging from 1 to 10,000. The σ^2 of the roughened hexagonal column is 0.1.

Two integral scattering properties, the extinction efficiencies and asymmetry factors, of the smooth and roughened hexagonal columns as functions of the size parameter are shown in Figure 3.38. In the roughened hexagonal columns $\sigma^2 = 0.1$. A combination of the PSTD and IGOM are used to cover the size parameters from 1 to 10,000: with the edge effects being included in the IGOM, the extinction efficiencies given by the PSTD merge smoothly with the corresponding IGOM efficiencies. The extinction efficiencies and asymmetry factors of the smooth and roughened hexagonal columns with size parameters less than 20 are almost the same, but the extinction efficiencies show slight differences as the size parameter becomes larger. The asymmetry factors of the smooth and roughened particles differ until the size parameter reaches approximately 40. For particles with size parameters larger than 100, the

extinction efficiencies of both the smooth and roughened hexagonal columns converge at 2. However, the roughened particles have smaller asymmetry factors (values approximately 0.75) than the smooth ones (values approximately 0.77). Figure 3.32 and Figure 3.38 indicate that the surface roughness should be fully considered for particles with size parameters approximately 20 and larger for the surface defined here with ($\sigma^2 = 0.1$).

3.3.4 Conclusion

This section investigated the effect of surface roughness on the scattering properties of atmospheric particles with size parameters ranging from the Rayleigh to the geometric-optics regimes. A superposition of simple waves with prescribed spectral structure that involves parametric descriptions of roughness was used to represent the roughened surface of ice crystals, and a combination of the numerically exact PSTD method and the IGOM were used to calculate the light scattering properties of both smooth and roughened hexagonal columns over the wide size range.

We find using our idealized model that the influence of a given degree of roughness (σ^2) on the single-scattering properties of non-spherical particles becomes noticeable when the size parameters of the particles exceed a critical value. For our model with $\sigma^2 = 0.1$, this critical size parameter is 20. The scattering properties (both the phase matrix elements and integral scattering properties) for both smooth and roughened particles given by the IGOM agree very well with the PSTD results for hexagonal columns with size parameters of 100. We found that for IGOM, the detailed surface structure in our model is relatively unimportant in determining the optical scattering properties of particles once the degree of roughness, which we take to be the variance σ^2 of surface slopes, is determined. The PSTD and IGOM results are used to examine the validity of those given by the TF method. Considering just

the comparison between TF and IGOM results, the two methods agreed quite well for mild degrees of roughening. But as the degree of roughness increases, details of the phase matrix element results obtained by the two geometric optics methods begin to differ from each other, suggesting weakness in the TF method at large roughness amplitude. This result is essentially the same as that for 2-D case studied in [47].

These results have been obtained using a highly idealized model of surface roughness, and must be considered with that fact in mind. However idealized the model may appear in comparison with any one particular instance of a rough particle, it does seem to show at least qualitative similarity to some reported images. We have made no systematic attempt to determine the effects of changes in the value of the σ^2; this is a definite possible use of the model, but we are not aware of observational data currently available that could help suggest the useful variations to consider. Furthermore, the approach to surface roughening we have described, like the IGOM and PSTD methods that we used in the investigation of the associated scattering properties, has a great deal of flexibility in terms of basic particle geometry to which it can be applied. We considered here only hexagonal columns because variation in overall particle geometry was not our focus. But exactly the same roughening model could be applied in the case of particles of all sorts with flat faces. Furthermore, it is easy to see that extension to, for example, spherical particles could be easily made by replacing planar harmonics with spherical harmonics.

3.4 Summary

This section investigated the effects of particle complexities on the light scattering properties of atmospheric particles, and discussed three independent parts: irregularity, inhomogeneity, and roughness. By either introducing new models to represent the realistic atmospheric particles (i.e. fractal model for dust particles, and irregular

roughness model) or testing the accuracy of the widely-used approximations (i.e. the EMA, and TF), we try to conclude more accurate and reliable scattering properties of the atmospheric particles. Our numerical results indicate the importance of particle complexities on the scattering properties and the limitation of the current approximations, and, with the improvement of the scattering model and supercomputer facility, all those aspects should be fully included in the light scattering simulations as well as the further applications.

However, considering the irregularity and diversity of the atmospheric particles, none of those numerical models are supposed to be general and realistic enough for all aerosol particles or ice crystals, and the fundamental motivation of these investigations is to capture the important effects of those complexity on the scattering properties, which are important for the radiative transfer and remote sensing applications. Besides the investigation on the scattering model, significant researches are still needed to build more realistic particle models, e.g. size, shape, and components, which can better represents the atmospheric particles.

4. SUMMARY AND CONCLUSION

This dissertation investigated a new parallelized PSTD implementation for simulating the single-scattering properties of particles with arbitrary shapes and components. A scheme of spectral filter that is introduced to eliminate the Gibbs phenomenon significantly enhances the applicability of the PSTD. To demonstrate the applicability, efficiency, and accuracy of the PSTD, comparisons are carried out for both spherical and non-spherical particles with relatively large size parameters and several refractive indices. The resultant PSTD simulations show close agreement with both the rigorous Lorenz-Mie solutions and the highly reliable T-matrix results. The PSTD is shown to be applicable to spheres with size parameters up to 200 in conjunction with moderate refractive indices, and size parameters up to 100 for randomly oriented nonspherical particles. The performance of the PSTD on inhomogeneous particles is also validated. On the basis of results shown here, we believe that the PSTD method shows real promise for pushing the boundary of what is feasible in the wide regime of particle sizes, refractive indices and complex geometries, and broad range of applicability for atmospheric particles, i.e. ice crystal and aerosol particles.

Furthermore, a systematic comparison between the PSTD and DDA that share similar areas of applicability was carried out by requiring the same prescribed accuracy criteria on the same multi-processor hardware, and the computational time was used as the key parameter to evaluate and compare the two methods for both spheres and spheroids. The DDA was more economical for numerical simulations of spheres with small refractive indices and small size parameters; whereas, the PSTD was more economical for large x and m. The critical size parameter, above which

the PSTD outperformed the DDA, decreased from 80 to 30 as the refractive index increased from 1.2 to 1.4. The PSTD was more CPU-efficient and applicable to a wider range of x when the refractive index was larger than 1.4. Similar conclusions were obtained for the spheroids. Furthermore, the overall accuracy of the asymmetry factor, backscatter, and linear polarization given by the PSTD and DDA were in agreement

With the enhancement on the light scattering simulations provided by the PSTD, the effects of atmospheric particle complexities on the light scattering properties are investigated. Three topics corresponding to the irregular geometry, inhomogeneous components and surface roughness are considered:

(1). We proposed the fractal model to model the single-scattering properties of various mineral dust aerosols at two wavelengths, and the highly irregular concave geometry shows significantly applicability and reliability to reproduce phase matrix elements from the laboratory measurements;

(2). With respect to the inhomogeneity of atmospheric particles, we found that the mixing state should be fully considered to simulate their scattering properties, and the effective medium approximations can be used only when the materials are uniformly mixed;

(3). An irregular rough model that can be considered in both PSTD and IGOM algorithms are used to cover the roughened particle with size range extending from the Rayleigh to the geometric optics regimes is developed, and the effects of those small-scale surface roughness on the scattering properties of atmospheric particles are systematically investigated.

In conclusion, to consider the scattering properties of realistic atmospheric particles, their complexities should be fully considered, and extreme caution should be exercised if approximations are performed.

By developing numerical models on both light scattering algorithm and representation of realistic particles, this doctoral study represents an effort to improve our understanding on the single scattering properties of the atmospheric particles and to provide more accurate optical properties for applications related to the radiative transfer and remote sensing. The investigation and improvement on the PSTD method substantially enhanced the capability of numerically exact methods for the single-scattering simulations, and, with the wide range of applicability provided by the PSTD, this dissertation accounts the effects of the complexities, e.g. irregularity, inhomogeneity and surface roughness, of the ice crystal and aerosol particles more accurately. In the perspective of applications, the more accurate simulations of the single-scattering properties will serve as the essential interpretation for the in-situ or laboratory measurements, satellite retrieval algorithm, and provide fundamental parameters for the radiative and climate studies.

REFERENCES

[1] H. C. van de Hulst, *Light scattering by small particles* (Dover, New York, NY, 1981).

[2] C. F. Bohren and D. R. Huffman, *Absorption and scattering of light by small particles* (Wiley, New York, NY, 1983).

[3] M. I. Mishchenko, J. W. Hovenier, and L. D. Travis, *Light scattering by nonspherical particles: theory, measurement, and application* (Academic Press, San Diego, CA, 2000).

[4] M. I. Mishchenko, L. D. Travis, and A. A. Lacis, *Scattering, absorption, and emission of light by small particles* (Cambridge University Press, New York, NY, 2002).

[5] F. M. Kahnert, "Numerical methods in electromagnetic scattering theory," J. Quant. Spectrosc. Radiat. Transfer **79**, 775–824 (2003).

[6] M. Kahnert, "Electromagnetic scattering by nonspherical particles: Recent advances," J. Quant. Spectrosc. Radiat. Transfer **111**, 1788–1790 (2010).

[7] L. Lorenz, "Lysbevegelser i og uden for en af plane lysbolger belyst kugle," Naturvidenskab. Math. Sic. **V1**, 2–62 (1890).

[8] G. Mie, "Beitrage zur optik truber medien, speziell kolloidaler metallosungen," Ann. d. Phys. **25**, 337–445 (1908).

[9] P. Debye, "Der lichtdruck auf kugeln von beliebigem material," Ann. Phys. **335**, 57–136 (1909).

[10] A. L. Aden and M. Kerker, "Scattering of electromagnetic waves from two concentric spheres," J. Appl. Phys. **22**, 1242–1246 (1951).

[11] O. B. Toon and T. P. Ackerman, "Algorithms for the calculation of scattering by stratified spheres," Appl. Opt. **20**, 3657–3660 (1981).

[12] Y. L. Xu, "Electromagnetic scattering by an aggregate of spheres," Appl. Opt. **34**, 4573–4588 (1995).

[13] Y. L. Xu and R. T. Wang, "Electromagnetic scattering by an aggregate of spheres: theoretical and experimental study of the amplitude scattering matrix," Phys. Rev. E **58**, 3931–3948 (1998).

[14] P. C. Waterman, "Matrix formulation of electromagnetic scattering," Proc. IEEE **53**, 805–812 (1965).

[15] P. C. Waterman, "Symmetry, unitarity, and geometry in electromagnetic scattering," Phys. Rev. D **3**, 825–839 (1971).

[16] M. I. Mishchenko, L. D. Travis, and D. W. Mackowski, "T-matrix computations of light scattering by nonspherical particles: A review," J. Quant. Spectrosc. Radiat. Transfer **55**, 535–575 (1996).

[17] M. I. Mishchenko and L. D. Travis, "Capabilities and limitations of a current fortran implementation of the T-matrix method for randomly oriented, rotationally symmetric scatterers," J. Quant. Spectrosc. Radiat. Transfer **60**, 309–324 (1998).

[18] B. R. Johnson, "Invariant imbedding T-matrix approach to electromagnetic scattering," Appl. Opt. **27**, 4861–4873 (1988).

[19] L. Bi, P. Yang, G. W. Kattawar, and M. I. Mishchenko, "Efficient implementation of the invariant imbedding T-matrix method and the separation of variables method applied to large nonspherical inhomogeneous particles," J. Quant. Spectrosc. Radiat. Transfer **116**, 169–183 (2013).

[20] E. M. Purcell and C. R. Pennypacker, "Scattering and absorption of light by nonspherical dielectric grains," Astrophys. J. **186**, 705–714 (1973).

[21] B. T. Draine, "The discrete-dipole approximation and its application to interstellar graphite grains," Astrophys. J. **333**, 848–872 (1988).

[22] B. T. Draine and P. J. Flatau, "Discrete-dipole approximation for scattering calculations," J. Opt. Soc. Amer. A **11**, 1491–1499 (1994).

[23] M. A. Yurkin and A. G. Hoekstra, "The discrete dipole approximation: An overview and recent developments," J. Quant. Spectrosc. Radiat. Transfer **106**, 558–589 (2007).

[24] M. A. Yurkin and A. G. Hoekstra, "The discrete-dipole-approximation code ADDA: Capabilities and known limitations," J. Quant. Spectrosc. Radiat. Transfer **112**, 2234–2247 (2011).

[25] K. S. Yee, "Numerical solution of initial boundary value problems involving Maxwell's equations in isotropic media," IEEE Trans. Antenn. Propag. **Ap14**, 302–307 (1966).

[26] P. Yang and K. N. Liou, "Finite-difference time domain method for light scattering by small ice crystals in three-dimensional space," J. Opt. Soc. Amer. A **13**, 2072–2085 (1996).

[27] W. B. Sun, Q. Fu, and Z. Z. Chen, "Finite-difference time-domain solution of light scattering by dielectric particles with a perfectly matched layer absorbing boundary condition," Appl. Opt. **38**, 3141–3151 (1999).

[28] P. Yang, B. A. Baum, A. J. Heymsfield, Y. X. Hu, H. L. Huang, S. C. Tsay, and S. Ackerman, "Single-scattering properties of droxtals," J. Quant. Spectrosc. Radiat. Transfer **79**, 1159–1169 (2003).

[29] L. Bi, P. Yang, G. W. Kattawar, and R. Kahn, "Single-scattering properties of triaxial ellipsoidal particles for a size parameter range from the rayleigh to geometric-optics regimes," Appl. Opt. **48**, 114–126 (2009).

[30] M. A. Yurkin, V. P. Maltsev, and A. G. Hoekstra, "The discrete dipole approximation for simulation of light scattering by particles much larger than the wavelength," J. Quant. Spectrosc. Radiat. Transfer **106**, 546–557 (2007).

[31] R. S. Brock, X. H. Hu, P. Yang, and J. Q. Lu, "Evaluation of a parallel FDTD code and application to modeling of light scattering by deformed red blood cells," Opt. Express **13**, 5279–5292 (2005).

[32] A. Macke, "Scattering of light by polyhedral ice crystals," Appl. Opt. **32**, 2780–2788 (1993).

[33] A. Macke and M. I. Mishchenko, "Applicability of regular particle shapes in light scattering calculations for atmospheric ice particles," Appl. Opt. **35**, 4291–4296 (1996).

[34] A. Macke, J. Mueller, and E. Raschke, "Single scattering properties of atmospheric ice crystals," J. Atmos. Sci. **53**, 2813–2825 (1996).

[35] P. Yang and K. N. Liou, "Geometric-optics-integral-equation method for light scattering by nonspherical ice crystals," Appl. Opt. **35**, 6568–6584 (1996).

[36] P. Yang and K. N. Liou, "Light scattering by hexagonal ice crystals: solutions by a ray-by-ray integration algorithm," J. Opt. Soc. Amer. A **14**, 2278–2289 (1997).

[37] L. Bi, P. Yang, G. W. Kattawar, B. A. Baum, Y. X. Hu, D. M. Winker, R. S. Brock, and J. Q. Lu, "Simulation of the color ratio associated with the backscattering of radiation by ice particles at the wavelengths of 0.532 and 1.064 μm," J. Geophys. Res. **114**, D00H08, doi:10.1029/2009JD011759 (2009).

[38] L. Bi, P. Yang, G. W. Kattawar, Y. X. Hu, and B. A. Baum, "Scattering and absorption of light by ice particles: Solution by a new physical-geometric optics hybrid method," J. Quant. Spectrosc. Radiat. Transfer **112**, 1492–1508 (2011).

[39] C. Magono and C. W. Lee, "Meteorological classification of natural snow crystals," J. Faculty Sci. Hokkaido University **2**, 321–335 (1966).

[40] J. D. Cross, "Study of the surface of ice with a scanning electron microscope," in "Physics of ice," , N. Riehl, B. Bullemer, and H. Engelhardt, eds. (Plenum Press, New York, NY, 1968), pp. 81–94.

[41] H. Volten, O. Munoz, E. Rol, J. F. de Haan, W. Vassen, J. W. Hovenier, K. Muinonen, and T. Nousiainen, "Scattering matrices of mineral aerosol particles at 441.6 nm and 632.8 nm," J. Geophys. Res. **106**, 17375–17401 (2001).

[42] Z. Ulanowski, E. Hesse, P. H. Kaye, and A. J. Baran, "Light scattering by complex ice-analogue crystals," J. Quant. Spectrosc. Radiat. Transfer **100**, 382–392 (2006).

[43] M. Bailey and J. Hallett, "Growth rates and habits of ice crystals between -20^o and -70^o C: Confirmation from wave cloud studies," J. Atmos. Sci. **61**, 514–544 (2004).

[44] K. Adachi, S. H. Chung, and P. R. Buseck, "Shapes of soot aerosol particles and implications for their effects on climate," J. Geophys. Res. **115**, D15206, doi:10.1029/2009JD012868 (2010).

[45] M. Kahnert, T. Nousiainen, and P. Mauno, "On the impact of non-sphericity and small-scale surface roughness on the optical properties of hematite aerosols," J. Quant. Spectrosc. Radiat. Transfer **112**, 1815–1824 (2011).

[46] L. Bi, P. Yang, G. W. Kattawar, and R. Kahn, "Modeling optical properties of mineral aerosol particles by using nonsymmetric hexahedra," Appl. Opt. **49**, 334–342 (2010).

[47] P. Yang, G. W. Kattawar, G. Hong, P. Minnis, and Y. X. Hu, "Uncertainties associated with the surface texture of ice particles in satellite-based retrieval of cirrus clouds - Part I: Single-scattering properties of ice crystals with surface roughness," IEEE Trans. Geosci. Remote Sens. **46**, 1940–1947 (2008).

[48] P. Yang, G. Hong, G. W. Kattawar, P. Minnis, and Y. X. Hu, "Uncertainties associated with the surface texture of ice particles in satellite-based retrieval of cirrus clouds - Part II: Effect of particle surface roughness on retrieved cloud optical thickness and effective particle size," IEEE Trans. Geosci. Remote Sens. **46**, 1948–1957 (2008).

[49] J. D. Jackson, *Classical electrodynamics* (John Wiley & Sons, Hoboken, NJ, 1999), 3rd ed.

[50] K. N. Liou, *An introduction to atmospheric radiation* (Academic Press, San Diego, CA, 2002).

[51] W. Wendisch and P. Yang, *Theory of atmospheric radiative transfer* (Wiley-VCH, Weinheim, Germany, 2012).

[52] H. O. Kreiss and J. Oliger, "Comparison of accurate methods for the integration of hyperbolic equations," Tellus **24**, 199–215 (1972).

[53] S. A. Orszag, "Comparison of pseudospectral and spectral approximation," Stud. Appl. Math. **51**, 253–259 (1972).

[54] Q. H. Liu, "The PSTD algorithm: A time-domain method requiring only two cells per wavelength," Microw. Opt. Tech. Lett. **15**, 158–165 (1997).

[55] Q. H. Liu, "The pseudospectral time-domain (PSTD) method: A new algorithm for solutions of Maxwell's equations," IEEE Antenn. Propag. Soc. International Symposium **1**, 122–125 (1997).

[56] Q. H. Liu, "The pseudospectral time-domain (PSTD) algorithm for acoustic waves in absorptive media," IEEE Trans. Ultrason. Ferr. **45**, 1044–1055 (1998).

[57] Q. H. Liu, "PML and PSTD algorithm for arbitrary lossy anisotropic media," IEEE Microw. Guid. Wave. Lett. **9**, 48–50 (1999).

[58] B. Yang, D. Gottlieb, and J. S. Hesthaven, "Spectral simulations of electromagnetic wave scattering," J. Comput. Phys. **134**, 216–230 (1997).

[59] B. Yang and J. S. Hesthaven, "A pseudospectral method for time-domain computation of electromagnetic scattering by bodies of revolution," IEEE Trans. Antenn. Propag. **47**, 132–141 (1999).

[60] B. Yang and J. S. Hesthaven, "Multidomain pseudospectral computation of Maxwell's equations in 3-D general curvilinear coordinates," Appl. Numer. Math. **33**, 281–289 (2000).

[61] B. Tian and Q. H. Liu, "Nonuniform fast cosine transform and Chebyshev PSTD algorithms," J. Electromagnet Wave. **14**, 797–798 (2000).

[62] G. Chen, P. Yang, and G. W. Kattawar, "Application of the pseudospectral time-domain method to the scattering of light by nonspherical particles," J. Opt. Soc. Amer. A **25**, 785–790 (2008).

[63] G. Chen, "Modeling of the optical properties of nonspherical particles in the atmosphere," Ph.D. thesis, Texas A&M University (2007).

[64] S. D. Gedney, "An anisotropic perfectly matched layer-absorbing medium for the truncation of FDTD lattices," IEEE Trans. Antenn. Propag. **44**, 1630–1639 (1996).

[65] R. L. Panetta, C. Liu, and P. Yang, "A pseudo-spectral time domain method for light scattering computations," in "Light scattering reviews 8," , A. A. Kokhanovsky, ed. (Springer-Praxis, Chichester, UK, 2013), pp. 139–188.

[66] J. S. Hesthaven, S. Gottlieb, and D. Gottlieb, *Spectral methods for time-dependent problems* (Cambridge University Press, New York, NY, 2007).

[67] J. P. Berenger, "A perfectly matched layer for the absorption of electromagnetic-waves," J. Comput. Phys. **114**, 185–200 (1994).

[68] Z. S. Sacks, D. M. Kingsland, R. Lee, and J. F. Lee, "A perfectly matched anisotropic absorber for use as an absorbing boundary condition," IEEE Trans. Antenn. Propag. **43**, 1460–1463 (1995).

[69] J. P. Berenger, "Three-dimensional perfectly matched layer for the absorption of electromagnetic waves," J Comput Phys **127**, 363–379 (1996).

[70] P. W. Zhai, C. H. Li, G. W. Kattawar, and P. Yang, "FDTD far-field scattering amplitudes: Comparison of surface and volume integration methods," J. Quant. Spectrosc. Radiat. Transfer **106**, 590–594 (2007).

[71] M. A. Yurkin, A. G. Hoekstra, R. S. Brock, and J. Q. Lu, "Systematic comparison of the discrete dipole approximation and the finite difference time domain method for large dielectric scatterers," Opt. Express **15**, 17902–17911 (2007).

[72] S. G. Warren and R. E. Brandt, "Optical constants of ice from the ultraviolet to the microwave: A revised compilation," J. Geophys. Res. **113**, D14220, doi:10.1029/2007JD009744 (2008).

[73] P. Yang, G. W. Kattawar, K. N. Liou, and J. Q. Lu, "Comparison of cartesian grid configurations for application of the finite-difference time-domain method to electromagnetic scattering by dielectric particles," Appl. Opt. **43**, 4611–4624 (2004).

[74] W. B. Sun and Q. Fu, "Finite-difference time-domain solution of light scattering by dielectric particles with large complex refractive indices," Appl. Opt. **39**, 5569–5578 (2000).

[75] P. W. Zhai, Y. K. Lee, G. W. Kattawar, and P. Yang, "Implementing the near-to far-field transformation in the finite-difference time-domain method," Appl. Opt. **43**, 3738–3746 (2004).

[76] Y. You, G. W. Kattawar, P. W. Zhai, and P. Yang, "Zero-backscatter cloak for aspherical particles using a generalized DDA formalism," Opt. Express **16**, 2068–2079 (2008).

[77] B. T. Draine and P. J. Flatau, "User guide for the discrete dipole approximation code DDSCAT 7.1," http://arxiv.org/abs/1002.1505 (2010).

[78] K. V. Gilev, E. Eremina, M. A. Yurkin, and V. P. Maltsev, "Comparison of the discrete dipole approximation and the discrete source method for simulation of light scattering by red blood cells," Opt. Express **18**, 5681–5690 (2010).

[79] O. Munoz, F. Moreno, D. Guirado, D. D. Dabrowska, H. Volten, and J. W. Hovenier, "The Amsterdam-Granada light scattering database," J. Quant. Spectrosc. Radiat. Transfer **113**, 565–574 (2012).

[80] N. B. Piller and O. J. F. Martin, "Increasing the performance of the coupled-dipole approximation: A spectral approach," IEEE Trans. Antenn. Propag. **46**, 1126–1137 (1998).

[81] M. A. Yurkin, M. Min, and A. G. Hoekstra, "Application of the discrete dipole approximation to very large refractive indices: Filtered coupled dipoles revived," Phys. Rev. E **82**, 036703 (2010).

[82] A. Bunse-Gerstner and R. Stover, "On a conjugate gradient-type method for solving complex symmetric linear systems," Linear Algebra Appl. **287**, 105–123 (1999).

[83] I. Ayranci, R. Vaillon, and N. Selcuk, "Performance of discrete dipole approximation for prediction of amplitude and phase of electromagnetic scattering by particles," J. Quant. Spectrosc. Radiat. Transfer **103**, 83–101 (2007).

[84] M. Kahnert, T. Nousiainen, and B. Veihelmann, "Spherical and spheroidal model particles as an error source in aerosol climate forcing and radiance computations: A case study for feldspar aerosols," J. Geophys. Res. **110**, D18S13, doi:10.1029/2004JD005558 (2005).

[85] H. Volten, O. Munoz, J. W. Hovenier, and L. B. F. M. Waters, "An update of the Amsterdam light scattering database," J. Quant. Spectrosc. Radiat. Transfer **100**, 437–443 (2006).

[86] P. Yang, Q. Feng, G. Hong, G. W. Kattawar, W. J. Wiscombe, M. I. Mishchenko, O. Dubovik, I. Laszlo, and I. N. Sokolik, "Modeling of the scattering and radiative properties of nonspherical dust-like aerosols," J. Aerosol Sci. **38**, 995–1014 (2007).

[87] S. R. Osborne, B. T. Johnson, J. M. Haywood, A. J. Baran, M. A. J. Harrison, and C. L. McConnell, "Physical and optical properties of mineral dust aerosol during the dust and biomass-burning experiment," J. Geophys. Res. **113**, D00C03, doi:10.1029/2007JD009551 (2008).

[88] S. R. Osborne, A. J. Baran, B. T. Johnson, J. M. Haywood, E. Hesse, and S. Newman, "Short-wave and long-wave radiative properties of Saharan dust aerosol," Q. J. Roy. Metor. Soc. **137**, 1149–1167 (2011).

[89] J. M. Haywood, B. T. Johnson, S. R. Osborne, A. J. Baran, M. Brooks, S. F. Milton, J. Mulcahy, D. Walters, R. P. Allan, A. Klaver, P. Formenti, H. E. Brindley, S. Christopher, and P. Gupta, "Motivation, rationale and key results from the GERBILS Saharan dust measurement campaign," Q. J. Roy. Metor. Soc. **137**, 1106–1116 (2011).

[90] M. I. Mishchenko, A. A. Lacis, B. E. Carlson, and L. D. Travis, "Nonsphericity of dust-like tropospheric aerosols - implications for aerosol remote-sensing and climate modeling," Geophys. Res. Lett. **22**, 1077–1080 (1995).

[91] E. Zubko, K. Muinonen, Y. Shkuratov, G. Videen, and T. Nousiainen, "Scattering of light by roughened Gaussian random particles," J. Quant. Spectrosc. Radiat. Transfer **106**, 604–615 (2007).

[92] S. Merikallio, H. Lindqvist, T. Nousiainen, and M. Kahnert, "Modelling light scattering by mineral dust using spheroids: assessment of applicability," Atmos. Chem. Phys. **11**, 5347–5363 (2011).

[93] T. Nousiainen, M. Kahnert, and B. Veihelmann, "Light scattering modeling of small feldspar aerosol particles using polyhedral prisms and spheroids," J. Quant. Spectrosc. Radiat. Transfer **101**, 471–487 (2006).

[94] E. Zubko, K. Muinonen, O. Munoz, T. Nousiainen, Y. Shkuratov, W. Sun, and G. Videen, "Light scattering by feldspar particles: Comparison of model agglomerate debris particles with laboratory samples," J. Quant. Spectrosc. Radiat. Transfer **in press** (2013).

[95] B. B. Mandelbrot, *The fractal geometry of nature* (W. H. Freeman and Company, New York, NY, 1983).

[96] K. J. Falconer, *Fractal geometry: mathematical foundations and applications* (Wiley, London, UK, 2003).

[97] A. Macke and F. Tzschichholz, "Scattering of light by 2-dimensional deterministic Koch islands," Physica A **191**, 545–548 (1992).

[98] A. A. Kokhanovsky, *Polariztion optics of random media* (Springer Paxis Publishing, Chichester, UK, 2003).

[99] A. A. Kokhanovsky, *Light scattering media optics: problems and solutions* (Springer Praxis Publishing, Chichester, UK, 2004).

[100] A. J. M. Clarke, E. Hesse, Z. Ulanowski, and P. H. Kaye, "A 3D implementation of ray tracing combined with diffraction on facets: Verification and a potential application," J. Quant. Spectrosc. Radiat. Transfer **100**, 103–114 (2006).

[101] E. Hesse, "Modelling diffraction during ray tracing using the concept of energy flow lines," J. Quant. Spectrosc. Radiat. Transfer **109**, 1374–1383 (2008).

[102] O. Dubovik, A. Sinyuk, T. Lapyonok, B. N. Holben, M. Mishchenko, P. Yang, T. F. Eck, H. Volten, O. Munoz, B. Veihelmann, W. J. van der Zande, J. F. Leon, M. Sorokin, and I. Slutsker, "Application of spheroid models to account for aerosol particle nonsphericity in remote sensing of desert dust," J. Geophys. Res. **111**, D11208, doi:10.1029/2005JD006619 (2006).

[103] M. O. Andreae, "Aerosols before pollution," Science **315**, 50–51 (2007).

[104] N. Meskhidze, J. Xu, B. Gantt, Y. Zhang, A. Nenes, S. J. Ghan, X. Liu, R. Easter, and R. Zaveri, "Global distribution and climate forcing of marine organic aerosol: 1. model improvements and evaluation," Atmos. Chem. Phys. **11**, 11689–11705 (2011).

[105] U. Poschl, "Atmospheric aerosols: Composition, transformation, climate and health effects," Angew. Chem. Int. Edit **44**, 7520–7540 (2005).

[106] P. Chylek, G. Videen, D. J. W. Geldart, J. S. Dobie, and H. C. W. Tso, "Effective medium approximations for heterogeneous particles," in "Light scattering

by nonspherical particles: theory, measurements, and applications," , M. I. Mishchenko, J. W. Hovenier, and L. D. Travis, eds. (Academic Press, San Diego, CA, 2000), pp. 273–308.

[107] L. Kolokolova and B. A. S. Gustafson, "Scattering by inhomogeneous particles: microwave analog experiments and comparison to effective medium theories," J. Quant. Spectrosc. Radiat. Transfer **70**, 611–625 (2001).

[108] J. C. M. Garnett, "Colours in metal glasses and in metallic films," Phil. Trans. Roy. Soc. Lond. **203**, 385–420 (1904).

[109] J. C. M. Garnett, "Colours in metal glasses, in metallic films, and in metallic solutions - II," Phil. Trans. Roy. Soc. Lond. **205**, 237–288 (1906).

[110] D. R. Longtin, E. P. Shetle, J. R. Hummel, and J. D. Pryce, "A wind dependent desert aerosol model: radiative properties," Tech. rep., AFGL-TR-88-0112, Air Force Geophysics Laboratory (1988).

[111] D. A. G. Bruggeman, "The calculation of various physics constants of heterogenous substances I: The dielectric constants and conductivities of mixtures composed of isotropic substances," Annalen Der Physik **24**, 636–664 (1935).

[112] X. C. Zeng, D. J. Bergman, P. M. Hui, and D. Stroud, "Effective-medium theory for weakly nonlinear composites," Phys. Rev. B **38**, 10970–10973 (1988).

[113] I. N. Sokolik and O. B. Toon, "Incorporation of mineralogical composition into models of the radiative properties of mineral aerosol from uv to ir wavelengths," J. Geophys. Res. **104**, 9423–9444 (1999).

[114] O. V. Kalashnikova and I. N. Sokolik, "Modeling the radiative properties of nonspherical soil-derived mineral aerosols," J. Quant. Spectrosc. Radiat. Transfer **87**, 137–166 (2004).

[115] P. Chylek, V. Srivastava, R. G. Pinnick, and R. T. Wang, "Scattering of electromagnetic-waves by composite spherical-particles - experiment and effective medium approximations," Appl. Opt. **27**, 2396–2404 (1988).

[116] J. M. Perrin and P. L. Lamy, "On the validity of effective-medium theories in the case of light extinction by inhomogeneous dust particles," Astrophys. J. **364**, 146–151 (1990).

[117] N. V. Voshchinnikov, G. Videen, and T. Henning, "Effective medium theories for irregular fluffy structures: aggregation of small particles," Appl. Opt. **46**, 4065–4072 (2007).

[118] C. Liu, R. L. Panetta, and P. Yang, "The influence of water coating on the optical scattering properties of fractal soot aggregates," Aerosol Sci. Tech. **46**, 31–43 (2012).

[119] V. Lucarini, K. Peiponen, J. J. Saarinen, and E. M. Vartiaiene, *Kramers-Kronig relations in optical material research* (Springer, New York, NY, 2005).

[120] T. C. Bond, G. Habib, and R. W. Bergstrom, "Limitations in the enhancement of visible light absorption due to mixing state," J. Geophys. Res. **111**, D20211, doi:10.1029/2006JD007315 (2006).

[121] A. D. Clarke, Y. Shinozuka, V. N. Kapustin, S. Howell, B. Huebert, S. Doherty, T. Anderson, D. Covert, J. Anderson, X. Hua, K. G. Moore, C. McNaughton, G. Carmichael, and R. Weber, "Size distributions and mixtures of dust and

black carbon aerosol in Asian outflow: Physiochemistry and optical properties," J. Geophys. Res. **109**, D15S09, doi:10.1029/2003JD004378 (2004).

[122] K. Adachi, E. J. Freney, and P. R. Buseck, "Shapes of internally mixed hygroscopic aerosol particles after deliquescence, and their effect on light scattering," Geophys. Res. Lett. **38**, L13804, doi:10.1029/2011GL047540 (2011).

[123] M. O. Andreae, R. J. Charlson, F. Bruynseels, H. Storms, R. Vangrieken, and W. Maenhaut, "Internal mixture of sea salt, silicates, and excess sulfate in marine aerosols," Science **232**, 1620–1623 (1986).

[124] G. B. Ellison, A. F. Tuck, and V. Vaida, "Atmospheric processing of organic aerosols," J. Geophys. Res. **104**, 11633–11641 (1999).

[125] J. P. Schwarz, J. R. Spackman, D. W. Fahey, R. S. Gao, U. Lohmann, P. Stier, L. A. Watts, D. S. Thomson, D. A. Lack, L. Pfister, M. J. Mahoney, D. Baumgardner, J. C. Wilson, and J. M. Reeves, "Coatings and their enhancement of black carbon light absorption in the tropical atmosphere," J. Geophys. Res. **113**, D03203, doi:10.1029/2007JD009042 (2008).

[126] W. C. Pfalzgraff, R. M. Hulscher, and S. P. Neshyba, "Scanning electron microscopy and molecular dynamics of surfaces of growing and ablating hexagonal ice crystals," Atmos. Chem. Phys. **10**, 2927–2935 (2010).

[127] A. J. Baran, "From the single-scattering properties of ice crystals to climate prediction: A way forward," Atmos. Res. **112**, 45–69 (2012).

[128] B. A. Baum, P. Yang, Y. X. Hu, and Q. Feng, "The impact of ice particle roughness on the scattering phase matrix," J. Quant. Spectrosc. Radiat. Transfer **111**, 2534–2549 (2010).

[129] C. H. Li, G. W. Kattawar, and P. Yang, "Effects of surface roughness on light scattering by small particles," J. Quant. Spectrosc. Radiat. Transfer **89**, 123–131 (2004).

[130] M. Kahnert, T. Nousiainen, M. A. Thomas, and J. Tyynela, "Light scattering by particles with small-scale surface roughness: Comparison of four classes of model geometries," J. Quant. Spectrosc. Radiat. Transfer **113**, 2356–2367 (2012).

[131] T. Nousiainen and K. Muinonen, "Surface-roughness effects on single-scattering properties of wavelength-scale particles," J. Quant. Spectrosc. Radiat. Transfer **106**, 389–397 (2007).

[132] M. Kahnert and T. Rother, "Modeling optical properties of particles with small-scale surface roughness: combination of group theory with a perturbation approach," Opt. Express **19**, 11138–11151 (2011).

[133] M. Doutriaux-Boucher, J. C. Buriez, G. Brogniez, L. C. Labonnote, and A. J. Baran, "Sensitivity of retrieved POLDER directional cloud optical thickness to various ice particle models," Geophys. Res. Lett. **27**, 109–112 (2000).

[134] A. J. Baran and L. C. Labonnote, "A self-consistent scattering model for cirrus. I: The solar region," Q. J. Roy. Metor. Soc. **133**, 1899–1912 (2007).

[135] B. H. Cole, P. Yang, B. A. Baum, J. Riedi, L. C. Labonnote, F. Thieuleux, and S. Platnick, "Comparison of PARASOL observations with polarized reflectances simulated using different ice habit mixtures," J. Appl. Meteor. Clim. **52**, 186–196 (2013).

[136] W. B. Sun, N. G. Loeb, G. Videen, and Q. Fu, "Examination of surface roughness on light scattering by long ice columns by use of a two-dimensional finite-difference time-domain algorithm," Appl. Opt. **43**, 1957–1964 (2004).

[137] K. Muinonen, "Light scattering by Gaussian random particles," Earth Moon Planets **72**, 339–342 (1996).

[138] K. Muinonen, T. Nousiainen, P. Fast, K. Lumme, and J. I. Peltoniemi, "Light scattering by Gaussian random particles: Ray optics approximation," J. Quant. Spectrosc. Radiat. Transfer **55**, 577–601 (1996).

[139] K. Muinonen and K. Saarinen, "Ray optics approximation for Gaussian random cylinders," J. Quant. Spectrosc. Radiat. Transfer **64**, 201–218 (2000).

[140] K. Muinonen, E. Zubko, J. Tyynela, Y. G. Shkuratov, and G. Videen, "Light scattering by Gaussian random particles with discrete-dipole approximation," J. Quant. Spectrosc. Radiat. Transfer **106**, 360–377 (2007).

[141] P. Yang and K. N. Liou, "Single-scattering properties of complex ice crystals in terrestrial atmosphere," Contr. Atmos. Phys. **71**, 223–248 (1998).

[142] C. Cox and W. Munk, "Measurement of the roughness of the sea surface from photographs of the Sun's glitter," J. Opt. Soc. Amer. A **44**, 838–850 (1954).

[143] V. Shcherbakov, J. F. Gayet, B. Baker, and P. Lawson, "Light scattering by single natural ice crystals," J. Atmos. Sci. **63**, 1513–1525 (2006).

[144] F. Schwenger and E. Repasi, "Sea surface simulation for testing of multiband imaging sensors," Proc. SPIE **5075**, 72–84 (2003).

[145] Y. You, P. W. Zhai, G. W. Kattawar, and P. Yang, "Polarized radiance fields under a dynamic ocean surface: a three-dimensional radiative transfer solution," Appl. Opt. **48**, 3019–3029 (2009).

[146] P. Yang, L. Bi, B. A. Baum, K. N. Liou, G. W. Kattawar, M. I. Mishchenko, and B. Cole, "Spectrally consistent scattering, absorption, and polarization properties of atmospheric ice crystals at wavelengths from 0.2 to 100 μm," J. Atmos. Sci. **70**, 330–347 (2013).